An investigation of magnetic nanofluids for various thermal applications

Rong Fu, MEng., MSc., BSc.

Thesis submitted to the University of Nottingham
for the degree of Doctor of Philosophy

April 2017

Abstract

Magnetic nanofluid (MNF) is one special kind of nanofluid which possesses both magnetic and fluid properties. Nowadays, extensive attention has been focussed on development of thermal applications. Investigations of magnetic hyperthermia are emerging as a new frontier in studies of cancer therapy. The theory of treatment is based on the fact that magnetic nanoparticles produce heat under an AC magnetic field *via* a mechanism called magnetic losses. Facing with the present technical limits and growing demands for safe treatment, researchers have realized the advantage of assembling superparamagnetic nanoparticles (SMNP) into colloidal clusters for effective heating at low field intensity and frequency. In contrary to the isolated particles, the magnetic losses of the clusters are affected by inter-particle dipole interactions. The role of dipole interactions is complex and contradictory findings have been reported. Understanding the role of dipole interactions is the key to optimizing the clusters for efficient hyperthermia heating.

Magnetic nanofluids have also been proven to be a highly thermally conductive working fluid. The dispersed SMNPs enable control over the fluid's thermal physical properties, flow and heat transfer processes via an external magnetic field. The main challenges include how to improve the applicability of theoretical models on predicting thermal physical properties

and interpreting the role of particle migration during a convective heat transfer process. Numerous results suggested that their anomalous physical properties should be attributed to particle aggregation since it changes the effective particle concentration and generates thermal percolation paths. Also, the rate of particle migration is heavily dependent of the size of aggregates. Therefore, it is necessary to study the effect of colloidal stability on thermal physical properties and convective heat transfer enhancement of the magnetic nanofluid.

At the beginning of this doctoral research project, we investigated the effect of dipole interactions on hyperthermia heating cluster composed of multi SMNPs by time-quantified Monte Carlo simulation. The cluster's shape is characterized by treating it as an equivalent ellipsoid. When the shape is highly anisotropic such as in chain and cylinder, dipole interactions not only facilitate the magnetization process but also impede the demagnetization process by aligning the individual moments to the cluster's morphology anisotropy axis. Thus, the heating capability of chain and cylinder clusters are superior to non-interacting particles at the most angles between the field direction and morphology anisotropy axis. At high field intensity, the influence of dipole interactions on magnetic losses will be reduced to a minimum once the cluster loses its morphology anisotropy (i.e. cube or sphere); the probability to obtain improved heating becomes very low.

Then, experimental and theoretical works were conducted together to find out how to improve the heating ability of anisotropic-less clusters at lower field intensity and frequency. Hydrophobic Fe_3O_4 nanoparticles were assembled into sphere-like clusters using the emulsion droplet evaporation method. The hydrodynamic size of the cluster was controlled within the range of 70 – 140 nm. An induction heating system equipped with an Optic-fiber thermometer was set up to test the heating efficiency of as - prepared Fe_3O_4 clusters with different size. Meanwhile, standard Monte Carlo simulation was performed to study the contribution of dipole interactions at different sizes. The findings suggested that if one expects anisotropic-less clusters to heat better, he should reduce the cluster's size so that the clusters are in forms of dimer and/or trimers or use SMNP with high magnetization and magneto-crystalline anisotropy.

Finally, a stable and surfactant-free magnetic nanofluid was prepared for study of convective heat transfer enhancement. Ethylene glycol and water mixture was selected as the base liquid, which is often used for cooing an automotive engine. The surfaces of Fe_3O_4 nanoparticles were modified with citric acid to make the colloidal stability sensitive to the pH of the particle suspension. It was found that the density and specific heat of obtained MNF can be interpreted well by mixing theory and thermal equilibrium model respectively.

After the colloidally stability was optimized, the MNF exhibited Newtonian behavior. The viscosity barely changed with the shear rate despite variances in particle concentration and temperature. A modified Krieger and Dougherty model was used to explain the relationship between the size of aggregates and viscosity. Meanwhile, we found that the thermal conductivity can be predicted by the Maxwell model, which presumes the nanofluid has common features with a solid–liquid mixture. At last, it was demonstrated that the convective heat transfer coefficient of our MNF was 10 % higher than that of base liquid at transition and turbulent flow.

Publications

- Rong Fu, Yuying Yan, Mustafa Alsaady, Zeyu Liu, Yiyi Chen, Xiangrui Meng, Yong Shi, The effect of colloidal stability on viscosity of dispersant - free Fe3O4 ethylene glycol - water nanofluid, *Scientific Reports*, 2017, under revision.

- Rong Fu, Yuying Yan, Clive Roberts, Study of the effect of dipole interactions on hyperthermia heating the cluster composed of superparamagnetic nanoparticles, *AIP Advances*, 2015, 5, 127232.

- Mustafa Alsaady, Rong Fu, Bo Li, Rabah Boukhanouf and Yuying Yan, Thermo-physical properties and thermo-magnetic convection of ferrofluid, *Appl. Therm. Eng.*, 2015, 88(5), 14-21.

- Mustafa Alsaady, Rong Fu, Zeyu Liu, Yuying Yan, Shenyi Wu, Rabah Boukhanouf, An experimental investigation on the effect of ferrofluids on the efficiency of novel parabolic trough solar collector under laminar flow conditions, Heat Transfer Engineering, 2017, accepted.

- Rong Fu, Yuying Yan, The effect of the size of sphere-like clusters of magnetic nanoparticles on hyperthermia heating, The 5th International Conference of Bionic Engineering, June 21-24 2016, Ningbo, China

- Rong Fu, Clive Roberts, Yuying Yan, The study of the influence of morphology anisotropy of clusters of superparamagnetic nanoparticle on magnetic hysteresis by Monte Carlo simulations, 4th Micro and Nano Flows Conference, September 7-10 2014, London, UK.
- Rong Fu, Yuying Yan, Colloidal magnetic clusters for hyperthermia heating, Proceedings of the 15th International Heat Transfer Conference, August 10-15 2014, Kyoto, Japan.

Acknowledgements

I wish to express my deepest gratitude to Prof. Yuying Yan and Prof. Clive Roberts for their supervision and support throughout my PhD studies. I would like to thank the staff and technicians in SRB Building. Special thanks to Mr. Andy Mattews and Mr. Tony Gospel for test rig building. I would like to thank Dr. Bo Li, Dr. Xiangrui Meng, Miss Yiyi Chen, Mr. Zeyu Liu, Mr. Wei Gong and Mr. Kuo Huang for their kind supports in rig building, data collection, code programming and results discussion, and all others who have helped me throughout my study in Nottingham.

A special thank goes to Dr. Xianghui Hou. He kindly allows me to use his lab in L2 building for chemical synthesis.

At the last but not least, I am extremely grateful to my parents for their encouragement and support over these years.

Contents

List of Tables

List of Figures

Chapter 2

Chapter 3

Chapter 4

Chapter 5

Chapter 6

Nomenclature

Roman letters

A	The longest semi-principal axis of the equivalent ellipsoid of cluster
a	Coefficient of aperture angle
A_{001}	Integration of Z component of magnetization against Z component of magnetization of magnetic field
$A_{cluster}$	Hysteresis loop area of cluster
$A_{isolated}$	Hysteresis loop area of non-interacting particles
A_M	Hysteresis loop area
B (in chapter 2)	Magnetic induction (T)
B (in chapter 3, 4, 5)	The medium semi-principal axis of the equivalent ellipsoid of cluster
B_R	Remnant flux density (T)
c	Particle mass per tissue volume (g/cm^3)
C	The shortest semi-principal axis of the equivalent ellipsoid of cluster
$C_{p,bl}$	Specific heat capacity of base liquid (J/(g K))
$C_{p,f}$	Specific heat of fluid
$C_{p,n}$	Specific heat capacity of particle (J/(g K))
$C_{p,nf}$	Specific heat capacity of magnetic nanofluid (J/(g K))
d	The length of semi-principal axis of the equivalent ellipsoid of cluster

d_f	Fractal dimension of aggregates
D_H	Hydrodynamic diameter
D_{in}	Inner diameter of copper pipe
D_{loop}	Diameter of induction wire loop (m)
D_{out}	Outer diameter of copper pipe
E	Energy
E_A	Magnetic anisotropy energy of particle (J/ m^3)
E_d	The energy of dipole interaction (J/ m^3)
E_{DISM}	The total energy of dipole interactions when a cluster is fully magnetized
E_H	Zeeman energy (J/ m^3)
f	Field frequency (Hz)
H	Intensity of magnetic field (A/m)
h	Convective heat transfer coefficient
H_0	Field amplitude (A/m)
H_a	Anisotropy field
H_c	Coercivity (A/m)
H_{dip}	Vector of dipolar field
H_{eff}	Effective magnetic field
K	Anisotropy constant
k_B	Boltzmann constant
k_{bl}	Thermal conductivity of base liquid(W/(K m))
k_{copper}	Thermal conductivity of copper
K_{eff}	Effective magnetic anisotropy constant of individual

	particle (J/m^3)
k_f	Thermal conductivity of fluid
k_{nf}	Thermal conductivity of nanofluid (W/(K m))
k_p	Thermal conductivity of particles (W/(K m))
k_r	Relative thermal conductivity of nanofluid (W/(K m))
K_S	Surface anisotropy (J/m^2)
k_t	thermal conductivity of tissue (W/(K m))
K_V	Volume anisotropy constant
L	Length of the copper pipe
M	Magnetization (A/m)
m	Mass of magnetic material of magnetic nanofluid (g)
M	Magnetization
M_d	Domain magnetization (A/m)
M_{max}	Maximum magnetization
M_r	Remanence magnetization (A/m)
M_s	Saturation magnetization (A/m)
N_c	The number of clusters
N_{cycle}	The number of field cycle
N_{MCS}	The number of Monte Carlo step per field cycle
P	Volumetric heating power of magnetic nanofluid (W/m^3)
Q	Added heat (J/ m^3)
q	Added heat flux
R	Radius of tumor (cm)

r_a	Radius of aggregates
r_m	Radius of particle's magnetic fraction (nm)
r_p	Radius of particle
r_{sphere}	Radius of large sphere in which particles are set to undergo elastic collisions (nm)
S	Surface area of particle's magnetic fraction (m^2)
T	Temperature (K)
t	Time (s)
T_B	Blocking temperature (K)
t_f	Temperature of fluid
T_I	The moment of inertia tensor
t_{in}	Inlet temperature
t_{out}	Outlet temperature
t_{step}	Time step
$t_{w,in}$	Inner wall temperature of copper pipe
U	Inner energy of unit volume (J/ m^3)
u	Velocity of fluid
v	Switching rate
V_H	Hydrodynamic volume of particle (m^3)
V_{nf}	Volume of magnetic nanofluid (mL)
V_p	Volume of particle (m^3)
v_r	Reduction rate of the radius of large sphere in which particles are set to undergo elastic collisions (nm/s)
W	Magnetic work (J/ m^3)

Greek letter

ρ_{bl}	Density of base liquid (g/cm^3)
ρ_{nf}	Density of magnetic nanofluid (g/ml)
$\rho_{s,m}$	Mass of magnetic part per unit volume of particle (g/cm^3)
ρ_s	Density of particle (g/cm^3)
ϕ_a	Effective volume fraction of particles
ϕ_m	Volume fraction of densely packed particles
μ_{bl}	Dynamic viscosity of the base liquid ((N·s)/m^2)
μ_f	Dynamic viscosity at bulk temperature of fluid
μ_{nf}	Dynamic viscosity of nanofluid
μ_r	Relative viscosity of nanofluid
$\mu_{w,f}$	Dynamic viscosity at the temperature of inner wall of copper pipe
α	Dimensionless Gilbert damping factor
γ	Gyromagnetic ratio
$\delta\theta$	Aperture angle
θ	Angle (^{o})
θ_{MA}	Angle between the magnetization direction and the axis of morphology anisotropy of cluster
λ	Principal moments of inertia of a cluster
μ_0	Vacuum magnetic permeability (N/A^2)
ξ	Langevin parameter
τ_0	Attempt time (s)

τ_B	Brownian relaxation time (s)
τ_e	Effective relaxation time (s)
τ_N	Nèel relaxation time (s)
φ	Volume fraction of particles
χ	Magnetic susceptibility
χ_0	Static susceptibility
φ	Angle (^{o})

Abbreviations

AMA	Axis of morphology anisotropy
CA	Citric acid
DLS	Dynamic light scattering measurement
DSC	Differential Scanning Calorimeter
EG	Ethylene glycol
FCC	Face-centered cubic lattice
FTIR	Fourier transform infrared spectra
HCl	Hydrochloric acid
KMC	Kinetic Monte Carlo simulation
MA	Morphology Anisotropy
MC	Monte Carlo simulation
MCS	Monte Carlo step
MNF	Magnetic nanofluid
MNP	Magnetic nanoparticle

Nu	Nusselt number
OA	Oleic acid
PdI	Polydispersity index
Re	Renold number
RSD	Relative standard deviation
SAR	Specific absorption rate
SDS	Sodium dodecylsulfate
SMNP	Superparamagnetic nanoparticle
TEM	Transmission electron microscopy
TGA	Thermogravimetric analysis
XRD	X-Ray powder diffraction

Chapter 1 Introduction

1.1 General Background

Nanofluid is a liquid suspension of nano - sized particles. The particles are typically made of metal, metal oxide or a semi-conductor. Generally, conventional heat transfer liquids, including oil, water, and ethylene glycol mixture are used as the base liquid to disperse particles and make the suspension flowable. Magnetic nanofluids (MNF), also - called ferrofluids, are the kind of nanofluids whose particles are superparamagnetic. Without an external magnetic field, superparamagnetic nanoparticles (SMNP) behave as non-magnetic ones. Once a field is applied, these particles will react to the field, bringing impacts on the magnetism and physical properties of the whole suspension. MNF was discovered in the 1960s, when the scientists of NASA Research Centre were sorting out liquid manipulation in space. In recent decades, numerous works have been carried out to explore their potential in thermal applications.

Investigations of MNF-based hyperthermia heating treatments are emerging as a new frontier in studies of cancer therapy. [1-6] Hyperthermia is one kind of cancer therapy which treats cancerous tissues by keeping its temperature at 42 - 46^{o}C[7]. This treatment is developed based on the evidences that cancer cells are more sensitive than healthy cells to temperature higher than 41 °C [7-14] and a localized heating of tumor for about 30 min is sufficient to destroy tumor tissue[15]. Much higher temperatures up to 56 °C will cause widespread necrosis, coagulation or carbonization, and this is called “thermal ablation”. [7, 10, 16] Hyperthermia has been recognized as an alternative therapy that can be delivered alone or as an adjunct to radiation and/or chemotherapy to treat cancer[17]. Magnetic hyperthermia is the type of hyperthermia treatment raising the temperature of the tumor by inductively heating pre-implanted MNF with using AC magnetic field. The particles convert the magnetic work done by the field to heat through a mechanism called magnetic losses.

Compared with other thermotherapies,[7, 18-20] magnetic hyperthermia has several advantages. First, a localized hyperthermia treatment is guaranteed. A variety of approaches have been developed to obtain efficient tumor-targeted accumulation of SMNP, including arterial injection of MNF into the supply vessel of the tumor[4], direct injection[10, 21-24], or targeted particle delivery[25-28]. Furthermore, the particles can be confined within a region by means of magnetic forces. Sawyer *et al.* [29]modelled the temperature profile during magnetic hyperthermia, finding that the rise of temperature decreases to zero within 1 mm away from the edge of the tumor. Secondly, the damage to the healthy tissue can be controlled to the lowest level. Magnetic hyperthermia uses radio waves which only heats metal and magnetic materials. Thirdly, such a minute size at level of nanometer allows SMNPs to enter the regions locating deeply in body and/or surrounded by bones, making available the treatments that are difficult for traditional therapy, i.e. brain and prostate cancer[21, 30, 31]. Fourthly, the intensity and duration of treatment can be remote controlled by the adjustment of magnetic field outside of the body. At last but not least, multiple therapic purposes can be achieved by surface modification of MNP, *i.e.* thermo-responsive drug delivery[32].

The efficiency of magnetic hyperthermia are mainly controlled by three processes, including delivery of the energy to particles embedded within the body, conversion of the energy to heat, and transfer of heat to every corner of the tumor[4]. Facing with the present technical limits and the growing demand of reducing the frequency and amplitude for the safety of treatment, scientists in this field place more and more emphasis on optimization of SMNP properties for efficient hyperthermia heating. After using so many kinds of particles, researchers have now started to realize the great potential of using colloidal clusters of multi SMNPs. Such a close packing of particles favours inter-particle dipole interactions, which can enhance magnetic losses at specific conditions. However, the debate about the role of dipole interactions has been continuing for years, and the findings about its influence are quite different, even contradictory[33]. The heating performance of SMNP cluster has not been studied extensively yet, and lots of efforts are required to find out the dominant factors that control the heating efficiency of cluster. Several works suggested that clusters with high morphology anisotropy (*i.e.* in chain or cylinder) should heat better. [33, 34] However, it is much easier to massively prepare size - controlled anisotropic-less cluster in practice. How to improve the heating ability of anisotropic-less cluster is another challenge.

At present, rapid advances in highly integrated circuits and powerful engine systems have given rise to an ever-increasing demand for efficient heat transfer systems with controlled size. Different methods have been proposed to improve the heat transfer performance, which can be mainly classified into active and passive techniques. The former relies on addition of external energy (*e.g.* mechanical agitating, rotating and vibration), while the later involves the works improving thermal properties of working fluids and the surface geometry. Choi[35] came up with the idea of using nanofluid to enhance heat transfer efficiency. Considerable evidence shows that the thermal conductivity of a fluid increases significantly after dispersing particles into the base liquid.[36] The heat capacity of a nanofluid usually decreases with using the particles with lower heat capacity.[37] Moreover, the density of nanofluid is generally higher than the base liquid. Thus, Bigdeli *et al.* [38] suggested that nanofluids may represent a way to reduce the warm up time of a cooling system, which is very beneficial for automotive applications to reduce the catalyst light-off times and therefore reduce tail pipe pollutant emissions. People have found great potential of nanofluids to be novel coolant for electronic[39] and automotive components[40-44].

MNF is superior to other nanofluids since it possesses the magnetic property as well as flowability. Such a unique characteristic enables controlling the particle movement, particle dispersion and fluid flow by means of magnetic forces. It makes possible controlling thermo-physical properties of a MNF by adjusting the intensity and/or orientation of the field.[45, 46] Field – dependent thermal conductivity [47, 48] and magnetoviscous effect[49] have been reported by many works. Specific heat capacity of MNF is also found to be dependent on the field intensity.[50] What's more, when temperature and magnetic gradients co-exist, MNF can generate another new convection loop which is much more intensive than the gravitation one and does not arouse any energy consumption. This natural convection exclusive to MNF is called thermomagnetic convection. It has been suggested to be the solution when cooling of micro-sized geometries is considered. [45] Most importantly, forced convective heat transfer of MNF can be futher improved by means of magnetic forces.

Someone observed that the local Nusselt number was increased by 300 % when a great and constant magnetic gradient was applied. [51]

When nanofluids are considered for heat transfer applications, one of the biggest challenges is how to ensure the colloidal stability of particles in the base liquid. Poor colloidal stability will lead to particles aggregations even precipitations. Large precipitates of particles will cause problems of great pressure drop, clogging of flow channels and corrosion of the components. Furthermore, it is found that uncontrolled particles aggregations lead to anomalous thermo-physical properties of nanofluid.

It is well recognized that there are two main features dominating thermal conductivity of a nanofluid, including Kapitza resistance at the nanoparticle–fluid interface[52] and the thermal percolation paths formed by particle aggregations[53]. The later could be explained by faster heat transfer along a solid structure than through a liquid. In particular, the “chain up” of SMNPs driven by magnetic field can supply a “highway” for heat transfer, when the field is collinear with temperature gradient[48, 54]. However, once the scale of aggregation is beyond a critical level, it will turn to decrease thermal conductivity[38] because the major part of fluid is empty of particles. If particles undergo uncontrolled aggregations, no theory will be found useful to predict the thermal conductivity.

Moreover, aggregations may turn a nanofluid to a non - Newtonian fluid, regardless of whether the particles are magnetic or not. Shear thinning of nanofluids has been reported by many researchers who observed that the viscosity decreased with the shear rate during rheological measurements.[55-62] It is known that particle aggregates form spherical flow units with an effective volume fraction larger than that of isolated particles, thus fluid's viscosity is inreased. Zhou *et al.* [56] made a hypothesis that the decrease of viscosity under shear results from broken particle aggregates. Several studies show that the anomalous viscosity has to do with particle aggregations. [57, 58] If uncontrolled aggregations occur, no models will be effective to estimate the viscosity of the nanofluid.

There are two most - used approaches to improve particle dispersion in the engineering field, including long - time ultrasonic treatment and using surfactants. Vigorous ultrasonic vibration is able to break large aggregates. Although a short-term stability may be achieved after an ultrasonic treatment, aggregations will be still unavoidable as long as colloidal stability is poor. Colloidal stability depends on steric effect and/or electrostatic repulsion. [63] The former stabilizes a particle by coating it with a large molecule so that the particles cannot get too close to each other. The later relies on the electric repulsive force arising between two particles possessing charges with the same sign. Surfactants stabilize particles via enhancing one or both of them, depending on the molecular size of surfactant and its type. Surfactants stay at the surface of particle by physical absorption. In order to favour the absorption kinetic, there must be a large amount of free surfactants dispersed in liquid phase. These free surfactants produce foams during heating and pumping. What's more, adding solvent of low polarity (*i.e.* anti-freezer ethylene glycol) will trigger desorption of surfactant [64], making worse the colloidal stability. Therefore, a stable and surfactant-free nanofluid with predicable thermal physical properties should be much more promising for heat transfer enhancement.

1.2 Aim and objectives

At the beginning of this doctoral research project, I aimed to estimate the potential of different kinds of SMNP clusters for magnetic hyperthermia heating. Modeling work based on standard Monte Carlo simulation was carried out to study the effect of morphology anisotropy on dynamic magnetic losses of SMNP clusters. The role of dipole interaction was discussed in detail.

Later, experimental and theoretical works were conducted together to find out how to improve the heating ability of anisotropic-less clusters at lower field intensity and frequency. Hydrophobic Fe_3O_4 nanoparticles were assembled to sphere-like clusters by using the emulsion droplet evaporation method. An induction heating system equipped with Optic-fiber thermometer was set up to test the heating efficiency of as - prepared Fe_3O_4 clusters with different size. Meanwhile, standard Monte Carlo simulation was performed to study the variance of magnetic losses with the cluster's size.

Finally, I studied the effect of colloidal stability on thermal physical properties of MNF and demonstrated the advantage of obtained MNF for convective heat transfer enhancement. To achieve this goal, a stable and surfactant-free magnetic nanofluid was prepared for heat transfer applications. An ethylene glycol and water mixture was selected as the base liquid, which is often used for cooing automotive engines. A specific surface modification was taken to enhance the colloidal stability of Fe_3O_4 nanoparticles but also make it controllable in ethylene glycol and water mixture. The obtained MNF remained stable up to 12 months. No foams were produced after vigorous agitation. Density, DSC, rheology and hot-wire transient thermal conductivity measurements were carried out to study the effect of colloidal stability on thermo-physical properties of MNF, including density, specific heat, viscosity and thermal conductivity. A test rig was built to measure the convective heat transfer coefficient of MNF and the base liquid.

1.3 Thesis structure

This thesis is divided into seven chapters. An outline is shown below,

Chapter 1	Introduction of the general background and research objectives
Chapter 2	Literature review of research background about the MNF-based hyperthermia heating and heat and mass transfer phenomena related to nanofluids
Chapter 3	Detailed introduction of methodologies applied in the presented research work, including preparation and characterization of MNF, numerically investigation of hyperthermia heating of clusters, set-up of induction heating system for measurement of heating ability of MNF and a test rig for studying convective heat transfer efficiency of MNF
Chapter 4	Numerically study of the effect of dipole interactions on hyperthermia heating SMNPs clusters with different shapes
Chapter 5	Preparation of MNF composed of anisotropic-less clusters and study the effect of size on the hyperthermia heating efficiency of clusters composed of SMNPs
Chapter 6	Preparation of dispersant - free Fe_3O_4 ethylene glycol - water nanofluid, modelling its thermo-physical properties and demonstration of the convective heat transfer efficiency superior to base liquid.

Chapter 7 Conclusions

Chapter 2 Literature review

In this chapter, we will introduce the basic knowledge about magnetism of magnetic nanoparticle (MNP) and magnetic nanofluid (MNF), recent advances in synthesis technology, and the background of MNF - based hyperthermia and convective heat transfer enhancement.

2.1 Magnetism of MNP and magnetic nanofluid

For bulk material, according to the arrangement of atomic magnetic dipoles with and without an external magnetic field, there are mainly five kinds of magnetism, including diamagnetism, paramagnetism, ferromagnetism, ferrimagnetism, and anti - ferromagnetism.[65] Generally, the most used magnetic nanoparticles (MNP) for hyperthermia today are made of ferro- or ferrimagnetic materials[66]. MNPs' magnetic properties are usually characterized by measuring the magnetization of dry powder sample against the magnetic field strength. Figure 2.1 shows a typical M-H curve of ferro- or ferrimagnetic particles. By observing a M-H curve, one can know the saturation magnetization M_s, the maximum magnetization the particles can achieve; remanence magnetization M_r, the residual magnetization when the intensity of magnetic field is zero; and coercivity H_c, suggesting the intensity of an opposite magnetic field required to rectify the magnetization to zero. A hysteresis loop with non-zero M_s and H_c suggests an energy conversion via heat dissipation. The magnetic work done by the field is converted into the inner energy of particles. The ferro- and ferrimagnetic materials can further be classified into magnetically "soft" and "hard" material depending on the hardness of this material to be demagnetized. "Soft" material exhibits a small H_C, whereas, the H_C of "hard" material is large.

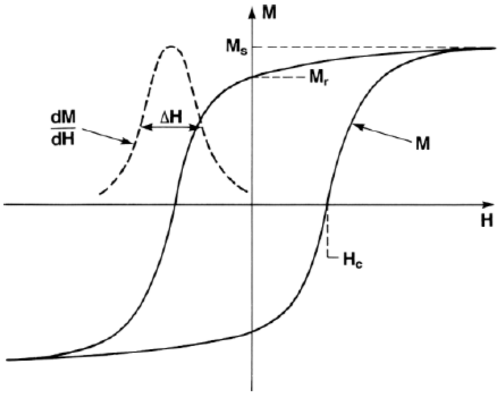

Figure 2. 1 The typical M-H curve of a ferro- or ferrimagnetic material, from which one can identify the saturation magnetization Ms, the maximum magnetization the particles can achieve; remanence magnetization Mr, the residual magnetization when the intensity of magnetic field is zero; and coercivity Hc, suggesting the intensity of an opposite magnetic field required to rectify the magnetization to zero. (reproduced from Ref [65] with permission from John Wiley and Sons, copy right 2006).

Two key factors of a particle dominate the magnetism of MNP. The one often given with higher priority is the size of particle. For a large magnetic particle, a multi-magnetic domain structure exists, where a group of aligned-orientated dipoles form each domain and domains are separated by a domain wall. When the size is reduced to below a certain critical value depending on the type of material, the dipole structure will change from multi-domain to single domain in favour of minimizing the total energy (Figure 2.2 a). Each particle can be thought of as a single giant magnetic moment. Due to the great magnetic anisotropy energy, this giant magnetic moment is inclined to stay parallel or antiparallel to the easy axis to reduce the energy (Figure 2.2 b). The magnetic anisotropy energy is defined as $K_{eff}V_p$, where K_{eff} is magnetic anisotropy constant and V_p is volume of particle. The rotation of the magnetic moment of a particle is hampered when the energy barrier is higher than thermal energy k_BT, where k_B is Boltzmann constant and T is temperature. The mean time required for the flip of the magnetic moment of particle is called Nèel relaxation time and determined by the following equation[67],

$$\tau_N = \tau_0 exp\left(\frac{K_{eff}V_p}{k_BT}\right) \qquad (2.1)$$

where τ_0 is attempt time that is often considered to be a constant in the range of 10^{-9}-10^{-13}s [68].

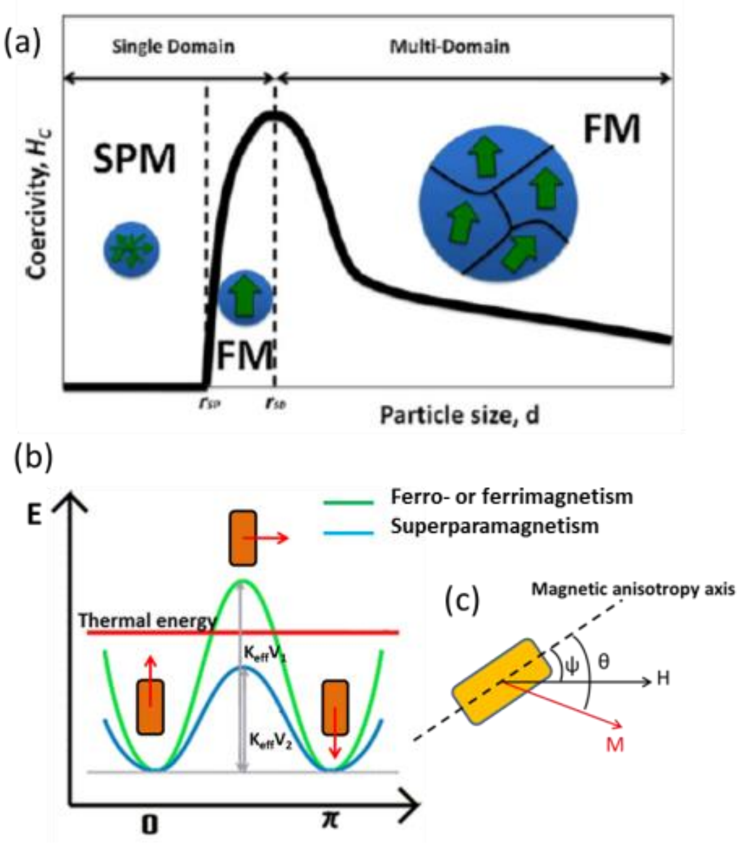

Figure 2. 2 (a) Variation of the coercivity (HC) of magnetic nanoparticles with size. SPM stands for superparamagnetism; FM represents ferro- or ferrimagnetism. (reproduced from Ref[1], with permission from Elsevier, copy right 2010) (b) The change of particle's energy with the angle between the particle magnetic moment and easy axis. (Re-edit the image downloaded from Internet) (c) Illustration of the vectors of easy axis, magnetic field (H) and particle moment (M).

If the size keeps further decreasing until the thermal energy k_BT eventually exceeds the energy barrier $K_{eff}V_p$ (< 15 nm in usual), the particle's magnetic moment starts to flip. A new magnetism, superparamagnetism, appears when it flips so fast that relaxation time is shorter than experimental time scales for measurement. The M-H curve of superparamagnetic particles measured at room temperature is just a single line due to no observation of M_r and H_c. In this situation, superparamagnetic particles behave almost like non-magnetic particles in the absence of a magnetic field; but under a magnetic field, those giant magnetic moments get aligned with this field just like nano-sized magnets.

Otherwise, the thermal energy k_BT suggests that superparamagnetism is a temperature-dependent magnetism. The blocking temperature T_B is used to describe the transition point at which the thermal energy is roughly comparable to the magnetic anisotropy energy[65]. Reducing temperature to below T_B can cause the transition back to ferro- or ferrimagnetism because the thermal energy is not large enough to make the magnetic moment flip freely at the easy axis. T_B is obtained by Zero-field-cooled and field-cooled magnetization measurements.

The other key factor is the surface effect. The extremely high surface to volume ratio pf MNP makes the surface and/or interface effects contribute much more to the magnetism of MNP than to the bulk material. For example, lots of evidences show that the saturation magnetization M_s of MNP decreases with the particle size[69-73]. The surface of the nanoparticles is considered to be composed of some canted or disordered spins that prevent the core spins to align along the field direction resultantly decreasing the saturation magnetization[74-76]. The surface may also behave like a dead or inert layer that has negligible magnetization[77-79]. Sometimes, specific fabrications of surface structure introduces surface anisotropy K_S, which enhances the total magnetic anisotropy of particle[80, 81]. And surface anisotropy is proportional to the surface area rather than the volume. In the simplest case of ideally sphere particle with uniaxial anisotropy,

$$K_{eff} = \left(K_V V_p + K_S S\right)/V_p = K_V + \frac{3}{r_m} K_S \qquad (2.2)^{82}$$

where K_V is the volume anisotropy constant, S is the surface of particle's magnetic fraction, and r_m is the diameter of particle's magnetic fraction.

Several other types of anisotropies also affect the total magnetic anisotropy of particle, such as shape anisotropy, anisotropy associated with the internal stress and external impact and exchange anisotropy. For example, the K_{eff} of iron oxide with size of 20 nm increases from 12 to 77 kJ/m^3 when the shape changes from a sphere to a cube.[83] Lee *et al.* [5]managed the K_{eff} of composite MNP from 3 to 200 kJ/m^3 by introducing exchange-coupled structure by means of the interfacial exchange interaction between hard and soft magnetic phases.

The interaction between the MNP and magnetic field can be described as processes that the particle tries to achieve the lowest energy level under an agitating field. In the simplest case of ideally sphere particle with uniaxial anisotropy, without an outside magnetic field, the angular dependence of the particle’s energy is given as,

$$E(\theta) = K_{eff}V_p sin^2\theta \qquad (2.3)$$

where θ is the angle between moment of particle and easy axis, also called magnetic anisotropy axis. The plot of E (θ) as a function of θ is shown in Figure 2.2 b. E(θ) achieves minimum value when θ is equal to 0 and π, the positions that moment stays at easy axis. In presence of magnetic field, the Stoner–Wohlfarth model is introduced to define the energy of single MNP with uniaxial anisotropy[84], which is expressed as,

$$E(\theta,\varphi) = K_{eff}V_p sin^2\theta - M_S V_p H cos(\theta-\varphi) \qquad (2.4)$$

where H is the intensity of magnetic field and φ is the angle between the easy axis and the vector of magnetic field. This equation suggests that any departure of moment from either easy axis or magnetic field raises the energy of MNP. Therefore, MNPs always keep the tendency to get to the state that particle magnetic moment, easy axis, and magnetic field, coincide together.

When a MNP is interacting with a magnetic field, the influence of thermal agitation makes it possess the potential to get back to the demagnetized state. This mechanism is called relaxation. If the motion of particle is nearly forbidden (*i.e.* in tumor), the relaxation mainly depends on Nèel relaxation – only moment flips and particle maintains immobilized. There is another relaxation mechanism existing in MNP liquid suspensions, Brownian relaxation – only particle rotates and the moment keeps locked at the easy axis. Figure 2.3 illustrates these two mechanisms.

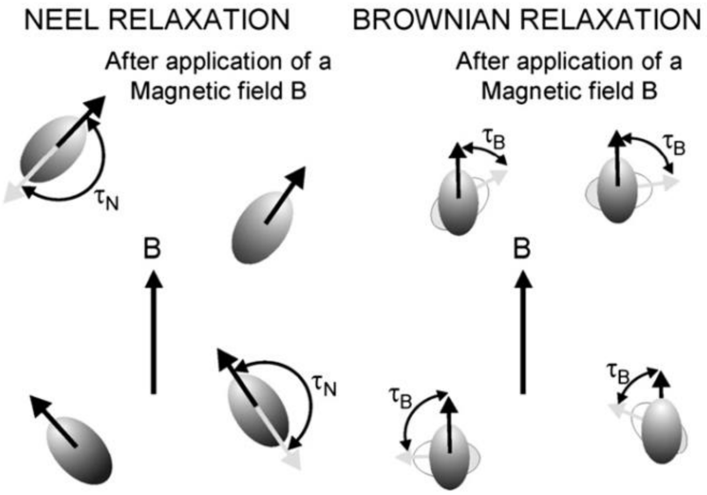

Figure 2. 3 Illustration of the two modes of the magnetic relaxation in a magnetic fluid. (reproduced from Ref [4] with permission from Elsevier, copy right 2011)

The Brownian relaxation time is given by the following equation,

$$\tau_B = \frac{3\mu_{bl}V_H}{k_B T} \tag{2.5}$$

Where μ_{bl} is the dynamic viscosity of the base liquid, V_H is the hydrodynamic volume of particle. Both equations (2.1) and (2.5) vary with the reciprocal of k_BT, indicating these two relaxations are fuelled by thermal energy. It is customary to define an effective relaxation time to combine the contributions of τ_N and τ_B as,

$$\frac{1}{\tau_e} = \frac{1}{\tau_N} + \frac{1}{\tau_B} \tag{2.6}$$

Figure 2.4 shows plots of calculated τ_N, τ_B, and τ_e of isolated and non-interacting MNP suspending in liquid against particle radius at room temperature. As the particle size increases the prior relaxation mode taken by MNP switches from Nèel relaxation to the Brownian relaxation.

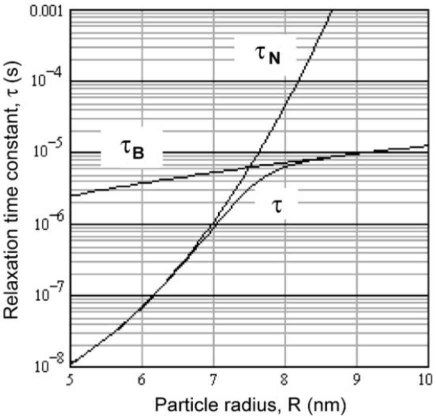

Figure 2. 4 Plots of calculated τ_N, τ_B, and τ_e of isolated and non-interacting magnetite nanoparticle suspending in liquid against particle radius at room temperature. (reproduced from Ref[85] with permission from Elsevier, copy right 2002)

The equilibrium magnetization (M-H curve) of isolated and non-interacting MNP liquid suspension could be described by the Langevin equation,

$$M = M_S\phi(\coth\xi - 1/\xi) \tag{2.7}$$

where $\xi = \mu_0 M_S V_p H / k_B T$ is the Langevin parameter, μ_0 is the vacuum magnetic permeability, and φ is the volume fraction of particles in the suspension. Once MNPs are interacting with each other, the Stoner–Wohlfarth model and Langevin equation won’t be suitable to discuss the energy and magnetism of the MNP ensemble system.

It is important to notice that large particles may behave like SMNPs after being dispersed in liquid, as long as Brownian rotation is fast enough to completely randomize the particle moments. L. De Los Santos V. *et al.*[86] dispersed 4.32 µm Amine-functionalized ferromagnetic beads into concentrated aqueous sucrose solution, and no coercivity was observed in DC M-H measurement. However, if Brownian rotation is retarded due to *i.e.* high viscosity and aggregations, ferromagnetism will come back. Otherwise, several works found that immobilized small particles might exhibit ferromagnetism when the particle concentration is extremely large to let them interact via dipole couplings.[87-89]

2.2 Synthesis of magnetic nanofluid

MNF is synthesized by dispersing MNP into non-magnetic carrier fluids such as water, ethylene glycol, hydrocarbonoil, etc [90]. There are two strategies to prepare particle suspension, including one – step and two – step methods. One-step technique combines the synthesis of nanoparticles and dispersion of nanoparticles in the base fluid within one single step. Akoh *et al.* [91] developed the single-step direct evaporation approach to prepare oil – based MNF. In this method, the MNF is obtained by evaporating a metal onto a running oil substrate. This method is also called Vacuum Evaporation onto a Running Oil Substrate technology. The obtained particles could be very small (about 25 Å).

However, the base liquid must be non-evaporative oil, which is generally of very high viscosity. The laser ablation method is another potential one-step technique to produce MNF. It generates nanofluid by irradiating with a laser light a metal target that is immersed in the base liquid[92, 93]. Although it does not require any chemical reagents, the resulting nanofluid is too diluted for heat transfer application.

In a two – step approach, particles are prepared first and then dispersed into the base liquid. With using this method, one can select the optimal method to obtain the particles and the best strategy to stabilize particles in base liquid. A variety of synthetic procedures have been developed to synthesize magnetic nanoparticles. [82] Among them, thermal decomposition and co-precipitation are used the most. The former prepares the particles by thermal decomposition of organometallic compounds in high-boiling organic solvents containing stabilizing surfactants. The obtained particles are hydrophobic and mono-dispersed. The size and morphology can be precisely controlled by changing the ratios of the starting reagents including organometallic compounds, surfactant, and solvent as well as the reaction temperature and time and aging period. Peng *et al.*[94] nearly monodisperse Fe_3O_4 nanocrystals with sizes adjustable over a wide size range (3 – 50 nm), and the shape could be changed from cube to sphere by controlling the reaction time. Thermal decomposition has been proven to be successfully in synthesis of other MNPs, such as Cr_2O_3, MnO, Co_3O_4 and NiO. However, due to the low yield and tedious procedure of post treatment, it is not economic to massively prepare MNPs by thermal decomposition.

Co-precipitation is a facile and convenient way to synthesize iron oxide nanoparticles (either Fe_3O_4 or γ-Fe_2O_3). It is based on simultaneous precipitation of Fe^{3+} and Fe^{2+} ions in basic aqueous media. Once the synthetic recipe is fixed, the quality of the nanoparticles will be fully reproducible. Theoretically, its yield is nearly 100 % since it is a precipitation reaction. And the obtained particles are hydrophilic and can be directly dispersed into aqueous base liquid. With the aid of 2 h of ultrasonic treatment, Sundar *et al.*[95] dispersed Fe_3O_4 particles prepared by co-precipitation to ethylene glycol and water mixture directly, and the MNF was able to maintain stable up to 80 days. Moreover, the surfaces of particles are clean. The iron atoms on the surface can bind with several kinds of chemical groups (i.e. carboxyl[96-98], silane[99], phosphate[100] and amine[101, 102]) thorough formation of coordination bonds, which is beneficial for further surface modification. What's more, it is relatively cheap to prepare MNPs by co-precipitation method. For example, if all the chemicals are purchased from Sigma Aldrich, it will cost about 0.18 GBP per gram of Fe_3O_4 (only the expenditure of material is considered). To produce 1 L of water-based MNF with particle concentration of 1 %, it will cost less than 10 GBP. However, the reaction is too fast to be controlled, so the prepared particles are usually polydispersed in shape and size. It is possible to control the average size of particle by adding stabilizer (i.e. citrate[103]) to the reaction system.

It is known that MNPs have a great tendency to aggregate in solution caused by van der Waals attractive force.[63] MNPs are subjected to other attractive forces, inter-particle dipole interactions. [104] Usually, small MNPs (< 20 nm) is preferable than large particles with permanent magnetization, because it is hard to control the aggregations of later due to the strong dipole couplings among particles. Without taking any measures to stabilize MNPs, even small particles will undergo spontaneous aggregations. Shinoda *et al.* [105]found that magnetic ultrafine particles dispersing in water tend to agglomerate even in absence of magnetic field. Under a cryogenic electron microscopy, Philipse *et al.*[106] directly observed the coexistence of isolated particles, linear chain clusters, and aggregates in superparamagnetic iron nanoparticles in liquid dispersion at zero field.

In the engineering field, ultrasonic treatment is often used to help disperse particles in a certain based fluid.[107] Although vigorous ultrasonic vibration can break large aggregates[108], aggregations won’t be under control if no measures are carried out to enhance colloidal stability. Usually, there are two strategies to stabilize particles including steric stabilization and electrostatic stabilization.[63] The first one involves coating the particles with sufficiently large molecule. The coated large molecules stabilize particles by means of "steric effect". Steric effects arise from a fact that each atom within a molecule occupies a certain amount of space. When two large molecules located on different particles are trying to merge with each other, the atoms will be brought too close together, thus leading to an increase in energy. The increased energy will generate a repulsive force to stop the merging process. Due to this repulsive force the particles cannot approach too close. Steric stabilization should be the only option to stabilize particles in oil, since it is impossible for particles to carry charges in oil. Oleic acid is the most used surface activator to stabilize particles in oil. It is very easy to obtain oleic acid modified MNPs by heating the mixture of oleic acid and aqueous solution of particles prepared by co-precipitation under stirring.[109-111] Oleic acid modified particles are able to maintain stability in many organic solvent, *i.e.* cyclohexane[109, 110], octane[111], chloroform[64], transformer oil[112] and heat transfer oils [113]. The application of steric stabilization is not limited to preparation of oil – based nanofluid. In fact, its largest advantage is that the colloidal stability protected by steric stabilization is not vulnerable to high ionic strength. Nanoparticles modified with monomeric zwitterionic sulfobetaine ligands have been proven to be able to stand high salinity conditions.[114-117] For example, sulfobetaine-coated silica nanoparticles can maintain stability at room temperature in 3 M NaCl for 15 days.[115] Johnston *et al.* [118] reported that the silica particles modified with short chains of ether diol or zwitterionic sulfobetaine could keep dispersed in API brine (8% NaCl and 2% $CaCl_2$) at 80 °C for over 30 days. However, generally, such kind of ligand for steric stabilization is very expensive, which is not economic for industrial applications.

Another option is electrostatic stabilization, which relies on the electric repulsive force arising between two particles possessing charges with the same sign. According to the classic DLVO theory [119, 120], particles carrying charges do not undergo aggregations only when electric repulsive force is stronger than Van der Waals attractive force. The electric repulsive force can be enhanced by increasing the surface charges of particles. While un-treated Fe_3O_4 nanoparticles carry negatively charges by forming FeO^- at higher pH value or positively charges ($FeOH_2^+$) at lower pH value,[121] the isoelectric point of magnetite is known to be in the pH range from 6 to 7[80]. It means that it has to make the MNF acidic or alkaline to improve the colloidal stability.

Absorption of ionic dispersants is the effective way to cover the surface of particle with charged groups. Ionic dispersant has a hydrophilic head and hydrophobic tail. Once the concentration of dispersant is beyond critical micelle concentration, the hydrophobic tails of dispersants will come close together due to hydrophobic interactions, leaving hydrophilic heads stretching outward to the liquid phase, thus micelles will be formed. When particles are added to a concentrated solution of dispersant, the dispersants are inclined to stay at the surfaces of particles to reduce the surface energy. Thus, nanoparticles are captured within the micelles, which will protect them from aggregations. The more hydrophobic the particles are, the stronger the absorption kinetic will be. Fan *et al.*[122] developed a method to prepared almost ideally dispersed nanofluid by transferring oil – based particle suspension to water solution of micelles. After the evaporation of oil phase, the nanofluid is gained. For this time, the formation of nanoparticle-micelles was driven by the hydrophobic interactions between the hydrophobic chain of the ligands (i.e., oleic acid) and the hydrophobic tail of the surfactant.[123] With using this method, Cao *et al.* [64]obtained mono-dispersed MNF of oleic – acid modified Fe_3O_4 nanoparticles. Isojima *et al.*[124] reported emulsion droplet solvent evaporation method to prepare water-based MNF of sphere-like clusters composed of multi-MNP. Unlike Fan’s approach, oil – based MNF suspension is mixed with diluted dispersant solution with the aid of ultrasonic treatment. By changing the particle concentration of oil suspension, Yang *et al.* [109]produced nearly monodispersed Fe_3O_4 clusters whose sizes were controllable from 50 to 90 nm. However, dispersants produce foams during heating and pumping, which is not good for heat transfer applications.

Electrostatic stabilization can be also achieved by modification of ligands. The ligands used for modification of Fe_3O_4 nanoparticles must meet two requirements: (i) it is easy to graft the ligands onto the surface of particle via coordination bonding so that they cannot be washed off; (ii) the ligands which are attached on particles produce charged groups (i.e. COO^- and NH_x^+) at appropriate pH. Citric acid (CA) is often used as surface ligands to stabilize nanoparticles in water [96-98, 125, 126]. CA is a small molecule with three carboxyl groups. It can be chemically attached onto the surface of particle via formation of coordination bond between metal atom and carboxyl group, leaving one or two carboxyl groups stretching out forward into the surrounding liquid phase.[96] These free carboxyl groups are expected to dissociate in water, generating negatively charged group COO- on the surface of particle. It is known that a higher pH facilitates dissociation of CA. With increasing pH of particle suspension, more and more COO- groups will be generated on the surface of particle, thus resulting in an enhancement of surface potential [96-98]. So by changing the pH of particle suspension, one can control the scale of aggregation of CA modified particles. Fernández van Raap *et al.*[96] obtained isolated magnetite particles dispersing in water by controlling the pH and particle concentration during the CA modification. They found that the surface potential of modified particle achieved maximum at pH of 5, suggesting the attached CA dissociated completely. The main problem of electrostatic stabilization is that the colloidal stability is susceptible to ionic strength. Salt in solution screens the surface charges of particles, thus leading to a worse colloidal stability even agglomeration.[127, 128] Therefore, it must low down the concentration of electrolytes as much as possible when electrostatic stabilization is applied.

2.3 MNF - based magnetic hyperthermia

2.3.1 Heating mechanism

Hyperthermia heating behaviour of MNF depends on conversion of the work done by AC magnetic field to the inner energy of the particles through a mechanism called magnetic losses. If we assume that the particle system is adiabatic, according to the first thermodynamic law, $dU = \delta Q + \delta W = \delta W$, where U is the inner energy, Q is the added heat, and W is the magnetic work done on the system. By given that the differential magnetic work is described as $\delta W = \vec{H} \cdot d\vec{B}$, where $\vec{H}$ is the applied magnetic field and $\vec{B}$ is the magnetic induction within the magnetic material, and they are collinear, it can be deduced that,

$$dU = HdB \tag{2.8}$$

After substituting B = μ_0 (H + M) into equation (2.8) and followed with integration by parts, the increase of inner energy of unit volume for one cycle of AC magnetic field is presented as,

$$\Delta \mathrm{U} = -\mu_0 \oint M \, dH \tag{2.9}$$

If the magnetization lags the driven field, the integration will generate a non-zero value, so a closed hysteresis loop will appear on the M-H curve. If the particle system is thermally interacting with the environment, the increased inner energy will be dissipated in the form of heat to the surrounding environment. This process of energy dissipation is called magnetic losses. The equation (2.9) indicates that the area of magnetic hysteresis loop determines the amount of heat generated per cycle of AC magnetic field. So the power dissipation of unit volume is given by the product of frequency f and ΔU,

$$P = f\Delta U = -\mu_0 f \oint M \, dH \tag{2.10}$$

In hyperthermia experiment, specific absorption rate (SAR), also known by another name as specific power loss, is often used to estimate the heating ability of magnetic nanoparticle, and defined as the rate at which energy is absorbed per unit mass of a magnetic material and is expressed as,

$$\mathrm{SAR} = \frac{C_{p,nf}\rho_{nf}V_{nf}}{m}\frac{dT}{dt} \tag{2.11}$$

where $C_{p,nf}$ is the specific heat capacity of MNF, ρ_{nf} is the density of MNF, V_{nf} is the volume of MNF, and m is the mass of magnetic material of MNF. The relationship between SAR and the power dissipation is given as,

$$\mathrm{SAR} = \frac{P}{\rho_{s,m}\phi} \tag{2.12}$$

where $\rho_{s,m}$ is the mass of magnetic part per unit volume of particle.

For single-domain MNP system, there are two types of magnetic losses including hysteresis losses and delay in the relaxation. Hysteresis loss appears when the delay is caused by overturning the coercive field of a ferromagnetic system. Delay in the relaxation occurs when the frequency of magnetic field is so high that as the field intensity decreases to zero, a superparamagnetic system can't have enough time to demagnetize to zero through Nèel relaxation and/or Brownian Relaxation. In a MNP system with a wide size distribution, hysteresis loss and delay in the relaxation may take place together[129, 130].

Rosensweig[85] modelled the heating efficiency of isolated non-interacting single-domain MNP suspension. Because in AC magnetic field the magnetization is not in phase with the time-varying magnetic field, the magnetic susceptibility χ is divided into two parts,

$$\chi = \chi' - i\chi'' \tag{2.13}$$

where imaginary part χ'' is the loss component of susceptibility and represents the energy absorption from the magnetic work. The AC magnetic field can be expressed in the form of,

$$H(t) = H_0 cos(2\pi f t) = Re\left[H_0 e^{i2\pi f t}\right] \qquad (2.14)$$

where H_0 is the amplitude of AC magnetic field and t is the time. So the time-dependent magnetization is given as,

$$M(t) = Re\left[\chi H_0 e^{i2\pi f t}\right] = H_0(\chi' cos 2\pi f t + \chi'' sin 2\pi f t) \qquad (2.15)$$

After substituting (2.13 - 15) into (2.10) and followed by integration, the result is shown as,

$$P = \mu_0 \pi \chi'' f H_0^2 \qquad (2.16)$$

In this equation, the only parameter related to the magnetism of MNP suspension is the loss component of susceptibility χ''. Relating relaxation time of MNP with χ'' generates[85],

$$\chi'' = \frac{2\pi f \tau_e}{1+(2\pi f \tau_e)^2} \chi_0 \qquad (2.17)$$

where χ_0 is the static susceptibility. Substitute equation (2.17) into equation (2.16) and (2.12) generates[131],

$$SAR = \frac{\mu_0 \chi_0 H_0^2}{2\rho_{s,m}\phi}(2\pi f)\frac{2\pi f \tau_e}{1+(2\pi f \tau_e)^2} \qquad (2.18)$$

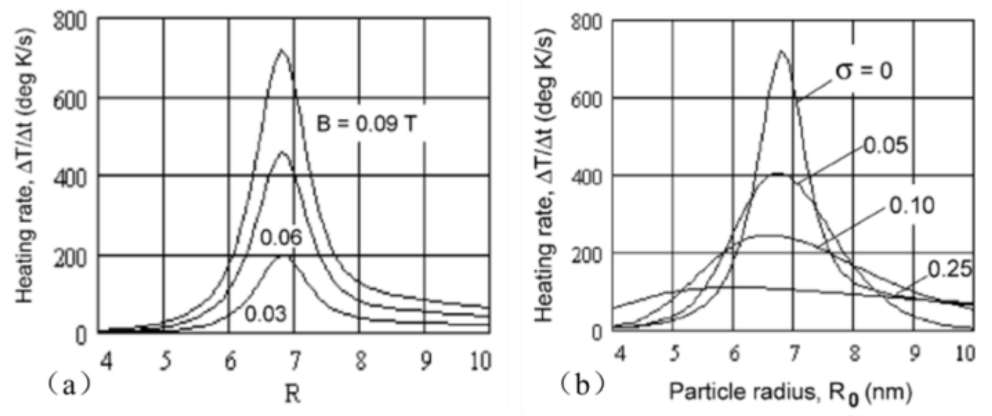

Figure 2. 5 The calculated heating rates of (a) monodispersed non-interacting magnetite samples in tetradecane solution as a function of particle radius and field intensity (f = 300 kHz) and (b) polydispersed non-interacting magnetite samples in tetradecane solution against particle radius and polydispersity index σ (f = 300 kHz). (reproduced from Ref[85] with permission from Elsevier, copy right 2002)

If χ_0 is assumed to be the chord susceptibility, corresponding to the Langevin equation: $\chi_0 = (\mu_0 M_S^2 \varphi V_{nf})/(k_B T) \times (\coth \xi - 1/\xi)$.[85] The equation (2.18) makes sense only when an isolated non-interacting MNP suspension system is consided. Being given a certain filed frequency, the profile of SAR against size exhibits a sharp peak when $2\pi f \tau_e = 1$. Figure 2.5 shows the plot of calculated H_0-dependent heating rate as functions of the particle radius for monodispersed non-interacting magnetite nanoparticles suspending in hydrocarbon (a) and the influence of size polydispersity (b). The narrow peak suggests a high dependence of SAR on size. However, the polydispersity in size widens the distribution of τ_e in system, thus broadening the profile and meanwhile lowering the maximum heating rate. Additionally, the heating efficiency increases with the increase of H_0, which is in agreement with the description of equation (2.18) that SAR is proportional to H_0^2.

The theory of Rosensweig is built on the assumption that the dependence of equilibrium magnetization of a stable ferrofluid on field intensity obeys the description of the Langevin equation, which presumes that the equilibrium magnetization of this ferroliquid must decrease to zero without external field. Therefore, once the coercivity of studied MNP system is too significant to be neglected, the theory of Rosensweig won't be suitable. Several works have given the evidences that the variance of heating efficiency against particle size doesn't exactly follow the description of theory expressed by equation (2.18) when the particle's size is close to the transition point from superparamagnetism to ferromagnetism or well into the ferromagnetism regime.[129, 132-135] For instance, for maghemite ($M_S \sim 400$ kA m^{-1}) heated by a field with amplitude of 10 kA m^{-1} and frequency of 400 Hz the validity of the Rosensweig's model restricts to size < 16 nm (e.g. Andrä *et al.*[134]). The clearest experimental evidence is given by the work of Bakoglidis *et al.*[133], who observed that the profile SAR of iron oxide nanoparticles suspending in water displayed a peak at 10 nm, and fell by one half at 13 nm, and then turned to increase again to 400 W/g at 18 nm. This is not in agreement with Rosensweig's theory that the magnetic losses should decrease to zero after achieving the maximum value. They attributed it to the transition of magnetic loss from delay in relaxations to hysteresis loss since the coercivity of particles increased dramatically when the size was beyond 10 nm. By discussing the magnetism of ensemble of non-interacting single domain MNP with Stoner–Wohlfarth model, Hergt *et al.*[129] found that the onset of hysteresis loss requires a threshold field amplitude H_o > coercivity H_c. For monodisperse single domain particles the dependence of SAR on the field amplitude H_o is approximated by,

$$SAR = \begin{cases} 0 & for\ H_0 \le H_c \\ \frac{4B_R H_c}{\rho}\left(1-\left(\frac{H_c}{H_0}\right)^5\right) & for\ H_0 > H_c \end{cases} \tag{2.19}$$

where B_R is the remnant flux density. As shown in Figure 2.6 a, the saturation ‘plateau’ of SAR locates at larger size and is bounded with a steep ‘cliff’ when the field amplitude falls to below a critical value. The hysteresis loss, the loss at large size, demands stronger field, and will finally surpasses the peak of loss at low size resulting from the delay in relaxations (Figure 2.6 b). However, smaller particles (< 20 nm) heat better when the field intensity is relatively low. Moreover, Singh *et al.*[136] reported that hysteresis loss may occur when a large amount of SMNP whose size are less than 10 nm are magnetically interacting with each other so as to create a anisotropic dipolar field. Therefore, the hysteresis loss is not restricted to the particle size. The discussion will become much more complex when MNPs magnetically interact with each other, which will be given later.

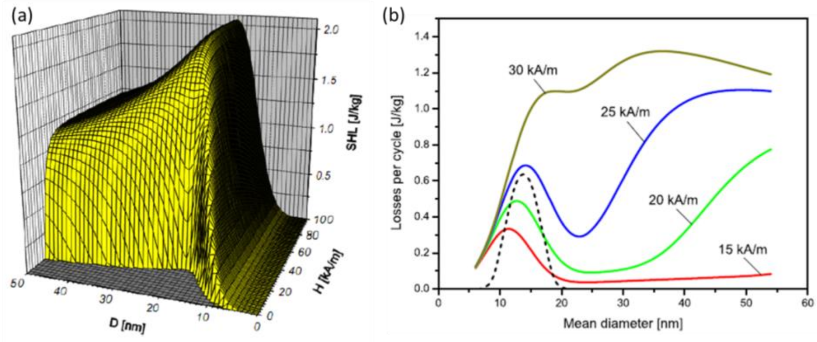

Figure 2. 6 (a) Dependence of the specific hysteresis loss per cycle on mean particle diameter and magnetic field amplitude for monodisperse maghemite nanoparticles. (b) Calculated dependence of total magnetic losses per cycle of monodispersed maghemite particles on the mean particle diameter for different values of the amplitude of the external magnetic ac field (full lines). For comparison, the size dependence derived by the theory of Rosensweig is shown as a dashed line for 25 kA/m. (reproduced from Ref[129] with permission from IOP Publishing , copy right 2008).

There is another type of magnetic loss very different from the two talked above. It produces heat through friction between rotating particles and the surrounding medium rather than energy conversion within the particle. This type of energy loss becomes significant in the case of well-dispersed larger ferro- or ferromagnetic particles, especially when the particle size is large than 100 nm[137]. The energy loss per cycle is given by $2\pi T$, where $T = \mu_0 M_s H V_p$ is the torque moment.[138]

2.3.2 Main advances and problems in magnetic hyperthermia

The most important advance in these years should be credited to the commencement of the clinical attempts of magnetic hyperthermia at 2007, which is led by the group of Andreas Jordan. To our best knowledge, Jordan et al is the only group in the world which is carrying out clinical studies of magnetic hyperthermia cancer therapy. In the review they published in 2001[10], the largest challenge in conceiving the magnetic hyperthermia system for clinical study refers to setting up an induction heating system that can fill up an operation volume for treatment of human (at least 5 - 10 000 cm^3 for regional hyperthermia) with a homogeneous AC magnetic field but also being safe to the patient as well as the operator. Field homogeneity is very crucial because a steady heating is obtained only when the particles are sitting in a homogeneous field. Furthermore, heating a small amount of nanoparticles locating deeply in body requires about 5 times higher field amplitudes (in the order of 10 kA/m) in comparison to in-vitro experiment. To produce such an AC magnetic field requires a very strong electric power system, which brings in potential safety problem. By the end of 2000, the first prototype of a clinical magnetic field hyperthermia therapy system was set up at the ChariteH Medical School, Campus Virchow-Klinikum, Clinic of Radiation Oncology in Berlin. It is a ferrite-core applicator with an adjustable vertical aperture of 30 - 45 cm. Figure 2.7 illustrates the first prototype MFH therapy system. Now the induction heating system for treatments on human is able to generate a homogeneous AC magnetic field with a frequency of 100 kHz and variable field strength of 2.5-15 kA/m[139]. In fact, most excellent results reported are gained from in-vitro heating tests or in-vivo studies on small animals whose frequency and amplitude is above 300 kHz and around 20 kA/m in general. The equation (2.18) suggests that the SAR highly depends on field f and H_0. Therefore, MNPs cannot receive plenty of power from the present system during therapy treatment.

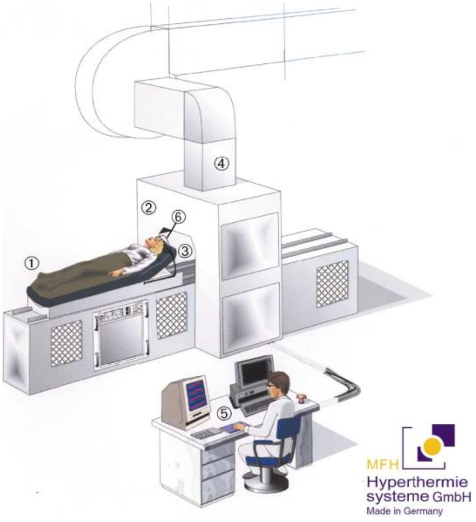

Figure 2. 7 Sketch of the first prototype MFH therapy system (Hyperthermia system GmbH, Berlin, Germany). The AC magnetic field axis is perpendicular to the axial direction of the patient couch (1). The therapy system is for universal application, *i.e.* suitable for MFH within, in principle, any body region. It is a ferrite-core applicator (2) operating at a frequency of 100 kHz with an adjustable vertical aperture of 30-50 cm (3). The field strength is adjustable from 0 to 15 kA/m. The system is air cooled (4). Aperture, field strength, thermometry and further system parameters are on-line monitored and adjusted manually by the physician at the control unit (5). The temperature is measured invasively with fuorooptic temperature probes within the tumor and at reference points outside the patient (6). Copy from Ref[10] with permission from Elsevier, copy right 2001

Hyperthermia demands the temperature of tumor to be kept steadily at 42 – 46 ^{o}C. During the treatment, the heat generated by MNPs keeps depleting to the surrounding tissue via heat conduction and convection through blood flows.[140] The effect of the later could be neglected because the blood flows are stopped by high pressure within tumor.[140] In 1999, Andrä *et al.*[141] theoretically studied the problem of heat dissipation only through conduction and came up with the relationship between the increase of temperature ΔT, the particle concentration c, SAR and tumor radius R based on the assumption of a spherical and small tumor filled homogeneously with magnetic particles. The relationship is given as,

$$\Delta T = SAR \cdot c \cdot R^2/3k_t \qquad (2.20)$$

where k_t is the heat conductivity of tissue. The particles can be introduced to the tumor by two manners, including intra-tumoural injection and targeted particle delivery. For a typical concentration of 10 mg per cm^3 of tumor applied in IT injection (e.g. Ref [11]), Figure 2.8 a shows the requirement of SAR for raising the temperature of tumor uniformly implanted with MNP by 15 K. The highest SAR published is about 3900 W/g [142]and is, technically, able to treat 2 mm of tumor according to this chart. But the diagnostic limit of tumor at present is 3 mm[140], which thus could be identical with the practical application limit for intra-tumoural injection.

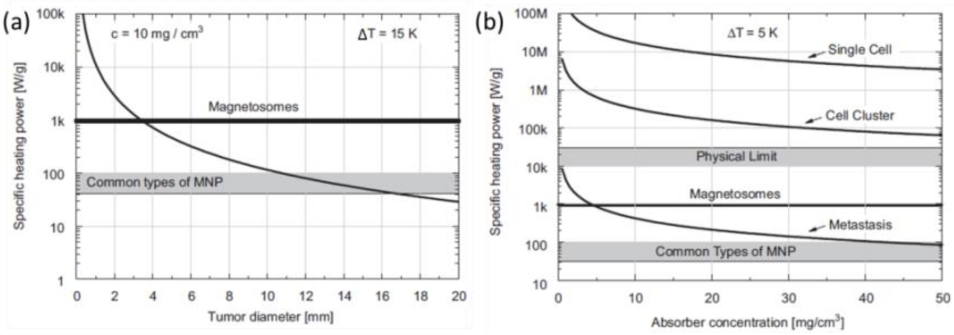

Figure 2. 8 (a) The demand of SAR for raising the temperature of tumor ideally uniformly implanted with MNP by 15 K. (b) SAR needed for hyperthermia ($\Delta T=5$ K) in dependence on particle concentration achieved in tumor tissue. Given are curves for metastases of 3mm diameter, a cell cluster (0.1 mm) and a single cell (15 µm). Both of these two data are gained form calculation of equation (2.20) with the assumption that MNPs are ideally uniformly dispersed in tumor (reproduced from Ref[140] with permission from Elsevier, copy right 2007).

Nevertheless, in IT injection, it is so difficult for the hyperthermia treatment to cover every corner of the tumor due to the inhomogeneous MNP distribution within the tumor. The great viscosity of tumor tissue hampers the diffusion of MNP, and no blood flow there can help motivate the dispersion of particles. Experimental study of Salloum *et al.* [143]in a tissue-equivalent agarose gel showed that the particle concentration was not uniform after the injection and were confined in the vicinity of the injection site. In addition, the particles might be washed away by the improved blood flow at treated place.[2] It is impossible to improve the distribution by injection of aqueous particle suspensions, for the reason that the injected liquid will tend to thrust aside the tumor spreading along the weak links of the tissue.[140] To deal with this problem, some group used viscous MNF as injection media instead of aqueous solution.[144] And Jordan’s group came up with interstitial heating via multiple-site direct injection of the nanoparticles.[145] They found that the heat can drive the extension of the particle distribution into the critical tumor margin and improve the homogeneity step by step, and they called it ‘thermal bystander effect'[145].

While IT injection is suitable for treatment of a relatively big tumor, the toughest task in cancer therapy refers to how to completely remove the cancer cells from the body and effectively suppress its relapse. Many works have claimed that, technically, it is with chance for MNPs modified with targeting agent molecule to capture the cancer cells within the body or get actively accumulated at tumor site.[146, 147] Figure 2.8 b shows the demand of SAR to raise the temperature of single cell, cell cluster and metastasis with size of 3 mm by 5 K at different the particle absorption concentration. The treatment of single cell demands amazingly high SAR (above 1MW/g) which is so far beyond the heating abilities of MNPs. Perhaps the highest SAR reported might allow catching the limit for treatment of cell cluster, but a more than 30 mg/mL of particle absorption concentration in a cell cluster is unrealistic. It is also important to notice that 3 mm is not only the diagnostic limit at present but also represents the stage that a tumor begins to build its own supply system by so-called angiogenesis[148]. This suggests once the size of tumor is smaller than 3 mm, it turns out to be undetectable, causing trouble in collecting information about its condition for further treatment arrangement, and meanwhile tumor can grow up back by utilizing its supply system. Therefore, 3 mm could be viewed as the treatment limit of magnetic hyperthermia for now.

Otherwise, recently the studies of this field begin to call on magnetic hyperthermia treatment with low f and H_0.[2, 140] It is because in addition to the expected heating generated by magnetic particles, alternating magnetic field also causes unavoidable non-selective heating of both cancerous as well as healthy tissue due to generation of eddy currents.[149] The heating power of eddy current in a conductor is proportional to $(H_0 \cdot f \cdot D_{loop})^2$, where D_{loop} is the diameter of induction wire loop. Experimentally, Brezovich[150] found for a loop diameter of about 30 cm that test persons were able to ‘‘withstand the treatment for more than one hour without major discomfort’’ when the produce of H_0 and f was equal to 4.85×10^8 A/ms. Based on this observation, Hergt *et al.* [140]made an assumption that for the safety of treatment the produce of H_0 and f should be less than 5×10^9 A/ms by considering that the exposed body region must be smaller than the loop. In the clinical magnetic hyperthermia of prostate cancer, Jordan *et al.* [31] found that once the field strength was increased above 5 kA/m, the patient experienced discomfort and pain. The field intensity tolerated during magnetic hyperthermia therapy of brain tumours was much higher, but it still needs to be controlled less than 10 - 14 kA/m[21]. Therefore, the requirement of low Hf magnetic hyperthermia gives rise to a huge challenge on selection of MNPs.

2.3.3 Optimization of MNF for magnetic hyperthermia

Facing the technical limits of induction heating system, some researchers have made lots of effort to improve the power conversion efficiency of particles since the very beginning of the story of magnetic hyperthermia. In 1993, Jordan *et al.*[66] for the first time demonstrated the advantage of colloidal single-domain nanoparticles for hyperthermia by experimentally comparing the heating abilities of colloidal superparamagnetic ferrite particles (diameter less than 10 nm) and multi-domain particles powder (diameter 1 – 400 μm). They embedded the particles into 2% agar matrix containing 4.7 g/l sodium chloride, and then measured the heating rate by monitoring the time-resolved temperature variance after exposing the matrix under an alternating magnetic field with $f = 520$ kHz and $H_0 = 13.2$ kA/m. They found that the SAR obtained from sub-domain nanoparticle (above 200 W/g ferrite) was much higher than multi-domain particle (less than 70 W/g ferrite), and attributed this difference to that heating of the former was exclusively due to the power absorption of particles.

From that time on, extensive attentions were put on the investigation of colloidal single-domain MNP for hyperthermia.[4] In 2002, Rosensweig[85] reported the mathematical relationships between heating efficiency, non-interacting single-domain MNP fluid and its magnetic relaxation. According to equation (2.18), only two parameters of MNP affect the SAR, including saturation magnetization M_S and relaxation time τ_e. M_S is determined by size (because of surface defects) and chemical composition; τ_e is affected by magnetic anisotropy K_{eff} and interactions between particles (i.e. inter-particle dipole couplings) as well as size, and meanwhile K_{eff} depends on chemical composition too. Therefore, it's hard to separate one parameter from the other and study it alone because of such complex associations between them.

In order to simplify the discussion of single-domain MNP, generally, researchers often skip the consideration of interactions between particles, and replace M_S by domain magnetization M_d, magnetization per magnetic domain, which doesn't vary with the size. In this case, chemical composition is naturally given with the biggest emphasis. At present, the material of MNP selected for magnetic hyperthermia could be roughly classified into three kinds: metal, alloy and metal oxide. As shown in Figure 2.9 a, heating efficiency of metal and alloy particles are supposed to be much higher than metal oxide particles due to their magnificent M_d. However, their poor chemical stability and rigorous preparation procedures[65] (i.e. Ar and H_2 synthesis atmosphere) limit their application in hyperthermia. On the other side, coprecipitation and thermal decomposition offers facile and productive approaches for preparations of magnetic metal oxide nanoparticles, especially ferrite particles[65, 82]. The excellent chemical stability of ferrite particles guarantees the stable magnetism of particles in bio-environment. Therefore, magnetic oxide nanoparticles are the most-used heating agent for magnetic hyperthermia. As shown in Figure 2.9 b, the maximum of heat rate of magnetic oxide nanoparticles is also determined by M_d.

	Fe_3O_4	γ-Fe_2O_3	FePt	FeCo	Co	Fe	$CoFe_2O_4$	$BaFe_2O_4$
M_d (kA/m)	446	414	1140	1790	1440	1750	425	380

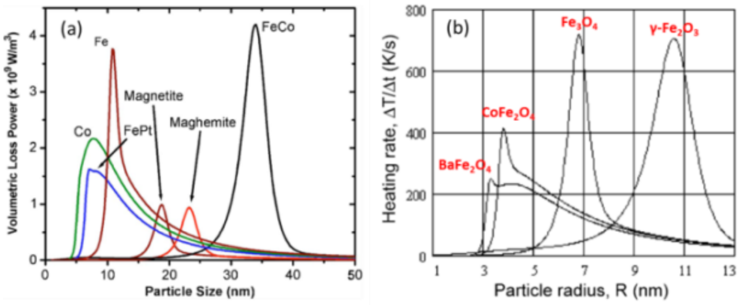

Figure 2. 9 (a) Calculated volumetric power loss for various magnetic metal and alloy and metal oxide materials at 300 kHz and 50 mT ac field in aqueous dispersion with 10% particle concentration (reproduced from Ref [151] with permission from AIP Publishing, copy right 2008). (b) Calculated heating rates for often-used magnetic metal oxide particles suspending in tetradecane (reproduced from Ref[85] with permission from Elsevier, copy right 2002). The inserted table summarises the domain magnetization of material listed in (a) and (b).

However, the low M_s limits the SAR of MNPs made of metal oxide. Given that SAR have a maximum value when $2\pi f\tau_e = 1$, decreasing τ_e significantly raises the optimal frequency, thus enhancing the power dissipation according to $P = f \cdot \Delta U$. Without the presence of inter-particle interactions, τ_e is controlled by K_{eff} and size of particle. When K_{eff} decreases to a relatively low level, the reduced magnetic anisotropy energy benefits Néel relaxation mode to take control over the relaxation, resulting in a significant decrease in τ_e (see equation (2.1) and (2.6)). Lee *et al.* [5]plotted the calculated SAR as functions of K_{eff} and size (Figure 2.10) with settings that M_s is kept as constant at 100 emu/g and f = 500 kHz and H_0 = 37.8 kA/m. The result shows that the SAR increased with the decrease of K_{eff} and achieved maximum value when K_{eff} is in the range of 15 - 20 kJ/m. In this work, they lowered down the K_{eff} to this range by formation of exchange-coupled core-shell structure by compositing low-K_{eff} $MnFe_2O_4$ (3 kJ/m) and high-K_{eff} $CoFe_2O_4$ (200 kJ/m). As a result, a SAR of 3034 W/g was obtained. Table 2.1 summarizes the good results of SAR that have been reported in these years. $Zn_{0.4}Co_{0.6}Fe_2O_4/Zn_{0.4}Mn_{0.6}Fe_2O_4$ won the golden medal due to the large M_s 150 emu/g as well as the magnificent Hf. However, it is hard to prepare such MNP massively but also with high quality.

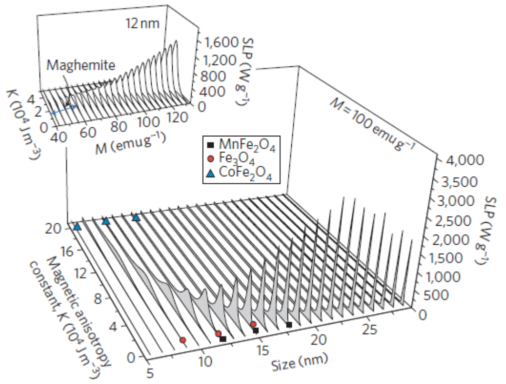

Figure 2. 10 Simulated plot of SLP based on nanoparticle size and magnetic anisotropy constant at a saturation magnetization value M_s of 100 emu/g with settings of f = 500 kHz and H_0 = 37.8 kA/m. (reproduced from Ref[5] with permission from Nature Publishing Group, copy right 2011)

Table 2.1 Experimental results of SAR values of various magnetic nanoparticles. (copy from Ref[5] with permission from Nature Publishing Group, copy right 2011)

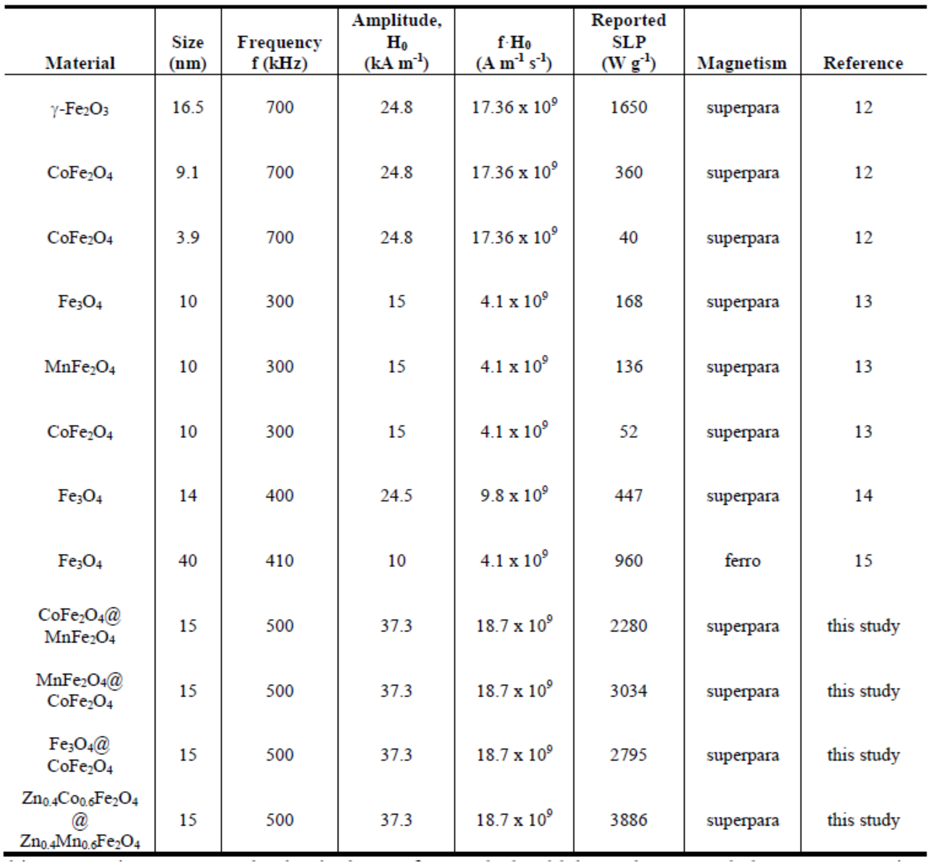

Material	Size (nm)	Frequency f (kHz)	Amplitude, H_0 (kA m^{-1})	f·H_0 (A m^{-1} s^{-1})	Reported SLP (W g^{-1})	Magnetism	Reference
γ-Fe_2O_3	16.5	700	24.8	17.36 x 10^9	1650	superpara	12
$CoFe_2O_4$	9.1	700	24.8	17.36 x 10^9	360	superpara	12
$CoFe_2O_4$	3.9	700	24.8	17.36 x 10^9	40	superpara	12
Fe_3O_4	10	300	15	4.1 x 10^9	168	superpara	13
$MnFe_2O_4$	10	300	15	4.1 x 10^9	136	superpara	13
$CoFe_2O_4$	10	300	15	4.1 x 10^9	52	superpara	13
Fe_3O_4	14	400	24.5	9.8 x 10^9	447	superpara	14
Fe_3O_4	40	410	10	4.1 x 10^9	960	ferro	15
$CoFe_2O_4$@ $MnFe_2O_4$	15	500	37.3	18.7 x 10^9	2280	superpara	this study
$MnFe_2O_4$@ $CoFe_2O_4$	15	500	37.3	18.7 x 10^9	3034	superpara	this study
Fe_3O_4@ $CoFe_2O_4$	15	500	37.3	18.7 x 10^9	2795	superpara	this study
$Zn_{0.4}Co_{0.6}Fe_2O_4$ @ $Zn_{0.4}Mn_{0.6}Fe_2O_4$	15	500	37.3	18.7 x 10^9	3886	superpara	this study

As mentioned before, a high Hf AC magnetic field demands powerful electric system and generates strong non-selective eddy current heating, both of which cause safety problems to patient as well as the operator. The research interest now is shifting to the fabrication of MNPs for low Hf hyperthermia treatment that the produce of H_0 and f is kept less than 5×10^9 A/ms. However, the reduction in H_0f comes with sharp decrease of SAR.[131, 152-154] Fortin *et al.*[131] investigated the changes of SARs of superparamagnetic γ-Fe_2O_3 and $CoFe_2O_4$ nanoparticles with different sizes suspending in pure water or 5% glycerol water solution with reducing the frequency and amplitude. They found that the SAR of all of suspensions was reduced by two orders when H_0f decreased from 17×10^9 to 3.5×10^9 A/ms.

Lots of prior studies chose large MNPs with permanent magnetization for hyperthermia, in hope that hysteresis losses can contribute to magnetic loss to enhance the heating efficiency.[83, 155-157] In fact, it is very difficult to obtain a well-dispersed ferromagnetic MNP liquid suspension, because the strong inter-particle interactions should have already caused clustering of particle.[155, 158-161] The process of clustering of ferromagnetic particles is spontaneous. The sizes of clusters often range from several hundred nm to µm. In addition, under an AC magnetic field ferromagnetic particles liquid suspension undergo further aggregations and form needle-like assemblies whose lengths range in micrometer. The optimal size for targeted particle delivery is 100-200 nm in order to avoid being removed by human clearance system and elongate duration time in vessel system after being intravenously injected.[162, 163] Most importantly, as mentioned before, the onset of hysteresis losses demands high filed amplitude, which increases with the particle size, but the MFH system in clinical study now can only supply an alternating field with amplitude less than 20 kA/m. For maghemite particles, it requires 25-30 kA/m of field amplitude to intrigue hysteresis loss of large particles to surpass the loss produced by delay in relaxations on small particles (Figure 2.6 b).

As a matter of fact, a number of works have confirmed that SMNPs also undergo non-uniform spontaneous clustering in suspension even in absence of magnetic field.[106, 136] However, without a permanent particle magnetic moment, the clustering of SMNP is much easier to be controlled. There are so many approaches that have been came up with to prepare SMNP clusters with different size and particle spacial arrangement[109, 164, 165]. Meanwhile considering too small particles may 'leak' from the pores of fenestrated capillaries in normal tissues during targeted particle delivery, some people tried heating SMNP clusters and found their great potential for magnetic hyperthermia. Hayashi *et al.*[166] observed the SAR increased from 156 to 248 W/g after controllably assembling isolated 9 nm of magnetite nanoparticle into sphere-like 100 nm of clusters. And the product of filed frequency and amplitude was only 1.8 × 10^9 A/ms. Nevertheless, several works indicated that the clustering of MNP doesn't always improve the SAR. The work of Dutz *et al.* [167]found the SAR is dependent on the cluster size. In this work, they prepared a ferrofluid made of magnetic clusters (Figure 2.11 a b) ranging from 50 to 160 nm in hydrodynamic diameter. The results of heating efficiency of clusters with different sizes are summarized in the table shown in Figure 2.11. When the size of iron oxide particle cluster increased from 50 to 160 nm, the SAR raised at first to 332 W/g and then fell down to 50 W/g. Liu *et al.*[168] observed a reduction of heating efficiency when 6 nm SMNPs were high-contently loaded into a sphere-like polymer latex, but loading 18 nm SMNPs generated an increase in efficiency. Actually, when SMNPs form into cluster, the close pack of particle favors inter-particle interactions, which cast a great influence on magnetic loss. Therefore, it is urgent to get clear of the role of inter-particles dipole interactions in hyperthermia.

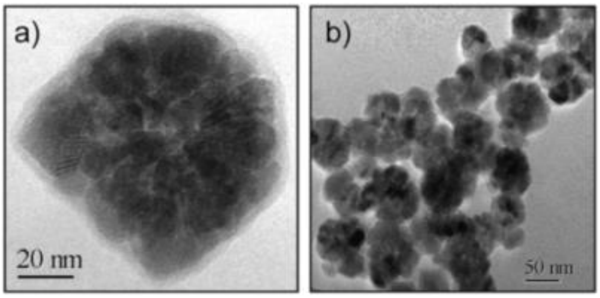

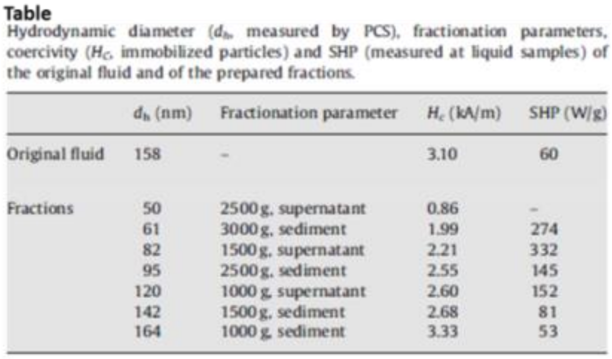

Table
Hydrodynamic diameter (d_h, measured by PCS), fractionation parameters, coercivity (H_C, immobilized particles) and SHP (measured at liquid samples) of the original fluid and of the prepared fractions.

	d_h (nm)	Fractionation parameter	H_c (kA/m)	SHP (W/g)
Original fluid	158	–	3.10	60
Fractions	50	2500 g, supernatant	0.86	–
	61	3000 g, sediment	1.99	274
	82	1500 g, supernatant	2.21	332
	95	2500 g, sediment	2.55	145
	120	1000 g, supernatant	2.60	152
	142	1500 g, sediment	2.68	81
	164	1000 g, sediment	3.33	53

Figure 2. 11 TEM images of a single cluster (a) and an ensemble of clusters (b) formed by 14 nm (characterized by XRD) of iron oxide particles obtained by coprecipitation method. The table summarizes the hydrodynamic diameter, filtering conditions, coercivity and SAR of gained clusters with different size. (reproduced from Ref [167] with permission from Elsevier, copy right 2009)

2.3.4 The role of inter-particle dipole interactions in magnetic hyperthermia

Numerical simulation should be the best way to study the role of inter-particle dipole interactions in magnetic hyperthermia. It is because that few technologies are found to be useful for characterizing dipole interactions during a real hyperthermia heating. Theoretically, the energy of dipole couplings between two single-domain particle i and j separated by $\vec{r}_{ij}$ is given as,

$$E_D^{(i,j)} = \frac{\mu_0 M_d^2 V_p^2}{4\pi}\left[\frac{\vec{s}_i\cdot\vec{s}_j}{r_{ij}^3} - \frac{3(\vec{s}_i\cdot\vec{r}_{ij})(\vec{s}_j\cdot\vec{r}_{ij})}{r_{ij}^5}\right] \qquad (2.21)$$

where $\vec{s}_i$ is the unit vector of particle moment. From this equation, it can be seen that the dipole interaction is effective in long range and its intensity depends on the magnitude and orientation of individual moments and the distance between them. If the particle moments get aligned with a magnetic field, all of dipoles are coupled with each other head to tail, and this equation can be simplified to,

$$\sum_{i<j} E_D^{(i,j)} = \sum_{i<j} \frac{\mu_0 M_d^2 V_p^2}{4\pi} [\frac{1-3(cos\theta_{ij})^2}{r_{ij}^3}] \quad (2.22)$$

where θ_{ij} is the angle between the direction of the external magnetic field and the line joining the centers of the two particles i and j. The equation (2.22) suggests that dipole interaction is highly anisotropic: when angles θ is smaller than 55°, the energy E_D is negative, so the dipole interaction is stable; but for 55° < θ < 125°, the E_D turns to be positive, indicating that the two dipoles are repelling each other.

When multi MNPs keep interacting with each other, numerical simulation can be used to quantitatively investigate the effect of dipole interactions on the magnetism of MNP system, such as coercity[169-172], the blocking temperature[170, 171, 173, 174], and magnetic susceptibility[155, 173, 175]. Almost all of models are built on the same energy model of MNP system, which includes three main sources: anisotropy E_A, Zeeman E_H and dipolar interaction E_D. The uniaxial anisotropy E_A of each particle is given by,

$$E_A^{(i)} = -K_{eff} M_d V_p (\vec{s}_i \cdot \vec{n}_i)^2 \qquad (2.23)$$

where $\vec{n}_i$ is the unit vector along the easy axis direction. The interaction with the applied field $\vec{H}$ is described by,

$$E_H^{(i)} = -\mu_0 M_d V_p (\vec{s}_i \cdot \vec{H}) \qquad (2.24)$$

By combining equation (2.21), (2.23) and (2.24), the total energy of system is expressed as,

$$E = \sum_i E_A^{(i)} + \sum_i E_H^{(i)} + \sum_{i<j} E_H^{(i,j)} \qquad (2.25)$$

There are two often-used simulation approaches. One of them is Langevin dynamics simulation. In this method, it is assumed that the individual particle moment only response to an imaginary field, called effective field $\vec{H}_{eff}$, which combines the effects of particle anisotropy field, magnetic field, and dipole coupling field, and the motion of the particle moment during the process of getting aligned with the $\vec{H}_{eff}$ should proceed in a rigorously predefined damping fashion. The magnetization dynamics of each particle is described by the Landau-Lifshitz-Gilbert (LLG) equation of motion with Langevin dynamics, which is given as,

$$\frac{\partial \vec{s}_i}{\partial t} = -\frac{\gamma}{(1+\alpha^2) M_S V_i} \vec{S}_i \times \left[\vec{H}_{eff(i)}(t) + \alpha \vec{S}_i \times \vec{H}_{eff(i)}(t)\right] \qquad (2.26)$$

Where the coefficient γ denotes the absolute value of the gyromagnetic ratio, and α is the dimensionless Gilbert damping constant. The time-dependence $\vec{S}_i(t)$ is gained by integration of equation (2.26) with respect to time. The magnetization of the MNP system is recorded as the projection of the magnetic moments along the field direction. Although this approach has a solid physical basis, it is pronounced only when the time interval needed for a single spin precession is discretized sufficiently to ensure an acceptable numeric accuracy.[176]

So, the second numerical method, termed the standard Monte Carlo method, turns out to be important. In this approach, a so-called Metropolis algorithm is employed to simulate the time-dependence magnetization of each particle. Very different from Langevin dynamics simulations, it doesn't study how the motion of particle moment proceeds but how possible this motion will happen. The Markovian chain of Metropolis Algorithm is formed by generating each new state directly from the preceding state. It processes the simulation in a stochastic manner by directly agitating the moment of a randomly-picked particle to a new orientation chosen inside of a spherical segment around the present orientation with an aperture angle $\delta\theta$. And then the new orientation is accepted with probability min $[1, \exp(-\Delta E/k_B T)]$, where ΔE is is the change in the total energy of cluster system caused by the agitation. For a system of N-particles, one MC step is defined by the repetition of this process N times until all of particles' moments are agitated. The magnetization of the system is recorded after a certain amount of MC steps as the projection of the magnetic moments along the field direction. The accuracy of this simulation method is controlled by $\delta\theta$ and the amount of MC step per unit variance of magnetic field[155]. The main problem of this simulation approach is that it cannot describe a dynamic magnetic hysteresis in a quantified manner without a theory to associate physical time with the Monte Carlo step.

The debate about the role of inter-particle dipole interactions in hyperthermia has been continuing for years. The points about its influence are quite different, even contradictory. The most people hold negative attitude. The first experimental observation of SAR decrease believed to be caused by dipole interactions was published by Urtizberea *et al.*[175] in 2010. They found that SAR of superparamagnetic MNF decreased by one half as the concentration of particle increased by 4.5 folds under driven by a field of H_0 = 3 kA/m and f =109 kHz. In the same year, Serantes *et al.*[155] reported the reduction of SAR observed on induction heating condensed aqueous 75 nm of Fe/MgO particle solution. Both works attributed the reduction in efficiency to dipole interactions. In 2012, Haase *et al.*[177] gave the evidence of negative effect of dipole interactions that the loss per cycle decreased as enhancing the dipole interactions of ferromagnetic particle suspension system modeled by Langevin dynamics simulations. They found that both of remanence magnetization and coercivity of particle system decreases with the increase of the particle concentration. Futhermore, the decline of the loss per cycle of free particle system is much more obvious than the repellent particle system whose tendency to cluster was reduced intentionally.

Different opinions appeared first in 2008, Dennis *et al.*[178] manipulated the strength of dipole interactions by changing the thickness of stabilizer on the particle surface, finding that the measured SAR of tightly associated ferromagnetic particle is 7 fold higher than very loosely associated particles under a field of 86 kA/m and 150 kHz. In 2012, Martinez-Boubeta *et al.* [179] found that the influence of dipole interactions on the SAR of ferromagnetic 40-65 nm Fe/MgO particle fluid appeared only when the field amplitude was large enough; and the profile of concentration-dependent SAR presented a peak when the size was 40 nm; but this peak was flattened as increasing the size and finally the influence turned to be totally negative at 65 nm. In the same year, Singh *et al.*[136] applied mean field theory to theoretically investigate the heating of non-clustered superparamagnetic Fe_3O_4 particle suspension by a field of 100 Oe. The results showed that the heating power per particle kept increasing with the concentration at 6-8 nm, but an optimal concentration existed when the size was 10 nm. In 2015, based on experimental and modelled findings, Serantes *et al.* [180] proposed a general picture to explain the heating performance of ferromagnetic MNF as a function of field amplitude and particle concentration. As shown in Figure 2.12, at low concentration, the magnetic loss of MNF is single particle- type, with total energy determined by anisotropy and Zeeman energies. As increasing the concentration, stronger dipole interactions decrease the overall anisotropy energy[181], thus leading to a reduction of heating efficiency. By further increasing the concentration, the magnetic loss can be understood in terms of a competition between the local dipolar field and the applied field. Too strong dipole interactions will prevent magnetization process, damaging the heating efficiency. In 2016, Ovejero *et al.* [182]reported a very similar trend after studying the influence of particle concentration on the heating efficiency of liquid suspension of 20 nm of iron oxide particles. They found that the hysteresis loop is dominated by the values of magnetizations, including maximum magnetization and remaining magnetization.

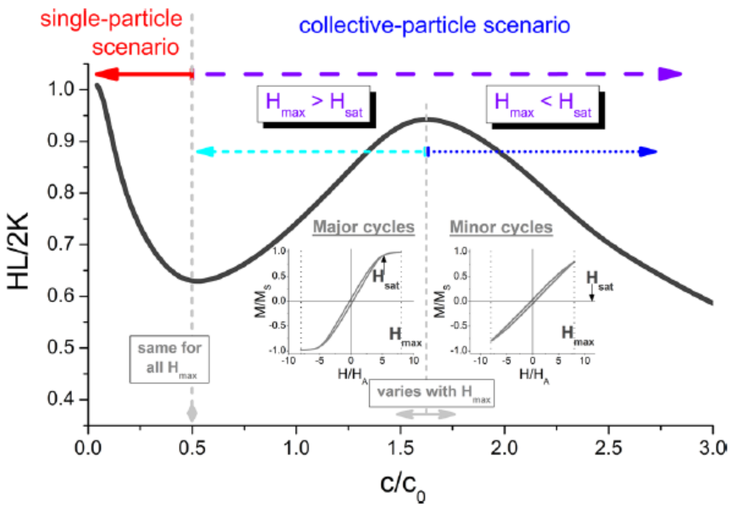

Figure 2. 12 Schematic description of the magnetic hyperthermia scenario (copy from Ref[180] with permission from American Chemical Society, copy right 2015).

There are several reasons to explain why the role of dipole interactions is so complex. According to classic DLVO theory, as increasing the concentration, being affected by dipole attraction, MNPs suspending in liquid preferred to form chain-like cluster at the early stage of aggregation. And the further increase of concentration will shorten the distance between particles, forcing particles to overcome the potential barrier, leading to irreversible aggregates. Actually, the work of Urtizberea *et al.*[175] has already suggested that non-uniform spontaneous clustering should make worse the heating efficiency. It can be deducted that a great diversity of MNP clusters in solution must cause a wide distribution of magnetic susceptibility to a certain alternating field.

It is more difficult to discuss the magnetic losses of a cluster of multi MNP. For large particles, the strong dipole interactions might make them to form dipolar magnetism. Varón *et al.*[183] proved the roughness of such dipolar magnetism formed by ferromagnetic particle via applying electron holography technology to characterize the dipole orientations of two-dimensional 15 nm Co particles assemblies. Even under a very strong magnetic field as 2 Tesla, not all of dipoles get aligned with this field. In this situation, it is hard to predict how such magnetism reacts to a magnetic field. Although the dipole of SMNP is not so powerful to form such solid dipolar magnetism, 'spin glass' may play an important role in determining the magnetic response of aggregate.

Since the energy of dipole interactions heavily relies on the relative positions of particles, the morphology of cluster and particle spacial arrangement turn out to be crucial in determining the role of dipole interactions. It is reasonable to infer that chain or cylinder-like assemblies should perform the best heating efficiency. It is because that the head to tail particle arrangement in a chain prompt particle dipoles to couple along the chain axis, which make the reversal of the magnetization of cluster harder. Martinez-Boubeta *et al.* [83] suggested that the hysteresis loop area of individual chain cluster should increase with the number of particles. However, their experiment results disproved it; the SAR was lowered by prompting the chain clustering via increasing the concentration. Mehdaoui *et al.*[33] argued that inter-particle dipole interactions can generate a new uniaxial magnetic anisotropy to improving the heating only when MNPs form clusters with high morphology anisotropy, but higher filed amplitude was required to initiate the magnetic loss of such clusters and low individual magnetic anisotropy is desired. Branquinho *et al*.[184] reported that only at high damping factor the heating efficiency of short chain clusters would increase with the chain length; but at lower damping factor formation of chains could lead to low heating efficiency, because the individual magnetic anisotropy became farther away from the optimal value although dipole interactions reinforce the cluster's effective magnetic anisotropy. The role of dipole interactions is also dependent upon the relative orientation of the magnetic field with respect to the clusters. Several modelling results suggest that chain cluster will produce less heat once the field direction does not align with the chain axis[185] [34]. Serantes *et al.* [186]studied the effect of cluster's shape and field orientation on hyperthermia heating agar gel containing 44 nm of iron oxide particles. Their results suggested that although chain-like clusters have the superior heating performance, their heating efficiency becomes worse with increasing the angle between field direction and chain axis. In order to understand how dipole interactions dominate the hysteresis losses of a cluster, it is necessary to develop a method to associate the influence of dipole interactions with the cluster's characteristics as well as the magnetic field orientation; and it can be applied to the cluster with any shape and particle arrangement.

2.4 MNF-based heat transfer enhancement

2.4.1 Thermo-physical properties

Density, specific heat capacity, viscosity and thermal conductivity are the four fundamental parameters for evaluating overall thermal performance of nanofluids. Typically, thermal conductivity and viscosity increase with adding more particles. The thermo-physical properties of MNF can be changed by an external magnetic field except density. In this section, the review will mainly discuss the applicability of present models and the effect of colloidal stability on thermo-physical properties.

2.4.1.1 Density

Density is an important property of nanofluids that affects the Reynolds number, friction factors, pressure loss and Nusselt number. Generally, density of a nanofluid is proportional to the volume fraction of particles. At most times, the density of solid particles is larger than the base liquid, the density of nanofluid is supposed to increase with particle concentration linearly. Usually, the density of nanofluids has been reported to be consistent with the mixing theory[187] given by,

$$\rho_{nf} = (1-\phi)\rho_{bl} + \phi\rho_s \tag{2.27}$$

where ρ_{nf} is the density of nanofluid, ϕ the volume fraction of particle, ρ_{bl} the density of base liquid and ρ_s the density of particles. Paketal *et al.* [187] and Hoetal *et al.* [188]reported an good agreement between the measured density and calculated ones of alumina – water nanofluids. The density of MNF also coincides well with the result suggested by mixing theory. [189] Besides particle concertation, the density of a nanofluid is also dependent on temperature[190, 191] and pressure[192]. After investigation of density of nanofluids of alumina, antimony-tin oxide or zinc oxide particles, Vajjha *et al.* [191] decided to attribute the effect of temperature all to the change of ρ_{bl}, with assuming that ρ_s kept constant. In this way, equation (2.27) will be still valid as long as ρ_{bl} at a certain temperature is known.

2.4.1.2 Specific heat capacity

Recently, the study of the specific heat capacity of a nanofluid has gained more and more attentions. This is because the specific heat capacity plays an important role in evaluating the thermal performance of nanofluids. For example, it is required in the measurements of thermal conductivity[193], thermal diffusivity[194, 195] and the spatial temperature inside the flow[196, 197]; in natural convection, it is one of the key parameters for describing the nanofluids and the convective flow status[198-200]. Shahrul *et al.* [37] did excellent work on summarizing the technologies used for measuring the specific heat of nanofluids. Differential scanning calorimeter (DSC) has been proven to be successful in measuring the specific heat of nanofluids. [201-203]

Evidence has shown that the specific heat capacity of a nanofluid is affected by various parameters, including particle concentration[37], temperature[204, 205], particle size[206], particle material[207] and the type of base liquid[207]. It is found that the heat capacity of nanofluid often decreases when using the particles of lower heat capacity.[37] For example, the specific heat capacity of alumina nanofluids decreases with increasing particle concentration. [201, 208] However, opposite behaviour is observed when the specific heat of particles is higher than the base liquid. For instance, the specific heat capacity of carbon nanotubes ethylene glycol nanofluids is enlarged with increasing concentration. [208, 209] Temperature affects the heat capacity of nanofluid in a complex way. In general, it increases with temperature (see Figure 2.13). However, several works suggested completely opposite trend of specific heat with the rise of temperatures. [210, 211] Otherwise, Wang *et al.* [206] demonstrated that the specific heat capacity of particle is dependent upon the particle size. Thus, it is possible that the specific heat capacity of nanofluid changes with the particle size.

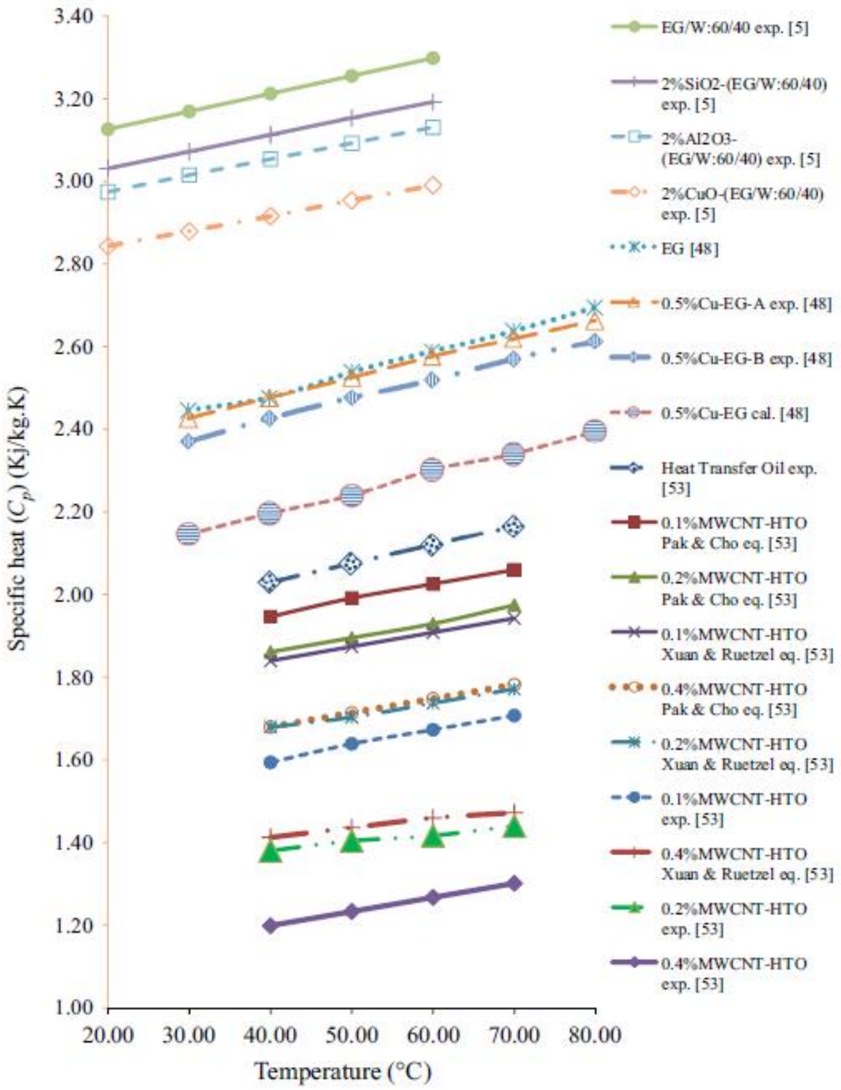

Figure 2. 13 Specific heat of nanofluids increases accordingly with temperature (the chart including the legends are completely copied from Ref[37] with permission from Elsevier, copy right 2014)

Many efforts have been made to theoretically model the specific heat capacity of nanofluid. In 1998, for the first time, Pak and Cho [187]used the following equation to explain the effect of particle concentration on the specific heat of nanofluids.

$$C_{p,nf} = \phi C_{p,n} + (1-\phi)C_{p,bl} \qquad (2.28)$$

where subscripts nf, n, and f refer to the nanofluid, nanoparticle and base liquid. In 2000, Xuan and Roetze[212] proposed the following model, which is based on the classical and statistical mechanism[200, 213].

$$C_{p,nf} = \frac{\phi\rho_n C_{p,n} + (1-\phi)\rho_{bl} C_{p,bl}}{\phi\rho_n + (1-\phi)\rho_{bl}} \qquad (2.29)$$

Where ρ_n and ρ_{bl} are the density of particle and base liquid respectively. Equation (2.28) considers the effect of density, but model 1 doesn't. It has been suggested that this model is more fit than the equation (2.29) for interpreting ϕ – dependent $C_{p,nf}$.[37] Several empirical relations were proposed to estimate the effect of temperature.[208 214, 215] No theory has been come up with to explain it up to now.

While no evidence has been reported about the relationship between particle aggregations and the specific heat of nanofluid, Chiu *et al.* [216]suggested that the specific heat of MNF is sensitive to the intensity of an external magnetic field. They measured the specific heat capacity of a water – based MNF which was exposed to weak or strong field. Under a weak field, the specific heat capacity barely changed with temperature, but the specific heat capacity decreased dramatically with temperature under a strong field. They attributed this decrease to the reduction in the degrees of freedom of MNPs under the field. In fact, MNPs form chain-like clusters under the guidance of magnetic field. What's more, normal aggregations can also reduce the mobility of particles.

2.4.1.3 Viscosity

A good thermal working fluid should produce a high heat transfer efficiency but also a low pressure drop to reduce the pumping power. However, it is widely recognized that the viscosity of nanofluids increases with the rise of the volume fraction of particles,[55, 62]although which often leads to enhancement of thermal conductivity. [217] Figure 2.14 gives examples of increment of viscosity of nanofluids as a function of volume fraction. Tiwari *et al.*[218] reported that increasing particle concentration brought larger viscosity and density of nanofluid, which enlarged pressure drop, thus resulting in an increase of pumping power. Vajjha and Das[214] reported that it required more power to pump CuO nanofluid than the base liquid when the particle concentration was higher than 3 %. Furthermore, at large Reynolds number, the high concentration can cause more increment of pressure drop in comparison with the case of small Reynolds number (see Figure 2.15). In other words, the enhanced convective heat transfer efficiency could be offset by increased pumping power. Most importantly, the dispersed particles sometimes make the nanofluid behave like a non-Newtonian fluid,[55, 62] and the viscosity becomes hard to be predicted.

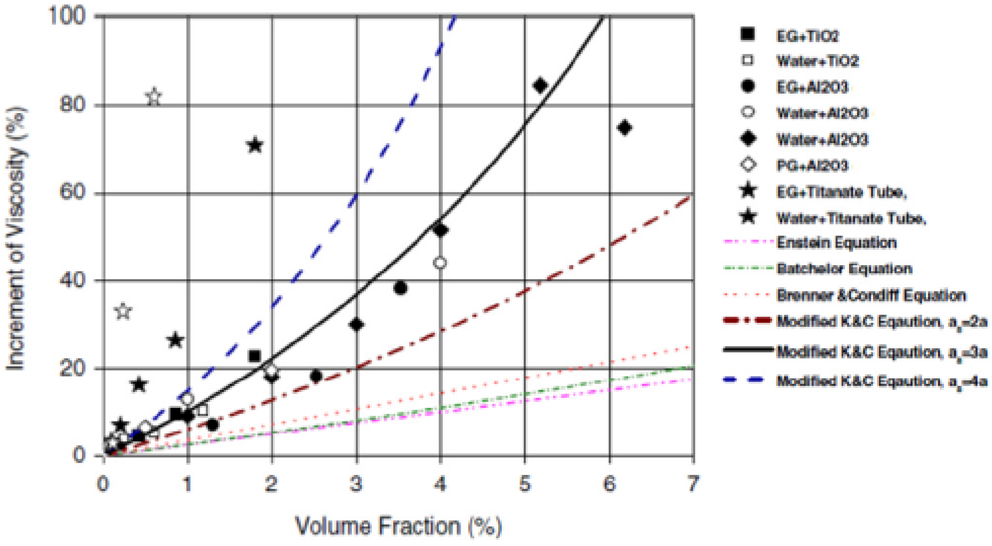

Figure 2. 14 Viscosity of nanofluids as a function of nanoparticle concentration (copy from[219] with permission from Springer, copy right 2009)

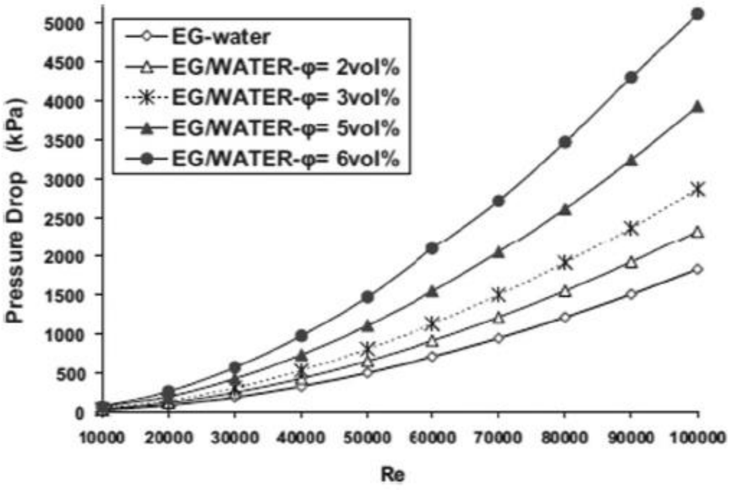

Figure 2. 15 Pressure drop as a function of Reynolds number at different particle volume fraction. (copy from Ref[220] with permission from Elsevier, copy right 2012)

Shear thinning of nanofluids has been reported by many researchers who found that the viscosity decreased with the shear rate during rheological measurements.[55-62] Lots of evidences show that shear thinning becomes significant with increasing particle concentration.[56-59, 221-223] Nanofluids are more likely to behave as Newtonian fluid when temperature is increased [59, 222, 224] or spherical particles are used [56]. It is known that nanoparticles have a great tendency to aggregate in solution caused by van der Waals attractive forces.[63] Once particles undergo aggregations, the aggregates have an effective volume fraction larger than isolated particles would, thus leading to an increase of fluid's viscosity.[108] If a strong shear stress could destroy particles aggregates, a decrease of viscosity should be expected, as a result, the viscosity decreases with shear rate. Zhou et al. [56] made such a hypothesis to explain the shear thinning behaviour of alumina polyalphaolefins nanofluid. Pastoriza-Gallego *et al.* [57] investigated the viscoelastic behaviour of ethylene glycol-based Fe_2O_3 nanofluids and observed a peak showing on the profile of loss modulus against strain. They interpreted the peak as that some kind of structure formed by particles within fluid is lost during the increase of strain. Duan *et al.* [58] found that the shear thinning of alumina water nanofluids disappeared after the samples were ultrasonically treated to reduce particle aggregations. If the shear thinning of nanofluid has to do with the aggregates being broken under shear, enhancing the colloidal stability to suppress aggregations should make the viscosity less dependent of shear rate. Furthermore, the more dispersed particles are supposed to reduce the viscosity of nanofluid, hence helping saving pumping power.

A variety of models has been developed to predict the viscosity of nanofluid at a specific particle concentration.[167] Einstein[225] theoretically studied the visocosty of infinite dilute suspensions of idealy dispersed and non-interacting hard spheres, with the assumpsion that particles rotate under shear. The relation he proposed is described as,

$$\mu_r = 1 + 2.5\phi \qquad (2.30)$$

where μ_r is the ratio of the viscosity of nanofluid to that of the base liquid. Einstein model applies to low volume concentration ϕ < 1%.[108] Brickman model[226] is the extension of Einstein model, which can be used for moderate volume concentrations.

$$\mu_r = \frac{1}{(1-\phi)^{2.5}} \qquad (2.31)$$

When $\phi \geq 1\%$, hydrodynamic interactions between particles become important as the disturbance of the fluid around one particle interacts with that around other particles. Batchelor model[227] takes Brownian motion and particles' interactions into considerations, which is suggested to be useful at $\phi \sim 1\%$.

$$\mu_r = 1 + 2.5\phi + 6.5\phi^2 \qquad (2.32)$$

A semi-empirical relationship for the shear viscosity covering the full range of particle volume fraction was obtained by Krieger and Dougherty[228],

$$\mu_r = (1 - \phi/\phi_m)^{-2.5\phi_m} \qquad (2.33)$$

where ϕ_m is the volume fraction of densely packed particles, which varies from 0.495 to 0.54, and is approximately 0.605 at high shear rate. To take aggregations into considerations, Chen *et al.* [108] modified Krieger and Dougherty's model to,

$$\mu_r = (1 - \phi_a/\phi_m)^{-2.5\phi_m} \qquad (2.34)$$

with $\phi_a = \phi\left(r_a/r_p\right)^{3-d_f}$ (2.35)

where r_a is the radius of the aggregates, r_p the radius of particles and d_f the fractal dimension of the aggregates which is around 1.8[229]. Figure 2.16 shows a comparison between the measured data and calculated results by equation (2.34). They found that the model fits best when $r_a\,/r_p$ is about 3. When ϕ_a is very small, Prasher *et al.* [230] suggested that it could perform a binomial expansion to reduce equation (2.34) to a linear relationship

$$\mu_r = 1 + 2.5\phi_a \qquad (2.36)$$

ϕ_a is the slope and a_a determines how fast the viscosity increases with particle concentration. For ideally dispersed particles, ϕ_a equals ϕ, thus the Krieger and Dougherty model is the same with Einstein model.

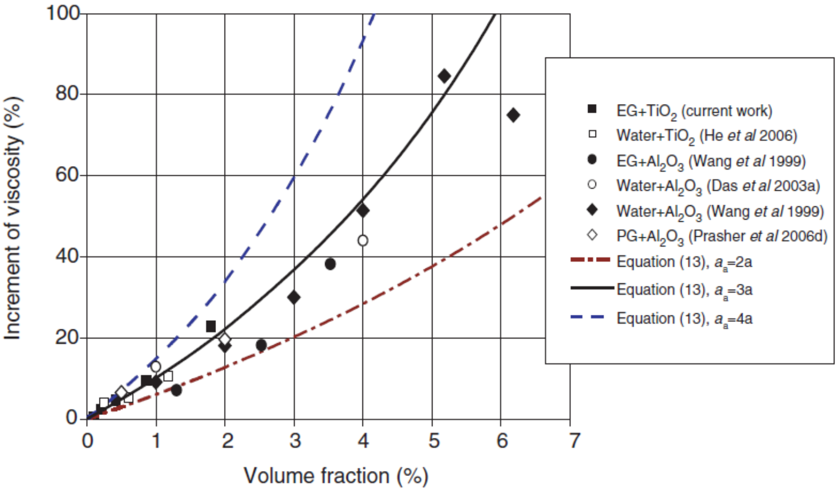

Figure 2. 16 Increment of viscosities for spherical particle nanofluids (copy from[108] with permission from Elsevier, copy right 2016)

However, the researchers in this field usually prefer to use the empirical equation which is developed based on the measured results of a certain nanofluid. Shear thinning of nanofluids is one reason. Another one is that the viscosity of nanofluid is affected by temperature and it cannot be attributed all to the viscosity variance of base liquid. For example, as shown in Figure 2.17, the μ_r of dilute Fe_3O_4 nanofluid increases with ϕ much quicker at higher temperature; however, an opposite scenario is found on condensed CuO nanofluid. According to equation (2.34) and (2.35), a faster increment with ϕ suggests bigger particle aggregates. Several works suggest that higher temperature could prompt particles aggregations.[231-233] Chen *et al.* [233] summarized two reasons. Firstly, the viscosity of the base liquid is lower at higher temperature, which often leads to a larger collision frequency rate among particles. Secondly, temperature changes the interaction energy between particles. Nonetheless, it is hard to explain why the μ_r of a condensed nanofluid increases quicker at low temperature. It is known that aggregation proceeds faster at higher particle concentrations. It is possible that the aggregation condition in a diluted solution is different from that in a condensed one.

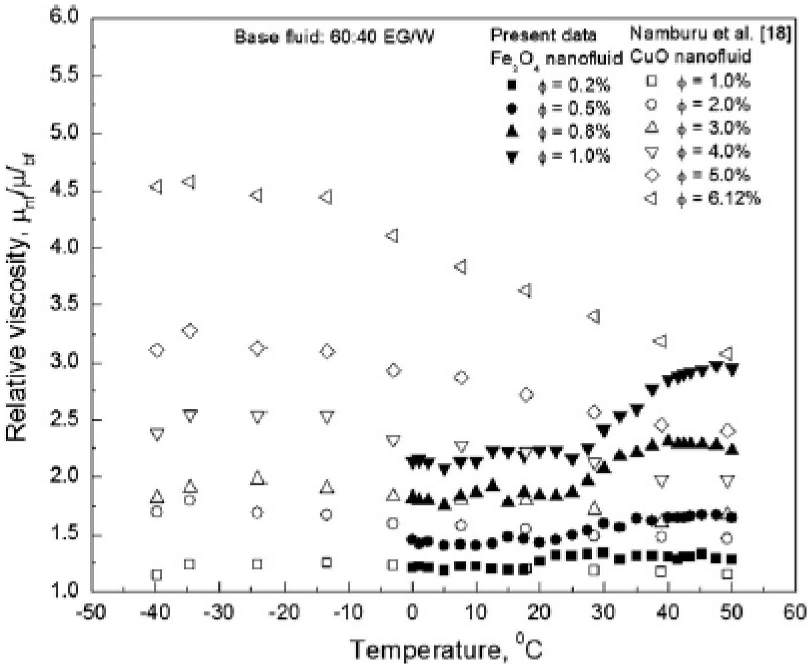

Figure 2. 17 Comparison of relative viscosity of Fe_3O_4 and CuO nanofluid at different temperature. The base liquid is ethylene glycol and water mixture. EG stands for ethylene glycol and W for water. (Copy from[95], with permission from Elsevier, copy right 2012, the data of CuO nanofluid is cited from[234])

Moreover, the viscosity of MNF is susceptible to an external magnetic field, and this feature is known as magnetoviscous behaviour.[49] When a MNF is exposed to a field, the particles tend to get aligned with the field. This alignment confines the movement of particles and eventually increases the effective viscosity of the suspension. Several researchers have tried to use magnetic field to enhance convective heat transfer efficiency of MNF.[51, 235, 236] Thermomagnetic convection is suggested to be the solution of cooling of micro-sized geometries, but which is hindered by magnetoviscous effect.[45] The particle aggregations should make the estimation of magnetoviscous behaviour more complex. Therefore, it is necessary to study the relationship between colloidal stability and viscosity of nanofluid.

2.4.1.4 Thermal conductivity

Enhanced thermal conductivity of nanofluids could be the one of the most attractive features to the researchers in heat transfer engineering. For example, Abareshi *et al.*[237] reported a 11.5 % of enhancement in the thermal conductivity of water – based Fe_3O_4 nanofluid at 40 °C after the particle volume fraction was increased to 3 %. Singh *et al.*[238] found that the thermal conductivity of ethylene glycol and water mixture based Fe_3O_4 nanofluid increased by 33 – 46 % at 60 °C when particle volume fraction was 2 %. In addition, thermal conductivity of MNF can be further improved by applying a magnetic field. Although, in general, thermal conductivity of nanofluid increases by adding more particles, it is so difficult to predict the amount of increment with using established theoretical models.

Most of reported models are derived from the well-known Hamilton–Crosser model[239]. As nanofluid is a two-phase fluid; therefore, one may expect that it would have common features with solid–liquid mixtures. So, Hamilton–Crosser model is described as,

$$k_n = k_{bl}\left[\frac{k_p+(n-1)k_{bl}+(n-1)\phi(k_p-k_{bl})}{k_p+(n-1)k_{bl}-\phi(k_p-k_{bl})}\right] \quad (2.37)$$

where subscripts nf, bl and p stand for nanofluid, base liquid and particle, n is the empirical shape factor. For spherical particles, the value of n is equal to 3, and then we get Maxwell model,

$$k_{nf} = k_{bl}\left[\frac{k_p+2k_{bl}+2\phi(k_p-k_{bl})}{k_p+2k_{bl}-\phi(k_p-k_{bl})}\right] \quad (2.38)$$

Maxwell model is suggested to be satisfactory for spherical shaped particles with low particle volume concentrations.[240] Bruggeman *et al.*[241] proposed a model for full range of particle concentration.

$$\phi\left(\frac{k_p-k_r}{k_p+k_r}\right)+(1-\phi)\left(\frac{k_{bf}-k_r}{k_{bf}+2k_{nf}}\right)=0 \quad (2.39)$$

where k_r is the ratio of k_{nf} to k_{bl}. It is noticeable that at low volume fractions, Maxwell model and Bruggeman model generate similar results.[242, 243]

Lots of evidences demonstrate the mismatch between the experimental data and value calculated by the above models.[193, 238, 244-248] To improve the accuracy, the models were modified to consider several other effects, *i.e.*

formation of solid – like "nanolayer" on the particle's surface [249-251] , interfacial thermal resistance[252] and Brownian motion[253-255]. The theory of "nanolayer" presumes that the base fluid molecules close to the solid surface of the nanoparticles form solid-like layered structures. Hence the nanolayer works as a thermal bridge between the liquid base fluid and the solid nanoparticles, and this will enhance the effective thermal conductivity. The effect of Brownian motion is interpreted in two ways, heat transport caused by motion of nanoparticles and micro-convection of fluid surrounding individual nanoparticles. [256] However, it has been suggested that the effect of Brownian motion should be overestimated. [46] Keblinski *et al.*[257] showed that thermal diffusion is much faster than Brownian diffusion, even through particles are extremely small. In other words, heat transfer is supposed to be already finished before particle moves.

However, most researchers still prefer to use empirical equations. Based on the reviewing of reported experimental results, Tawfik *et al.*[258] summarized seven parameters that can affect thermal conductivity of nanofluid, including particle's concentration, size, shape and thermal conductivity, base liquid type, temperature and preparation method. In fact, the first six ones have been discussed by the reported models (the effect of particle size can be included by using theory of Brownian motion). There are several reasons that limits their applicability. First, it is hard to propose one simple equation which simultaneously considers all these factors. Secondly, they often depend on parameters unknowable. For example, to use theory of "nanolayer", one must assume the thickness of this layer.

The last parameter, preparation method, mainly determines the stability of particle dispersion. It is widely accepted that heat transfer should be much faster along the structure of aggregate than through the body of base liquid. Bigdeli *et al.*[38] suggested that most enhancements beyond predictions of effective medium theories come from the formation of thermal percolating paths due to aggregation of nanoparticles[229, 259, 260], which is illustrated in Figure 2.18. For instance, Gavili *et al.* [261] found that thermal conductivity of water – based Fe_3O_4 nanofluid was increased by 200 % under a 1000 G of magnetic field at 25 ^oC. The mechanism responsible for such significant enhancement is believed to be chain - like particle alignment in the direction of the applied magnetic field, parallel to the temperature gradient. [262] Otherwise, by modelling the contribution of aggregations to thermal conduction, Prasher[229] reported that there should be an optimal scale of aggregation for enhancement of thermal conductivity (see Figure 2.19). Fully aggregated and dispersed nanofluid should generate the thermal conductivity comparable to the value predicted by Maxwell model. If the particles undergo uncontrolled aggregations, it could be impossible to predict thermal conductivity of nanofluid. Xuan *et al.* [263]developed a model considering Brownian motion and the diffusion-limited aggregation. However, it has been suggested that there is something wrong with the Brownian motion part of their model.[264]

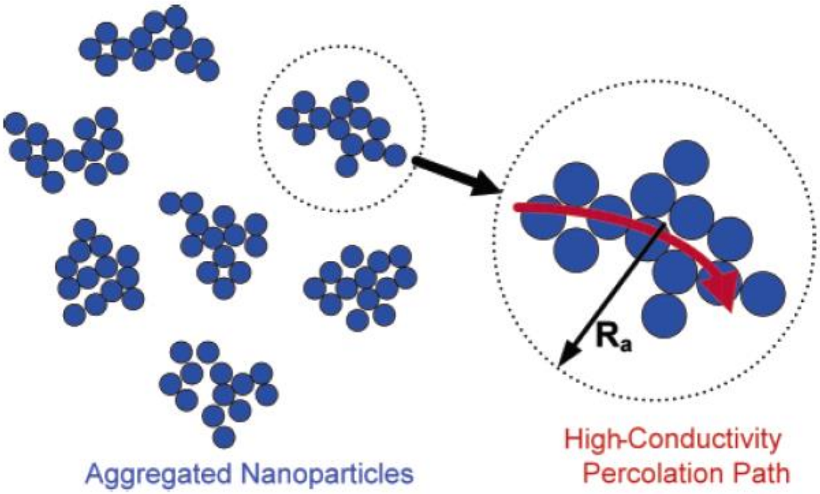

Figure 2. 18 Schematic of well-dispersed aggregates. Aggregates have a higher mass than individual particles, thus they can generate high-conductivity percolation path (copy from[229] with permission from American Chemical Society, copy right 2006).

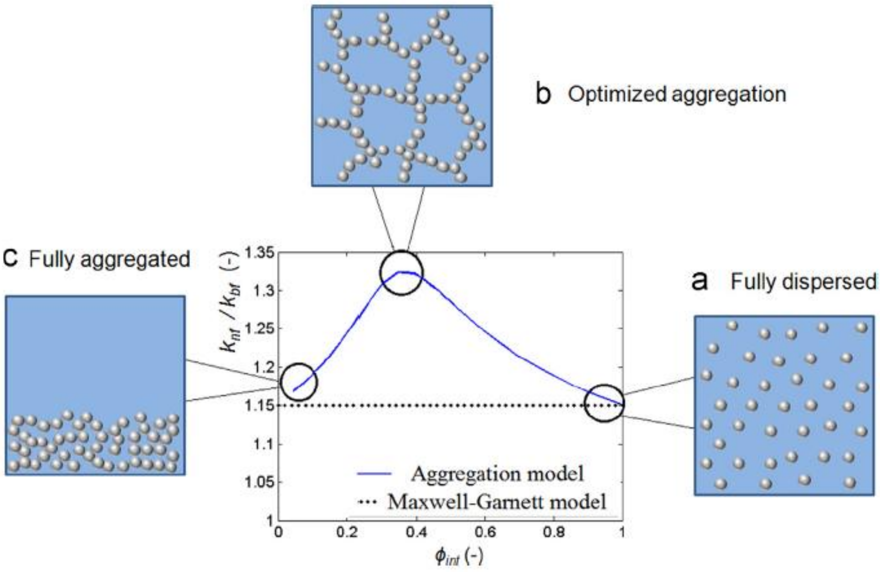

Figure 2. 19 The dependence of enhancement of thermal conductivity on aggregation. (a) For a well-dispersed nanofluid, the thermal conductivity should be in agreement with the value suggested by Maxwell model. (b) Optimal scale of aggregation for the best thermal conductivity. (c) Futher aggregations will reduce thermal conducitivity. It is because the majority part of nanofluid is empty of particles and thus the heat transfer mainly accounts on the base liquid. (copy from[38] with permission from Elsevier, copy right 2016)

2.4.2 Enhancement of convective heat transfer

Lots of works has been carried out to investigate convective heat transfer of nanofluids. In most studies, nanofluids are pumped through a circular tube uniformly heated with constant power. Undoubtedly, the enhancement of the heat transfer coefficient should be much more attractive that the improvement of thermal conductivity to people in thermal fluid engineering. The enhancement in heat transfer coefficient with respect to base fluids could range from a few percent up to 350% (for carbon nanotubes[197]). It is found that the abnormal heat transfer performance of the nanofluids can’t only be explained by its high thermal conductivity. Wen *et al.*[196] studied the heat transfer enhancement of Al_2O_3 water nanofluid under laminar flow up to turbulence. They found that the heat transfer coefficient could be increased by 40 % using nanofluid, while the enhancement of thermal conductivity was less than 10 %. Moreover, homogeneous flow model is not suitable for study of nanofluid. Xuan *et al*. [265] reported that Nusselt number for water - based Cu nanofluid in turbulent regime was 30 % higher than the value predicted by Dittus–Boelter correlation.

Besides properties of particles and base liquids and particle concentration, particle migration is suggested to be one of the primary reasons for the abnormal heat transfer enhancement of nanofluids.[266] Sohn and Kihm[267] confirmed that particle migration mainly depends on thermophoresis and Brownian diffusion. By using scale analysis, Bahiraei and Hosseinalipour[268] suggested that particle fluxes due to Brownian diffusion and thermophoresis have orders of 10^{-10} and 10^{-8}, respectively. Hence, thermophoresis should contribute more to particle migration. Thermophoresis is one kind of nanoparticle transport driven by temperature gradient. The liquid molecules at hot region will push particles to the cold region. When a nanofluid is heated, thermophoresis is supposed to reduce nanoparticle concentration in the wall boundary layer, leading to a decrease of viscosity and increase of velocity near the wall, and thus thinning the boundary layer. [269, 270] If a nanofluid is cooled down, thermophoresis should increase the concentration near the wall. By using MRI technology, our research group has demonstrated that when a MNF is cooled, the concentration near to the wall is higher than that at the centre of pipe. [271] So, thermophoresis truly plays an important role in determining the distribution of particle concentration in a flow. Otherwise, Yu *et al.* [272] reported the enhancement of heat transfer is almost the same no matter with the nanofluid is heated or cooled. This may be explained by the increase of thermal conductivity in the boundary layer.

Application of magnetic nanoparticle enables controlling particle migration by magnetic forces. It is known that MNFs are inclined to move following magnetic gradient. Remarkable heat transfer enhancements have been reported with using MNF under forced convection conditions. Evidences show that it is most likely to obtain enhanced heat transfer efficiency when the magnetic field is perpendicular to the direction of flow. [51, 235, 236, 273, 274] Even, Sha *et al.*[275] reported that heat transfer coefficient decreased when the field was parallel with the flow despite of whether the flow is in laminar or turbulence condition. However, contradictory results were reported about the effect of a constant magnetic field on the laminar forced convective heat transfer of a ferrofluid in a heated tube. Several researchers suggested that applying a constant magnetic field perpendicular to flow direction enhances the heat transfer performance of

MNF, [51, 236,273, 274] while Ghofrani *et al.*[276] and Yarahmadi *et al.* [277] observed an opposite trend. Azizian *et al.*[51] assumed that the increase in Nusselt number with using constant field is associated with the aggregation of particles in the direction of the field. At first, aggregations could improve the local thermal conductivity. And the aggregates near the wall of pipe may act like local obstacles that disturb the flow pattern and the thermal boundary layer and make the flow turbulent, thus leading to a further increase of the local convective heat. Based on the previous studies and their findings, Yarahmadi *et al.* [277] tried to explain the contradiction with the following: when the field intensity is relatively low, the increase in the fluid viscosity and the decline of the fluid flow velocity near the wall reduces the heat transfer of MNF, whereas at higher field intensity, the increase in the thermal conductivity and decline in the thermal boundary layer would explain the enhancement in the heat transfer. What's more, both Ghofrani *et al.*[276] and Yarahmadi *et al.* [277] demonstrated that an alternating magnetic field is better than a constant one and the local heat transfer coefficient increases with increasing the alternating frequency. Goharkhah explained it that repeating attraction and releasing of nanoparticles bring better mixing and the disturbance of boundary layer. However, Shahsavar *et al.*[274] found that increasing the frequency reduced the enhancement of local Nusselt number, after studying laminar forced convective heat transfer of ferrofluid of MNP - carbon nanotubes composites under alternating magnetic fields. Otherwise, Yarahmadi *et al.* [277] also show that the effect of magnetic field decreases with increasing Reynolds number no matter with it is positive or not. When particles suspend in forms of aggregates, the size of aggregates determines how fast the particles response to a magnetic field. If the response is very fast, too much accumulation of particle near the wall should decrease the flow velocity in this area, so increasing the frequency will be better; If it is very slow, there might not be enough particles in the boundary layer, thus reducing the frequency should be better. Therefore, the convective heat transfer experiment should be developed based on A MNF whose colloidal stability is under control.

2.5 Summary

This chapter introduced basic knowledge and recent advances of MNF – based hyperthermia heating treatment and convective heat transfer enhancement. The largest challenge in the field of magnetic hyperthermia rely on how to obtain efficient heating with using AC magnetic field of low intensity and frequency. Clusters of magnetic particle represent a solution because they enable inter-particle couplings to make the largest effort to change the magnetic losses. Contradictory points have been reported on the role of dipole interactions in hyperthermia heating. Besides the properties of particles, its role also depends on the cluster’s shape and size and the field orientation with respect to cluster. All of these have not been fully investigated.

In heat transfer engineering, MNF has been paid with extensive attentions because its thermal physical properties and convective heat transfer performance can be controlled by an external magnetic field. However, the main problems are: i) the limited applicability of theoretical models to predict the viscosity and thermal conductivity of MNF ii) the unclear effect of magnetic field on convective heat transfer enhancement. Evidences show that particle aggregations associate intimately with its thermal physical properties and convective heat transfer performance. However, it lacks systematic study.

Chapter 3 Research Methodology

3.1 Preparation and characterizations of Ferrofluids

3.1.1 Materials

Ferric chloride ($FeCl_3 \cdot 6H_2O$, ≥99%), ferrous chloride ($FeCl_2 \cdot 4H_2O$, ≥99%), ammonium hydroxide (25%), citric acid (≥99.5%), Oleic acid (OA, 90%), sodium dodecylsulfate (SDS, 99%), cyclohexane (99.8%), ethanol (200 proof), hydrochloric acid (HCl, 37%) were purchased from Sigma Aldrich. Ethylene glycol (EG) was obtained from VWR Chemicals. DI water was used for preparing all aqueous solutions and nanofluids.

3.1.2 Preparation of Fe_3O_4 nanoparticles

Fe_3O_4 nanoparticles were prepared by co-precipitation method.[111] In a typical procedure, 24 g of $FeCl_3 \cdot 6H_2O$ and 8.8 g of $FeCl_2 \cdot 4H_2O$ was dissolved in 100 ml of water at first. The solution was heated to 50 ^oC and bubbled with N_2 for 15 min to remove oxygen. And then, 50 ml of ammonium hydroxide was added under vigorous stirring. After 30 min, the black precipitate was collected at the bottom of flask with using a magnet and washed with water 5 times. After dumping the supernatant, Fe_3O_4 particles were obtained.

3.1.3 Preparation of oil-based ferrofluids

In order to stabilize Fe_3O_4 nanoparticles in an oil phase, the surfaces of particles were hydrophobically treated via modification of oleic acid. In a typical procedure, 0.008 mol of Fe_3O_4 particles was dispersed in 100 mL of water with the aid of ultrasound. The pH of particle suspension was adjusted to about 8.5 by adding diluted HCl solution. The dark suspension was heated to 70 ^{o}C and kept stirred under the protection of N_2. 1.33 mL of oleic acid was added to the suspension. After 2 h, all of particles precipitated down to the bottom of the flask. The oily precipitates were washed with ethanol for 5 times and then dispersed to cyclohexane. After drying with a N_2 blower, Fe_3O_4 nanoparticles modified with a monolayer of oleic acid were obtained. At last, a certain amount of modified particles were re-dispersed to cyclohexane or octane to generate oil-based ferrofluids.

3.1.4 Preparation of water-based ferrofluids composed of Fe_3O_4 clusters with tunable size

Clusters of Fe_3O_4 nanoparticles were prepared by the emulsion droplet solvent evaporation method. Typically, 1.5 mL of cyclohexane - based ferrofluids (0.16 g/mL) was mixed with 30 mL of aqueous SDS solution (1 CMC) with aid of ultrasonic treatment to form a mini-emulsion system. After 6 h of evaporating the cyclohexane at 60 ^{o}C under the protection of N_2, the clusters of

Fe_3O_4 nanoparticles stabilized by SDS were produced. A centrifugation at 8000 rmp was used to separate the clusters from the solution. After dumping the supernant, the clusters were re-dispersed to diluted SDS solution (0.5 CMC). The size of final Fe_3O_4 clusters was controlled by changing the particle concentration of cyclohexane - based ferrofluids.

3.1.5 Preparation of EG and water based ferrofluids

To stabilize the Fe_3O_4 nanoparticles in a EG and water mixture, the surfaces of particles were modified with citric acid. Typically, 0.044 mol of Fe_3O_4 particles was dispersed in 120 mL of water with the aid of ultrasound. After adding 2g of citric acid, the suspension was stirred at 50 ^oC under the protection of N_2 for 2.5 hours. The particles were washed for 5 times with diluted HCl solution. After dumping the supernatant, CA modified Fe_3O_4 particles were re-dispersed to water and stored at 8 ^oC. For preparation of nanofluids, a certain amount of modified particles in aqueous solution were added to EG – water mixture whose volume ratio was adjusted so that the final ratio could achieve 1:1.

3.1.6 Characterizations

3.1.6.1 Characterizations of Fe_3O_4 particles and clusters

The morphology and size of as-prepared particles and clusters were observed under a Transmission electron microscopy (TEM). The samples for TEM observation were prepared via dropping diluted particle dispersion onto a TEM copper grid followed by drying under a reduced pressure overnight. TEM images were taken by a JEOL-2000 electron microscope operating at 200 kV and equipped with a CCD camera. The size distribution was gained based on at least 300 particles or clusters.

The crystal structure of particles and clusters were analyzed by X-Ray powder diffraction (XRD) measurements. The samples were grounded before the test. A Bruker D8 Advance Powder X-ray diffractometer was applied to obtain XRD pattern. The step size and time were kept at 0.02 degree and 2 s respectively.

Thermogravimetric analysis (TGA) was carried out on a TGA-SDTQ600 thermogravimetric analyser to measure the amount of stabilized attached on the particles' surfaces. The modified Fe_3O_4 nanoparticles were heated to 1000 ^oC under the protection of N_2. The rate of temperature increase was kept at 10 $^oC/min$.

Fourier transform infrared (FT-IR) spectra were gained by using a Perkin-Elmer Spectrum One FT-IR spectrophotometer at a resolution of 4 cm^{-1}. All samples were prepared into KBr tablets, and the number of scans was set at 20 to collect the spectra.

The density of unmodified and citric acid modified Fe_3O_4 nanoparticles was measured by using a Accupyc 1330 pycnometer. Before the test, the particle sample was dried under a reduced pressure for 3 days. The equipment was calibrated by conducting 10 purges and 10 runs for the empty cell followed by 10 purges and 10 runs for cell + two calibration balls. The sample was measured for 5 times and the standard deviation is only 0.048%.

A JDM-13 vibrating sample magnetometer was used to measure the saturation magnetization of the Fe_3O_4 nanoparticles clusters. The field dependence of magnetization was changed over a range from -10 to +10 kOe at room temperature. The measurement was conducted for three times to obtain the average result.

Dynamic light scattering (DLS) and zeta-potential measurements were carried out on a Malvern Zen 3600 Zetasizer to study the hydrodynamic diameter and surface potential of particles. All the samples were diluted first. The temperature was set at 25 ^{o}C.

3.1.6.2 Characterizations of ferrofluids

The density of ferrofluids was determined by measuring the mass of 1mL of particle suspension. The measurement was performed for three times to obtain the average value of density.

The rheological behaviour of the base liquid and nanofluids was measured by using an Anton Paar MCR 302 rheometer equipped with a CP50-1 measuring cone. The diameter of cone is 50 mm and cone angle is 1 ^{o}. During the rheological measurements, the shear rate was changed from 50 to 2500 s^{-1}. At each shear rate, the measurements were conducted under steady-shear conditions for 120 s. The viscosity was measured every 6 s, and the mean value was used as the final viscosity for each shear rate.

The thermal conductivity of ferrofluids was measured with using a TC3020L Liquid Thermal conductivity meter (Xi’an Xiatech Electronic Technology Co., China), which is based on the transient hot-wire method. A water bath was used to generate a circulation flow to keep the temperature of the sample at a certain value during the measurement. After setting the temperature for test, the sample was heated for half an hour to achieve thermal stabilization. Then, the thermal conductivity was measured for 5 times to obtain the mean value.

The specific heat of ferrofluids was measured by using a Differential Scanning Calorimeter (DSC) (TA Instruments Q2000). The sample was held in an aluminum pan and covered with a lid. An empty pan with lid was used as the reference. The scan was conducted in a nitrogen atmosphere. At the beginning, the temperature was maintained at 5 °C for 15 min, and then the sample was heated rapidly to 85 °C at a heating rate of 25 °C/min. For minimizing the system errors, the scan was repeated for three times to gain the averaged profile of the specific heat as a function of temperature. It was found that the specific heat of nanofluids increases little after temperature was higher than 60 ^{o}C. So, the average specific heat in range of 30 to 60 ^{o}C was used as the final result at a certain volume fraction.

3.2 Methodology for numerically investigation of hyperthermia heating of clusters composed of multi particles

3.2.1 Numerically assembling nanoparticles into clusters

To study the effect of morphology anisotropy on hysteresis losses of a cluster, SMNPs are assembled into nine kinds of clusters, including one chain cluster, four cylinder clusters, two cube clusters one spherical cluster. Table 3.1 gives the details of structure and the number of particles used to create each cluster. The particles are mono-sized and ideally spherical in shape. Usually, a SMNP is covered with a layer of organic stabiliser in practice to stabilize the particle in the suspension. The thickness of this stabilizer layer is set at 1 nm in the modelling, and the radius of magnetic fraction is kept at 5 nm. All the clusters were formed by 64 of particles except cube 2, which contains 63 of particles. The particles of the chain cluster are lined up along the Z-axis. The four cylinder clusters and cube 1 are created by putting the repeating unit directly on top of last layer. For cylinder 1, 3 and 4, the 64th particle is placed directly on the top of the particle which is at the centre of the top surface of the cluster. The structure of cube 2 cluster is fabricated with face-centered cubic (FCC) lattice.

To assemble particles into a sphere-like cluster, a certain number of particles are allowed to undergo ideally elastic collisions within a large sphere. The collision between particle and the inner wall of the sphere is also treated as elastic collision. The radius of this sphere decreases by a very small amount at each time until the radius cannot be reduced any more. As a result, a sphere-like cluster is obtained. The algorithm can be described by a simple recipe,

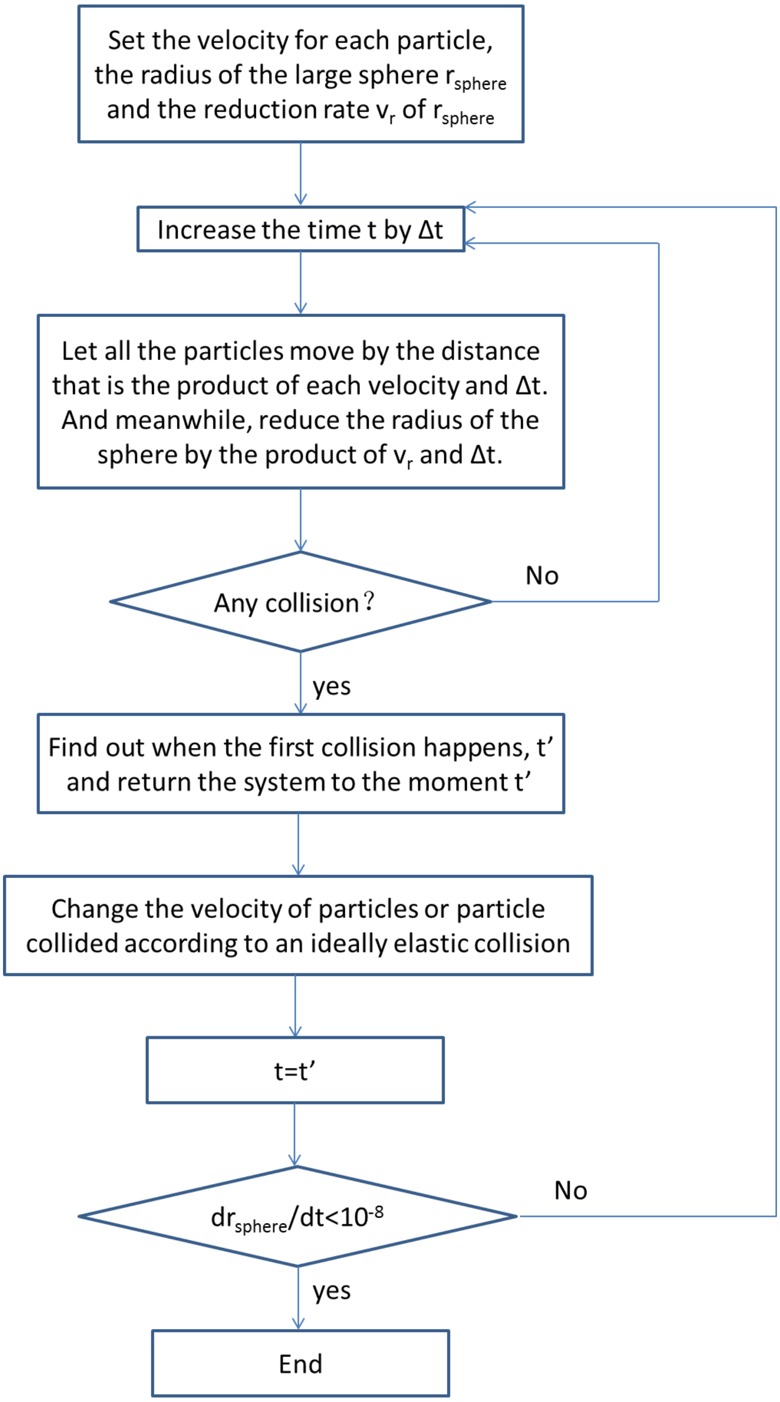

Detailed Matlab programme of assemble particles into a sphere-like cluster can be found in Appendix 1.

Table 3.1 Details of modelled clusters

Name	Structure	Repeating unit	No. of particles
Chain	-		64
Cylinder 1	Triangular array		64
Cylinder 2	Simple cubic lattice		64
Cylinder 3	Primitive hexagonal array	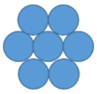	64
Cylinder 4	Simple cubic lattice	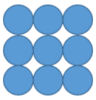	64
Cube 1	Simple cubic lattice	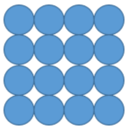	64
Cube 2	FCC lattice	-	63
Sphere	-	-	64

3.2.2 Numerical characterization of cluster's morphology anisotropy

The morphology anisotropy of one cluster is characterised by treating it as an equivalent ellipsoid with uniform mass distribution in 3D. The ellipsoid has the same mass and principal moments of inertia as the cluster does. The morphology anisotropy is defined in terms of the ratios of the length of its semi-principal axes. Each particle is divided into 280 unit volume elements.

The moment of inertia tensor, T_I, for a cluster composed of N discrete point masses (N = 280 × the number of particle) is described as,

$$T_I = \sum_{l=1}^{N} \begin{pmatrix} y_l^2 + z_l^2 & -x_l y_l & -x_l z_l \\ -x_l y_l & x_l^2 + z_l^2 & -y_l z_l \\ -x_l z_l & -y_l z_l & x_l^2 + y_l^2 \end{pmatrix} \qquad (3.1)$$

where (x_l, y_l, z_l) are the coordinates of point mass l. The original point locates at the mass centre of the cluster. Diagonalising T_I works out the principal moments of inertia of the cluster, $\lambda_i (i = 1, 2, 3)$. The length of semi-principal axis of the equivalent ellipsoid d_i is obtained by,

$$d_i = \sqrt{\frac{5}{2} \frac{\lambda_j + \lambda_k - \lambda_i}{N}} \qquad (3.2)$$

where i, j and k equals 1 or 2 or 3, respectively, and $i \neq j \neq k$. Then, $d_i (i = 1, 2, 3)$are assigned to A, B and C, ordered from the largest to smallest. A long d_i comes with a small λ_i, which suggests that the mass of the cluster is distributed close to the principal axis of rotation i. Therefore, high ratios of A to B and C indicate a heterogeneous mass distribution of the cluster with respect to different axes, indicating a high anisotropy in morphology. The longest principal axis A is arbitrarily defined as the axis of morphology anisotropy (AMA).

3.2.3 Numerically estimation of directionally dependent influence of dipole interactions

When one cluster is magnetically saturated, the total energy of dipole interaction $\sum_{i<j} E_D^{(i,j)}$ can be described as,

$$\sum_{i<j} E_D^{(i,j)} = \sum_{i<j} \frac{\mu_0 M_d^2 V_p^2}{4\pi} \left[\frac{1-3(cos\theta_{ij})^2}{r_{ij}^3}\right] \qquad (3.3)$$

where μ_0 is the vacuum permeability, M_d the domain magnetization, V_p the magnetic volume of particle, θ_{ij} the angle between the direction of magnetization and the line joining the centers of particle i and j, and $\vec{r}_{ij}$ the distance between the centers of particles. We denote it as E_{DISM}. Set θ_{MA} is the angle between the magnetization direction and AMA. Therefore, $E_{DISM}\,(\theta_{MA})$ suggests the total energy of dipole interactions when the magnetization direction departs from AMA It is evidenced that the clusters formed by SMNPs can inherit superparamagnetism from the particles,[109, 278-280] as long as T is high enough to make the moments rotate too rapidly to generate permanent magnetization. Moreover, the blocking temperature of the densest assembly of SMNPs can be much lower than room temperature.[171, 174] When body temperature is considered, it can be assumed that $\sum_{i<j} E_D^{(i,j)}$ of the SMNP cluster whose magnetization is completely relaxed is independent upon its structure and shape. In this case, E_{DISM} dominates the difference of $\sum_{i<j} E_D^{(i,j)}$ before and after the cluster is magnetized. Decreasing E_{DISM} is expected to

make magnetizing the cluster easier. Here, the direction of the cluster's magnetization is set always in parallel with the field direction.

3.2.4 Monte Carlo simulation

To investigate the effect of dipole interactions on hysteresis losses of the cluster composed of superparamagnetic nanoparticles, a standard Monte Carlo approach featured with the Metropolis algorithm was carried out to produce magnetization – field intensity curve (M-H curve). The transition possibility in Metropolis algorithm depends on the energy difference between the present and attempted states. Each particle possesses a uniaxial magnetic anisotropy, and the orientation of the easy axis is randomly chosen in a 3D space. The magnetic properties of particle are set the same as the published data of magnetite nanoparticles: the effective magnetic anisotropy constant K_{eff} is 9000 J/m^3 and M_d 446 kA/m.[151] For the sake of simplicity, we assume that both of them are temperature-independent. The energy model of the cluster system consists of three major sources, namely, anisotropy energy E_A, Zeeman energy E_H and dipolar interaction energy E_D.[173] The uniaxial anisotropy $E_A^{(i)}$ of each particle is given by,

$$E_A^{(i)} = -K_{eff} M_d V_p (\vec{s}_i \cdot \vec{n}_i)^2 \qquad (3.4)$$

where $\vec{n}_i$ is the unit vector along the easy axis direction and $\vec{s}_i$ is the unit vector of particle's magnetic moment. The coupling with the applied field $\vec{H}$ is described by,

$$E_H^{(i)} = -\mu_0 M_d V_p (\vec{s}_i \cdot \vec{H}) \qquad (3.5)$$

The energy of dipole interaction is given by,

$$E_D^{(i,j)} = \frac{\mu_0 M_d^2 V_p^2}{4\pi} \left[\frac{\vec{s}_i \cdot \vec{s}_j}{r_{ij}^3} - \frac{3(\vec{s}_i \cdot \vec{r}_{ij})(\vec{s}_j \cdot \vec{r}_{ij})}{r_{ij}^5} \right] \qquad (3.6)$$

Therefore, the total energy of the cluster system can be expressed as,

$$E = \sum_i E_A^{(i)} + \sum_i E_H^{(i)} + \sum_{i<j} E_H^{(i,j)} \qquad (3.7)$$

At the beginning of each MCS, one particle is picked randomly and the moment is directly agitated to a new direction, which is chosen inside of a spherical segment around the present direction with an aperture angle $\delta\theta$. According to the reported work[155], temperature dependence of $\delta\theta$ is given by $\delta\theta = (0.05 k_B T / 2 K_{eff} V)^{0.5}$ in an usual reduced unit, where k_B is the Boltzmann constant. This agitation is accepted with probability $min[1, \exp(-\Delta E / k_B T)]$, where ΔE is the change of the total energy of the cluster system caused by agitation. The above procedure is repeated until all particles are agitated to complete one MCS. During the simulation, the particles only relax through Néel mechanism and the particle positions are fixed. Before simulating cluster's hysteresis losses, 275000 MCSs are used for thermalization. After that, an external magnetic field $\vec{H}$ is introduced and increased until reaching H_0; then it is decreased to $-H_0$, and increased again to H_0 to finish the cycle. The simulation time increases by MCS. The inverse of N_{MCS} per cycle is used as the computational frequency. The field oscillates in sinusoidal waveform. The time returns to 0 before a new cycle is started. The magnetization of the cluster is collected by summing the moment projections on the positive direction of field variation. The hysteresis loops were computed for typically 200 times and then averaged. Detailed Matlab programme of standard MC simulation can be found in Appendix 2.

In the chapter 4, Kinetic Monte Carlo (KMC) simulation is also performed to generate the time dependent magnetization of SMNP ensemble at different temperature and K_{eff}. Unlike Metropolis algorithm, kinetic Monte Carlo algorithm calculates dynamic hysteresis loop within two-level approximation. As mentioned in Chapter 2, when the ratio of $K_{eff}V_p$ to k_BT is large enough, one can consider that the magnetization of one particle flips only between two positions: the two minima of the energy landscape. The minima of the energy landscape must be found within the plane formed by the effective magnetic field $\vec{H}_{eff}$ acting on this particle and its easy axis. $\vec{H}_{eff}$ acting on particle i is the sum of $\vec{H}$ and the dipolar field created by the other particles, which is given by,

$$\vec{H}_{dip} = \frac{M_d V_p}{4\pi} \sum_{i \neq j} \frac{3(\vec{s}_j \cdot \vec{r}_{ij})\vec{r}_{ij}}{{r_{ij}}^5} - \frac{\vec{s}_j}{{r_{ij}}^3} \qquad (3.8)$$

The energy of a particle is given by,

$$E(\theta, \phi) = K_{eff} V_p sin^2(\theta) - \mu_0 M_d V_p H_{eff} \cos(\theta - \varphi) \qquad (3.9)$$

where θ is the angle between the easy axis and the magnetization and φ the angle between the easy axis and $\vec{H}_{eff}$. To produce the hysteresis loop, time increases by time step t_{step} during which the magnetic field is assumed constant. As a typical value, the loop is completed by taking 2000 equal time steps. The algorithm inside the main loop of the program is the following:

(1) $\vec{H}_{eff}$ acting on each particle is calculated.

(2) The present magnetization vector of one particle is projected onto the plane formed by $\vec{H}_{eff}$ acting on it and its easy axis followed by re-normalization.

(3) Find the positions and values of the extremumsof $E(\theta)$. For this purpose, the profile of $E(\theta)$ is divided into 360 position. At each point, the first derivative of the energy is calculated. Let θ_1, θ_2 and θ_3 be the angles of the two minima and the angle of the lower energy maximum with energies E_1, E_2 and E_3. If there is only one minima, turn the magnetization to the passion of this minima and then go to step. If there are two minima, go to step 4.

(4) The magnetization "falls" directly into one of these two minima. The probability for the magnetization to change well is calculated. The rate for the magnetization to switch from $\theta_1$to θ_2 is given by,

$$v_1 = v_1^0 \exp(-\frac{E_3 - E_1}{k_B T}) \qquad (3.10)$$

Similarly, the switching rate from $\theta_1$to θ_2 is given as,

$$v_2 = v_2^0 \exp(-\frac{E_3 - E_2}{k_B T}) \qquad (3.11)$$

v_1^0 and v_2^0 are jump attempt frequencies and equal with each other. If the magnetization is initially in the minimum θ_2, the switch is accepted with probability [281],

$$Probability = \frac{v_2}{v_1 + v_2}\{1 - \exp[-(v_1 + v_2)t_{step}]\} \qquad (3.12)$$

(5) Return to step (2).

The magnetization of the cluster is collected by summing the projections of each particle's magnetization on the positive direction of field variation. The hysteresis loops were computed typically 50 times and then averaged. Detailed Matlab programme of KMC simulation can be found in Appendix 3.

3.2.5 Calculation of frequency-dependent hysteresis loop area by Rosensweig's model

The time scale of one Monte Carlo step of standard MC is estimated by comparing the hysteresis loop area of non-interacting particles gained from the simulation with the result calculated by Rosensweig's model. Calculations are carried out based on the Rosensweig's model, but a minor modification has been made in the present modelling. The loop area per unit volume of magnetic material is equal to the absolute value of the amount of magnetic work done by the field per cycle. Therefore, loop area $A = |\oint MdH|$, where M is the magnetization and H the field intensity. A non-interacting particle system responds to a field, which can be described as $\mathrm{M(t)} = \chi\mathrm{H(t)}$, where χ is the magnetic susceptibility and *t* the time. Because under a high-frequency field the magnetization is not in phase with the field, the magnetic susceptibility χ has two components, $\chi = \chi' - \mathrm{i}\chi''$, where

$$\chi' = \chi_0/[1 + (2\pi f\tau)^2] \qquad (3.13)$$

and

$$\chi'' = 2\pi f\tau\chi_0/[1 + (2\pi f\tau)^2] \qquad (3.14)$$

χ_0 is the equilibrium susceptibility, τ is the relaxation time of the particle and f is the field frequency. The AC magnetic field is expressed in the form,

$$\mathrm{H(t)} = H_0\cos(2\pi f\tau) \qquad (3.15)$$

where H_0 is the field amplitude Therefore, the time-dependent magnetization is described as,

$$\mathrm{M(t)} = H_0(\chi' cos2\pi ft + \chi'' sin2\pi ft) \qquad (3.16)$$

In fact, the equilibrium susceptibility $\chi_0$is field-dependent and described as,

$$\chi_0 = \frac{M_s}{H(t)}(coth\xi - \frac{1}{\xi}) \quad (3.17)$$

where$\xi = \mu_0 M_s V H(t)/k_B T$. In the work of Rosensweig, χ_0 was assumed to be chord susceptibility for a conservative estimation of heating ability. In the present work, χ_0 is set to change with field intensity so that the model can be applied to the case of high field intensity. Substituting equations (3.13, 3.14, 3.17) into (3.16), followed by the integration with respect to $H(t)$ and divided by the product of M_s and H_a, the calculated loop area is obtained in reduced units. The properties of the particles and field amplitude are set the same as those used in our Monte Carlo simulations. The temperature is kept at 310 K. The value of pre-exponential factor τ_0 is typically chosen to be 10^{-9} s^{-1}. By using correlation $\tau_0 = \frac{M_d}{2\gamma_0 K_{eff}} \frac{1+\alpha^2}{\alpha}$ [184], the damping factor α is found to be 0.14, where γ_0 is the electron gyromagnetic ratio.

3.3 Experimental study of hyperthermia heating ability of ferrofluid

An induction heating system was built to test the heating ability of ferrofluid. Figure 3.1 shows the set-up of the rig. The sample was put into a thermal insulation container and place at the centre of a copper coil of inner diameter of 4.13 cm, which was cooled by water flow during the induction heating. A Roy 1500 Induction Heater (80 kHz, 13.1 kA/m, Fluxeon Inc., USA) was used to generate AC current going through the coil, and the coil converted the current to AC magnetic field. The temperature of sample was probed with a fluoro-optic fiber thermometer (OPSENS SOLUTIONS INC, Canada). The initial linear rise in temperature versus time dependence, dT/dt, was measured as illustrated in Figure 3.2. The specific absorption rate is defined as the thermal power dissipation divided by the mass of magnetic crystal and can be expressed as,

$$\mathrm{SAR} = \frac{C_{p,nf}\rho_{nf}V_{nf}}{m}\frac{dT}{dt} \qquad (3.18)$$

where $C_{p,nf}$ is the specific heat capacity of MNF, ρ_{nf} is the density of MNF, V_{nf} is the volume of MNF, and m is the mass of magnetic material of MNF. The weight fraction of magnetic fraction of particles was determined by TGA measurement. All the samples were prepared into water-based ferrofluids, and the particle concentration was kept at 40 mg/mL. For such a low concentration, the $C_{p,nf}$ and ρ_{nf} of sample was set as the same as those of water, which is 4.186 J/(g K) and 1 g/mL.

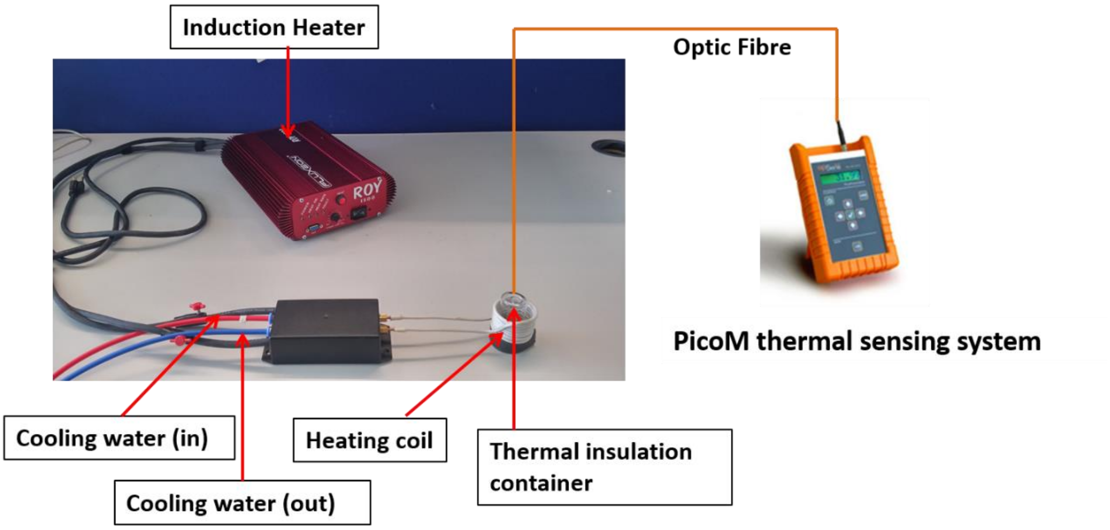

Figure 3. 1 Set up of induction heating system equipped with fluoro-optic fiber thermometer.

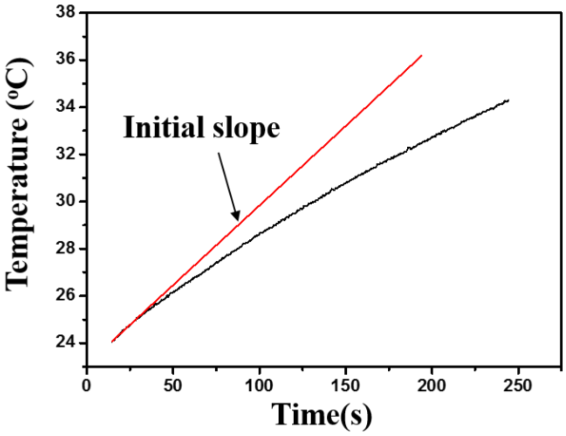

Figure 3. 2 the rise of temperature of ferrofluid as a function of time during an induction heating.

3.4 Experimental study of convective heat transfer enhancement

An experimental setup for measurements of the heat transfer coefficient of Fe_3O_4 EG - water nanofluids in the circular pipe is shown in Figure 3.3. The test section was a copper-made tube with the inner diameter of 6.8 mm and the length of 1000 mm. The fluids were circulated through the loop by a volumetric pump. The cooper tube was heated by a rope heater wrapped around it with a maximum power of 400 W (FGR-080/240V, Omega, UK). One K – type thermal couple was placed at each end of the tube to measure the inlet or outlet temperature. Three other thermocouples were attached on the surface of tube to measure the surface temperature of tube. A differential pressure meter was used to obtain the pressure drop between inlet and outlet. The whole test section was covered with thermal insulation material to reduce heat loss. After the fluid passed the heating section, it was cooled down to inlet temperature by using a heat exchanger connected to a thermostat water bath.

The thermocouples used in this project were calibrated by comparison with the fluorooptic fiber thermometer (OPSENS SOLUTIONS INC, Canada). The thermocouples and the fluorooptic fiber thermometer were put into a water bath where water was heated from 10 to 70 ^{o}C. A temperature increment of 5 ^{o}C was set at each calibration data captured. All the temperature data were captured when they reached steady state temperature. The volumetric flow rate was gained with using an ultrasonic flow meter (UF8B, Cynergy 3, UK). The output signal of flow meter was voltage. To calibrate the meter, liquid was pumped into a 1 Litter cylinder, and we measured how much liquid was pumped out in 10 second. The voltage increased proportionally with flow rate.

The proportion constant was found to be 1.66 L/(min V) for water and 1.51 L/(min V) for base liquid and MNF.

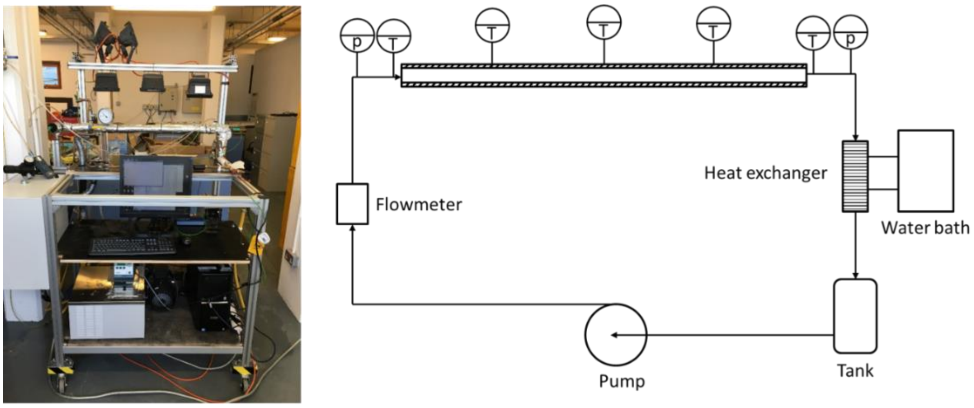

Figure 3. 3 Experimental setup for the measurement of heat transfer coefficient of nanofluid

The convective heat transfer coefficient was calculated from:

$$h = \frac{q}{(t_{w,in} - t_f)} \qquad (3.19)$$

where q was the input heat flux based on thermal power, $t_{w,in}$ was the inner wall temperature and $t_f = 0.5(t_{out} - t_{in}) + t_{in}$ was the average bulk temperature of fluid. The heat supplied to the system was calculated by $mC_{p,f}(t_{out} - t_{in})$, where m is the mass flow rate. $t_{w,in}$ was calculated with using the analytical solution,

$$t_{w,in} = t_{w,out} - \frac{q}{2\pi L k_{copper}} ln \frac{D_{in}}{D_{out}} \qquad (3.20)$$

Where $t_{w,out}$ is the outer surface temperature of tube, L is the length of tube, k_{copper} is the thermal conductivity of copper (385 W/mK), D_{in} and D_{out} are inner and outer diameter respectively.

The Nusselt numbers of water calculated from experimental data were compared with those predicted by Seider – Tate equation[282] for laminar flow and Dittus – Boelter equation for turbulent flow.

$$Nu = \frac{hD_{in}}{k_f} \qquad (3.21)$$

Seider–Tate equation: $Nu = 1.86(Re \cdot Pr \cdot \frac{D_{in}}{L})^{\frac{1}{3}}(\frac{\mu_f}{\mu_{w,f}})^{0.14}$ (3.22)

Dittus – Boelter equation: $Nu = 0.023Re^{0.8}Pr^{0.4}$ (3.23)

Re and Pr are defined as follow,

$$Re = \frac{\rho_f u D_{in}}{\mu_f} \qquad (3.24)$$

$$Pr = \frac{C_{p,f}\mu_f}{k_f} \qquad (3.25)$$

where μ_f and $\mu_{w,f}$ are dynamic viscosity at t_f and $t_{w,in}$ respectively, u is the velocity of the fluid, $C_{p,f}$ is the specific heat of fluid and k_f is the thermal conductivity. All the values of thermal physical properties of water were the same with reported ones. The uncertainty of experimental results may be originated from the measuring errors of temperatures and flow rate. The measurement uncertainty of temperature and flow rate was 0.1 °C and 3% of readings respectively. During the investigation of convective heat transfer of MNF, it also has to take into considerations the measuring errors of thermal physical properties of MNF. The uncertainties of the Reynolds number, convective heat transfer and Nusselt number are analysed with using the method described by Moffat[283]. If y was a function of several independent variables, x_i, each with their own uncertainties, δxi, the overall uncertainty in y was calculated as

$$\delta y = \sqrt{\sum_{i=1}^{n} (\frac{\partial y}{\partial x_i})^2 (\delta x_i)^2} \qquad (3.26)$$

Chapter 4 Numerical study of the effect of dipole interactions on hyperthermia heating SMNPs clusters with different shapes

4.1 Introduction

Much attention has been focussed on magnetic hyperthermia due to its great potential to be a cancer treatment.[1-6] Different from other approaches developed to raise the temperature of bio-tissue[7, 18-20], magnetic hyperthermia heats the cancerous tissues through inductively heating pre-implanted single-domain magnetic nanoparticles. The particles convert magnetic work done by the field to particles' internal energy via the mechanism called "magnetic losses". The amount of energy converted per field cycle is equal to the area of the magnetic hysteresis loop.[85, 284] Someone suggests that the temperature of particles could be increased rapidly at a rate of 10^2 to 10^3 °C/s.[32] Then, the heat is released to the surrounding tissue to treat the tumor.

Many researchers have applied large single-domain particles retaining permanent magnetic moments at room temperature for hyperthermia heating.[83, 133, 155, 156, 285, 286] Triggering the magnetic losses of large particles requires a high threshold field amplitude stronger than the coercivity field.[287, 288] However, it has been suggested that the field frequency f and amplitude H_0 should be reduced to some level in order to conduct a safe hyperthermia

Some part of this chapter has been published treatment.[2, 140] Therefore, the use of small single-domain particles seem to be more important.[4] When the magnetic anisotropy energy becomes comparable with the thermal energy at room temperature, the moment of individual particles will start to flip freely through Néel Relaxation in the absence of an external magnetic field; thus, the permanent magnetization will disappear; and those particles are referred to as superparamagnetic nanoparticles (SMNPs).[65] However, almost null coercivity field confines the hysteresis loop area.[284]

Colloidal clusters composed of multi-magnetic nanoparticles have shown great potential in magnetic hyperthermia heating.[33, 280] Different from the isolated particles, the magnetic losses of the clusters are affected by inter-particle dipole interactions. The role of dipole interactions is complex, and apparently contradictory findings have been reported. Several evidences show that the dipole interactions can improve heating performance when the shape of cluster is highly morphologically anisotropic, such as in chain or cylinder.[33, 34] Mehdaoui *et al.*[33] found that dipole interactions could improve the heating performance of SMNP columns by generating an additional magnetic uniaxial anisotropy, especially when the magnetocristalline anisotropy is low and column is long. However, other results suggest that chain-like clustering may cause a reduction in heating efficiency.[83, 184, 186] Branquinho *et al.*[184] reported that only at high damping factor the heating efficiency of short chain clusters would increase with the chain length; but at lower damping factor formation of chains could lead to low heating efficiency, because the present magnetocrystalline anisotropy became farther away from the optimal value although dipole interactions reinforce the cluster's effective magnetic anisotropy. The role of dipole interactions is also dependent upon the relative orientation of the magnetic field with respect to the clusters. Several modelling results suggest that chain cluster will produce less heat once the field direction does not align with the chain axis[185] [34]. Serantes *et al.*[186] experimentally demonstrated a reduction in heating efficiency as increasing the relative orientation of field with respective to the chain formed by ferromagnetic particles. And their simulation results predicted that the loss per cycle would decrease when the cluster's shape is changed from chain to cube. In fact, assembling particles into anisotropy-less clusters, such as in sphere, can change the heating efficiency in either positive[166] or negative way[168]. In order to understand how dipole interactions dominate the magnetic losses of a cluster, it is necessary to develop a method to associate the influence of dipole interactions with the cluster's characteristics as well as the magnetic field orientation; and it can be applied to the cluster with any shape and particle arrangement.

Metropolis algorithm is widely used for studying time-dependent magnetization of magnetic nanoparticle system by Monte Carlo (MC) method.[155, 169, 180, 281, 289] Not like kinetic Monte Carlo algorithm[290, 291], which calculate dynamic hysteresis loop within two-level approximation, the transition possibility of Metropolis algorithm mainly depends on the energy difference between the present and attempted states. However, without a theory to associate physical time with the Monte Carlo step (MCS), it cannot describe a dynamic magnetic hysteresis in a quantified manner. Nowak *et al.*[292] pioneered the work on relating one MCS of heat-bath MC algorithm to the time scale of Langevin dynamics in fluctuation dissipation theorem. Cheng *et al.*[293] used the Fokker-Planck equation to link the Metropolis MC algorithm and Langevin dynamics schemes, and gained accurate quantification at a large range of the damping factor. Melenev *et al.*[294] estimated the time scale of MCS for simulating dynamic magnetic hysteresis for the first time. They considered a model of non-interacting SMNPs responding to an oscillating field. The MC simulation was manipulated until the simulated hysteresis loop was in good agreement with the one produced by Brown's kinetic equation at a certain frequency. By correlating MCSs per field cycle, N_{MCS}, with the frequency, the time scale of each MCS was obtained. One can expect an improved accuracy of the time quantification if a series of frequencies are considered.

4.2 Problem Description

In this chapter, the effect of dipole interactions on the magnetic losses of the cluster composed of SMNPs is studied. Four typical morphologies, namely chain, cylinder, cube and sphere, are selected to shape the cluster. The morphology anisotropy of the cluster is quantitatively characterised by treating it as an equivalent ellipsoid [295]. An approach has been proposed to quantify the directionally dependent influence of dipole interactions in terms of energy. At first, standard MC method featured with Metropolis algorithm and KMC method are both performed to simulate DC magnetizations of clusters to find out which method is suitable for study of SMNPs' magnetic hysteresis. Then, the dynamic magnetic hysteresis of clusters are simulated via the MC method featured with Metropolis algorithm. The time scale of one Monte Carlo step is estimated by comparing the hysteresis loop area of non-interacting particles gained from MC simulation with the result calculated by Rosensweig's model[85]. Our simulation results suggest that when the cluster is highly morphologically anisotropic, the dipole interactions try to align the individual magnetic moment of each particle to the axis of shape anisotropy. The strength of the alignment associates intimately with the magnitude of the morphology anisotropy. Once the cluster loses its morphology anisotropy, the influence of dipole interactions on the hysteresis loss will be reduced to the minimum and the chance of obtaining improved heating will become very low.

4.3 Results and discussions

4.3.1 Characterization of cluster's morphology anisotropy

SMNPs are assembled into eight kinds of clusters, including one chain cluster, four cylinder clusters, two cube clusters and one spherical cluster. Figure 4.1 shows 3D schematics of all the clusters. All the particles are mono-sized and touch the neighbour ones by point to point. The particles of chain cluster are arranged into a straight line. The four cylinder clusters are created by placing the repeating unit directly on the top of the last layer. Two cube clusters are fabricated to be with either simple cubic or fcc lattice. To obtain a cluster sphere-like in shape, particles are allowed to undergo elastic collisions within a large sphere whose diameter decreases continuously. The clustering is completed until the sphere cannot shrink any more. See details of creation process of each cluster in Chapter 3.

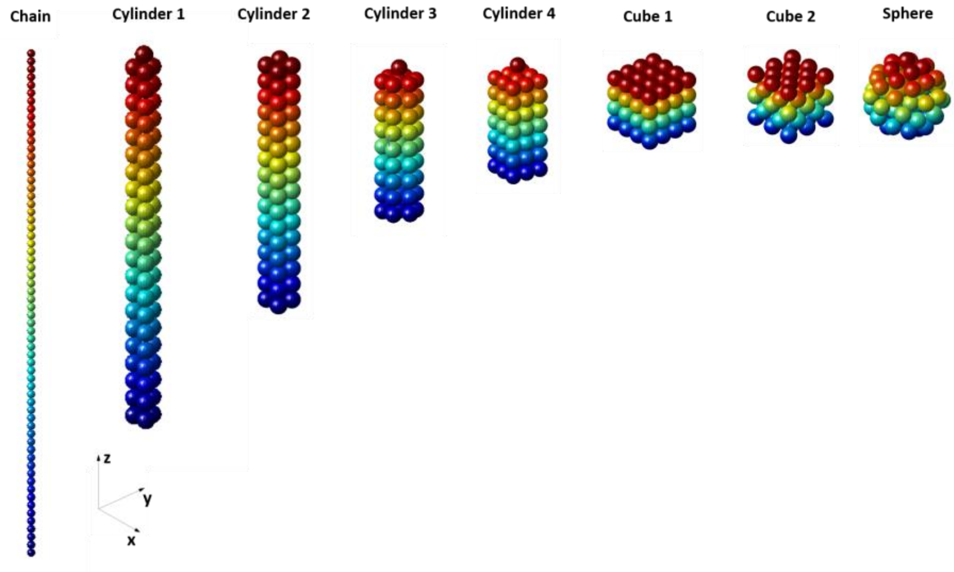

Figure 4. 1 3D schematics of eight kinds of clusters

The morphology anisotropy of SMNP clusters is characterised by treating it as an equivalent ellipsoid. The morphology anisotropy is defined in terms of the ratios of the length of the ellipsoid's semi-principal axes. Table 4.1 gives the ratio of the length of the ellipsoid's semi-principal axes of each cluster. A, B and C represent the length of three semi-principal axes of the ellipsoid respectively, ordered from the largest to smallest. Because the mass distribution of both clusters is rotationally symmetric with respect to Z-axis, the two shorter semi-principal axes B and C equal each other. As shown in Figure 4.2, as expected, the morphology anisotropy is reduced as the shape of cluster changes from chain to cylinder and to cube or sphere. The inserted image of Figure 4.2 shows examples of equivalent ellipsoids, including chain, cylinder 2, cube 1 and sphere cluster. For chain and cylinder 1 to 4, the longest principal axes coincide with Z-axis. In contrast, the ellipsoids of two cube clusters and sphere cluster are visually isotropic in geometrics. Obviously, the finding of A/B=A/C=1 (Table 1) further confirms that the mass distribution of these three clusters is truly isotropic, regardless of the type of lattice and shape. It suggests that the morphology anisotropy vanishes as the shape changes to cube or sphere. In this chapter, the longest principal axis is arbitrarily defined as the axis of morphology anisotropy (AMA).

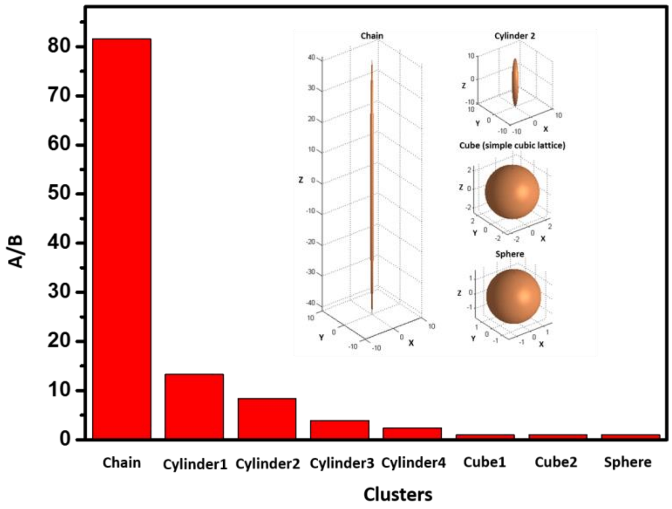

Figure 4. 2 The ratio of the length of the ellipsoid's semi-principal axes of each cluster. Insert: the equivalent ellipsoid of the chain cluster, cylinder cluster 2, cube cluster with simple cubic lattice and sphere cluster.

Table 4.1 Characterization of clusters' morphology and distribution of E_{DISM}

Sample	*A/B*	*A/C*	K_0($\times 10^3$ J/m^3)	K_1($\times 10^3$ J/m^3)
Chain	81.6	81.6	-14.18	22.27
Cylinder 1	13.3	13.3	-12.28	18.42
Cylinder 2	8.41	8.41	-11.32	16.98
Cylinder 3	3.84	3.84	-8.23	12.35
Cylinder 4	2.45	2.45	-6.73	10.09
Cube 1	1	1	0	0
Cube 2	1	1	0	0
Sphere	1	1	0	0

4.3.2 Estimation of directionally dependent influence of dipole interactions

In Chapter 3, a method is proposed to estimate directionally dependent influence of dipole interactions. This method is based on the calculation of E_{DISM} , which suggests the total energy of dipole interactions when a cluster is magnetized completely by a field orientated to a certain direction. Figure 4.3 (left) gives the 3d orientation distribution of E_{DISM} of chain, cylinder 2, cube 1 and sphere clusters as examples. For chain and four cylinder clusters, the orientation distributions of E_{DISM} all display typical uniaxial anisotropy, and the easy axis of each coincide with the AMA. Figure 4.3 (right) shows the angular dependent E_{DISM} . The dependence of E_{DISM} on θ_{MA} obeys the correlation, $E_{DISM} = K_0 + K_1 sin^2\theta_{MA}$, where K_0 and K_1 are constants (θ_{MA} is the angle between the unit vector of magnetization of the cluster and the AMA). The values of K_0 and K_1 are given in Table 4.1. All the profiles of E_{DISM} of these five clusters have a deep valley with the bottom at $\theta_{MA} = 0$. It suggests that as θ_{MA} gets close to 0^o the dipole interactions are expected to help maintain the current magnetization of the cluster; however, once θ_{MA} approaches to 90^o, the dipole interactions will turn to compel the cluster to lose the magnetization. From the discussion in 4.3.1, we have known that the morphology anisotropy is reduced when the cluster changes from chain to cylinder 1 to 2 to 3 and to 4. As a result, improved morphology anisotropy brings a lower K_0 and higher K_1 (Figure 4.4). Therefore, with the strongest morphology anisotropy, the moments of chain cluster should be most inclined to stay at AMA. This also explains why the valley of E_{DISM} of chain cluster is deepest. And this tendency would become smaller and smaller when the four cylinder clusters are considered. In contrast, E_{DISM} of the two cube clusters and sphere cluster are independent of direction. The angular dependent E_{DISM} is fixed at 0 (Figure 4.3 right). This is further validated by the presence of almost null K_0 and K_1 (Table 4.1). So, after the cluster loses its shape anisotropy, dipole interactions can be expected to contribute little to the cluster's magnetism.

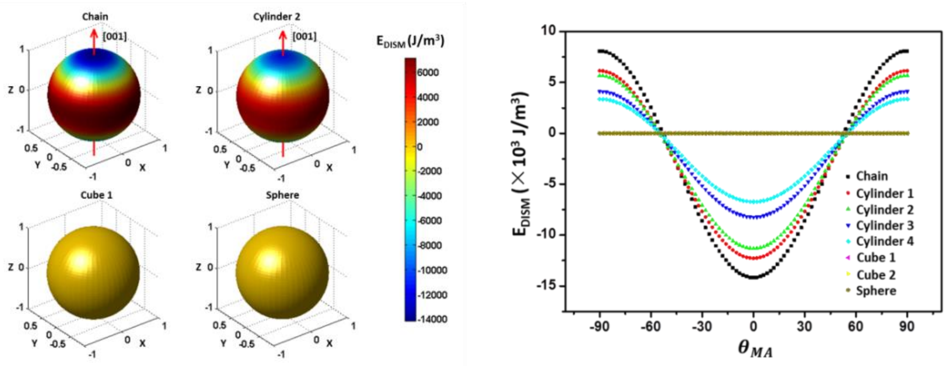

Figure 4. 3 Left: orientation distribution of E_{DISM} of the chain cluster, cylinder cluster 2, cube cluster with simple cubic lattice and sphere cluster. Right: E_{DISM} as a function of θ_{MA}.

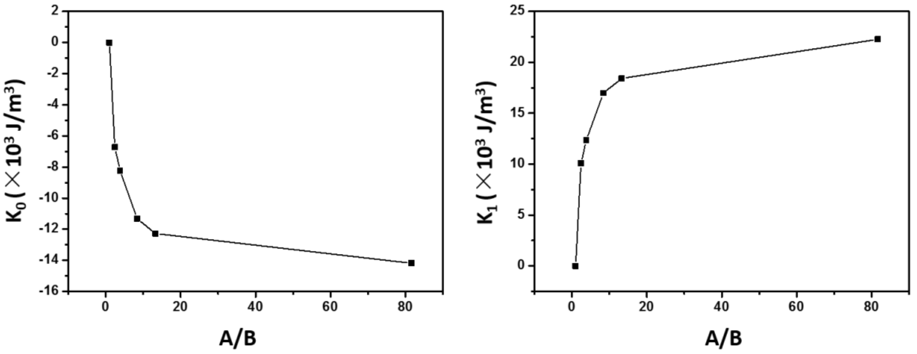

Figure 4. 4 The changes of K_0 and K_1 .with morphology anisotropy.

4.3.3 Comparison between MC with Metropolis algorithm and KMC method for study of magnetic losses of SMNPs

To investigate the effect of dipole interactions on magnetic losses of a SMNP cluster, the Monte Carlo approach is performed to generate hysteresis loop at a certain temperature. The standard MC with Metropolis algorithm is the most used approach for simulating time-dependent magnetization, but it suffers from the difficulty of precise time quantification of the MC step. Compared with standard MC, KMC method doesn't need any calibration of the time scale of Monte Carlo step because its model naturally includes the time scales of intrinsic thermal fluctuations. Here, both these two approaches are conducted to see which one is more suitable for study of magnetic losses of SMNPs. At first, the simulations are validated by reproducing the DC equilibrium magnetic magnetization of non-interacting SMNPs at T $\approx$ 0 K. The magnetic properties of particle are set the same as the published data of magnetite nanoparticles: the effective magnetic anisotropy constant K_{eff} is 9000 J/m^3

and the domain magnetization M_d 446 kA/m.[151] In KMC simulation, the frequency is set at 100 Hz to obtain a DC equilibrium magnetization. For standard MC, the number of Monte Carlo step N_{MCS} per cycle is adjusted to be large enough to let the system to have enough time to achieve equilibrium. As show in Figure 4.5, the hysteresis loops produced by two methods are nearly the same. The remanence magnetization and coercivity are 0.5 M_S and 0.48 H_a respectively. Both of them are in good agreement with the expected values proposed by Stoner and Wohlfarth[155, 296].

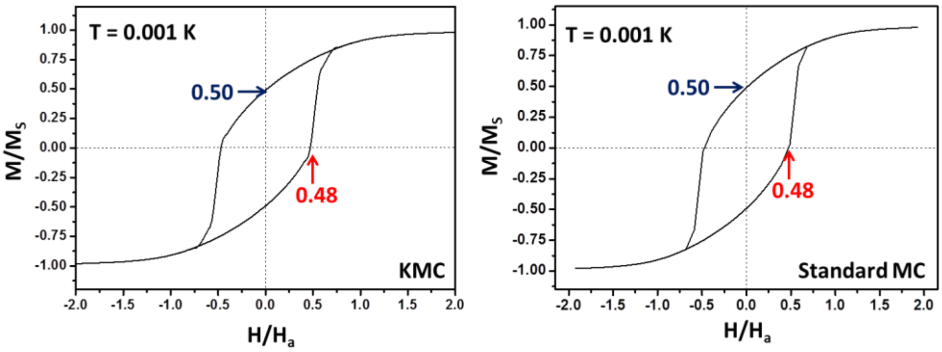

Figure 4. 5 Simulated DC equilibrium magnetization of non-interacting particles at T = 0.001 K. Left: KMC algorithm; right: standard MC method.

Then, the temperature is increased to 310 K (body temperature). Figure 4.6 shows the DC magnetizations performed by KMC (left) and standard MC (right). Except non-interacting particles, the curves of DC magnetization produced by KMC all exhibit apparent hysteresis loops despite of the changes in cluster's shape and packing manners. To the contrary, all the M-H curves produced by standard MC show minute loops, suggesting the presence of superparamagnetism. It has been demonstrated that the blocking temperature of 10 nm of magnetite particles is below 150 K. So, it is clear that the results of the standard MC are more close to the experimentally findings than KMC.

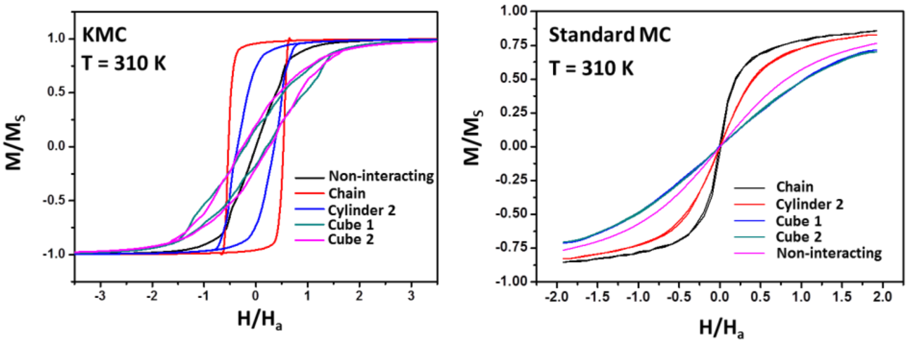

Figure 4. 6 DC magnetization of non-interacting particles at 310 K performed by KMC (left) and standard MC (right).

KMC method is developed based on a two-level approximation. As mentioned in Chapter 2, as long as the magnetic anisotropy energy of particle is large enough, one can consider that the magnetization of this particle has only two positions: the two minima of the energy landscape. If there is only one minima, the effect of thermal agitation will be removed arbitrarily and the magnetization must be found at this minima. Chantrell and Walmsley[281] suggested that KMC works well when the magnetic anisotropy energy of particle is no less than $3k_BT$. We performed KMC to simulate DC magnetization of cube 1 cluster at magnetic anisotropy constant K_{eff} of 9000, 22500, 45000 and 90000 J/m^3. The temperature is changed from 100 K to 1200 K. T_B can be calculated by considering the time window of the measurement.

For example, the experimental measuring time with a magnetometer (roughly 100 s) gives by $T_B = K_{eff}V/30k_B$.[54] For 10 nm of particle, T_B is 11.3, 28.4, 56.9 and 113.8 K when K_{eff} is 9000, 22500, 45000 and 90000 J/m^3 respectively. So, the particles are supposed to present superparamagnetism as long as T is not lower than these values Figure 4.7 gives the results of DC magnetization. When K_{eff} is 9000 J/m^3, the thermal flocculations is totally disfunctioned. The hysteresis loop remains almost the same even though the temperature increases to 1200 K. To find out why thermal flocculations is totally disfunctioned, a very weak field ($H_0 \approx 0$) is applied on cube 1 cluster at 300 K and followed by thermalization. We find that the probability for appearance of only one minima is almost 100 %, in other words, the dipolar field is so strong that the landscape of particle's energy no longer exhibits two minimas which generally are attributed to the magnetic anisotropy energy of particle. The mean of the energy at this minima is found to be 2.3 k_BT. It could be easy for thermal agitations to drag the particle's magnetization away from this point. So, in this case, it is wrong to arbitrarily remove the influence of thermal flocculation. When K_{eff} increases to 22500, 45000 and 90000 J/m^3, superparamagnetism appears at 600 K, which are still much higher than the expected values. Therefore, compared with standard MC, KMC method is not appropriate for studying the time-dependent magnetization of SMNPs of 10 nm.

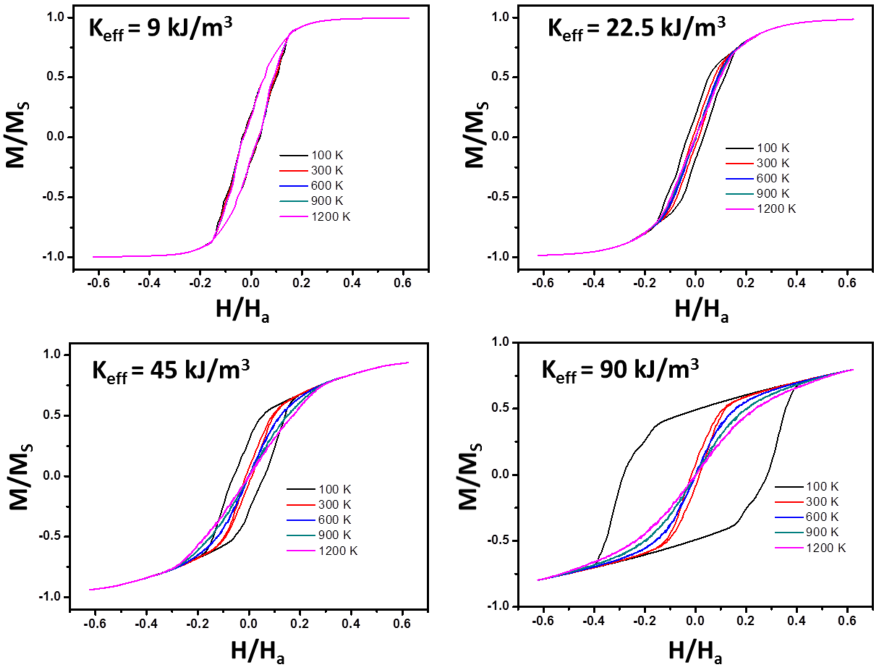

Figure 4. 7 DC magnetization of non-interacting particles performed by KMC.

4.3.4 Estimation of the time scale of Monte Carlo step of standard MC

In order to simulate AC dynamic hysteresis of SMNPs in a quantified manner, the estimation of the time scale of MCS is demanded. Rosensweig's model has been suggested to be useful in predicting heating behavior of non-interacting SMNPs.[4] In the present work, Rosensweig's model is modified to be suitable for describing dynamic hysteresis driven by high field intensity. The equilibrium susceptibility is s set to change with field intensity, and the loop area is calculated via integrating magnetization against field. Details are given in chapter 3. The properties of the particle and field amplitude are set to be the same as those used in MC simulation. The value of pre-exponential factor $\tau_0$is typically chosen as 10^{-9} s^{-1}, which corresponds to the damping factor of 0.28 (see chapter 3 for details). Figure 4.8 shows that the calculated loop area is proportional to the field frequency. The proportionality constant is of 8.736×10^{-7} s^{-1}.

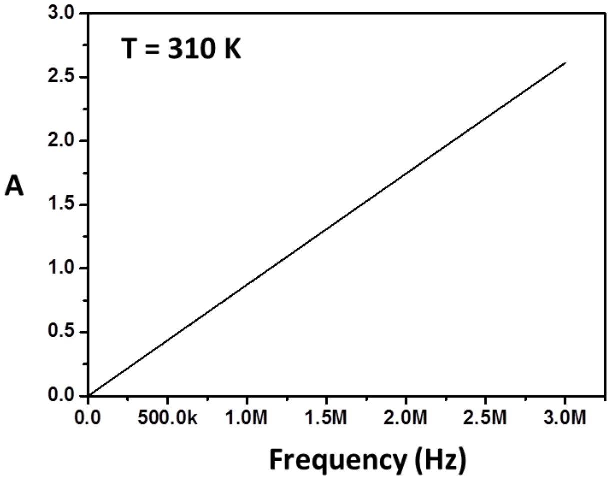

Figure 4. 8 Calculated Loop area of non-interacting nanoparticles as a function of field frequency.

In the simulation, the inverse of N_{MCS} per field cycle is used as the computational frequency. The temperature is maintained at 310 K and the value of δθ is fixed. The field oscillates in sinusoidal waveform $H = H_0 sin2\pi(1/N_{MCS})(l\times N_{MCS}/400), l = 1,2,3 \ldots 400$. H_0 is set at 200 kA/m to magnetize the cluster completely. Before a new cycle is started, time returns to 0. The cluster's magnetization is collected by summing the moment projections on the positive direction of field variation every N_{MCS}/ 400. As the growth of cycle numbers, N_{cycle}, the time dependent magnetizations keep being averaged across all of existing cycles to generate the matrix of cycle-averaged magnetization $\boldsymbol{M}(l, N_{cycle})$. Figure 4.9 shows the evolution of Euclidean distance d ($\boldsymbol{M}(:, N_{cycle})$, $\boldsymbol{M}(:, \infty)$) when chain, cylinder and two cube clusters are magnetized by the field oscillating along the Z-axis. It can be seen that d ($\boldsymbol{M}(:, N_{cycle})$, $\boldsymbol{M}(:, \infty)$) decreases with N_{cycle} and reaches stable after N_{cycle} larger than 60. In all of the simulations conducted in this work, $\mathbf{M}(:, N_{cycle})$ changes little after $N_{cycle} > 60$. The loop area is produced by integrating each column of $\boldsymbol{M}$ $(:, N_{cycle}$>60) against H followed by averaging work. Finally, the loop area is converted to one in reduced units via being divided the product of saturation magnetization M_S and $H_a = 2K_{eff}/M_S$. The magnetization–field (M-H) curves shown in this chapter are the plots of $\boldsymbol{M}$ $(:, N_{cycle} = 100)$ against $H(t)$.

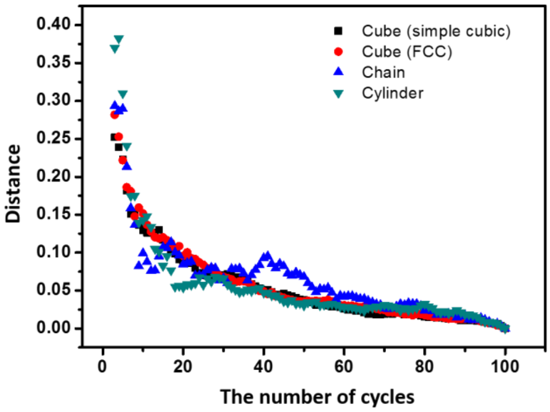

Figure 4. 9 Euclidean distance d (M(:, N_{cycle}), M(:, ∞)) changes with the number of cycles.

Figure 4.10 shows the plot of simulated loop area in reduced units against 1/ N_{MCS} per cycle. It can be seen that the loop area is excellently proportional to

1/ N_{MCS} per cycle. By using linear regression without the intercept term, the proportionality constant is found to be 23812.6 MCS^{-1}. The coefficient of determination is 0.997. Relating the constant calculated by Rosensweig's model to this one, we find that one MCS is comparable to 3.67×10^{-11} s. 54800 MCSs per cycle is used for the study of the magnetic losses of chain, cylinder and two cube clusters, which corresponds to 500 kHz.

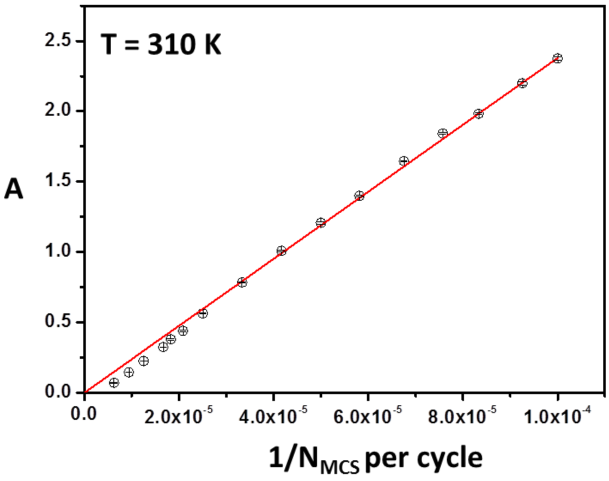

Figure 4. 10 Loop area in reduced units of non-interacting SMNPs vs 1/N_{MCS} per cycle. The temperature is fixed at 310 K. The aperture angle is kept constant. The fitting curve is presented as a red line.

4.3.5 study of hyperthermia heating behavior of clusters in different shapes

4.3.5.1 Chain and cylinder clusters

Figure 4.11 show *M-H* curves of chain and four cylinder clusters obtained at different θ_{MA}. All the hysteresis loops shrink quickly with θ_{MA}. This is further demonstrated by continuous reduction of the loop area, denoted by A_M in Figure 4.12 (a). According to the discussion in 4.3.2, E_{DISM} of chain and all the cylinder clusters increase with θ_{MA}. When the moments are required to overcome a high energy barrier to get aligned with the field, a reduced heating efficiency is understandable. If it assumes that the cluster is randomly orientated with respect to the field direction in practice, the mean of A_m decreases from 0.92 to 0.69 to 0.63 to 0.50 and to 0.47 when the morphology anisotropy of cluster is 81.6 (chain), 13.3 (cylinder 1), 8.4 (cylinder 2), 3.8 (cylinder 3) and 2.5 (cylinder 4) respectively. The blue dashed line in Figure 4.12 presents the A_M of non-interacting SMNPs, which is 0.38. So, as long as the particles form into cylinder or chain cluster, at least a 25 % of enhancement in hyperthermia heating efficiency could be expected, and the enhancement can exceed 100% by improving the morphology anisotropy. In terms of the particle's properties and τ_0 chosen for the simulation, the damping factor of isolated particle is around 0.14, which is already higher than that of the particles studied in work of Branquinho *et al.*[184] Their work also suggests that the damping factor tend to increase with chain size. Perhaps high damping behavior might exist in our simulation and prompt dipole interactions to contribute positively to the chain cluster’s magnetic losses.

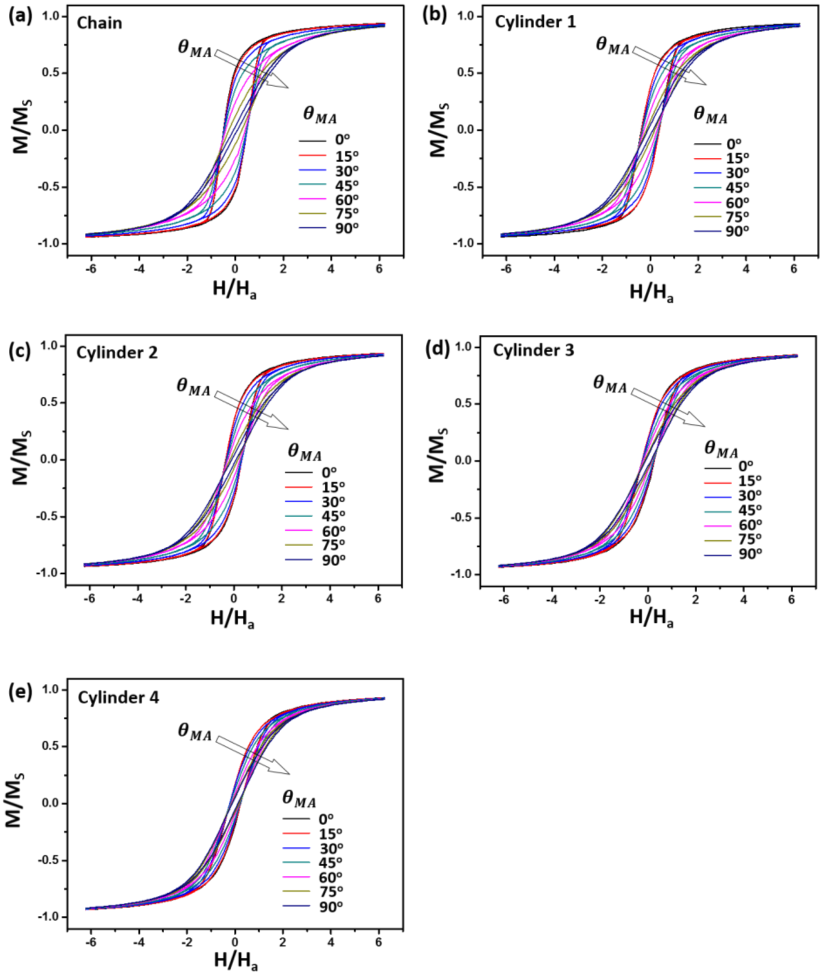

Figure 4. 11 Dynamic hysteresis simulations of chain and four kinds of cylinder clusters with settingθ_{MA} at 0°, 15°, 30°, 45°, 60°, 75°, and 90°.

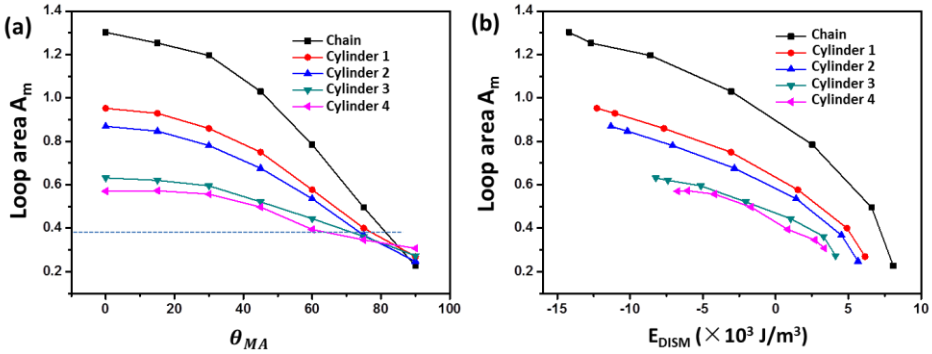

Figure 4. 12 Hysteresis loop area chain and four kinds of cylinder clusters as a function of θ_{MA} (a) and E_{DISM} (b).

Figure 4.12 b gives A_m as a function of E_{DISM}. It can be seen that the profile of A_m against E_{DISM} of one cluster is parallel with others' and a lower E_{DISM} cannot guarantee a higher A_m. There must be some other factor that dominates the heat efficiency. E_{DISM} dependent A_m is polynomially fitted with order of 3. After subtracting the interception, all the results follow the same trend no matter with the type of cluster, and the value is determined by E_{DISM} (Figure 4.13 left). The physics behind the interception is the other factor that dominates the efficiency. In fact, the interception is supposed to be the A_m when the cluster is magnetized along the direction which generates null E_{DISM}. And the magnitude increases with improving the morphology anisotropy of cluster (Figure 4.13 right).

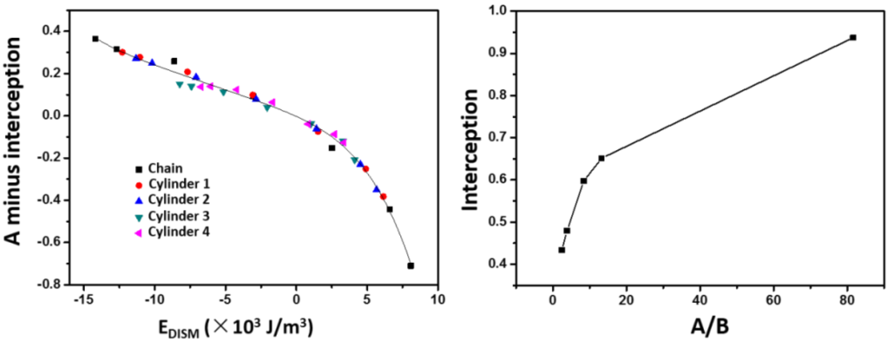

Figure 4. 13 Left: the dependence of the difference between loop area and interception gained by polynomial fitting on E_{DISM} . Right: the interception at different morphology anisotropy.

In section of 4.3.2, it was found that the distributions of E_{DISM} of these five clusters all exhibit deep valleys with the bottoms at $\theta_{MA} = 0$. To minimize the energy of dipole interactions, the particles' moments should be inclined to stay at AMA. During the simulation, the projections of moments in [001] direction are collected simultaneously. Figure 4.14 a – e gives the sum of moment projection on Z-axis against Z-component of field intensity. The height of the loop decreases continuously with θ_{MA}, suggesting that pulling magnetization direction away from AMA makes more difficult for moments to stay close to AMA. However, despite θ_{MA} is large up to 60° and 75°, the sum of moment projection on Z-axis increases apparently with reduced field intensity regardless the type of cluster. This indicates that the moments truly have a tendency to get aligned with the AMA. The loop area in reduced unit, denoted by A_{001}, is obtained through the same way as A_M, except for the integration against the Z-component of the field. Figure 4.14 f shows the difference between A_m and A_{001} at different θ_{MA}. For a chain cluster, A_{001} keeps nearly the same with A_m until θ_{MA} is larger than 45°, and the difference maintains below 20 % before reaching 75°. With reducing the morphology anisotropy, the difference between A_m and A_{001} increases faster during the departure of field direction away from AMA. For cylinder 1 and 2, a 20% of difference is observed at $\theta_{MA} = 60^o$; but the difference is already larger than 20 % when θ_{MA} reaches 45° for cylinder 3 and 4. So, higher morphology anisotropy brings stronger such alignment to AMA. To answer whether this alignment brought by dipole interactions is the additional uniaxial anisotropy mentioned in the work of Mehdaoui *et al.*,[33] an investigation on the relationship between the alignment strength and θ_{MA} will be necessary. However, such a strong alignment to AMA must impede the relaxations of particles' moments, thus enhancing the hyperthermia heating efficiency. In this case, an increase in A_m at null E_{DISM} can be understood.

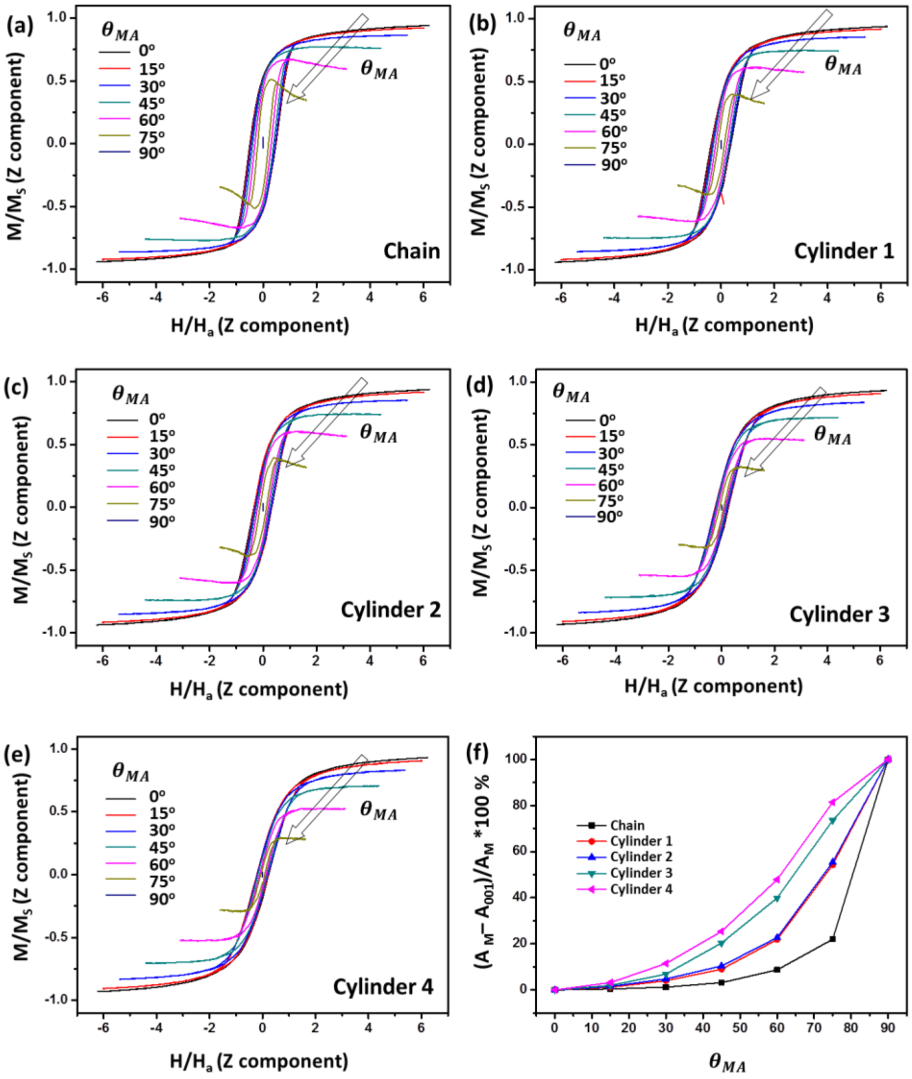

Figure 4. 14 The sum of moment projection of chain and four kinds of cylinder clusters on Z-axis vs Z-component of field intensity (a to e). (f) Comparison of A_m and A_{001} at different θ_{MA}.

4.3.5.2 Anisotropy-less clusters

On the other hand, once the cluster loses its morphology anisotropy, we find that the magnetic losses begin to react almost numbly to the change of field orientation with respect to cluster. The field direction is specified with cartesian reference frame. As shown in Figures 4.15, all *M-H* curves of the cube cluster with a simple cubic lattice appear roughly the same, despite the change of field direction from [001] to [112], [111] and [110], as do the curves of cube cluster with a FCC lattice. Figure 4.15 c compares the loop area of these two cube clusters in these four directions. The loop area of two cube clusters varies little with the field direction and is slightly lower than the non-interacting particles. The average loop area is found to be 0.37 (± 4.7 %), which is very close that of non-interacting particles.

So far, the synthesis of sphere-like SMNP clusters with a disordered structure has been widely developed.[46, 109, 164] Hayashi *et al.*[280] found that the heating efficiency was increased by 50 percent after assembling 9 nm of magnetite nanoparticles into sphere-like clusters with a disordered arrangement. However, Liu *et al*. [168] observed a sharp decrease in the heating ability after forming a dense spherical pack of particles by loading 6 nm of $MnFe_2O_4$ into a polymer latex. It can be expected that a disordered particle arrangement might bring an impact on the cluster's magnetic losses. Figures 4.16 shows the hysteresis loops and loop area of sphere cluster magnetized in different directions. Similar to the results of heating cube clusters, the hysteresis loops are almost the same despite of the change in direction. The average loop area is 0.34 (± 4.4 %), comparable to that of non-interacting particles and cube clusters. The finding of inefficient magnetic losses caused by losing shape anisotropy is consistent with Mehdaoui *et al.* [33] and Saville *et al.* [155]. E_{DISM} of both cube clusters and sphere cluster are directionally independent and kept at 0. The nearly null contribution of dipole interactions minimizes the difference between clusters with less morphology anisotropy and non-interacting particles.

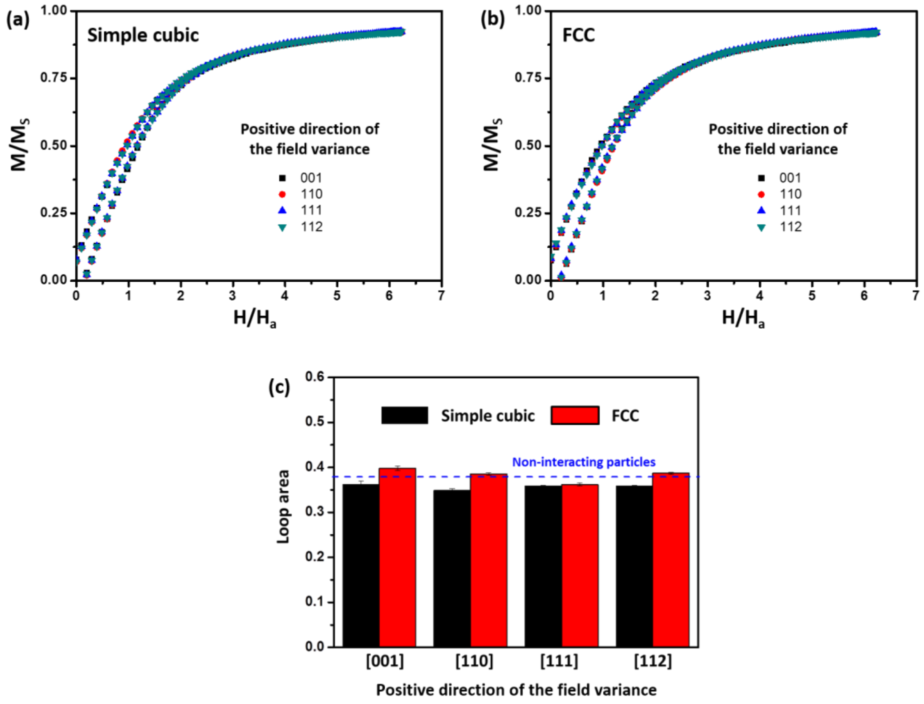

Figure 4. 15 Zoom-in dynamic hysteresis loops of cube clusters with a (a) simple cubic and (b) FCC lattice. The field direction is changed from [001] to [112], [111] and [110]. (c) Comparison of the loop area in reduced units, which are calculated by integration of the M-H curves given in (a) and (b).

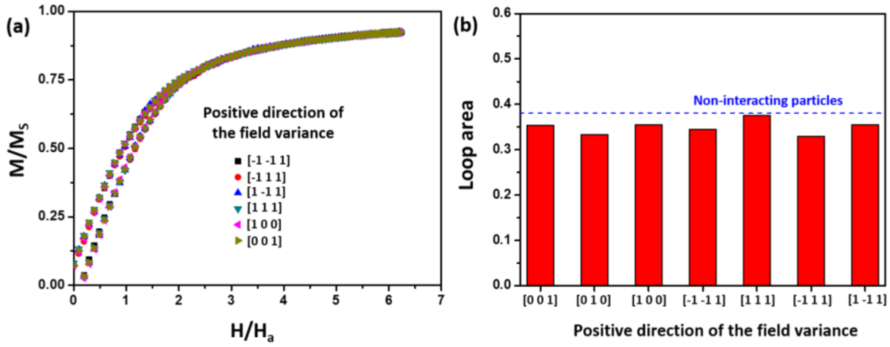

Figure 4. 16 (a) Zoom-in dynamic hysteresis loops of sphere cluster. (b) Comparison of the loop area in reduced units, which are calculated by integration of the M-H curves given in (a).

Then, we intend to find out if a semi-ordered structure can help enhance hyperthermia heating efficiency of anisotropy-less clusters.50000 such clusters are fabricated by omitting 16 randomly picked particles from cube clusters with a simple cubic lattice. As a result, the average A/B and A/C are 1.06 and 1.14 with a relative standard deviation of 2.88% and 4.55%, respectively. As shown in Figure 4.17, E_{DISM} can achieve the minimum at any angle with respect to the AMA.

To find out the relationship between E_{DISM} and the magnetic losses of anisotropy-less clusters with imperfect lattice, numerical simulations are carried out with setting the field to oscillate along the Z-axis. Figure 4.18 a shows the plots of the loop area against E_{DISM} when N_{MCS} is adjusted to 20000, 30400 and 54800, which correspond to 1300, 900 and 500 kHz respectively. The dashed lines represent the loop area of non-interacting particles at these three $\mathrm{N}_{\mathrm{MCS}}$. It can be seen that at 54800 MCSs per cycle the E_{DISM} influences the loop area slightly, and the loop area remains comparable to non-interacting particles. When the N_{MCS} per cycle is reduced to 30400, the loop area turns to decrease with E_{DISM}. And this tendency becomes to be much obvious at 20000 MCSs per cycle. In other words, only at an extremely high frequency, the dipole interactions could be expected to change the magnetic losses, and it requires E_{DISM} to be lower than -1.0 ×10^3 J/m^3 to produce a better heating efficiency. Figure 4.18 b shows the probability distribution of E_{DISM} when magnetization is along with [001] direction and the distribution averaged over 1000 directions uniformly distributed in 3D space. Both distributions suggest that the chance of E_{DISM} being lower than -1.0 ×10^3 J/m^3 is quite low (< 3 %). Obviously, it is difficult for a cluster with less anisotropy in shape to convert more magnetic work to heat.

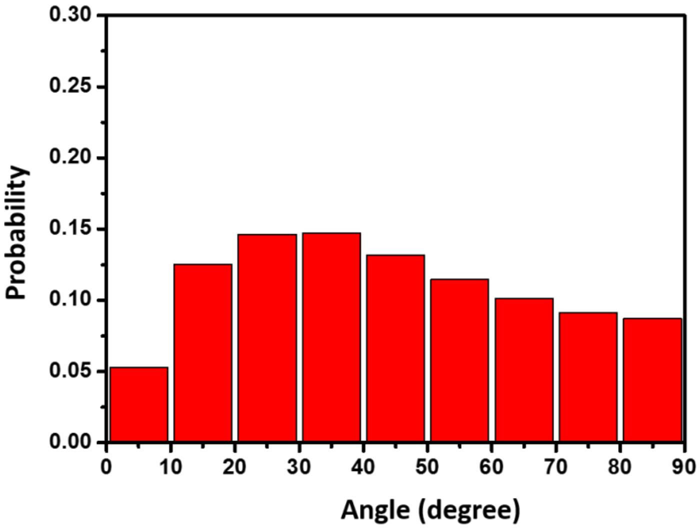

Figure 4. 17 Probability distribution of the angle between the axis where is the minimum and the axis of the morphology anisotropy.

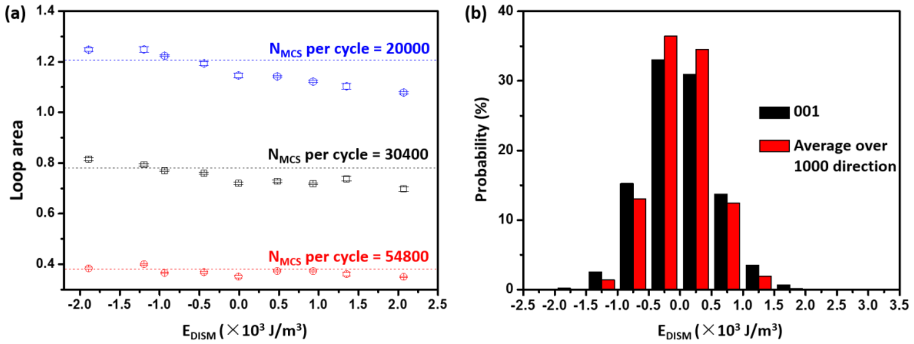

Figure 4. 18 (a) E_{DISM}-dependent loop area of anisotropy-less cluster with an imperfect lattice. The magnetic field oscillates along the Z- axis. (b) The probability distribution of E_{DISM} when the clusters' magnetization aligns with the [001] direction, as well as the probability distribution averaged over 1000 directions. These 1000 directions are uniformly distributed in a 3D space.

4.4 Summary

In this work, we investigated the effect of dipole interactions on hyperthermia heating SMNP clusters via time-quantified Monte Carlo simulation. The cluster's shape is characterized by treating it as an equivalent ellipsoid. The morphology anisotropy is defined in terms of the ratios of the length of the ellipsoid's semi-principal axes. As the shape of cluster is changed from chain to cylinder and to cube or sphere, cluster's morphology anisotropy keeps decreasing to 0.

The standard MC with Metropolis algorithm is more suitable than KMC algorithm for simulating magnetic losses of SMNPs with low magnetocrystalline anisotropy. According to the Rosensweig's model, the hysteresis loop area of non-interacting particles is supposed to be proportional to the field frequency. In our simulation, the inverse of total number of Monte Carlo step per field cycle is considered as a computational frequency. By comparing the two proportionality constants gained from the simulation and the Rosensweig's model, the time scale of one Monte Carlo step is found to be 3.67×10^{-7} s, which is 100 times larger than the relaxation time of the particle.

E_{DISM} is applied to estimate the energy barrier brought by dipole interactions before the individual moments align with the direction of the cluster's magnetization. A low E_{DISM} is supposed to be in favor of the magnetization process and help maintain the current magnetization of the cluster, thus enhancing the magnetic hysteresis. The orientation distribution of E_{DISM} of chain and cylinder clusters displays typical uniaxial anisotropy. When the field direction is parallel to the cluster's morphology anisotropy axis, the value of E_{DISM} achieves the minimum; and E_{DISM} increases with the angle between field direction and this axis. However, once the cluster loses the morphology anisotropy like cube cluster, the orientation distribution of E_{DISM} becomes isotropic and the value is fixed at 0, indicating that a minimized influence of dipole interactions can be expected.

Our simulation results suggest that as the increase of the angle between field direction and the cluster's morphology anisotropy axis, the hysteresis loop area of chain and cylinder cluster decreases continuously due to the growth of

E_{DISM}. With the aid of low E_{DISM}, the hysteresis loop area of chain and cylinder cluster remains superior to that of non-interacting particles at the most angles. In addition, higher shape anisotropy also prompts the dipole interactions to benefit cluster's magnetic losses via aligning the moments to the cluster's morphology anisotropy axis. Such alignment helps cluster with higher morphology anisotropy heat better. However, once the cluster loses its shape anisotropy, it will be hard to obtain enhanced heating efficiency at least when the field is strong enough to fully magnetize the cluster. The loop area of cube or sphere cluster is almost the same as that of non-interacting particles. Moreover, formation of semi-ordered structure won't enlarge the probability for anisotropy-less cluster to produce heat more efficiently. Only at extremely high frequency the E_{DISM}can get the chance to affect the magnetic losses of anisotropy-less cluster with imperfect lattice.

Chapter 5 The effect of size on the hyperthermia heating efficiency of clusters composed of SMNPs

5.1 Introduction

In chapter 4, it has been suggested that the dipole interactions will contribute less to the magnetic losses once a cluster of SMNPs lose the morphology anisotropy. In fact, the notion is made based on the calculation of angular dependent of E_{DISM} , which is the total energy of dipole interactions at saturation magnetization Ms. If a field is not strong enough to get all particle's moments aligned, E_{DISM} may not be suitable for estimation of the change of dipole interaction energy, in other words, the heating behaviour could be no longer affected by E_{DISM} .

Experiments have shown that the product of the amplitude and frequency of AC magnetic field should be lower than 5×10^{9} $Am^{-1}s^{-1}$ to conduct a safe hyperthermia treatment.[140] At present, the induction heating system designed for treatments on human is able to generate a homogeneous AC magnetic field with a frequency of 100 kHz and variable field strength of 2.5 - 15 kA/m[139]. For a frequency of 100 kHz, the amplitude must be lower than 50 kA/m so as to keep that product within the range of 5×10^{9} $Am^{-1}s^{-1}$. According to Rosensweig's model, the field intensity should be at least 150 kA/m in order to increase the magnetization of 10 nm of non-interacting magnetite nanoparticles to 90 % of Ms.

What’s more, generally, to assembly nanoparticles into clusters of high shape anisotropy i.e. chain and cylinder, there should be anisotropic elements incorporated within the synthesis procedure, such as anisotropic interactions, i.e. dipole interactions[297, 298], anisotropic building block[299] and/or use of anisotropic template[300]. To the contrary, it is much easier to synthesize anisotropy-less clusters by assembling spherical particles. The emulsion droplet evaporation method has been proven to be successful in massively preparation of almost mono-dispersed sphere-like clusters of SMNPs.[109] Therefore, it is important to figure out how to enhance the hyperthymia heating efficiency of anisotropy-less clusters but also keep field intensity at a low level.

There are only a few works carried out to study hyperthermia heating behaviour of anisotropy-less clusters. Hayashi *et al*.[166] observed the specific absorption rate (SAR) was improved by 60 % after assembling 9 nm of magnetite nanoparticle into sphere-like clusters with size of 100 nm. And the product of filed frequency and amplitude was only 1.8×10^{9} $Am^{-1}s^{-1}$. Liu *et al.*[168] observed a reduction of heating efficiency when 6 nm of SMNPs were high-contently loaded into a sphere-like polymer latex, but loading 18 nm SMNPs brought an improvement in efficiency. The results of Dutz *et al.* [167]

suggest that the size of cluster changes SAR in a non-monotonical way. They prepared sphere - like clusters with different sizes by using centrifugation to separate the clusters according to size. With increasing the size of clusters from 50 to 160 nm, SAR raised at first and then followed by a sharp decrease. Ovejero *et al.*[182] also demonstrated that the SAR of SMNP clusters was dependent on the size of cluster. Clustering of particles were triggered by either reducing the surface potential or augment of ionic strength so as to make worse the colloidal stability. As a result, the plot of SAR against the average size of cluster presented a peak, when the size distribution of clusters was relatively narrow (polydispersity index, PdI < 0.2). Once the distribution was widened (PdI > 0.2), SAR would decrease with the size continuously. Therefore, to improve the heating efficiency of anisotropy-less clusters, it is necessary to study the relationship between the cluster's size and heating efficiency and meanwhile the size distribution must be narrowed down.

5.2 Problem description

In this chapter, we investigated the effect of size on the hyperthermia heating efficiency of clusters composed of Fe_3O_4 nanoparticles. Emulsion droplet solvent evaporation method was used to assembly oleic acid (OA) modified Fe_3O_4 particles into clusters that were stabilized by surfactant in water. The modification of oleic acid made Fe_3O_4 nanoparticles hydrophobic so that the particles were inclined to form sphere-like clusters in water. The properties of modified particles and clusters were characterized, including the particles' morphology, size, crystal structure, weight fraction of oleic acid attached and density. DLS measurement was carried out to determine the hydrodynamic diameter of clusters and polydispersity index (PDI). An induction heating system was built to obtain SAR of the clusters of different sizes. The concentration of particles was fixed. A standard Monte Carlo approach featured with the Metropolis algorithm was implemented to produce dynamic hysteresis loops. Experiments showed that the SAR of clusters of Fe_3O_4 nanoparticles was strongly dependent on the size. The simulated results gave the whole picture of the relationship between cluster's size and heating performance.

5.3 Results and discussions

5.3.1 Preparation and characterizations of Clusters of Fe_3O_4 nanoparticles

Fe_3O_4 nanoparticles were prepared by the Massart method. To facilitate formation of particle clusters in water phase, the surface of Fe_3O_4 nanoparticles were hydrophobically treated with one monolayer of OA. Figure 5.1 shows the TEM image and the histogram of size distribution of Fe_3O_4 nanoparticles prepared by co-precipitation method. The particles were sphere-like in shape. The particles are poly-dispersed in size ranging from 4 to 22 nm and the average size was about 10 nm (± 20.1%). There were few changes in the shape and size of the particles after the modification of OA (Figure 5.2 left), and the weight fraction of modified OA was found to be about 20% by TGA measurement (Figure 5.2 right).

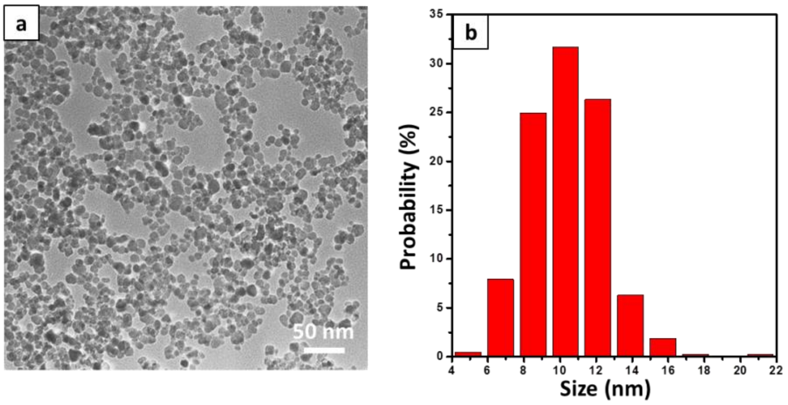

Figure 5. 1 TEM image and histogram of size distribution of Fe_3O_4 nanoparticles prepared by co-precipitation method.

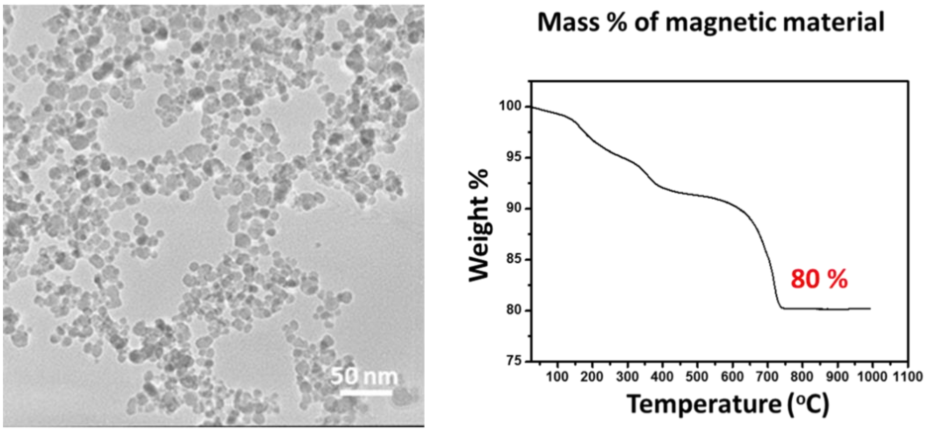

Figure 5. 2 TEM image (left) and TGA measurement (right) of OA modified Fe_3O_4 nanoparticles prepared by co-precipitation method.

The colloidal clusters were produced by assembling OA modified Fe_3O_4 nanoparticles via emulsion droplet solvent evaporation method. At first, the particles were dispersed in cyclohexane to form an oil solution. The solution was then mini-emulsified by SDS solution to generate nano-sized oil droplets containing magnetic particles. After evaporation of cyclohexane, the solvophobic interaction between the ligands and water phase drove the particles to form compact clusters in water. Figure 5.3 gives the TEM image and the histogram of size distribution of clusters of Fe_3O_4 nanoparticles prepared by using the oil phase with concentration of 0.16 mg/ml. The clusters are well-dispersed in water and sphere-like in shape. Each cluster consists of multi particles. The average size and size distribution were measured over 400 clusters. The size of cluster ranges from 50 to 145 nm and the average diameter is 92 nm with relative standard deviation of 17.2%.

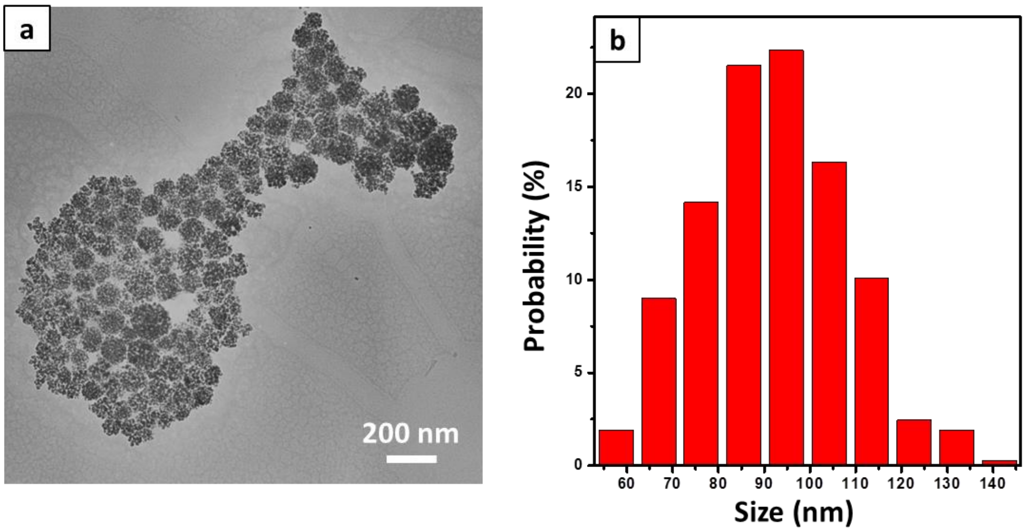

Figure 5. 3 TEM images (a) and size distributions (b) of clusters of Fe_3O_4 nanoparticles.

Figure 5.4 shows the XRD patterns of the Fe_3O_4 nanoparticles before and after the modification of OA and the as-prepared clusters. All the patterns are quite identical to pure magnetite and matched well with that of it (JCPDS No. 82-1533), presenting the same characteristic peaks of cubic inverse spinel structure.[301, 302] Therefore, the crystal structure of magnetite nanoparticle maintains the same no matter with the modification of OA and further assembling.

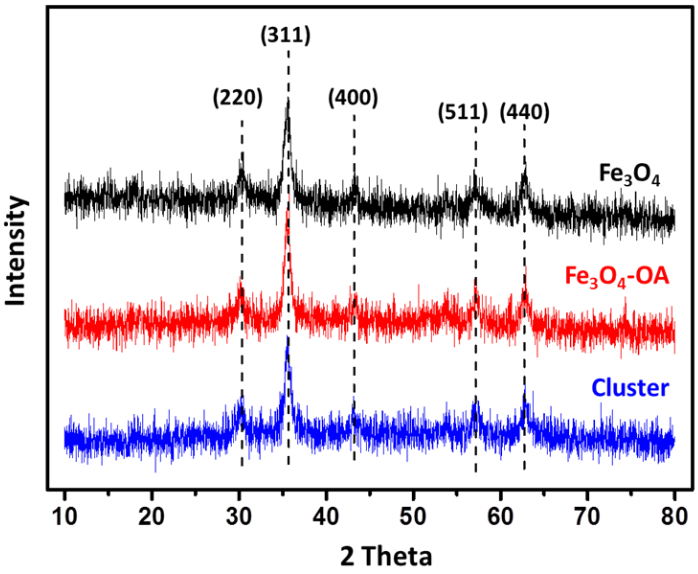

Figure 5. 4 XRD patterns of naked Fe_3O_4 nanoparticles, OA modified Fe_3O_4 nanoparticles and clusters.

Figure 5.5 shows the FTIR spectrums of the naked Fe_3O_4 nanoparticles, Fe_3O_4-OA and clusters stabilized by SDS. The strong vibrations at 580 cm^{-1} observed on all spectrums are attributed to Fe-O stretch of Fe_3O_4 nanoparticles.[303-305]

Compared with naked Fe_3O_4 nanoparticles, the ones modified with oleic acid present strong peaks at 2923 and 2852 cm^{-1}, attributed to the vibration of CH_2, and 1527 and 1430 cm^{-1}, caused by the stretching of COO-Fe, suggesting the presence of OA on the particle surfaces.[306-308] There is no peak at 1710 cm^{-1} which is supposed to belong to the vibration of C=O, proving no existence of free OA molecules on the surfaces of particles.[309] The clear characteristic peaks of OA in the spectrum of the cluster suggest that the OA molecules are still located on the surface of the Fe_3O_4 nanoparticles after the assembling. It was also found that the thermal-responsive PEO-PPO-PEO polymers (Kolliphor P188) can be absorbed quickly onto the surface of cluster after direct dispersing clusters in polymer solution. After the attachment of the polymer, there is a clear absorption at 1116 cm^{-1} appearing on the FTIR spectrum of the cluster, indicating the presence of the polymers. So, the clusters have great potential to be the template for development of thermal responsive drug delivery system.

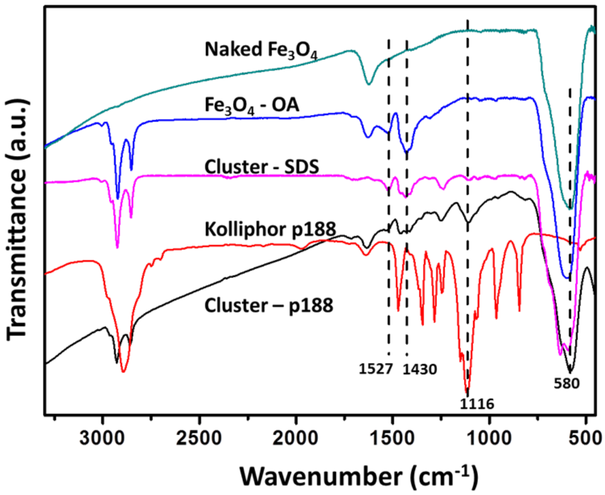

Figure 5. 5 FTIR spectrums of naked Fe_3O_4 nanoparticles, OA modified Fe_3O_4 nanoparticles, clusters before and after the attachment of kolliphor p188 and the pure kolliphor p188.

The sensitivity of a cluster’s magnetic response is tested by a simple experiment with applying a static magnetic field. As shown in Figure 4, when a magnet was placed beside the cluster solution, nearly all of clusters settled down to the wall of the tube within 1.5 h. When the test was carried out on the aqueous suspension of singe OA modified Fe_3O_4 nanoparticles, quantities of particles stay still in solution after 20 h of magnetic attraction. Figure 5.7 shows the DC magnetizations of unmodified Fe_3O_4 nanoparticles and the clusters at room temperature. Both curves present neglectable hysteresis loops, demonstrating they are superparamagnetic. Due to the modification of OA, the saturation magnetization of clusters is slightly lower than that of unmodified particles.

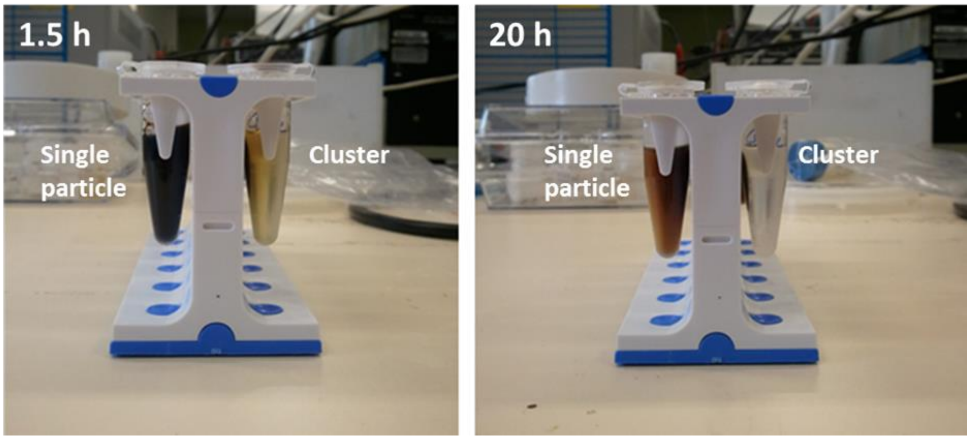

Figure 5. 6 Photos of isolated particle and cluster in the solution after 1.5 h (left) and 20 h (right) of magnetic attraction.

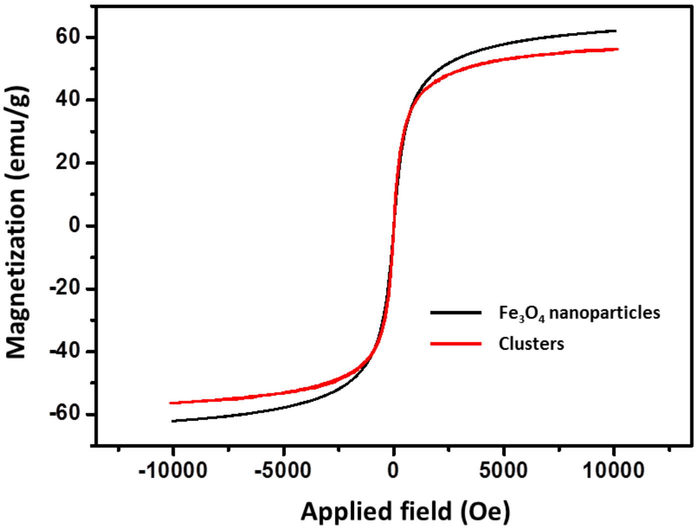

Figure 5. 7 DC magnetization of Fe_3O_4 nanoparticles and clusters at room temperature.

The size of clusters was controlled by changing the amount of particles and/or surfactant used during the preparation. Table 5.1 supplies the details of synthesis recipe and the hydrodynamic diameter D_H of obtained clusters. It is identified that using more particles and less surfactant produce bigger clusters. Generally, the viscosity of particle suspension increases with particle concentration. An oil phase with higher viscosity should make more difficult the emulsion process. During the emulsion, surfactant will absorb onto the interface between oil and water to stabilize the droplet by reducing the surface energy. Once there is not enough surfactant to stabilize emulsion droplets at a certain size, the droplets will undergo Ostwald ripening so as to impede the increase of surface energy by reducing specific surface area. The D_H of clusters can be controlled within the range from 70 to 130 nm. All the PdI were below 0.2. Figure 5.8 gives TEM images of cluster with D_H at 94, 114, 122 and 134 nm. For larger clusters, particles are inclined to form compact sphere-like clusters (Figure 5.8 c and d) due to hydrophobic interactions. For smaller ones, the structure of cluster is compact but the shape is poly-dispersed.

Table 5.1 Synthesis recipe of clusters of Fe_3O_4 nanoparticles

	Particles (mg)	V_{oil} (ml)	SDS (mg)	V_{water} (ml)	D_H (nm)	PdI
c1	60	1.5	375	30	73	0.161
c2	60	1.5	150	30	94	0.186
c3	120	1.5	75	30	114	0.179
c4	240	1.5	75	30	122	0.111
c5	360	1.5	75	30	134	0.096

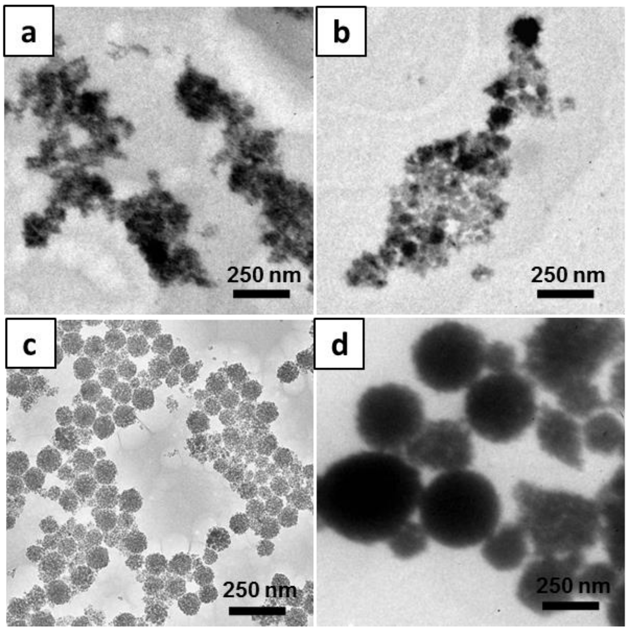

Figure 5. 8 TEM images of clusters of Fe_3O_4 nanoparticles numbered by c2 (a), c3 (b), c4 (c) and c5 (d).

5.3.2 Investigation of hyperthermia heating ability of clusters of Fe_3O_4 nanoparticles

An induction heating system was built to test the heating ability of ferrofluids of SMNP clusters. 1 ml of sample (40 mg/ml) was put into a thermal insulation container, which was placed at the centre of a copper coil of diameter. An induction Heater (80 kHz, 13.1 kA/m) was used to generate AC current going through the coil, and at the same time coil converted the current to AC magnetic field. The temperature of sample was probed with a fluorooptic fiber thermometer. The specific absorption rate (SAR) is defined as the thermal power dissipation divided by the mass of magnetic material. Find more experiment details in Chapter 3. Figure 5.9 shows SAR produced by clusters at different sizes. At the first glance, during the increase of D_H, SAR decreases sharply at first, and then turns to increase, finally ends with a small decrease. There is one more decrease of SAR occurred before the peak, compared with the result of Dutz *et al.* [167]. This circumstance is so similar to the findings of Ovejero *et al.* [182] who studied the influence of particle concentration on the heating efficiency of liquid suspension of 20 nm of iron oxide particles. They found that the hysteresis loop is dominated by the values of magnetizations, including maximum magnetization M_{max} and remaining magnetization M_r. Conde-Leboran *et al.*[180] also reported a similar picture about the relationship between concentration and heating performance of an ensemble of ferromagnetic particles. They suggested that the appearance of a peak on the profile of SAR at larger concentration was caused by transition from a major to minor loop.

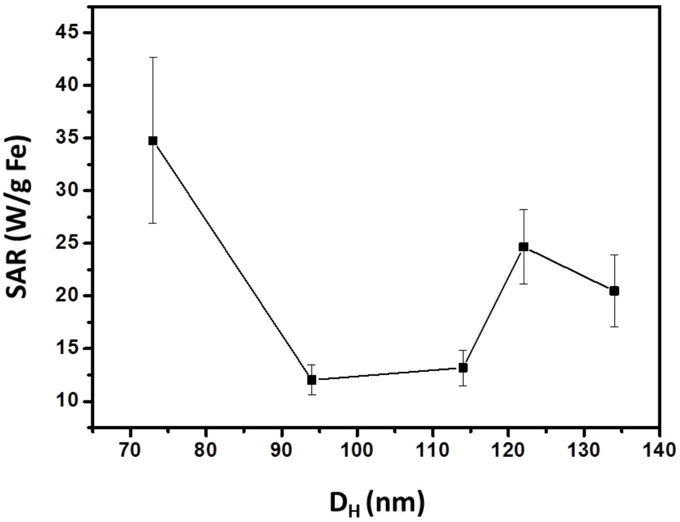

Figure 5. 9 SAR of clusters of Fe_3O_4 nanoparticle against D_H.

Simulation work based on standard Monte Carlo approach is implemented to produce dynamic hysteresis loops. To assembly particles into clusters, 100 of 12 nm of particles are randomly distributed to a certain number (N_c = 80, 50, 30, 20, 10, 6, 5, 4, 3, 2, 1) of groups first. The number of particles in each group must not be lower than integer part of 100/ N_c. Then, the particles in each group underwent clustering process (described in chapter 3) for formation of spherical clusters. All the particles are mono-sized and touch the neighbour ones by point to point. The diameter of magnetic core of particle is kept at 10 nm. The average diameter of N_c of clusters was defined as the size of the cluster. By changing N_c, modelled clusters of different sizes were gained. The morphology anisotropy of clusters is characterised by treating it as an equivalent ellipsoid (the same method used in the last chapter). The morphology anisotropy is defined in terms of the ratio of the longest semi-principal axis to the shortest one of the ellipsoid. Figure 5.10 shows the change of morphology anisotropy with the radius of cluster and 3D schematics of clusters at different sizes. The largest ratio of A to C is only 2.5, which is much lower than chain and cylinder cluster studied in chapter 4. The highest morphology anisotropy is obtained when the radius of cluster is 12 nm (N_c = 50), which is the diameter of single particle. For this size, each cluster contains two particles, thus, the shape of cluster is a dimer. Either increasing or reducing the number of particles within one cluster will change the shape of dimer, leading to a decrease in morphology anisotropy. When the radius of cluster increases to 13.1 nm ($N_c = 30$), the morphology anisotropy decrease by only a little bit. The most of clusters are trimers, whose shape is like a plate. As the radius of cluster reaches to 20 nm, the ratio A/C stop decreasing and maintains at 1, suggesting the morphology anisotropy vanishes, since the clusters become sphere-like in shape.

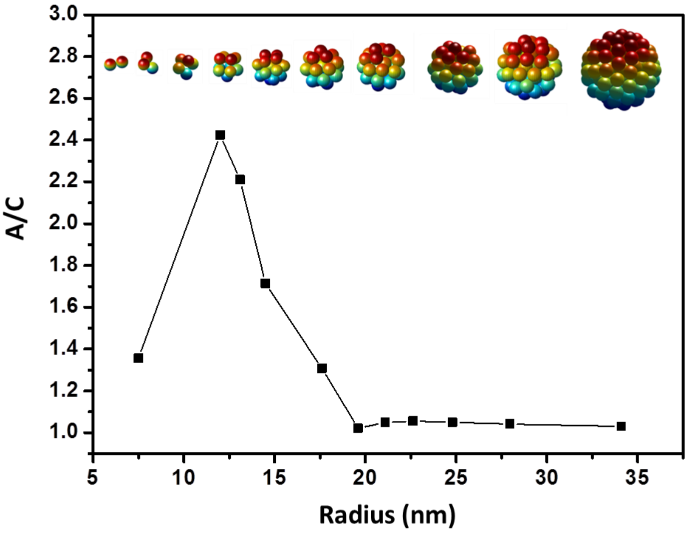

Figure 5. 10 The change of morphology anisotropy with the radius of cluster and 3D schematics of clusters at different sizes.

The settings of Monte Carlo simulation are a little different from the one used in Chapter 4. Expect for particular specification, the temperature is set at 298 K and the magnetic properties of particle are set the same as those of magnetite nanoparticles: the effective magnetic anisotropy constant K_{eff} is 9000 J/m^3 and the domain magnetization M_d 446 kA/m. The easy axes are oriented randomly. The field oscillates in sinusoidal waveform $H = H_0 sin2\pi(1/N_{MCS})(l\times N_{MCS}/100)$, $l = 1,2,3 \dots 100$. The inverse of N_{MCS} per field cycle can be thought of as the computational frequency. To simulate the minute hysteresis loops at low frequency, N_{MCS} should be increased to a great number. According to the discussion of chapter 3, simulating magnetic losses driven by a field oscillating at 100 kHz requires 272480 of Monte Carlo steps per cycle. Meanwhile, a reduction of H_0 will make the dynamic hysteresis loop so minute that considerate magnetization cycles must be taken to generate a convincible result. To save computation time, N_{MCS} per field cycle is kept as constant at 10000. 200 of magnetization cycles are performed to obtain the final loop. A coefficient, a independent of any properties of particle is added to adjust the magnitude of aperture angle $\delta\theta = a(0.05k_BT/2K_{eff}V)^{0.5}$. Figure 5.11 shows the hysteresis loop area of non-interacting particles, denoted by $A_{isolated}$ as a function of a. It is so clear that $A_{isolated}$ decreases with a. Without changing the properties of particles, temperature or N_{MCS} to accelerate the spin rate of moment, the reduced loop area suggests that the moments are given more time for relaxations, in other words, a decrease of field frequency. When a is large enough, $A_{isolated}$ is reduced to 0, indicating that the particle ensemble exhibits superparamagnetism.

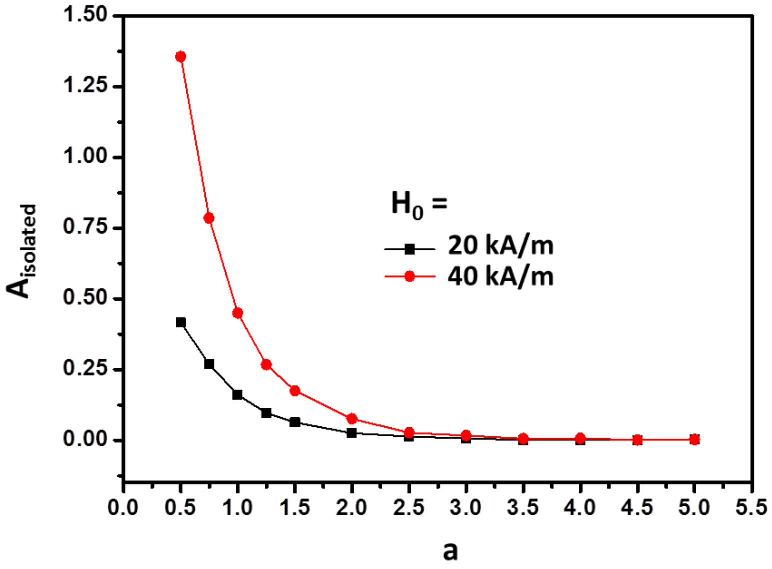

Figure 5. 11 Hysteresis loop area of non-interacting particles as a function of a.

Figure 5.12 gives the whole picture about size-dependent hyperthermia heating performance of SMNP clusters. During the simulation, magnetic interactions between clusters are not taken into consideration. The loop area of cluster is denoted by $A_{cluster}$. The ratio of $A_{cluster}$ to $A_{isolated}$ is defined as the relative loop area to estimate the influence of dipole interactions on dynamic magnetic losses at different cluster size. At the first glance, the heating ability of clusters should have two peak values: the first one, Peak 1 comes when the radius of cluster is around 12 – 13 nm; the second one, Peak 2 could be found at 21 - 24 nm. Regardless of the change in H_0, the first one grows higher with increasing coefficient a. The second one is apparently weaker than the first one, and the peak becomes flatter a peak at smaller a. In chapter 4, we have known that dipole interactions have great tendency to enhance magnetic losses when clusters are of strong morphology anisotropy. So, the first peak can be attributed to the high morphology anisotropy gained when clusters are dimers and trimers. However, it is hard to use the influence of morphology anisotropy to explain the second one. It is because morphology anisotropy vanishes and the cluster becomes sphere-like in shape when the radius is larger than 20 nm. According to chapter 4, once a cluster loses the morphology anisotropy, the dipole interactions should contribute less to the magnetic losses. Thus, the loop area of anisotropy-less cluster is supposed not to be affected by aggregation degree and should keep almost the same with that found on non-interacting nanoparticles. However, except the case of 200 kA/m of H_0 and 0.5 of a (Figure 5.12 d), nearly all $A_{cluster}$ are apparently different from each $A_{isolated}$. Therefore, during reduction of low frequency and field intensity, dipole interactions will play more and more important role in hyperthermia heating of anisotropy-less clusters.

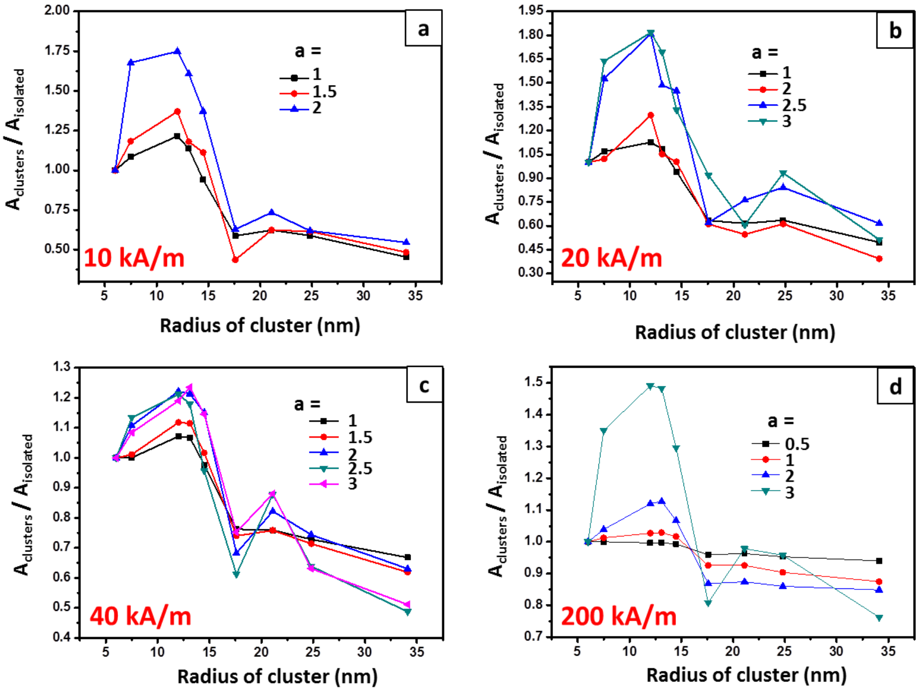

Figure 5. 12 The ratio of hysteresis loop of cluster to non-interacting particles at different cluster's size.

Figure 5.13 shows the maximum magnetization in the reduced unit as a function of the radius of cluster. The major loop, mentioned in the work of Conde-Leboran *et al.*[180], represents the magnetic losses that a particle system can achieve saturation magnetization. It can be seen that all M_{max} shown in Figure 5.13 are lower than 1, suggesting that all the clusters do not achieve saturation magnetization during the simulations, despite of the changes in H_0 and a. Thus, the appearance of both two peaks cannot be explained by a transition from a major to minor loop. It can be seen that after experiencing a short plateau, M_{max} decreases sharply as the radius increases from 12.5 to 17.5 nm, which coincides with the decrease of morphology anisotropy (see Figure

5.10). With further increasing the radius, there is no peak existing on the profile of M_{max} against the radius for each H_0. M_{max} still keeps decreasing only but at slower rate. Therefore, the occurrence of the second peak has little to do with M_{max}.

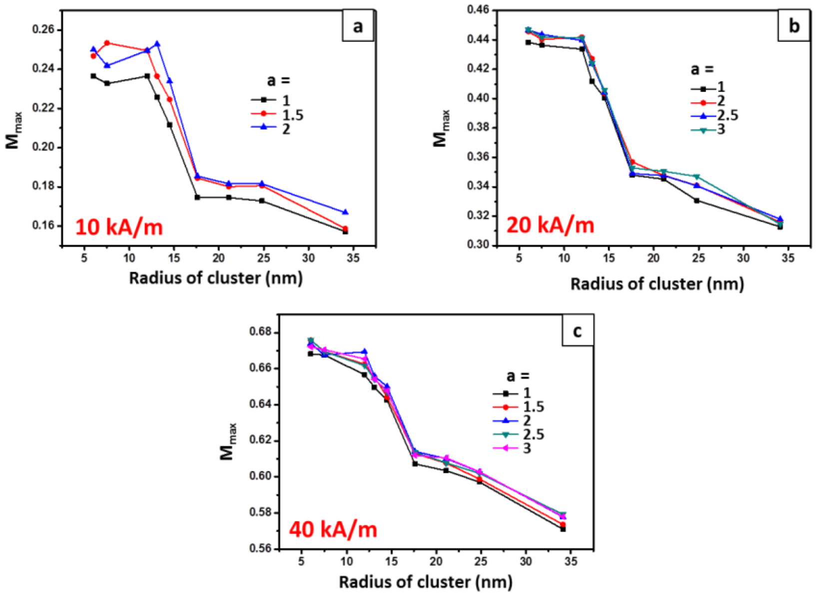

Figure 5. 13 Maximum magnetization achieved of cluster against the radius of cluster.

Here, we come up with a possible explanation. A general scenario is schematically illustrated in Figure 5.14. Several works suggest that the effect of dipole interactions on magnetic losses can be interpreted as changing the effective magnetic anisotropy.[33, 172] When a SMNP cluster is of high morphology anisotropy, dipole interactions improve heating performance by generating a new magnetic anisotropy which spreads throughout the whole cluster, as a result, effective magnetic anisotropy is improved.[33] However, once the morphology anisotropy is weakened, dipole interactions will no longer produce the new magnetic anisotropy. In addition, when dipole interactions are not so strong that the energy barrier for moment's spin is still determined by individual anisotropic energy $K_{eff}V_p$, enhancing dipole interactions will reduce effective magnetic anisotropy [181]. This explains why Peak 1 appears at the region of smaller cluster. Nonetheless, when a cluster contains more particles, the dipole couplings should help resist relaxations of moments, which works like retarding the decrease of K_{eff}. At a lower field frequency, particles are supposed to have more time to form stronger dipole couplings. This explains why a sharper Peak 2 is obtained at larger a (Figure 5.12). However, it would take longer for a large cluster to form dipole couplings. So, further increasing cluster's size accelerates the decrease of K_{eff}, leading to a worse heating efficiency.

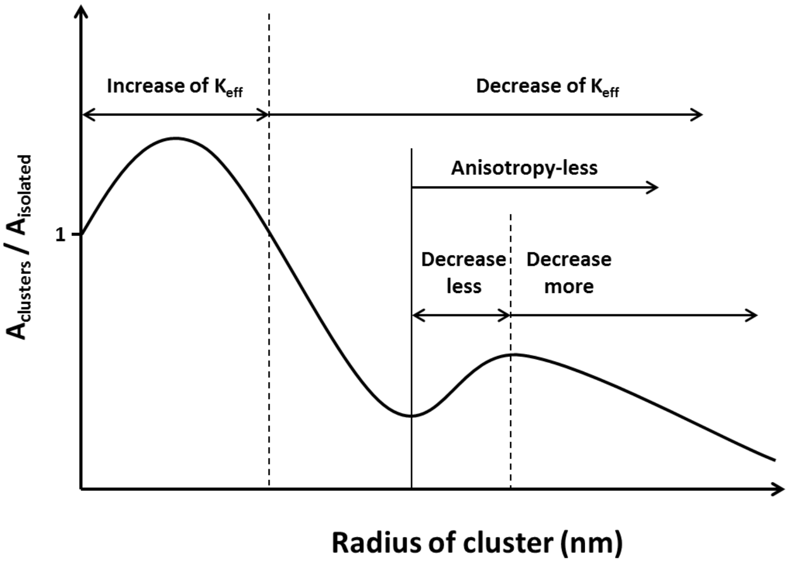

Figure 5. 14 Schematic description of the magnetic hyperthermia scenario of anisotropy – less clusters.

More simulations are conducted to supply a detailed picture about the variance of magnetic losses within the range from 17.5 to 34 nm. Figure 5.15 shows the Peak 2 obtained at different temperature. It is known that intense thermal flocculation promotes relaxations of moments, which results in randomly oriented moment. It can be deduced that promoted relaxations are not beneficial for dipole couplings. Increasing T to 328 and to 358 K makes Peak 2 disappear (Figure 5.15 left). Although a small decrease of T reduces the influence of thermal flocculation by somehow, the spin of moment is slowed, which means, it could take longer to form dipole couplings. Consequently, Peak 2 disappears too at 268 K. However, Peak 2 recurs after further lowering down T to 179 K (Figure 5.15 right). It suggests that suppressing relaxations of moments is crucial for dipole couplings.

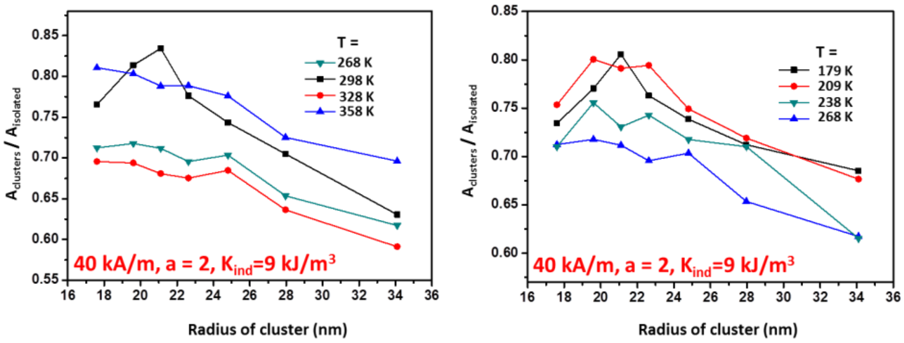

Figure 5. 15 Change of Peak 2 with temperature. The field intensity H_0 is kept at 40 kA/m and a is set at 2 and K_{eff} is 9 kJ/m^3.

Figure 5.15 left shows the Peak 2 obtained at lowered K_{eff}. The peak becomes flattened with intentionally decreasing K_{eff}. A weakened individual magnetic anisotropy promotes randomization of the directions of moments, thus it could be more difficult to form strong dipole couplings. Meanwhile, the maximum point of peak tends to shift to larger size. A lowered K_{eff} leads to a short relaxation time of moment. As a result, it saves the time required for formation of dipole couplings, which allows more particles to form dipole couplings within a limited period. Even though the optimum size of anisotropy-less cluster shits to large value, the heating efficiency is getting worse with decreasing K_{eff} (Figure 5.16 right).

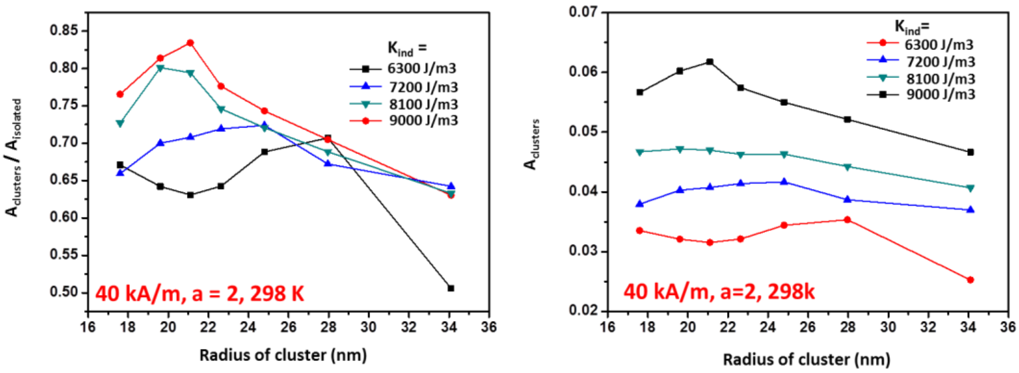

Figure 5. 16 Change of Peak 2 with individual magnetic anisotropy. The field intensity H_0 is kept at 40 kA/m and a is set at 2 and room temperature is considered.

We also investigate how Peak 2 changes with domain magnetization of particles. As shown in Figure 5.17, the loop area is improved with increasing M_d. Peak 2 grows higher during the increase of M_d from 446 to 1784 kJ/m^3. And the optimum size shifts slightly from 21 to 25 nm. An increased M_d reinforces not only dipole interactions but also the coupling with the external field. Therefore, if one expects anisotropy-less clusters to heat better, SMNP with strong domain magnetization and magnetic anisotropy must be used.

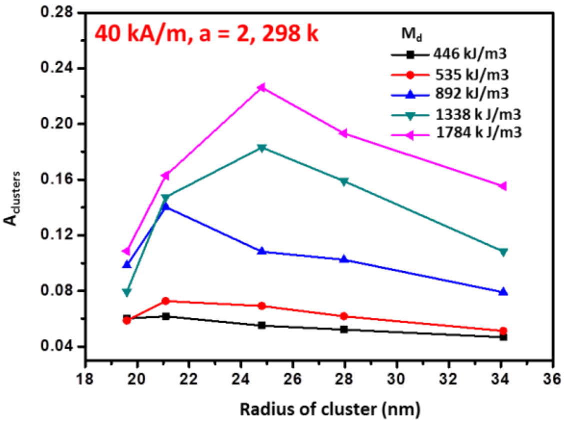

Figure 5. 17 Change of Peak 2 with domain magnetization. The field intensity H0 is kept at 40 kA/m and a is set at 2 and room temperature is considered.

5.4 Summary

In this chapter, we investigated the effect of size on the hyperthermia heating efficiency of clusters composed of Fe_3O_4 nanoparticles. Emulsion droplet solvent evaporation method was used to assembly oleic acid modified Fe_3O_4 particles into clusters that were stabilized by surfactant in water. The size of cluster was controlled by changing the particle concentration of oil phase and/or the concentration of surfactant solution. The obtained clusters are superparamagnetic at the room temperature and the magnetic response is much faster than isolated particles. Based on the analysis of experimental and simulated results, we present a general picture describing the relationship between the heating performance of SMNP clusters and cluster's size. The profile exhibits dual peaks. The higher one located at smaller size can be attributed to the change of morphology anisotropy of cluster. Clusters in shape of dimer and trimers heat better, compared with others. The second peak is observed when the cluster loses morphology anisotropy completely and becomes anisotropy-less one. The small increase of heating efficiency should be associated with the dipole couplings. if one expects anisotropy-less clusters to heat better, SMNP with strong domain magnetization and magnetic anisotropy must be used.

Chapter 6 Study of thermal physical properties of dispersant - free Fe_3O_4 ethylene glycol - water nanofluid and enhancement of forced convective heat transfer

6.1 Introduction

Many works have been carried out to study thermo-physical properties of nanofluids[107], due to their great potential to be novel coolants for both electronic[39] and automotive components[40-44]. Their cooling efficiency mainly depends on 4 kinds of thermo-physical properties, including thermal conductivity, specific heat capacity, viscosity and density. The dispersed particles can help enhance the thermal conductivity of fluid significantly in comparison with the base liquid. [240] The heat capacity of nanofluid often decreases with using the particles with lower heat capacity.[37] Moreover, the density of nanofluid is generally higher than the base liquid. Thus, Bigdeli *et al.* [38] suggested that nanofluids may represent a way to reduce the warm up time of a cooling system, which is very beneficial for automotive applications to reduce the pollutant emissions. However, adding particles augments the viscosity of fluid, which often leads to a larger pressure drop, but also sometimes turns the liquid into non-Newtonian fluid.[55, 62] Shear thinning of nanofluids has been reported by many researchers who found that the viscosity decreased with the shear rate during rheological measurements.[55-62] Several works related shear thinning of nanofluids with particles aggregations. Aggregations also change the thermal conductivity of nanofluid in a non-monotonic way. [38] What's more, nanofluid with poor colloidal stability can bring several problems such as sedimentation and clogging of channels.

Usually, there are two strategies to stabilize particles, including steric stabilization and electrostatic stabilization.[63] The first one involves coating the particles with sufficiently large molecule (*i.e.* polymer) to prevent them from approaching too close. A coating of large organic molecule should reduce the thermal conductivity of particles. The other option is electrostatic stabilization, which relies on the electric repulsive force arising between two particles possessing charges with the same sign. According to the classic DLVO theory [119, 120] increasing the surface charges of particles will enhance electric repulsive force, thus reducing particles' tendency to aggregate. Absorption of ionic dispersants and modification of activators are the most used ways to cover the surface of particle with charged groups. Dispersants may produce foams during heating and pumping. What's more, addition of solvent with lower polarity, *i.e.* ethylene glycol could trigger desorption of dispersants[64].

Citric acid (CA) is often used as surface activators to stabilize nanoparticles in water [96-98, 125, 126]. CA is a small molecule with three carboxyl groups. It can be chemically attached onto the surface of particle via formation of coordination bond between medal atom and carboxyl group, leaving one or two carboxyl groups stretching out forward into the surrounding liquid phase.[96] These free carboxyl groups are expected to dissociate in water, generating negatively charged group COO- on the surface of a particle. It is known that a higher pH facilitates dissociation of CA. With increasing pH of particle suspension, more and more COO- groups will be generated on the surface of particle, thus resulting in an enhancement of surface potential [96-98]. In order to prevent freezing of water coolant in cold regions, ethylene glycol is often added to water to low down the freezing point. Few works were carried out to discuss the effect of pH on stability of CA modified particles in EG – water mixture.

6.2 Problem description

In this chapter, we studied the effects of particle concentration and/or colloidal stability thermo-physical properties of Fe_3O_4 EG - water nanofluid. Fe_3O_4 nanoparticles were synthesized by the co-precipitation method and then modified with CA to stabilize them in a EG - water mixture. The ratio of EG to water was kept at 1:1 (the ratio was selected by the project funder). The properties of modified particles were characterized first, including the particles' morphology, size, crystal structure, weight fraction of CA attached and density. Zeta-potential measurement and DLS measurement were carried out to estimate the stability of CA modified particles in 1:1 mixture at different pH. The density and specific heat capacity of nanofluid were measured at different particle concentration. Rheological measurements were conducted to investigate the dependence of the nanofluid's viscosity on shear rate at different pH, temperature and particle concentrations. At neutral pH, the nanofluids behaved as Newtonian fluids despite the changes in particle concentration and temperature. The nanofluids with neutral pH were kept at room temperature for one week. Rheological measurements were carried out again to see whether shear thinning recurred. A modified Krieger and Dougherty model[230] was used to explain the the effect of the size of particle aggregates on the viscosity of the nanofluids with neutral pH. We also found that the viscosity of nanofluid could be reduced further by rising up pH to weak basic condition. It is known that the pH of coolant should be carefully designed, since it has direct impact on the corrosion of radiator and tubes in automotive cooling systems: for most of the cars, pH should be maintained in the range 7.5–10.5[310]. However, increased ionic strength caused by pH adjusting will make worse the colloidal stability of particles. Therefore, pH of 8.5 was selected to prepare MNFs for investigating the increment in thermal conductivity and the enhancement of convective heat transfer efficiency. And a bunch of rheological measurements were also conducted to figure out the relationship among viscosity, particle concentration and temperature at this pH.

6.3 Results and discussion

6.3.1 Characterizations of CA modified Fe_3O_4 nanoparticles

Figure 6.1 shows the TEM image of CA modified Fe_3O_4 nanoparticles. There were few changes in the shape and size of particles after the modification. The particles were sphere-like in shape. The particle size ranged from 4 to 22 nm and the average size was about 10 nm. The XRD pattern presents the characteristic peaks of cubic inverse spinel structure, indicating that the crystal structure of Fe_3O_4 nanoparticles was also not changed (Figure 6.2). The weight fraction of modified CA was found to be about 4% by TGA measurement (Figure 6.3). Due to CA modification, the density of particles decreased to 4.36 g/cm^3, compared with that of unmodified particles, 4.51 g/cm^3. A small amount of modified and unmodified particles was added to 1:1 EG – water mixture separately to compare their stability in the mixture. As shown in Figure 6.4 a, the modified particles remained suspended in the mixture after being kept at room temperature up to 8 months, but unmodified ones already precipitated down to the vial’s bottom. After vigorous shaking, the nanofluid of CA modified particles produced little foam (Figure 6.4), since there was no surfactant in the solution. To the contrary, the one stabilized by surfactant SDS generated lots of foam.

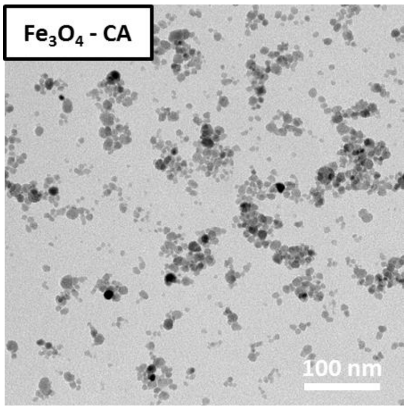

Figure 6. 1 TEM image of citric acid-modified Fe_3O_4 particles which had been dispersed in 1:1 EG - water mixture before being prepared into TEM sample.

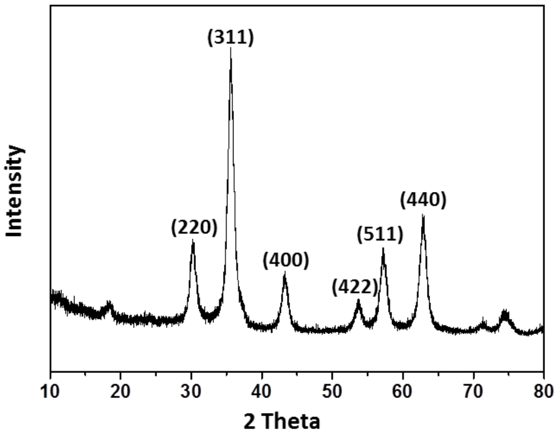

Figure 6. 2 XRD characterization of modified Fe_3O_4 nanoparticles.

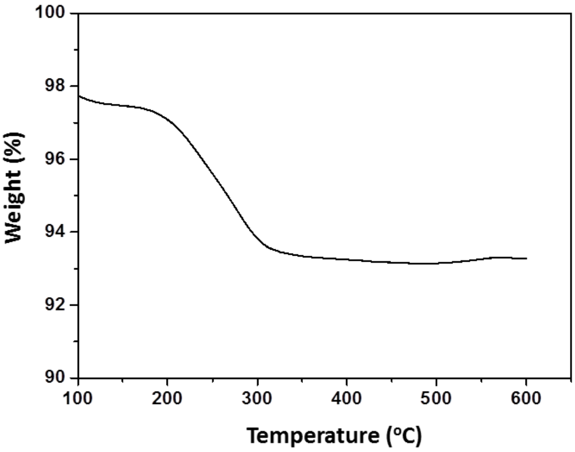

Figure 6. 3 TGA characterization of modified Fe_3O_4 nanoparticles.

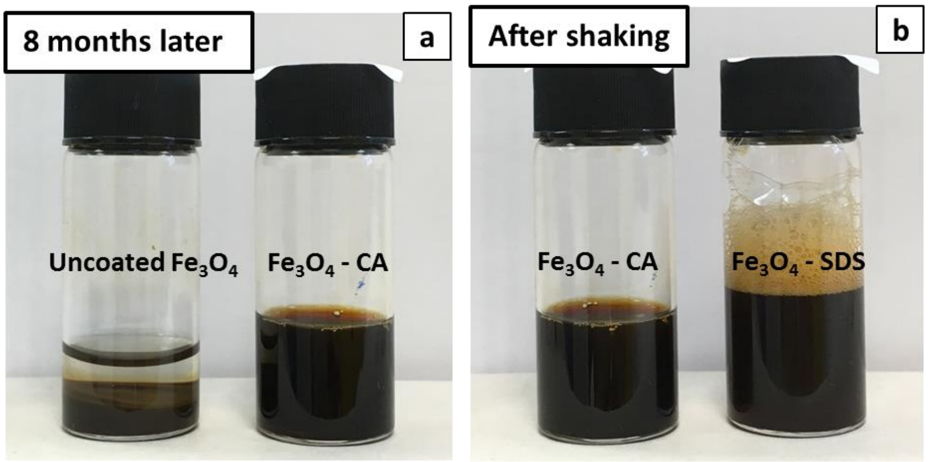

Figure 6. 4 Comparison of colloidal stability (a) and foaming (b) of naked and modified nanoparticles in 1:1 EG and water mixture.

6.3.2 Density

Figure 6.5 shows the density of nanofluid of CA modified Fe_3O_4 nanoparticles against volume fraction of particles. The pH of particle suspension was found to be 3 - 4. Since the density of modified particle is higher than that of the base liquid, which is found to be 1.0685 g/mL, the density of nanofluidis enlarged with adding more particles. The increase is slow at first and then is accelerated after the concentration is higher than 0.23 %. Usually, the density of nanofluids has been reported to be consistent with the mixing theory[187] given by,

$$\rho_{nf} = (1-\phi)\rho_{bl} + \phi\rho_s \quad (6.1)$$

where ρ_{nf} is the density of nanofluid, ϕ the volume fraction of particle, ρ_{bl} the density of base liquid and ρ_s the density of particles. The results calculated by mixing theory is also represented in Figure 6.5 as the black line. It can be seen that the experimental results are lower than those calculated. It is known that once particles undergo aggregations, the aggregates will form spherical flow units with an effective volume fraction larger than that of isolated particles. As a result, ρ_{nf} is lower than expected at each concentration. However, the maximum relative deviation is only 0.8 %. Therefore, the mixing theory is accurate enough for predicting ρ_{nf} of ferrofluid of CA modified Fe_3O_4 nanoparticles, even though the best colloidal stability has not been achieved and particles underwent aggregations (see section 6.3.4).

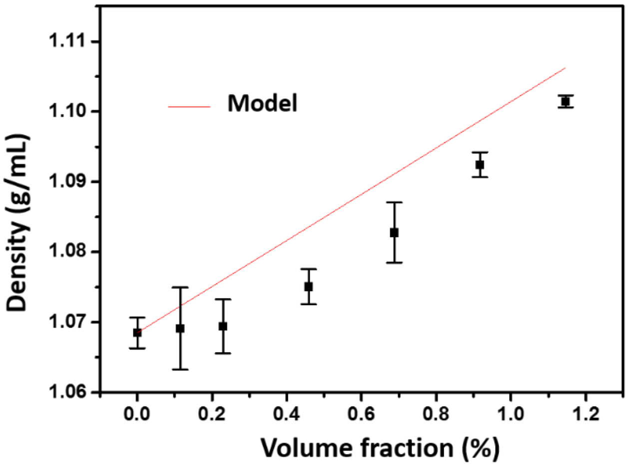

Figure 6. 5 Density of CA modified Fe_3O_4 nanofluids as a function of particle concentration.

6.3.3 Specific heat capacity

There are two models often used to predict ϕ-dependent $C_{p,nf}$.

(1) Model 1, similar to the mixing theory for ideal gas mixtures, the relationship between $C_{p,nf}$ and ϕ is[187],

$$C_{p,nf} = \phi C_{p,n} + (1-\phi) C_{p,bl} \quad (6.2)$$

where subscripts nf, n, and f refer to the nanofluid, nanoparticle and base liquid.

(2) Model II. This model is developed based on the classical and statistical mechanism.[200, 213] So it is sometimes called thermal equilibrium model.[37] Assuming that the base fluid and the nanoparticles achieve thermal equilibrium, $C_{p,nf}$ can be described as,

$$C_{p,nf} = \frac{\phi \rho_n C_{p,n} + (1-\phi)\rho_{bl} C_{p,bl}}{\phi \rho_n + (1-\phi)\rho_{bl}} \quad (6.3)$$

Where ρ_n and ρ_{bl} are the density of particle and base liquid respectively. Model 2 considers the effect of density, but model 1 doesn't. It has been suggested that this model is more fit than the Model 1 for interpreting ϕ – dependent $C_{p,nf}$. [37]

Figure 6.6 shows $C_{p,nf}$ of as-prepared nanofluid as a function of the volume fraction of modified particles. The results calculated by using Model 1 and 2 are represented as black dash and blue straight line respectively. $C_{p,n}$, $C_{p,bl}$ and $C_{p,nf}$ were measured by using a Differential Scanning Calorimeter. The details of measurement are supplied in Chapter 3. As expected, $C_{p,nf}$ decreases with particle concentration, since the $C_{p,n}$ (1.08 J/g K) is much lower than $C_{p,bl}$ (3.3

J/g K). It can be seen that model 2 fits the measured results slightly better than Model 1. The mean of the relative deviation is only 0.9 %; and for model 1, it is 1.6 %. Both are so accurate even though the best colloidal stability has not been achieved (see section 6.3.4). The reason why model 2 fits a little better has been suggested that that it gives the specific heat when the nanofluid achieves thermal equilibrium.[201] The specific heat is often given in the unit of J/g K. As a matter of fact, it must use the mass fraction of particle to relate $C_{p,nf}$ to $C_{p,n}$ and $C_{p,bl}$ rather than volume fraction. The only difference between model 2 and model 1 is that the former coverts ϕ to mass fraction. So, a better fitting is guaranteed with using Model 2.

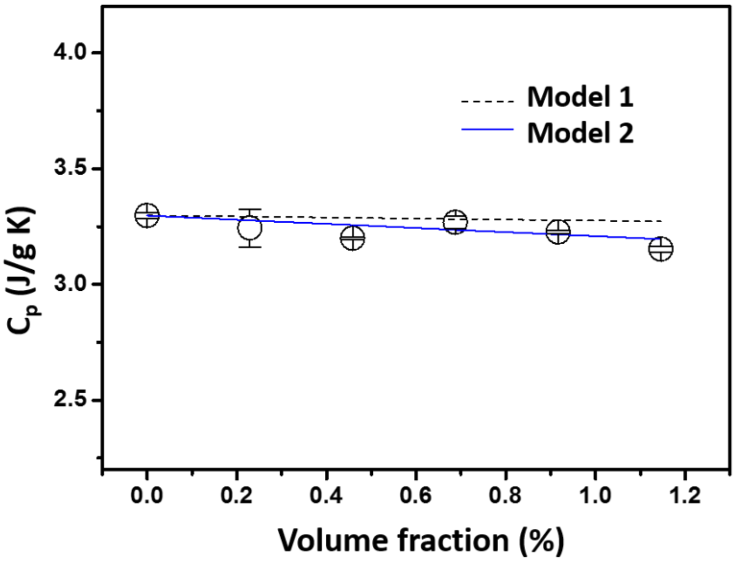

Figure 6. 6 Specific heat capacity of CA modified Fe_3O_4 nanofluids against particle concentration.

6.3.4 Viscosity

At first, the viscosity of modified Fe_3O_4 nanofluids was investigated immediately after the particles were dispersed to EG - water mixture. The volume ratio of EG and water was kept at 1:1; temperature was maintained at 30 ^oC during the measurement; shear rate was changed from 50 to 2500 s^{-1}. Figure 6.7 a shows the viscosity as a function of shear rate at different particle concentrations. As expected, the base liquid (particle volume fraction ϕ = 0) behaved as a Newtonian fluid. The mean value of viscosities obtained at different shear rates was 2.60 m Pa·s. In this work, relative standard deviation (RSD) was used particularly to quantify the amount of dispersion of viscosities obtained at different shear rate. A low RSD indicates that the viscosities obtained at different shear rates tend to be close to the mean. Such a low RSD suggests that its viscosity changes very little with shear rate. However, the fluid no longer exhibited Newtonian behaviour after particles were added. As shown in Figure 6.7 a, the viscosity kept decreasing until shear rate reached 1200 s^{-1}, for the nanofluids whose particle volume fractions were below 1 %. Then, the viscosity maintained at almost the same value as shear rate increased further to 2500 s^{-1}. Figure 6.7 b gives the decrease percentage of viscosity against ϕ. The decrease percentage is defined as $\frac{\mu_{max}-\mu_{min}}{\mu_{max}} * 100\%$. Except the base liquid, all the nanofluid exhibited apparent non-Newton behaviour. Once the ϕ exceeded 1%, the viscosity would keep decreasing all the way with shear rate (Figure 3a). It decreased by 40% when shear rate reached 2500 s^{-1} (Figure 6.7 b). The pH of nanofluids was measured before rheological measurements, and it was 3 – 4 for all particle concentrations. CA has three known acid dissociation constants pKa1 = 3.13, pKa2 = 4.76, and pKa3 = 6.40 in water. A pH of 3 – 4 is supposed to hamper the dissociations of attached CA, leading to a poor colloidal stability.

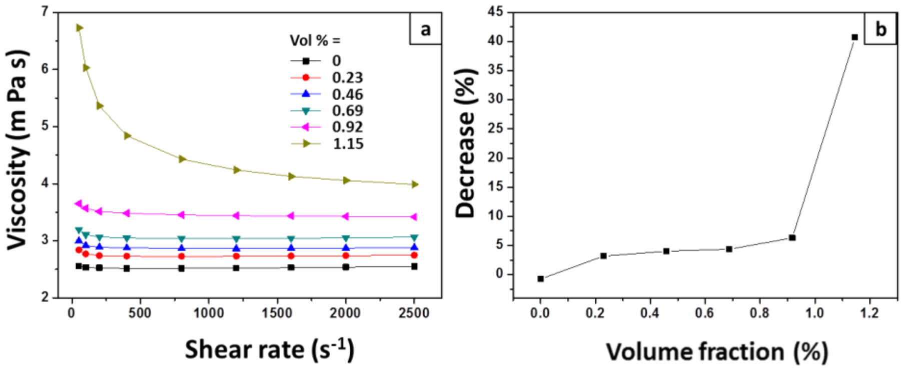

Figure 6. 7 (a) Viscosity as a function of shear rate for CA coated Fe_3O_4 nanofluids at different particle concentrations without pH adjustment. (b) Decrease percentage of viscosity at each particle concentration.

Zeta potential and DLS measurements were carried out to study the effect of pH on the colloidal stability of modified Fe_3O_4 particles in EG - water mixture. Figure 6.8 gives the zeta potential, number weighted mean hydrodynamic diameter and the size distribution of modified particles in 1:1 mixture at different pH values. At pH of 2, zeta potential was only -5.2 mV. Such a weak surface potential could not make particles repellent to each other, so particles underwent severe aggregations. A huge hydrodynamic diameter (≈ 1 μm) was observed at pH = 2 (Figure 6.8b). As increasing the pH to 5, zeta potential decreased quickly to – 33.8 mV (Figure 6.8a). More and more carboxyl groups of attached CA were turned into negatively charged groups COO-. The enhanced surface potential improved the colloidal stability and suppressed aggregations. The hydrodynamic diameter of particles decreased to 33.8 nm as pH reached 5 (Figure 6.8b). The zeta-potential of particles decreased by 15 mV as increasing pH from 5 to 7. However, a stronger surface potential did not bring a further reduction in hydrodynamic diameter for this time. The size remained at about 34 nm during the increase of pH from 5 to 9. Meanwhile, the size distribution also shows that the distribution peak shifts to lower value with increasing pH from 2 to 5, and stays at 28.2 nm for pH of 5, 7 and 9 (Figure 6.8c). Thus, at pH of 5 the particles aggregations have been suppressed to the lowest level. When pH was below 5, the particles were more inclined to undergo aggregations. The reduction of zeta potential stopped at neutral pH (Figure 6.8a). It indicates that the dissociations of carboxyl groups were completed, which suggests the best colloidal stability was obtained. Otherwise, an increase of zeta potential at pH of 11 might be related to the increased ionic strength of suspension[311, 312], caused by Na^+ added during the pH adjustment. And the decrease of the diameter at pH of 11 (Figure 6.8b) should also be caused by the increased ionic strength, which reduces the thickness of electric double layer.

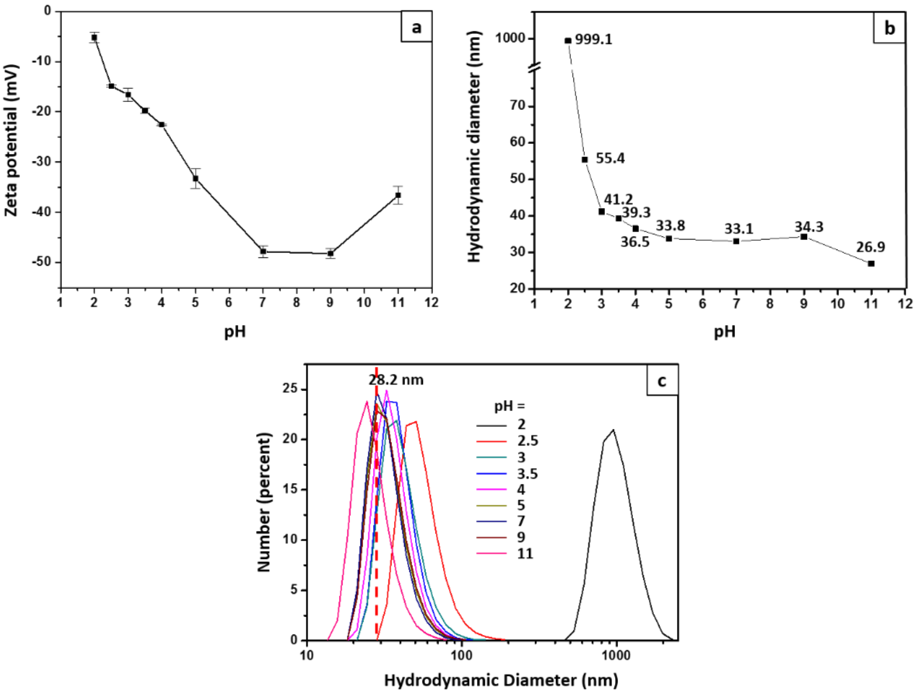

Figure 6. 8 Zeta-potential (a) and DLS (b) measurements and number weighted size distribution (c) of CA coated Fe_3O_4 particles dispersed in 1:1 EG – water mixture.

In the following, the viscosity of modified Fe_3O_4 nanofluids was studied at different pH. The particle volume fraction was fixed at 0.69 %; temperature was also set at 30 ^{o}C. As shown in Figure 6.9 a, it is very clear that the nanofluids at pH of 2.5 and 3.0 were totally Non-Newtonian fluids. The viscosity decreased by 40 % as shear rate increased to 2500 s^{-1} (Figure 6.9 b). After pH increased to 3.5 and 4.0, the decrease of viscosity stopped at 800 s^{-1}, and the decrease percentages were 7 - 9 % (Figure 6.9 b). At pH of 7 and 9, the nanofluid behaved as a Newtonian fluid. The decrease percentages were very close to 0 (Figure 6.9 b). RSDs of viscosities obtained at different shear rates were all lower than 1% for these two pH values, suggesting the viscosity changed very little with shear rate. From the discussion above, we have known that when pH was lower than 5, the colloidal stability of modified particles was improved with increasing the pH. Therefore, a better colloidal stability will make the nanofluid behave more like a Newtonian fluid.

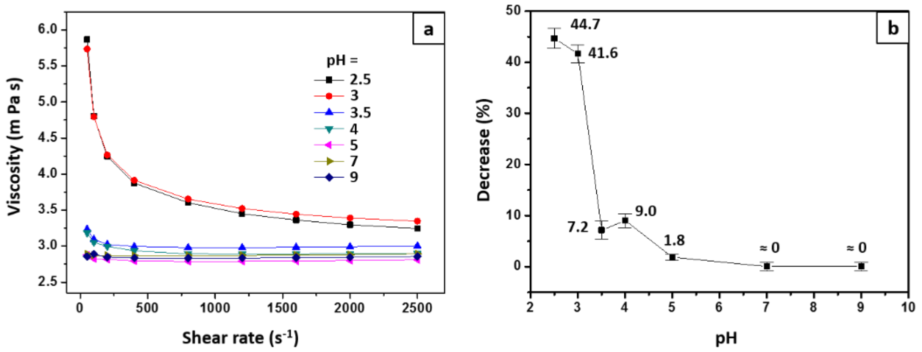

Figure 6. 9 (a) Viscosity as a function of shear rate for CA modified Fe_3O_4 nanofluids at different pH. (b) Decrease percentage of viscosity at each pH.

Otherwise, several works suggest that higher temperature could prompt particles aggregations.[231-233] Chen *et al.* [233] summarized two reasons. The most important one is that the viscosity of base liquid is lower at higher temperature, which often leads to a larger collision frequency rate among particles. So, it is naturally to expected that at higher temperature should promote shear thinning of nanofluid. However, Yu *et al.* [59, 222] found that the shear thinning of water-based aluminium nitride nanofluids and ZnO EG nanofluids became more obvious at lower temperature. We also carried out rheological measurements on CA modified Fe_3O_4 nanofluid at different temperature. The particle volume fraction was also fixed at 0.69 %. Figure 6.10 a shows the comparison of shear thinning of nanofluids whose pH adjusted to 3.5 and 7 respectively. At pH of 3.5, the nanofluid exhibited obvious shearing thinning behaviour when temperature was lowered down to 20 and to 10 °C. The viscosity decreased by about 10 %, which was slightly higher than that at 30 °C (Figure 6.10 b). Shear thinning disappeared when temperature was raised to 40 °C, but viscosity increased by 3.9 % as shear rate reached 2500 s^{-1} (Figure 6.10 b). Possibly, when the surface potential was not enough to suppress aggregations, higher temperature can promote aggregations even under shear. However, the nanofluid with neutral pH maintained Newtonian behaviour despite temperature was reduced to 10 and 20 °C or increased to 40 °C (Figure 6.10 a). The decrease percentage of viscosity was neglectable at each temperature (Figure 6.10 b), and RSDs of viscosities obtained at different shear rates were all kept below 1%. Therefore, it is so clear that optimizing the colloidal stability is key to gain Newtonian fluid at different temperature.

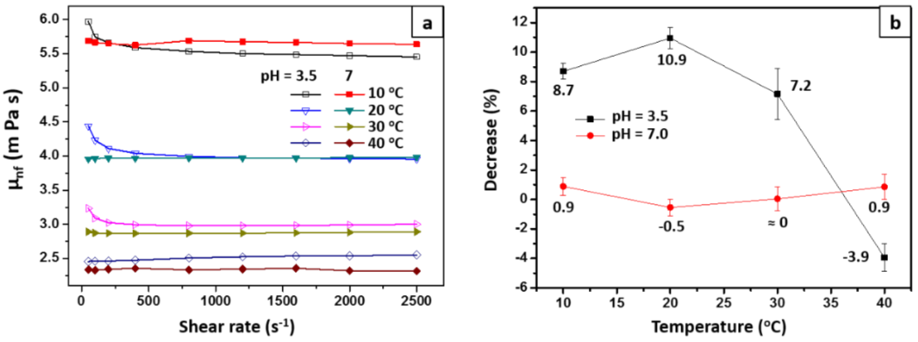

Figure 6. 10 (a) Viscosity against shear rate for CA modified Fe_3O_4 nanofluids with weakly acidic pH and neutral pH when temperature was set to 10, 20 ,30 and 40 °C. (b) Decrease percentage of viscosity at each temperature.

We investigated the effect of particle concentration on the viscosity of the nanofluids whose particles aggregations were suppressed to the lowest level. The pH of suspension was all adjusted to 7 in order to achieve completed dissociations of attached CA. During the rheological measurement temperature was still set at 30 ^{o}C. Figure 6.11 gives the decrease percentages of viscosity and RSDs of viscosities obtained at different shear rates against particle concentration. At neutral pH, the viscosity barely changed with shear rate despite of increasing the particle concentration. All the decrease percentages were very close to 0 (Figure 6.11 a), and the RSD was also kept below 1 % for each concentration (Figure 6.11 b). The rheological measurements were conducted again after the nanofluids had been kept for one week at room temperature to see whether shear thinning recurred. As a result, the nanofluids still behaved as Newtonian fluids. The decrease percentages of viscosity were very close to those found on freshly made ones (Figure 6.11 a), and no RSD was higher than 1 % (Figure 6.11 b).

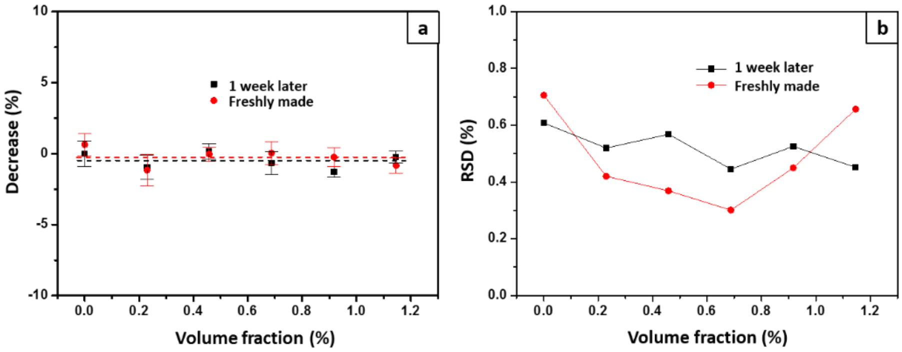

Figure 6. 11 (a) Decrease percentage of viscosity against particle concentration for CA modified Fe_3O_4 nanofluids with pH kept at 7. (b) Relative standard deviation of viscosities obtained at different shear rates against particle concentration.

Then, the mean value of viscosities obtained at different shear rates was used as the final viscosity to calculate relative viscosity $\mu_r = \mu_{nf}/\mu_{bl}$, where μ_{nf} and μ_{bl} represent the final viscosities of nanofluid and base liquid respectively. As shown in Figure 6.12, the relative viscosity increased with particle volume fraction almost linearly regardless of whether the nanofluids were freshly made or had been kept for one week. The slopes for freshly made and one - week aged nanofluids were found to be 10.9 and 13.0 respectively. It suggests that at the same particle concentration, the viscosity of one-week aged nanofluid should be 19% higher than that of freshly made one. At present, there are several models that can be used to explain a linear relationship between relative viscosity of nanofluid and particle concentration. When particle concentration is low and particles are ideally dispersed, the relative viscosity can be predicted by Einstein equation[225],

$$\mu_r = 1 + 2.5\phi \qquad (6.4)$$

Figure 6.12 shows that even though the aggregations were suppressed as much as possible, the relative viscosity of the nanofluid with neutral pH was still larger than the results predicted by Einstein equation. For aggregated particles, Krieger and Dougherty[228] proposed a semi-empirical relation to explain the relative viscosity,

$$\mu_r = (1 - \phi_a/\phi_m)^{-2.5\phi_m} \qquad (6.5)$$

where $\phi_a$is the volume fraction of aggregates and ϕ_m is the volume fraction of densely packed particles. When ϕ_a is very small, Prasher *et al.*[230] suggested that it could perform a binomial expansion to reduce equation 2 to a linear relationship $\mu_r = 1 + 2.5\phi_a$. For ideally dispersed particles, ϕ_a equals ϕ, thus the Krieger and Dougherty model is the same with Einstein equation. ϕ_a is given by $\phi_a = \phi(r_a/r_p)^{3-d_f}$, where r_a is the radius of the aggregates, r_p the radius of particles and d_f the fractal dimension of the aggregates which is around 1.8[229]. Therefore,

$$\mu_r = 1 + 2.5\phi(r_a/r_p)^{1.2} . \qquad (6.6)$$

It is easy to deduce that only when r_a barely changes with ϕ, the viscosity increases linearly with ϕ. And the slope equals,

$$Slope = 2.5(r_a/r_p)^{1.2} \qquad (6.7)$$

Substituting the slope for freshly made nanofluids into equation 6.7, r_a/r_p was calculated to be 3.4, which is very close to the value suggested by Prasher, 3.17. Since the average size of particle is 10 nm, the size of aggregates is estimated to be 34 nm, which is in good agreement with the number weighted mean hydrodynamic diameter found at pH of 7 (Figure 6.8b). For DLS measurements, the samples were diluted to 0.002 vol%. This was much lower than the concentration of nanofluid for rheological measurement. So, maximizing the surface potential is the key to suppress the aggregations. With using the same method, we found that the size of aggregates increased to 40 nm after the nanofluids had been kept for one week. Such a small augment in aggregations resulted in an about 19% of increase in viscosity for the same particle concentration. Therefore, enhancing colloidal stability to suppress aggregations is crucial to reduce the viscosity of nanofluid.

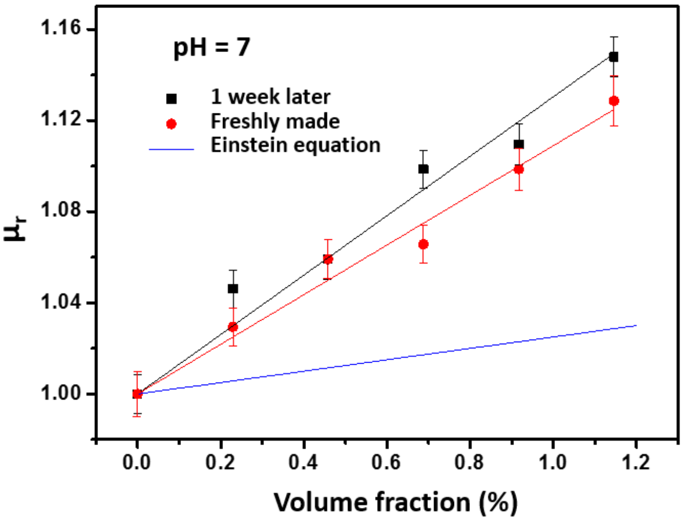

Figure 6. 12 Relative viscosity of CA modified Fe_3O_4 nanofluids against particle concentration. The pH of all nanofluids were kept at 7.

We found that the size of aggregates can be further reduced by adjusting the pH of nanofluid to weak basic. Figure 6.13 gives ϕ – dependent μ_r when pH is adjusted to 5, 7 and 8.5. Temperature was kept at 30 °C. It can be seen that a higher pH of nanofluid brings a slower increasing μ_r with ϕ. The slope decreases with pH. When the pH of particle suspension is 5, although there is no shear thinning happened, the slope increases to 14.5. By correlating equation 6, the size of aggregate is calculated to be 43 nm, which is larger than that found at neutral pH. At pH of 8.5, the line fitted is very close to the result calculated by Einstein equation. The slope is reduced to 3.91, and the size of aggregate is found to be 14.5 nm, only 4.5 nm larger than that of particle.

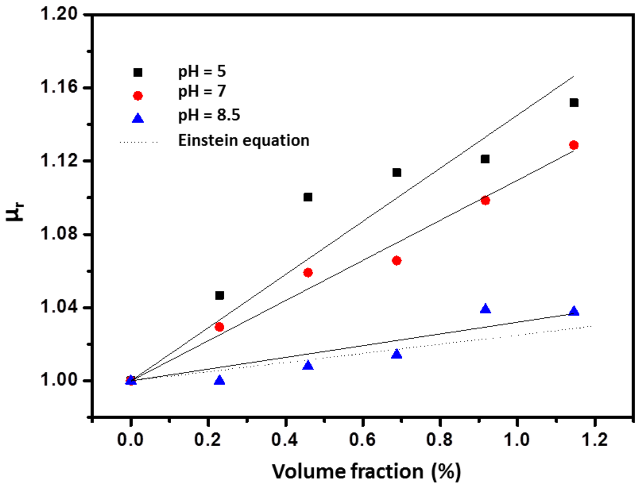

Figure 6. 13 Relative viscosity of CA modified Fe_3O_4 nanofluids against particle concentration at pH of 5, 7 and 8.5.

Generally, a liquid with lower viscosity often leads to a smaller pressure drop and helps saving pumping power. In the future work, the nanofluid of pH of 8.5 will be used for heat transfer enhancement research. A bunch of rheological measurements were conducted to show how viscosity changes with temperature and ϕ at pH of 8.5. Figure 6.14 shows μ_{nf} as a function of temperature T at different particle concentrations. The Temperature changes from 10 to 50 ^{o}C. Actually, the usual temperature of the car engine coolant at operating conditions is about 90 °C and 115 – 120 °C at maximum. However, the highest tolerant measurement temperature of the rheometer is 60 °C. Otherwise, the evaporation of the base liquid at higher temperature may cause a significant change in the particle concentration during the measurement. So the highest temperature was selected to be 50 °C. During all the measurements, the operator carefully looked at the meniscus between the cone and plate. No detectable changes were found in the shape of meniscus at the end of measurement, even though the shear rate was high as 2500 s^{-1}. So, I don't think the evaporation should be taken into considerations. The viscosity of nanofluid is reduced with rising up temperature. At lower temperature, the augment in ϕ doesn't generate a more significant increase of μ_{nf}, compared to the that occurred at higher temperature. This is so different from the results of Syam Sundar *et al.* [95]who investigated the viscosity of EG – water nanofluid of unmodified Fe_3O_4 particles.

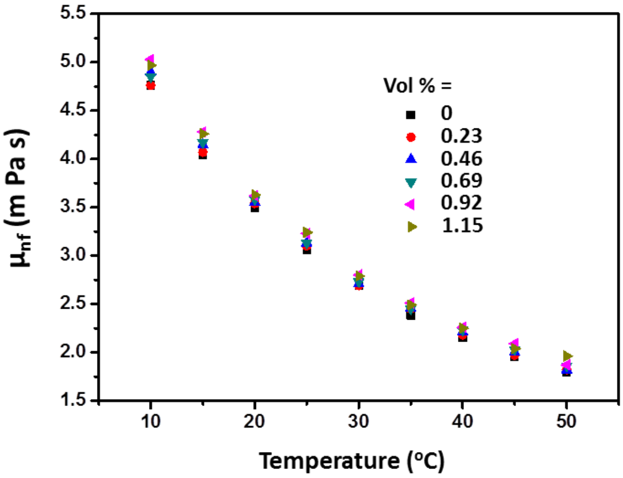

Figure 6. 14 Viscosity of CA modified Fe_3O_4 nanofluids against temperature at different particle concentration.

Figure 6.15 gives the variance of μ_{nf} against concentration at different temperature. As long as temperature is unchanged, the viscosity will increase almost linearly with ϕ. It suggests that aggregations have been suppressed successfully at each temperature. The linear relation $\mu_r = slop \cdot \phi + 1$ is used to associate viscosity and particle concentration. Figure 6.16 shows the slope C against temperature. Higher slope indicates a larger degree of aggregation. It seems that either increasing or decreasing T from 300 K will promote particles aggregations. Rising us temperature reduces the viscosity of base liquid, as a result, collision frequency rate among particles is enhanced. On the other side, lowering down temperature hampers the dissociation of CA[313]. By using polynomial fitting with order of 2, the effect of T on slope C is described as,

$$slop = 469.227T - 3.103T + 0.005T^2 \qquad (6.8)$$

Therefore,

$$\mu_{nf} = \mu_{bl}(469.227T - 3.103T + 0.005T^2) \cdot \phi + 1 \qquad (6.9)$$

For validation purpose, measure viscosities and the results calculated by equation 9 are all presented in Figure 6.17. The proposed equation is accurate for estimation of the viscosity of Fe_3O_4 nanofluid at specific temperature and particle concentration within the given range. The largest deviation is only 2.4 % and the average deviation is 0.7 %.

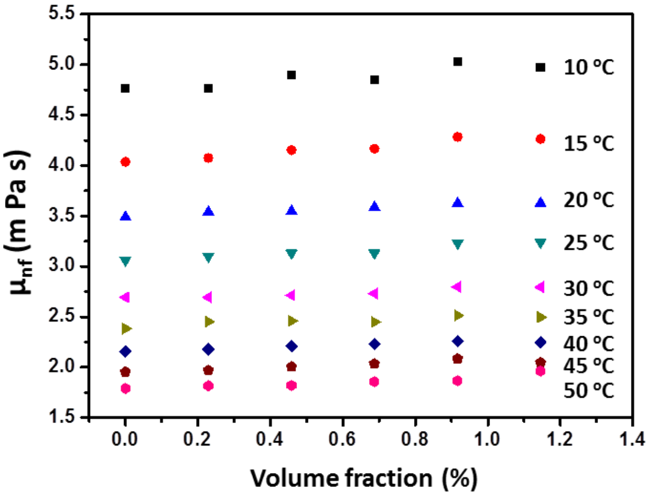

Figure 6. 15 Viscosity of CA modified Fe_3O_4 nanofluids against particle concentration at different temperature.

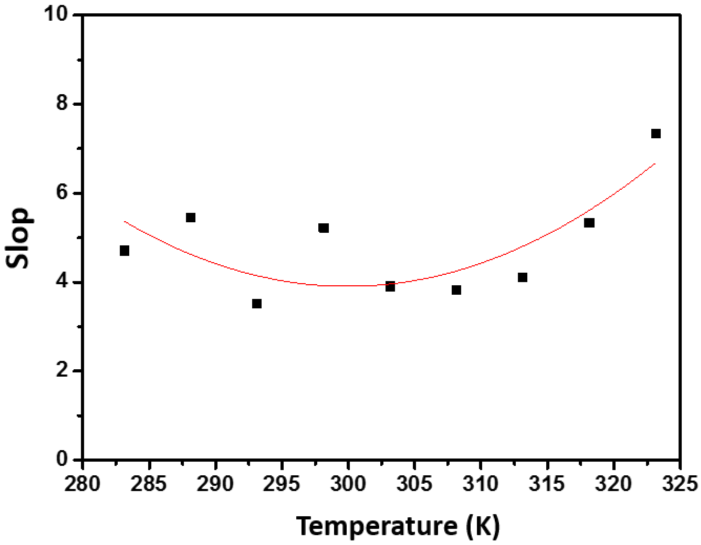

Figure 6. 16 Slope against temperature.

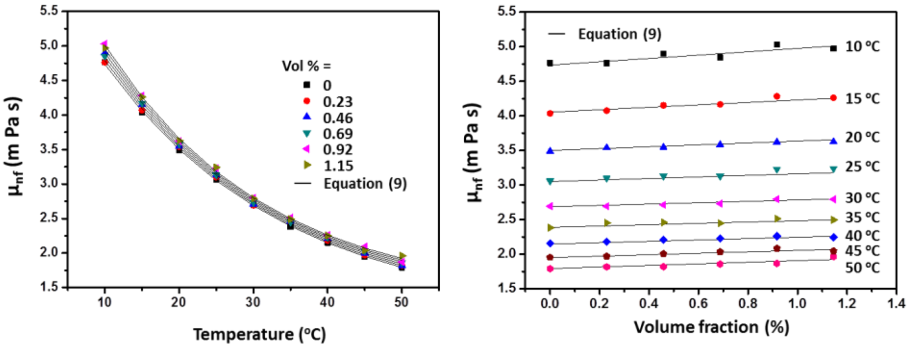

Figure 6. 17 Comparison of experimental data and developed correlation of equation 6.9.

6.3.5 Thermal conductivity

Figure 6.18 and Figure 6.19 shows thermal conductivity of nanofluid of CA modified Fe_3O_4 nanoparticles at different temperature and concentrations. Thermal conductivity is measured by transient hot-wire technology. The pH of nanofluids was all kept at 8.5. The volume fraction of particles was changed from 0 to 1.2 %. It can be seen that thermal conductivity increase with temperature as well as particle concentration. When temperature is at 30, 40, 50 and 60 ^{o}C, a 1.2 % of particle volume fraction brings 2.2, 2.3, 2.3 and 1.6 % of enhancement in thermal conductivity. Compared with reported results obtained upon Fe_3O_4 EG – water nanofluid[238], such enhancement is much lower.

At present, it is well recognized that thermal conductivity of nanofluid is mainly controlled by Kapitza resistance at the nanoparticle–fluid interface[252] and particle aggregations[53]. The latter of particular structure is able to form thermal percolation paths which work like "highway" for heat transfer.[314] Bigdeli *et al.* [38] suggested that there should be an optimum degree of aggregation to gain the best thermal conduction within nanofluid. Terrible aggregations will lead to sediment of particles, consequently, the heat conduction only accounts on the base liquid. However, when particles are ideally dispersed, no thermal percolation paths are formed to improve heat transfer. Evidences have shown that the enhancement observed on ideally dispersed particle suspension can be very little.[315] In addition, several works suggest that over using surface stabilizer (*i.e.* surfactants) also reduces thermal conductivity of nanofluid.[316]

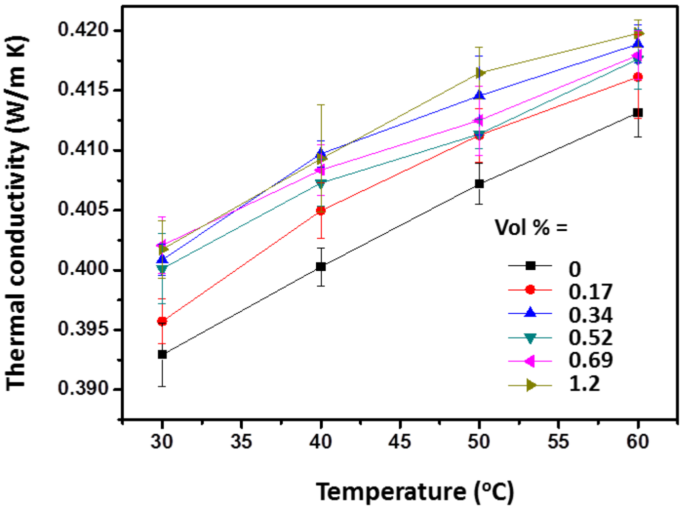

Figure 6. 18 Thermal conductivity of CA modified Fe_3O_4 nanofluids against temperature at different particle concentration.

The classic Maxwell model was used to fit the experimental data, which presumes that the nanofluid have common features with solid–liquid mixtures. The model is described as,

$$k_{nf} = k_{bl}\left[\frac{k_p+2k_{bl}+2\phi(k_p-k_{bl})}{k_p+2k_{bl}-\phi(k_p-k_{bl})}\right] \qquad (10)$$

The largest deviation between the result calculated by Maxwell model and measured one is only 1.5 %. Such a good match suggests that it won't be necessary to consider the effects including formation of solid – like "nanolayer" [249-251], interfacial thermal resistance[252] and Brownian motion[253-255] if the particle aggregations have been suppressed to the lowest level.

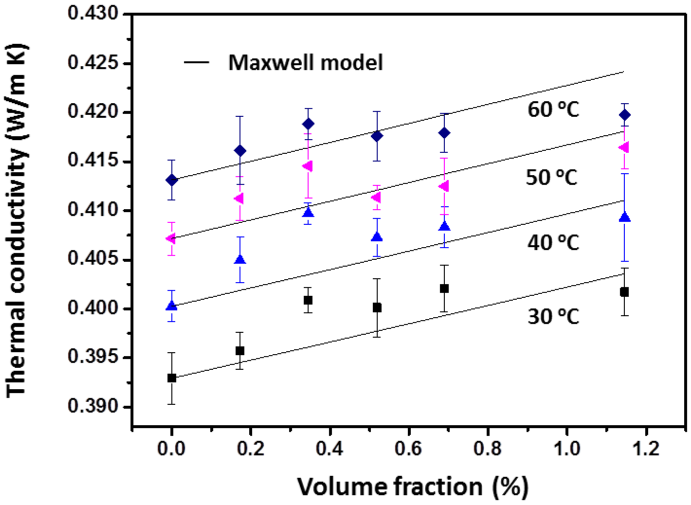

Figure 6. 19 Comparison of experimental data and Maxwell model.

6.3.6 Demonstration of convective heat transfer enhancement of ferrofluid

First, the accuracy of the rig was validated by measuring convective heat transfer characteristics of water at 40 °C. The collected data were then compared with the values calculated by Dittus – Boelter equation. The uncertainty of Re number is 3%. The average uncertainty in calculation of Nu number is 7.3 % when Re is less than 10000. As shown in Figure 6.20, the experimental results were in good agreement with the predicted values. The average deviation is 4%.

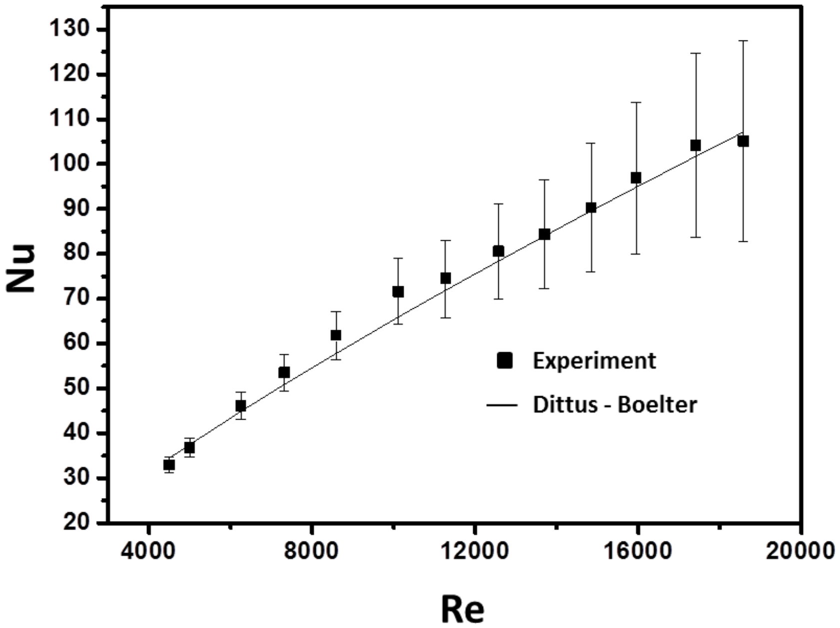

Figure 6. 20 Comparison between the experimental data of water with the ones calculated by Dittus – Boelter equation.

Then, experiments were carried out to measure the convective heat transfer coefficient h of base liquid and 0.23 vol % of MNF. The pH of MNF was adjusted to 8.5; the inlet temperature was kept at 40 °C. Figure 6.21 shows the comparison of h between base liquid and MNF at different Reynolds number. Uncertainty values had been calculated for all the measured cases. The uncertainty of Re number is 3%. The average uncertainty in calculation of convective heat transfer coefficient was 8.6 %. Most of the flow phenomena related with engineering applications are associated with turbulence, as is the coolant flow in an IC engine. To obtain a fully developed turbulent flow, Reynolds number generally should be higher than 10000. In this work, due to the limitation of pumping power, Reynolds number can only be increased to 6000.

As shown in Figure 6.21, for laminar flow (Re <2500), h of MNF is almost the same with base liquid. Once Re > 2500, h of MNF will becomes superior to base liquid. The average enhancement is found to be 11.9 % for Re > 2500. Usually, the heat transfer enhancement with using nanofluid is attributed to: first, the dispersed particles improve thermal conductivity of boundary layer; secondly, particle migration disturbs the boundary layer; thirdly, particle aggregates work like “obstacles” at the wall of pipe, which break the boundary layer, thus reinforcing local turbulence. Now, the first two reasons should be paid with more attentions since the colloidal stability of MNF has achieved the best. From the last section, it has been known that thermal conductivity increases by only 2 – 3 % as the particle concentration reaches 1 vol %. So, the increase in thermal conductivity of boundary layer wouldn’t play an important role. If particle migration is assumed to be the key factor and improve convective heat transfer by disturbance of boundary layer, the significant enhancement at transition and turbulent flow regions suggests that particle migration is facilitated by turbulent eddies.

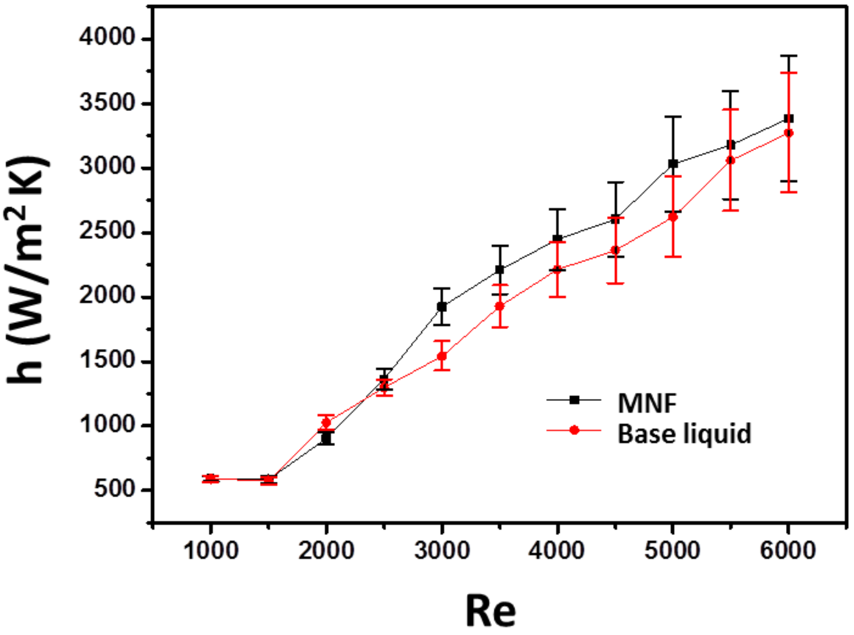

Figure 6. 21 Convective heat transfer coefficients of base liquid and MNF as a function of Re number.

6.4 Summary

In this chapter, we studied the effects of temperature, particle concentration and/or colloidal stability thermo-physical properties of Fe_3O_4 EG - water nanofluid. Fe_3O_4 nanoparticles were synthesized by co-precipitation method and then modified with CA to stabilize them in EG - water mixture. The volume ratio of EG to water was kept at 1:1. The average size of particles was about 10 nm. The effect of particle concentration on density and specific heat capacity of nanofluid can be interpreted by mixing theory and thermal equilibrium model respectively.

The colloidal stability of modified particles was improved by reducing the acidity of particle suspension. With increasing the pH to 7, the surface potential of particles kept growing stronger due to the dissociations of CA attached on the particles. As a result, the enhanced surface potential helped particles repel each other, resulting in a decrease of hydrodynamic size of particles. The particles aggregations were suppressed to the lowest level as pH reached 5. The dissociations of CA attached were completed at neutral pH, which suggests that the best colloidal stability was obtained. At neutral pH, the viscosity of Fe_3O_4 nanofluids barely changed with shear rate despite of the variance in particle concentration and temperature. Even though they were kept at room temperature for one week, the nanofluids still exhibited Newtonian behaviour. The relative viscosity of nanofluid with neutral pH increased almost linearly with particle concentration of whether they were freshly made or had been kept for one week. However, at the same particle concentration, the viscosity of one-week aged nanofluid was 19% higher than that of freshly made one. By using a reported modified Krieger and Dougherty model, we found that the size of aggregates increased very slightly by only 6 nm after one week. Therefore, optimisation of colloidal stability to suppress particles aggregations is the key to make nanofluid behave as Newtonian fluid and reduce its viscosity. The viscosity can be further decreased by increasing pH to 8.5 and the value is very close to that suggested by Einstein equation. An equation was proposed to predict estimate the viscosity of nanofluid of pH 8.5 at specific temperature and particle concentration. The average deviation is only 0.7 %.

It was found that at pH pf 8.5, thermal conductivity of nanofluid changed with particle concentration according to Maxwell model. Although the enhancement in thermal conductivity of a well- dispersed nanofluid is relatively low, smaller viscosity and better colloidal stability should be very competitive when the nanofluid is considered for convection heat transfer. In addition, once particle undergo uncontrolled aggregations, it could be difficult to predict the thermal conductivity and viscosity at a specific temperature and particle concentration. Therefore, nanofluid of pH of 8.5 was used for study of convective heat transfer. The convective heat transfer coefficient was found to be enhanced by more than 10 % for Re > 2500. The enhancement should be explained particle migration.

Chapter 7 Conclusions and future work

7.1 Conclusions

At the beginning of this doctoral research project, we numerically studied the effect of dipole interactions on hyperthermia heating SMNPs clusters in different shapes by timely quantified Monte Carlo (MC) simulations. Four typical morphologies, namely chain, cylinder, cube and sphere, are selected to shape the cluster. The following results have been obtained.

1. Standard MC with Metropolis algorithm is more suitable than Kinetic MC algorithm for simulating magnetic losses of SMNPs which have low magnetocrystalline anisotropy. It is because that the latter takes the influence of thermal flocculations into considerations only when the magnetocrystalline anisotropy is large enough.

2. Clusters with high morphology anisotropy can be expected to heat better than isolated particles as along as the direction of magnetic field is not perpendicular to the axis of morphology anisotropy. Two mechanisms: i) dipole interactions of clusters with high morphology anisotropy facilitate the magnetization process ii) dipole interactions impede the relaxations of particles' moments, because they always try to align the particles' moments to the axis of morphology anisotropy.

3. When the field intensity is strong enough to fully magnetize SMNP clusters, it will be hard to obtain enhanced heating efficiency with using anisotropy - less ones. The hysteresis loop area will become almost the same as that of non-interacting particles, regardless of the change in the direction of magnetic field. It is because the effect of dipole interactions is reduced to the minimum.

Then, we studied the effect of size on the hyperthermia heating efficiency of SMNP clusters without high morphology anisotropy at relatively low field intensity. Magnetic nanofluid of sphere-like clusters were synthesized by emulsion droplet solvent evaporation method. The size of clusters could be controlled from 70 - 130 nm. An induction heating system was set up to estimate the heating ability of the gained magnetic nanofluids. Based on the analysis of experimental and simulated results, we present a general picture describing the relationship between the heating performance of the clusters and cluster’s size. The profile should exhibit dual peaks. The higher one locates at smaller size, where the clusters should be in forms of dimers and/or trimers. The enhanced heating efficiency can be attributed to the increase of morphology anisotropy of cluster. The second peak is observed when the cluster loses morphology anisotropy completely. The small increase of heating efficiency should be associated with the dipole couplings. if one expects anisotropy-less clusters to heat better, SMNP with strong domain magnetization and magnetic anisotropy must be used.

Finally, we obtained a surfactant -free Fe_3O_4 ethylene glycol (EG) - water nanofluid with predictable thermo-physical properties. Fe_3O_4 nanoparticles were modified with citric acid to stabilize them in EG - water mixture. The colloidal stability of modified particles was controlled by changing the pH value of particle suspension. The most thermo-physical properties can be explained by classic models. The following results have been obtained.

1. The density of nanofluid at a certain particle concentration can be predicted accurately by mixing theory.

2. The specific heat of nanofluid at a certain particle concentration can be predicted accurately by thermal equilibrium model.

3. After the colloidal stability was optimized, the viscosity of magnetic nanofluids exhibited Newtonian behaviour, despite of the variance in particle concentration and temperature. The viscosity increased almost linearly with particle concentration, which can be explained by a modified Krieger and Dougherty model.

4. After the colloidal stability was optimized, thermal conductivity of nanofluid at a certain particle concentration can be predicted by Maxwell model.

7.2 Future work

1. Measurement of hyperthermia heating ability of mono-dispersed magnetic nanofluid of oleic - acid modified Fe_3O_4 nanoparticles. This result will demonstrate whether there are two peaks on the profile of hyperthermia heating efficiency of cluster against cluster's size.

2. Modelling hyperthermia heating of tumor tissue with MNF to optimize the heating plan.

3. Study of density of MNF of CA – modified particles at different pH to confirm whether colloidal stability affects the density much.

4. Study of specific heat of MNF of CA – modified particles at different pH to confirm whether colloidal stability affects the specific heat much.

5. Experimental investigation will be carried out on the convective heat transfer of MNF at higher particle concentrations and inlet temperature. It is known that particle migration becomes more significant at higher particle concentration and fluid's temperature. So, in this way, one can confirm the effect of particle migration on heat transfer process. Meanwhile, efforts will be

made to study the heat transfer process of MNF at different colloidal stability. Particle migration can be impeded by large particle aggregates. Thus, the enhancement theory regarding that particle aggregates work as obstacles at the wall of pipe can be validated.

6. The pump must be changed to investigate the convective heat transfer of MNF at Re > 10000.

7. Try to figure out a way prepare stable and surfactant-less nanofluids with using commercial products of nanoparticles. In this way, the cost of preparation will be reduced.

8. Lattice Boltzmann modelling of the role of particle migration in a forced convective heat transfer pf MNF.

9. An cooperation with Geely Automobile Holdings Ltd will be conducted to investigate the efficiency of cooling a real car engine with using the MNF.

Reference

1. Figuerola, A., Di Corato, R., Manna, L. & Pellegrino, T. From iron oxide nanoparticles towards advanced iron-based inorganic materials designed for biomedical applications. *Pharmacol. Res.* 62, 126-143 (2010).

2. Pankhurst, Q.A., Thanh, N.T.K., Jones, S.K. & Dobson, J. Progress in applications of magnetic nanoparticles in biomedicine. *J. Phys. D: Appl. Phys.* 42, 224001 (2009).

3. Hergt, R., Dutz, S., Müller, R. & Zeisberger, M. Magnetic particle hyperthermia: nanoparticle magnetism and materials development for cancer therapy. *J. Phys.: Condens. Matter* 18, S2919 (2006).

4. Laurent, S., Dutz, S., Häfeli, U.O. & Mahmoudi, M. Magnetic fluid hyperthermia: Focus on superparamagnetic iron oxide nanoparticles. *Adv. Colloid Interface Sci.* 166, 8-23 (2011).

5. Lee, J.-H. et al. Exchange-coupled magnetic nanoparticles for efficient heat induction. *Nat Nano* 6, 418-422 (2011).

6. Ivkov, R. Magnetic nanoparticle hyperthermia: A new frontier in biology and medicine? *Int. J. Hyperther.* 29, 703-705 (2013).

7. Jordan, A., Scholz, R., Wust, P., Fähling, H. & Roland, F. Magnetic fluid hyperthermia (MFH): Cancer treatment with AC magnetic field induced excitation of biocompatible superparamagnetic nanoparticles. *Journal of Magnetism and Magnetic Materials* 201, 413-419 (1999).

8. Rudolf, H., Silvio, D., Robert, M. & Matthias, Z. Magnetic particle hyperthermia: nanoparticle magnetism and materials development for cancer therapy. *J. Phys.: Condens. Matter* 18, S2919 (2006).

9. Roti Roti, J.L. Cellular responses to hyperthermia (40–46°C): Cell killing and molecular events. *International Journal of Hyperthermia* 24, 3-15 (2008).

10. Jordan, A. et al. Presentation of a new magnetic field therapy system for the treatment of human solid tumors with magnetic fluid hyperthermia. *J. Magn. Magn. Mater.* 225, 118-126 (2001).

11. Moroz, P., Jones, S.K. & Gray, B.N. Magnetically mediated hyperthermia: current status and future directions. *International Journal of Hyperthermia* 18, 267-284 (2002).

12. Maeda, H. Tumor-Selective Delivery of Macromolecular Drugs via the EPR Effect: Background and Future Prospects. *Bioconjugate Chemistry* 21, 797-802 (2010).

13. Gunnar, G. et al. The effect of field parameters, nanoparticle properties and immobilization on the specific heating power in magnetic particle hyperthermia. *Journal of Physics: Condensed Matter* 18, S2935 (2006).

14. Tanaka, K. et al. Heat immunotherapy using magnetic nanoparticles and dendritic cells for T-lymphoma. *Journal of Bioscience and Bioengineering* 100, 112-115 (2005).

15. Pankhurst, Q.A., Connolly, J., Jones, S.K. & Dobson, J. Applications of magnetic nanoparticles in biomedicine. *Journal of Physics D: Applied Physics* 36, R167 (2003).

16. Hilger, I. et al. Electromagnetic Heating of Breast Tumors in Interventional Radiology: In Vitro and in Vivo Studies in Human Cadavers and Mice. *Radiology* 218, 570-575 (2001).

17. Hartman, K., Wilson, L. & Rosenblum, M. Detecting and Treating Cancer with Nanotechnology. *Mol Diagn Ther.* 12, 1-14 (2008).

18. Franconi, C., Vrba, J., Micali, F. & Pesce, F. Prospects for radiofrequency hyperthermia applicator research. I – Pre-optimised prototypes of endocavitary applicators with matching interfaces for prostate hyperplasia and cancer treatments. *International Journal of Hyperthermia* 27, 187-198 (2011).

19. Sullivan, D.M., Ben-Yosef, R. & Kapp, D.S. Stanford 3D hyperthermia treatment planning system. Technical review and clinical summary. *International Journal of Hyperthermia* 9, 627-643 (1993).

20. Leybovicht, L.B., Myerson, R.J., Emami, B. & Straube, W.L. Evaluation of the Sigma 60 applicator for regional hyperthermia in terms of scattering parameters. *International Journal of Hyperthermia* 7, 917-935 (1991).

21. Maier-Hauff, K. et al. Intracranial Thermotherapy using Magnetic Nanoparticles Combined with External Beam Radiotherapy: Results of a Feasibility Study on Patients with Glioblastoma Multiforme. *J Neurooncol* 81, 53-60 (2007).

22. Funovics, M.A. et al. MR imaging of the her2/neu and 9.2.27 tumor antigens using immunospecific contrast agents. *Magnetic Resonance Imaging* 22, 843-850 (2004).

23. Yang, J. et al. Multifunctional Magneto-Polymeric Nanohybrids for Targeted Detection and Synergistic Therapeutic Effects on Breast Cancer. *Angewandte Chemie International Edition* 46, 8836-8839 (2007).

24. Le Renard, P.-E. et al. The in vivo performance of magnetic particle-loaded injectable, in situ gelling, carriers for the delivery of local hyperthermia. *Biomaterials* 31, 691-705 (2010).

25. Sonvico, F. et al. Folate-Conjugated Iron Oxide Nanoparticles for Solid Tumor Targeting as Potential Specific Magnetic Hyperthermia Mediators: Synthesis, Physicochemical Characterization, and in Vitro Experiments. *Bioconjugate Chemistry* 16, 1181-1188 (2005).

26. Rastogi, R. et al. Evaluation of folate conjugated pegylated thermosensitive magnetic nanocomposites for tumor imaging and therapy. *Colloids and Surfaces B: Biointerfaces* 82, 160-167 (2011).
27. Ito, A. et al. Magnetite nanoparticle-loaded anti-HER2 immunoliposomes for combination of antibody therapy with hyperthermia. *Cancer letters* 212, 167-175 (2004).
28. Shinkai, M., Suzuki, M., Iijima, S. & Kobayashi, T. Antibody-conjugated magnetoliposomes for targeting cancer cells and their application in hyperthermia. *Biotechnology and Applied Biochemistry* 21, 125-137 (1995).
29. Sawyer, C.A. et al. Modeling of temperature profile during magnetic thermotherapy for cancer treatment. *J. Appl. Phys.* 105, - (2009).
30. Johannsen, M. et al. Thermotherapy of Prostate Cancer Using Magnetic Nanoparticles: Feasibility, Imaging, and Three-Dimensional Temperature Distribution. *European Urology* 52, 1653-1662 (2007).
31. Johannsen, M. et al. Clinical hyperthermia of prostate cancer using magnetic nanoparticles: Presentation of a new interstitial technique. *International Journal of Hyperthermia* 21, 637-647 (2005).
32. Liu, T.-Y., Hu, S.-H., Liu, D.-M., Chen, S.-Y. & Chen, I.W. Biomedical nanoparticle carriers with combined thermal and magnetic responses. *Nano Today* 4, 52-65 (2009).
33. Mehdaoui, B. et al. Increase of magnetic hyperthermia efficiency due to dipolar interactions in low-anisotropy magnetic nanoparticles: Theoretical and experimental results. *Phys. Rev. B* 87, 174419 (2013).
34. Saville, S.L. et al. The formation of linear aggregates in magnetic hyperthermia: Implications on specific absorption rate and magnetic anisotropy. *J. Colloid Interface Sci.* 424, 141-151 (2014).
35. Choi, S.U.S. in ASME, Vol. 231 99 – 105 (1995).
36. Tawfik, M.M. Experimental studies of nanofluid thermal conductivity enhancement and applications: A review. *Renewable and Sustainable Energy Reviews* (2016).
37. Shahrul, I.M., Mahbubul, I.M., Khaleduzzaman, S.S., Saidur, R. & Sabri, M.F.M. A comparative review on the specific heat of nanofluids for energy perspective. *Renew. Sustainable Energy Rev.* 38, 88-98 (2014).
38. Bigdeli, M.B., Fasano, M., Cardellini, A., Chiavazzo, E. & Asinari, P. A review on the heat and mass transfer phenomena in nanofluid coolants with special focus on automotive applications. *Renew. Sustainable Energy Rev.* 60, 1615-1633 (2016).
39. Chandrasekar, M., Suresh, S. & Chandra Bose, A. Experimental studies on heat transfer and friction factor characteristics of Al2O3/water nanofluid in a circular pipe under laminar flow with wire coil inserts. *Experimental Thermal and Fluid Science* 34, 122-130 (2010).

40. Saidur, R., Leong, K.Y. & Mohammad, H.A. A review on applications and challenges of nanofluids. *Renewable and Sustainable Energy Reviews* 15, 1646-1668 (2011).

41. Corcione, M., Cianfrini, M. & Quintino, A. Optimization of laminar pipe flow using nanoparticle liquid suspensions for cooling applications. *Applied Thermal Engineering* 50, 857-867 (2013).

42. Hussein, A.M., Bakar, R.A. & Kadirgama, K. Study of forced convection nanofluid heat transfer in the automotive cooling system. *Case Studies in Thermal Engineering* 2, 50-61 (2014).

43. Ray, D.R. & Das, D.K. Superior Performance of Nanofluids in an Automotive Radiator. *Journal of Thermal Science and Engineering Applications* 6, 041002-041002-041016 (2014).

44. Amiri, A., Shanbedi, M., Chew, B.T., Kazi, S.N. & Solangi, K.H. Toward improved engine performance with crumpled nitrogen-doped graphene based water–ethylene glycol coolant. *Chemical Engineering Journal* 289, 583-595 (2016).

45. Bahiraei, M. & Hangi, M. Flow and heat transfer characteristics of magnetic nanofluids: A review. *Journal of Magnetism and Magnetic Materials* 374, 125-138 (2015).

46. Nkurikiyimfura, I., Wang, Y. & Pan, Z. Heat transfer enhancement by magnetic nanofluids—A review. *Renewable and Sustainable Energy Reviews* 21, 548-561 (2013).

47. Blums, E. Ferrofluids: Magnetically Controllable Fluids and Their Applications. (Springer-Verlag, 2002).

48. Li, Q., Xuan, Y. & Wang, J. Experimental investigations on transport properties of magnetic fluids. *Experimental Thermal and Fluid Science* 30, 109-116 (2005).

49. Afifah, A.N., Syahrullail, S. & Sidik, N.A.C. Magnetoviscous effect and thermomagnetic convection of magnetic fluid: A review. *Renewable and Sustainable Energy Reviews* 55, 1030-1040 (2016).

50. Chiu, Y.P. et al. Specific heat of magnetic fluids under a modulated magnetic field. *Journal of Applied Physics* 93, 2079-2081 (2003).

51. Azizian, R. et al. Effect of magnetic field on laminar convective heat transfer of magnetite nanofluids. *Int. J. Heat Mass Transf.* 68, 94-109 (2014).

52. Warzoha, R.J. & Fleischer, A.S. Heat flow at nanoparticle interfaces. *Nano Energy* 6, 137-158 (2014).

53. Prasher, R. et al. Effect of aggregation on thermal conduction in colloidal nanofluids. *Applied Physics Letters* 89, 143119 (2006).

54. Krichler, M. & Odenbach, S. Thermal conductivity measurements on ferrofluids with special reference to measuring arrangement. *Journal of Magnetism and Magnetic Materials* 326, 85-90 (2013).

55. Nwosu, P.N., Meyer, J. & Sharifpur, M. A Review and Parametric Investigation Into Nanofluid Viscosity Models. *J Nanotechnol Eng Med* 5, 031008-031008 (2014).
56. Zhou, S.-Q., Ni, R. & Funfschilling, D. Effects of shear rate and temperature on viscosity of alumina polyalphaolefins nanofluids. *J. Appl. Phys.* 107, 054317 (2010).
57. Pastoriza-Gallego, M.J., Lugo, L., Legido, J.L. & Piñeiro, M.M. Rheological non-Newtonian behaviour of ethylene glycol-based Fe2O3 nanofluids. *Nanoscale Res. Lett.* 6, 560 (2011).
58. Duan, F., Kwek, D. & Crivoi, A. Viscosity affected by nanoparticle aggregation in Al2O3-water nanofluids. *Nanoscale Res. Lett.* 6, 248 (2011).
59. Yu, W., Xie, H., Li, Y. & Chen, L. Experimental investigation on thermal conductivity and viscosity of aluminum nitride nanofluid. *Particuology* 9, 187-191 (2011).
60. Kulkarni, D.P., Das, D.K. & Chukwu, G.A. Temperature dependent rheological property of copper oxide nanoparticles suspension. *J. Nanosci. Nanotechnol.* 6, 1150–1154 (2006).
61. Chen, H., Ding, Y., Lapkin, A. & Fan, X. Rheological behaviour of ethylene glycol-titanate nanotube nanofluids. *J. Nanopart. Res.* 11, 1513 (2009).
62. Sharma, A.K., Tiwari, A.K. & Dixit, A.R. Rheological behaviour of nanofluids: A review. *Renew. Sustainable Energy Rev.* 53, 779-791 (2016).
63. Faraudo, J., Andreu, J.S. & Camacho, J. Understanding diluted dispersions of superparamagnetic particles under strong magnetic fields: a review of concepts, theory and simulations. *Soft Matter* 9, 6654-6664 (2013).
64. Zhuang, J., Wu, H., Yang, Y. & Cao, Y.C. Supercrystalline Colloidal Particles from Artificial Atoms. *J. Am. Chem. Soc.* 129, 14166-14167 (2007).
65. Jeong, U., Teng, X., Wang, Y., Yang, H. & Xia, Y. Superparamagnetic Colloids: Controlled Synthesis and Niche Applications. *Advanced Materials* 19, 33-60 (2007).
66. Jordan, A. et al. Inductive heating of ferrimagnetic particles and magnetic fluids: Physical evaluation of their potential for hyperthermia. *International Journal of Hyperthermia* 25, 499-511 (2009).
67. Néel, L. Théorie du traînage magnétique des ferromagnétiques en grains fins avec applications aux terres cuites. *Ann. Géophys.* 5, 99-136 (1949).
68. Leslie-Pelecky, D.L. & Rieke, R.D. Magnetic Properties of Nanostructured Materials. *Chem. Mater.* 8, 1770-1783 (1996).
69. Maaz, K. et al. Synthesis and magnetic characterization of nickel ferrite nanoparticles prepared by co-precipitation route. *J. Magn. Magn. Mater.* 321, 1838-1842 (2009).

70. Pedro, T., María del Puerto, M., Sabino, V.-V., Teresita, G.-C. & Carlos, J.S. The preparation of magnetic nanoparticles for applications in biomedicine. *J. Phys. D: Appl. Phys.* 36, R182 (2003).

71. Hanh, N., Quy, O.K., Thuy, N.P., Tung, L.D. & Spinu, L. Synthesis of cobalt ferrite nanocrystallites by the forced hydrolysis method and investigation of their magnetic properties. *Physica B: Condensed Matter* 327, 382-384 (2003).

72. Shi, Y., Ding, J. & Yin, H. CoFe2O4 nanoparticles prepared by the mechanochemical method. *J. Alloys Compd.* 308, 290-295 (2000).

73. Matsuura, H. et al. Influence of Oxidation and Size of Iron Nanoparticles on the Saturation Magnetization. *IEEE Trans. Magn.* 44, 2804-2807 (2008).

74. Berkowitz, A.E., Lahut, J.A., Jacobs, I.S., Levinson, L.M. & Forester, D.W. Spin Pinning at Ferrite-Organic Interfaces. *Phys. Rev. Lett.* 34, 594-597 (1975).

75. Berkowitz, A.E., Lahut, J. & VanBuren, C. Properties of magnetic fluid particles. *IEEE Trans. Magn.* 16, 184-190 (1980).

76. Coey, J.M.D. Noncollinear Spin Arrangement in Ultrafine Ferrimagnetic Crystallites. *Phys. Rev. Lett.* 27, 1140-1142 (1971).

77. Maaz, K., Mumtaz, A., Hasanain, S.K. & Ceylan, A. Synthesis and magnetic properties of cobalt ferrite (CoFe2O4) nanoparticles prepared by wet chemical route. *J. Magn. Magn. Mater.* 308, 289-295 (2007).

78. Nogués, J. & Schuller, I.K. Exchange bias. *J. Magn. Magn. Mater.* 192, 203-232 (1999).

79. Nogués, J. et al. Exchange bias in nanostructures. *Phys. Rep.* 422, 65-117 (2005).

80. Respaud, M. et al. Surface effects on the magnetic properties of ultrafine cobalt particles. *Phys. Rev. B* 57, 2925-2935 (1998).

81. Bødker, F., Mørup, S. & Linderoth, S. Surface effects in metallic iron nanoparticles. *Phys. Rev. Lett.* 72, 282-285 (1994).

82. Lu, A.-H., Salabas, E.L. & Schüth, F. Magnetic Nanoparticles: Synthesis, Protection, Functionalization, and Application. *Angew. Chem. Int. Ed.* 46, 1222-1244 (2007).

83. Martinez-Boubeta, C. et al. Learning from Nature to Improve the Heat Generation of Iron-Oxide Nanoparticles for Magnetic Hyperthermia Applications. *Sci. Rep.* 3 (2013).

84. Stoner, E.C. & Wohlfarth, E.P. A Mechanism of Magnetic Hysteresis in Heterogeneous Alloys. *Phil. Trans. R. Soc. Lond. A* 240, 599-642 (1948).

85. Rosensweig, R.E. Heating magnetic fluid with alternating magnetic field. *J. Magn. Magn. Mater.* 252, 370-374 (2002).

86. De Los Santos V, L. et al. Magnetic measurements of suspended functionalised ferromagnetic beads under DC applied fields. *J. Magn. Magn. Mater.* 321, 2129-2134 (2009).

87. Chakraverty, S. et al. Memory in a magnetic nanoparticle system: Polydispersity and interaction effects. *Phys. Rev. B* 71, 054401 (2005).

88. Brusentsova, T.N. & Kuznetsov, V.D. Synthesis and investigation of magnetic properties of substituted ferrite nanoparticles of spinel system Mn1−xZnx[Fe2−yLy]O4. *J. Magn. Magn. Mater.* 311, 22-25 (2007).

89. Shen, L. et al. Room-Temperature Ferromagnetism in ZnO-Encapsulated 1.9 nm FePt3 Nanoparticle–Composite Thin Films with Giant Interfacial Anisotropy. *Adv. Mater.* 25, 1639-1645 (2013).

90. Vékás, L., Bica, D. & Avdeev, M.V. Magnetic nanoparticles and concentrated magnetic nanofluids: Synthesis, properties and some applications. *China Particuology* 5, 43-49 (2007).

91. Akoh, H., Tsukasaki, Y., Yatsuya, S. & Tasaki, A. Magnetic properties of ferromagnetic ultrafine particles prepared by vacuum evaporation on running oil substrate. *Journal of Crystal Growth* 45, 495-500 (1978).

92. Tsuji, T., Iryo, K., Watanabe, N. & Tsuji, M. Preparation of silver nanoparticles by laser ablation in solution: influence of laser wavelength on particle size. *Applied Surface Science* 202, 80-85 (2002).

93. Mafuné, F., Kohno, J.-y., Takeda, Y., Kondow, T. & Sawabe, H. Structure and Stability of Silver Nanoparticles in Aqueous Solution Produced by Laser Ablation. *The Journal of Physical Chemistry B* 104, 8333-8337 (2000).

94. Jana, N.R., Chen, Y. & Peng, X. Size- and Shape-Controlled Magnetic (Cr, Mn, Fe, Co, Ni) Oxide Nanocrystals via a Simple and General Approach. *Chem. Mater.* 16, 3931-3935 (2004).

95. Syam Sundar, L., Venkata Ramana, E., Singh, M.K. & De Sousa, A.C.M. Viscosity of low volume concentrations of magnetic Fe3O4 nanoparticles dispersed in ethylene glycol and water mixture. *Chemical Physics Letters* 554, 236-242 (2012).

96. de Sousa, M.E. et al. Stability and Relaxation Mechanisms of Citric Acid Coated Magnetite Nanoparticles for Magnetic Hyperthermia. *J. Phys. Chem. C* 117, 5436-5445 (2013).

97. Campelj, S., Makovec, D. & Drofenik, M. Preparation and properties of water-based magnetic fluids. *J. Phys.: Condens. Matter* 20, 204101 (2008).

98. Nigam, S., Barick, K.C. & Bahadur, D. Development of citrate-stabilized Fe3O4 nanoparticles: Conjugation and release of doxorubicin for therapeutic applications. *J. Magn. Magn. Mater* 323, 237-243 (2011).

99. Mikhaylova, M. et al. BSA Immobilization on Amine-Functionalized Superparamagnetic Iron Oxide Nanoparticles. *Chemistry of Materials* 16, 2344-2354 (2004).

100. Sahoo, Y. et al. Alkyl Phosphonate/Phosphate Coating on Magnetite Nanoparticles: A Comparison with Fatty Acids. *Langmuir* 17, 7907-7911 (2001).

101. Griffete, N. et al. Amino covalent binding approach on iron oxide nanoparticle surface: Toward biological applications. *Colloids and Surfaces A: Physicochemical and Engineering Aspects* 415, 98-104 (2012).

102. Lu, Z., Wang, G., Zhuang, J. & Yang, W. Effects of the concentration of tetramethylammonium hydroxide peptizer on the synthesis of Fe3O4/SiO2 core/shell nanoparticles. *Colloids and Surfaces A: Physicochemical and Engineering Aspects* 278, 140-143 (2006).

103. Bee, A., Massart, R. & Neveu, S. Synthesis of very fine maghemite particles. *Journal of Magnetism and Magnetic Materials* 149, 6-9 (1995).

104. Lalatonne, Y., Richardi, J. & Pileni, M.P. Van der Waals versus dipolar forces controlling mesoscopic organizations of magnetic nanocrystals. *Nat Mater* 3, 121-125 (2004).

105. Shinoda, K. et al. Characterization of inherent clusters in water-based magnetite magnetic fluid. *J. Magn. Magn. Mater.* 252, 141-143 (2002).

106. Butter, K., Bomans, P.H.H., Frederik, P.M., Vroege, G.J. & Philipse, A.P. Direct observation of dipolar chains in iron ferrofluids by cryogenic electron microscopy. *Nat. Mater.* 2, 88-91 (2003).

107. Devendiran, D.K. & Amirtham, V.A. A review on preparation, characterization, properties and applications of nanofluids. *Renewable and Sustainable Energy Reviews* 60, 21-40 (2016).

108. Haisheng, C., Yulong, D. & Chunqing, T. Rheological behaviour of nanofluids. *New J. Phys* 9, 367 (2007).

109. Fu, R. et al. Preparation of nearly monodispersed Fe3O4/SiO2 composite particles from aggregates of Fe3O4 nanoparticles. *J. Mater. Chem.* 21, 15352-15356 (2011).

110. Yan, F., Li, J., Fu, R., Lu, Z. & Yang, W. Facile Preparation of Superparamagnetic Fe3O4/Poly(St-co-MPS)/SiO2 Composite Particles with High Magnetization by Introduction of Silanol Groups *J. Nanosci. Nanotechnol.* 9, 5874 (2009).

111. Xu, H., Cui, L., Tong, N. & Gu, H. Development of High Magnetization Fe3O4/Polystyrene/Silica Nanospheres via Combined Miniemulsion/Emulsion Polymerization. *J. Am. Chem. Soc.* 128, 15582-15583 (2006).

112. Stoian, F.D. & Holotescu, S. Experimental study of cooling enhancement using a Fe 3 O 4 magnetic nanofluid, in an applied magnetic field. *Journal of Physics: Conference Series* 547, 012044 (2014).

113. Wang, B., Wang, B., Wei, P., Wang, X. & Lou, W. Controlled synthesis and size-dependent thermal conductivity of Fe3O4 magnetic nanofluids. *Dalton Transactions* 41, 896-899 (2012).

114. Muro, E. et al. Small and Stable Sulfobetaine Zwitterionic Quantum Dots for Functional Live-Cell Imaging. *J. Am. Chem. Soc.* 132, 4556-4557 (2010).

115. Estephan, Z.G., Jaber, J.A. & Schlenoff, J.B. Zwitterion-Stabilized Silica Nanoparticles: Toward Nonstick Nano. *Langmuir* 26, 16884-16889 (2010).

116. Wei, H. et al. Compact Zwitterion-Coated Iron Oxide Nanoparticles for Biological Applications. *Nano Lett.* 12, 22-25 (2012).

117. Rouhana, L.L., Jaber, J.A. & Schlenoff, J.B. Aggregation-Resistant Water-Soluble Gold Nanoparticles. *Langmuir* 23, 12799-12801 (2007).

118. Worthen, A.J., Tran, V., Cornell, K.A., Truskett, T.M. & Johnston, K.P. Steric stabilization of nanoparticles with grafted low molecular weight ligands in highly concentrated brines including divalent ions. *Soft Matter* 12, 2025-2039 (2016).

119. Verwey, E.J.W. & Overbeek, J.T.G. Theory of the stability of lyophobic colloids. (Amsterdam : Elsevier, 1948).

120. Derjaguin, B.V., Churaev, N.V. & Muller, V.M. in Surface Forces 293-310 (Springer US, Boston, MA; 1987).

121. Elabd, Y.A. & Napadensky, E. Sulfonation and characterization of poly(styrene-isobutylene-styrene) triblock copolymers at high ion-exchange capacities. *Polymer* 45, 3037-3043 (2004).

122. Fan, H. et al. Self-Assembly of Ordered, Robust, Three-Dimensional Gold Nanocrystal/Silica Arrays. *Science* 304, 567-571 (2004).

123. Fan, H. et al. Ordered Two- and Three-Dimensional Arrays Self-Assembled from Water-Soluble Nanocrystal–Micelles. *Adv. Mater.* 17, 2587-2590 (2005).

124. Isojima, T., Suh, S.K., Vander Sande, J.B. & Hatton, T.A. Controlled Assembly of Nanoparticle Structures: Spherical and Toroidal Superlattices and Nanoparticle-Coated Polymeric Beads. *Langmuir* 25, 8292-8298 (2009).

125. Jiang, X.C., Chen, C.Y., Chen, W.M. & Yu, A.B. Role of Citric Acid in the Formation of Silver Nanoplates through a Synergistic Reduction Approach. *Langmuir* 26, 4400-4408 (2010).

126. Jeerage, K.M. et al. Citrate-stabilized gold nanoparticles as negative controls for measurements of neurite outgrowth. *Toxicol. In Vitro.* 29, 187-194 (2015).

127. Li, X., Lenhart, J.J. & Walker, H.W. Aggregation Kinetics and Dissolution of Coated Silver Nanoparticles. *Langmuir* 28, 1095-1104 (2012).

128. Pfeiffer, C. et al. Interaction of colloidal nanoparticles with their local environment: the (ionic) nanoenvironment around nanoparticles is different from bulk and determines the physico-chemical properties of the nanoparticles. *J. R. Soc. Interface* 11 (2014).

129. Rudolf, H., Silvio, D. & Michael, R. Effects of size distribution on hysteresis losses of magnetic nanoparticles for hyperthermia. *J. Phys.: Condens. Matter* 20, 385214 (2008).

130. Vallejo-Fernandez, G. et al. Mechanisms of hyperthermia in magnetic nanoparticles. *J. Phys. D: Appl. Phys.* 46, 312001 (2013).

131. Fortin, J.-P. et al. Size-Sorted Anionic Iron Oxide Nanomagnets as Colloidal Mediators for Magnetic Hyperthermia. *J. Am. Chem. Soc.* 129, 2628-2635 (2007).

132. Rudolf, H., Silvio, D. & Matthias, Z. Validity limits of the Néel relaxation model of magnetic nanoparticles for hyperthermia. *Nanotechnology* 21, 015706 (2010).

133. Bakoglidis, K.D., Simeonidis, K., Sakellari, D., Stefanou, G. & Angelakeris, M. Size-Dependent Mechanisms in AC Magnetic Hyperthermia Response of Iron-Oxide Nanoparticles. *IEEE Trans. Magn.* 48, 1320-1323 (2012).

134. Andrä, W., Häfeli, U., Hergt, R. & Misri, R. in Handbook of Magnetism and Advanced Magnetic Materials (John Wiley & Sons, Ltd, 2007).

135. Dutz, S. et al. Hysteresis losses of magnetic nanoparticle powders in the single domain size range. *J. Magn. Magn. Mater.* 308, 305-312 (2007).

136. Singh, V. & Banerjee, V. Ferromagnetism, hysteresis and enhanced heat dissipation in assemblies of superparamagnetic nanoparticles. *J. Appl. Phys.* 112, 114912 (2012).

137. Hiergeist, R. et al. Application of magnetite ferrofluids for hyperthermia. *J. Magn. Magn. Mater.* 201, 420-422 (1999).

138. Hergt, R. & Andrä, W. in Magnetism in Medicine 550-570 (Wiley-VCH Verlag GmbH & Co. KGaA, 2007).

139. Johannsen, M., Thiesen, B., Wust, P. & Jordan, A. Magnetic nanoparticle hyperthermia for prostate cancer. *Int. J. Hyperthermia* 26, 790-795 (2010).

140. Hergt, R. & Dutz, S. Magnetic particle hyperthermia—biophysical limitations of a visionary tumour therapy. *J. Magn. Magn. Mater.* 311, 187-192 (2007).

141. Andrä, W., d'Ambly, C.G., Hergt, R., Hilger, I. & Kaiser, W.A. Temperature distribution as function of time around a small spherical heat

source of local magnetic hyperthermia. *J. Magn. Magn. Mater.* 194, 197-203 (1999).

142. Jang, J.-t. et al. Critical Enhancements of MRI Contrast and Hyperthermic Effects by Dopant-Controlled Magnetic Nanoparticles. *Angew. Chem. Int. Ed.* 48, 1234-1238 (2009).

143. Salloum, M., Ma, R.H., Weeks, D. & Zhu, L. Controlling nanoparticle delivery in magnetic nanoparticle hyperthermia for cancer treatment: Experimental study in agarose gel. *Int. J. Hyperthermia* 24, 337-345 (2008).

144. Moroz, P., Jones, S.K. & Gray, B.N. Tumor response to arterial embolization hyperthermia and direct injection hyperthermia in a rabbit liver tumor model. *J. Surgical Oncol.* 80, 149-156 (2002).

145. Jordan, A. et al. Effects of Magnetic Fluid Hyperthermia (MFH) on C3H mammary carcinoma in vivo. *Int. J. Hyperthermia* 13, 587-605 (1997).

146. Mody, V. et al. Magnetic nanoparticle drug delivery systems for targeting tumor. *Appl Nanosci*, 1-8 (2013).

147. McBain, S.C., Yiu, H.H. & Dobson, J. Magnetic nanoparticles for gene and drug delivery. *Int. J. Nanomedicine* 3(2), 169-180 (2008).

148. Folkman, J. in Adv. Cancer Res., Vol. Volume 43. (eds. K. George & W. Sidney) 175-203 (Academic Press, 1985).

149. Reilly, J.P. Applied Bioelectricity: from Electrical Stimulation to Electropathology. (Springer New York, 1998).

150. Brezovich, I. Low frequency hyperthermia: capacitive and ferromagnetic
thermoseed methods. *Med. Phys. Monogr. Med. Phys.* 16, 82-111 (1988).

151. Habib, A.H., Ondeck, C.L., Chaudhary, P., Bockstaller, M.R. & McHenry, M.E. Evaluation of iron-cobalt/ferrite core-shell nanoparticles for cancer thermotherapy. *J. Appl. Phys.* 103, - (2008).

152. Mehdaoui, B. et al. Optimal Size of Nanoparticles for Magnetic Hyperthermia: A Combined Theoretical and Experimental Study. *Adv. Funct. Mater.* 21, 4573-4581 (2011).

153. Roca, A.G., Wiese, B., Timmis, J., Vallejo-Fernandez, G. & O'Grady, K. Effect of Frequency and Field Amplitude in Magnetic Hyperthermia. *IEEE Trans. Magn.* 48, 4054-4057 (2012).

154. Hergt, R. et al. Maghemite nanoparticles with very high AC-losses for application in RF-magnetic hyperthermia. *J. Magn. Magn. Mater.* 270, 345-357 (2004).

155. Serantes, D. et al. Influence of dipolar interactions on hyperthermia properties of ferromagnetic particles. *J. Appl. Phys.* 108, 073918 (2010).

156. Eiji, K. et al. Ferromagnetic nanoparticles for magnetic hyperthermia and thermoablation therapy. *J. Phys. D: Appl. Phys.* 43, 474011 (2010).

157. Kita, E. et al. Heating characteristics of ferromagnetic iron oxide nanoparticles for magnetic hyperthermia. *J. Appl. Phys.* 107, - (2010).

158. Charles, S.W. & Popplewell, J. Properties and applications of magnetic liquids. *J. EndeaVour* 6, 153-161 (1982).

159. Tripp, S.L., Pusztay, S.V., Ribbe, A.E. & Wei, A. Self-Assembly of Cobalt Nanoparticle Rings. *J. Am. Chem. Soc.* 124, 7914-7915 (2002).

160. Phenrat, T., Saleh, N., Sirk, K., Tilton, R.D. & Lowry, G.V. Aggregation and Sedimentation of Aqueous Nanoscale Zerovalent Iron Dispersions. *Environ. Sci. Technol.* 41, 284-290 (2006).

161. Klokkenburg, M. et al. Direct Imaging of Zero-Field Dipolar Structures in Colloidal Dispersions of Synthetic Magnetite. *J. Am. Chem. Soc.* 126, 16706-16707 (2004).

162. Reddy, L.H., Arias, J.L., Nicolas, J. & Couvreur, P. Magnetic Nanoparticles: Design and Characterization, Toxicity and Biocompatibility, Pharmaceutical and Biomedical Applications. *Chem. Rev.* 112, 5818-5878 (2012).

163. Muthu, M.S. & Singh, S. Targeted nanomedicines: effective treatment modalities for cancer, AIDS and brain disorders. *Nanomedicine* 4, 105-118 (2009).

164. Lu, Z. & Yin, Y. Colloidal nanoparticle clusters: functional materials by design. *Chem. Soc. Rev.* 41, 6874-6887 (2012).

165. Wang, T., LaMontagne, D., Lynch, J., Zhuang, J. & Cao, Y.C. Colloidal superparticles from nanoparticle assembly. *Chem. Soc. Rev.* 42, 2804-2823 (2013).

166. Hayashi K, N.M., Sakamoto W, Yogo T, Miki H, Ozaki S, Abe M, Matsumoto T, Ishimura K Superparamagnetic Nanoparticle Clusters for Cancer Theranostics Combining Magnetic Resonance Imaging and Hyperthermia Treatment. *Theranostics* 3, 366-376 (2013).

167. Dutz, S. et al. Ferrofluids of magnetic multicore nanoparticles for biomedical applications. *J. Magn. Magn. Mater.* 321, 1501-1504 (2009).

168. Liu, X.L. et al. Magnetic nanoparticle-loaded polymer nanospheres as magnetic hyperthermia agents. *J. Mater. Chem. B* 2, 120-128 (2014).

169. Figueiredo, W. & Schwarzacher, W. Magnetic properties of interacting nanoparticles in a triangular lattice: Monte Carlo simulations. *Phys. Rev. B* 77, 104419 (2008).

170. Weizenmann, A. & Figueiredo, W. EFFECTS OF THE DIPOLAR INTERACTION ON THE MAGNETIC PROPERTIES OF NANOPARTICLES ARRANGED IN DIFFERENT LATTICE SYMMETRIES. *Int. J. Mod. Phys. C* 23, 1240006 (2012).

171. Frankamp, B.L., Boal, A.K., Tuominen, M.T. & Rotello, V.M. Direct Control of the Magnetic Interaction between Iron Oxide Nanoparticles through

Dendrimer-Mediated Self-Assembly. *J. Am. Chem. Soc.* 127, 9731-9735 (2005).

172. Burrows, F. et al. Energy losses in interacting fine-particle magnetic composites. *J. Phys. D: Appl. Phys.* 43, 474010 (2010).

173. García-Otero, J., Porto, M., Rivas, J. & Bunde, A. Influence of Dipolar Interaction on Magnetic Properties of Ultrafine Ferromagnetic Particles. *Phys. Rev. Lett.* 84, 167-170 (2000).

174. Chen, J. et al. Collective Dipolar Interactions in Self-Assembled Magnetic Binary Nanocrystal Superlattice Membranes. *Nano Lett.* 10, 5103-5108 (2010).

175. Urtizberea, A., Natividad, E., Arizaga, A., Castro, M. & Mediano, A. Specific Absorption Rates and Magnetic Properties of Ferrofluids with Interaction Effects at Low Concentrations. *J. Phys. Chem. C* 114, 4916-4922 (2010).

176. Nowak, U. in In: Annual Review of Computational Physics IX, ed. by D. Stauffer (World Scientific, Singapore 2001 10--15 (2000).

177. Haase, C. & Nowak, U. Role of dipole-dipole interactions for hyperthermia heating of magnetic nanoparticle ensembles. *Phys. Rev. B* 85, 045435 (2012).

178. Dennis, C.L. et al. The influence of collective behavior on the magnetic and heating properties of iron oxide nanoparticles. *J. Appl. Phys.* 103, - (2008).

179. Martinez-Boubeta, C. et al. Adjustable Hyperthermia Response of Self-Assembled Ferromagnetic Fe-MgO Core–Shell Nanoparticles by Tuning Dipole–Dipole Interactions. *Adv. Funct. Mater.* 22, 3737-3744 (2012).

180. Conde-Leboran, I. et al. A Single Picture Explains Diversity of Hyperthermia Response of Magnetic Nanoparticles. *The Journal of Physical Chemistry C* 119, 15698-15706 (2015).

181. Abbasi, A.Z. et al. Magnetic Capsules for NMR Imaging: Effect of Magnetic Nanoparticles Spatial Distribution and Aggregation. *The Journal of Physical Chemistry C* 115, 6257-6264 (2011).

182. Ovejero, J.G. et al. Effects of inter- and intra-aggregate magnetic dipolar interactions on the magnetic heating efficiency of iron oxide nanoparticles. *Physical Chemistry Chemical Physics* 18, 10954-10963 (2016).

183. Varón, M. et al. Dipolar Magnetism in Ordered and Disordered Low-Dimensional Nanoparticle Assemblies. *Sci. Rep.* 3 (2013).

184. Branquinho, L.C. et al. Effect of magnetic dipolar interactions on nanoparticle heating efficiency: Implications for cancer hyperthermia. *Sci. Rep.* 3 (2013).

185. Kashevskii, B.É. Chain model of generation of heat in a solid dispersion of subdomain ferroparticles on exposure to a variable field. *J Eng Phys Thermophy* 81, 138-144 (2008).

186. Serantes, D. et al. Multiplying Magnetic Hyperthermia Response by Nanoparticle Assembling. *The Journal of Physical Chemistry C* 118, 5927-5934 (2014).

187. Pak, B.C. & Cho, Y.I. HYDRODYNAMIC AND HEAT TRANSFER STUDY OF DISPERSED FLUIDS WITH SUBMICRON METALLIC OXIDE PARTICLES. *Experimental Heat Transfer* 11, 151-170 (1998).

188. Ho, C.J., Liu, W.K., Chang, Y.S. & Lin, C.C. Natural convection heat transfer of alumina-water nanofluid in vertical square enclosures: An experimental study. *Int. J. Therm. Sc.* 49, 1345-1353 (2010).

189. Depeyrot, J. et al. Rare earth doped maghemite EDL-MF: a perspective for nanoradiotherapy? *Journal of Magnetism and Magnetic Materials* 252, 375-377 (2002).

190. Servati V, A.A., Javaherdeh, K. & Ashorynejad, H.R. Magnetic field effects on force convection flow of a nanofluid in a channel partially filled with porous media using Lattice Boltzmann Method. *Advanced Powder Technology* 25, 666-675 (2014).

191. Vajjha, R.S., Das, D.K. & Mahagaonkar, B.M. Density Measurement of Different Nanofluids and Their Comparison With Theory. *Petroleum Science and Technology* 27, 612-624 (2009).

192. Pastoriza-Gallego, M.J., Lugo, L., Legido, J.L. & Piñeiro, M.M. Enhancement of thermal conductivity and volumetric behavior of FexOy nanofluids. *J. Appl. Phys.* 110, 014309 (2011).

193. Das, S.K., Putra, N., Thiesen, P. & Roetzel, W. Temperature Dependence of Thermal Conductivity Enhancement for Nanofluids. *Journal of Heat Transfer* 125, 567-574 (2003).

194. Murshed, S.M.S., Leong, K.C. & Yang, C. Determination of the effective thermal diffusivity of nanofluids by the double hot-wire technique. *Journal of Physics D: Applied Physics* 39, 5316 (2006).

195. Venerus, D.C., Kabadi, M.S., Lee, S. & Perez-Luna, V. Study of thermal transport in nanoparticle suspensions using forced Rayleigh scattering. *Journal of Applied Physics* 100, 094310 (2006).

196. Wen, D. & Ding, Y. Experimental investigation into convective heat transfer of nanofluids at the entrance region under laminar flow conditions. *International Journal of Heat and Mass Transfer* 47, 5181-5188 (2004).

197. Ding, Y., Alias, H., Wen, D. & Williams, R.A. Heat transfer of aqueous suspensions of carbon nanotubes (CNT nanofluids). *International Journal of Heat and Mass Transfer* 49, 240-250 (2006).

198. Wen, D. & Ding, Y. Formulation of nanofluids for natural convective heat transfer applications. *International Journal of Heat and Fluid Flow* 26, 855-864 (2005).

199. Nnanna, A.G. Experimental Model of Temperature-Driven Nanofluid. *Journal of Heat Transfer* 129, 697-704 (2006).

200. Buongiorno, J. Convective Transport in Nanofluids. *Journal of Heat Transfer* 128, 240-250 (2005).

201. Zhou, S.-Q. & Ni, R. Measurement of the specific heat capacity of water-based Al2O3 nanofluid. *Appl. Phys. Lett.* 92, 093123 (2008).

202. De Robertis, E. et al. Application of the modulated temperature differential scanning calorimetry technique for the determination of the specific heat of copper nanofluids. *Applied Thermal Engineering* 41, 10-17 (2012).

203. Elias, M.M. et al. Experimental investigation on the thermo-physical properties of Al2O3 nanoparticles suspended in car radiator coolant. *International Communications in Heat and Mass Transfer* 54, 48-53 (2014).

204. Kumaresan, V. & Velraj, R. Experimental investigation of the thermo-physical properties of water–ethylene glycol mixture based CNT nanofluids. *Thermochimica Acta* 545, 180-186 (2012).

205. Saeedinia, M., Akhavan-Behabadi, M.A. & Razi, P. Thermal and rheological characteristics of CuO–Base oil nanofluid flow inside a circular tube. *Int. Commun. Heat MassTransf.* 39, 152-159 (2012).

206. Wang, B.-X., Zhou, L.-P. & Peng, X.-F. Surface and Size Effects on the Specific Heat Capacity of Nanoparticles. *Int. J. Thermophys.* 27, 139-151 (2006).

207. He, Q., Wang, S., Tong, M. & Liu, Y. Experimental study on thermophysical properties of nanofluids as phase-change material (PCM) in low temperature cool storage. *Energy Conversion and Management* 64, 199-205 (2012).

208. Vajjha, R.S. & Das, D.K. Specific Heat Measurement of Three Nanofluids and Development of New Correlations. *Journal of Heat Transfer* 131, 071601-071601-071607 (2009).

209. Amrollahi, A., Hamidi, A.A. & Rashidi, A.M. The effects of temperature, volume fraction and vibration time on the thermo-physical properties of a carbon nanotube suspension (carbon nanofluid). *Nanotechnology* 19, 315701 (2008).

210. Saeedinia, M., Akhavan-Behabadi, M.A. & Nasr, M. Experimental study on heat transfer and pressure drop of nanofluid flow in a horizontal coiled wire inserted tube under constant heat flux. *Experimental Thermal and Fluid Science* 36, 158-168 (2012).

211. Shin, D. & Banerjee, D. Enhancement of specific heat capacity of high-temperature silica-nanofluids synthesized in alkali chloride salt eutectics for solar thermal-energy storage applications. *I. J. Heat Mass Transfer* 54, 1064-1070 (2011).

212. Xuan, Y. & Roetzel, W. Conceptions for heat transfer correlation of nanofluids. *Int. J. Heat MassTransfer* 43, 3701-3707 (2000).

213. Avsec, J. & Oblak, M. The calculation of thermal conductivity, viscosity and thermodynamic properties for nanofluids on the basis of statistical nanomechanics. *International Journal of Heat and Mass Transfer* 50, 4331-4341 (2007).

214. Vajjha, R.S. & Das, D.K. A review and analysis on influence of temperature and concentration of nanofluids on thermophysical properties, heat transfer and pumping power. *International Journal of Heat and Mass Transfer* 55, 4063-4078 (2012).

215. Fakoor Pakdaman, M., Akhavan-Behabadi, M.A. & Razi, P. An experimental investigation on thermo-physical properties and overall performance of MWCNT/heat transfer oil nanofluid flow inside vertical helically coiled tubes. *Experimental Thermal and Fluid Science* 40, 103-111 (2012).

216. Chiu, Y.P. et al. Specific heat of magnetic fluids under a modulated magnetic field. *J. Appl. Phys.* 93, 2079-2081 (2003).

217. Yu, W., France, D.M., Routbort, J.L. & Choi, S.U.S. Review and Comparison of Nanofluid Thermal Conductivity and Heat Transfer Enhancements. *Heat Transf. Eng.* 29, 432-460 (2008).

218. Tiwari, A.K., Ghosh, P. & Sarkar, J. Heat transfer and pressure drop characteristics of CeO2/water nanofluid in plate heat exchanger. *Appl.Therm. Eng.* 57, 24-32 (2013).

219. Chen, H. & Ding, Y. in Advances in Transport Phenomena: 2009. (ed. L. Wang) 135-177 (Springer Berlin Heidelberg, Berlin, Heidelberg; 2009).

220. Bayat, J. & Nikseresht, A.H. Thermal performance and pressure drop analysis of nanofluids in turbulent forced convective flows. *Int. J. Therm. Sci.* 60, 236-243 (2012).

221. Duan, F., Wong, T.F. & Crivoi, A. Dynamic viscosity measurement in non-Newtonian graphite nanofluids. *Nanoscale Res Lett* 7, 360 (2012).

222. Yu, W., Xie, H., Chen, L. & Li, Y. Investigation of thermal conductivity and viscosity of ethylene glycol based ZnO nanofluid. *Thermochimica Acta* 491, 92-96 (2009).

223. Moghaddam, M.B., Goharshadi, E.K., Entezari, M.H. & Nancarrow, P. Preparation, characterization, and rheological properties of graphene–glycerol nanofluids. *Chem. Eng. J.* 231, 365-372 (2013).

224. Kole, M. & Dey, T.K. Effect of aggregation on the viscosity of copper oxide–gear oil nanofluids. *Int. J. Therm. Sci.* 50, 1741-1747 (2011).

225. Einstein, A. Eine neue Bestimmung der Moleküldimensionen. *Annalen der Physik* 324, 289-306 (1906).

226. Brinkman, H.C. The Viscosity of Concentrated Suspensions and Solutions. *J. Chem. Phys.* 20, 571-571 (1952).
227. Batchelor, G.K. The effect of Brownian motion on the bulk stress in a suspension of spherical particles. *J. Fluid Mech.* 83, 97-117 (1977).
228. Krieger, I.M. & Dougherty, T.J. A Mechanism for Non‐Newtonian Flow in Suspensions of Rigid Spheres. *Trans. Soc. Rheol.* 3, 137-152 (1959).
229. Prasher, R., Phelan, P.E. & Bhattacharya, P. Effect of Aggregation Kinetics on the Thermal Conductivity of Nanoscale Colloidal Solutions (Nanofluid). *Nano Lett.* 6, 1529-1534 (2006).
230. Prasher, R., Song, D., Wang, J. & Phelan, P. Measurements of nanofluid viscosity and its implications for thermal applications. *Appl. Phys. Lett.* 89, 133108 (2006).
231. Dutta, A., Paul, A. & Chattopadhyay, A. The effect of temperature on the aggregation kinetics of partially bare gold nanoparticles. *RSC Adv.* 6, 82138-82149 (2016).
232. Jia, Z., Wu, H., Xie & Morbidelli, M. Effect of Temperature and Surfactant Type on the Stability and Aggregation Behavior of Styrene−Acrylate Copolymer Colloids. *Langmuir* 23, 10323-10332 (2007).
233. Chen, Y.S., Huang, Y. & Li, K.G. Temperature Effect on the Aggregation Kinetics of CeO2 Nanoparticles in Monovalent and Divalent Electrolytes. *J. Environ. Anal. Toxicol.* 2:, 158 (2012).
234. Namburu, P.K., Kulkarni, D.P., Misra, D. & Das, D.K. Viscosity of copper oxide nanoparticles dispersed in ethylene glycol and water mixture. *Exp. Thermal Fluid Sci.* 32, 397-402 (2007).
235. Motozawa, M., Chang, J., Sawada, T. & Kawaguchi, Y. Effect of magnetic field on heat transfer in rectangular duct flow of a magnetic fluid. *Phys. Proc.* 9, 190-193 (2010).
236. Lajvardi, M. et al. Experimental investigation for enhanced ferrofluid heat transfer under magnetic field effect. *J. Magn. Magn. Mater.* 322, 3508-3513 (2010).
237. Abareshi, M., Goharshadi, E.K., Mojtaba Zebarjad, S., Khandan Fadafan, H. & Youssefi, A. Fabrication, characterization and measurement of thermal conductivity of Fe3O4 nanofluids. *J. Magn. Magn. Mater.* 322, 3895-3901 (2010).
238. Sundar, L.S., Singh, M.K. & Sousa, A.C.M. Thermal conductivity of ethylene glycol and water mixture based Fe3O4 nanofluid. *Int. J. Heat Mass Transf.* 49, 17-24 (2013).
239. Hamilton, R.L. & Crosser, O.K. Thermal Conductivity of Heterogeneous Two-Component Systems. *Ind. Eng. Chem. Fundamen.* 1, 187-191 (1962).

240. Azmi, W.H., Sharma, K.V., Mamat, R., Najafi, G. & Mohamad, M.S. The enhancement of effective thermal conductivity and effective dynamic viscosity of nanofluids – A review. *Renew. Sustainable Energy Rev.* 53, 1046-1058 (2016).

241. Bruggeman, D.A.G. Berechnung verschiedener physikalischer Konstanten von heterogenen Substanzen. II. Dielektrizitätskonstanten und Leitfähigkeiten von Vielkristallen der nichtregulären Systeme. *Annalen der Physik* 417, 645-672 (1936).

242. Pang, C., Lee, J.W., Hong, H. & Kang, Y.T. Heat conduction mechanism in nanofluids. *J. Mech. Sci. Technol.* 28, 2925-2936 (2014).

243. Khanafer, K. & Vafai, K. A critical synthesis of thermophysical characteristics of nanofluids. *Int. J. Heat Mass Transf.* 54, 4410-4428 (2011).

244. Murshed, S.M.S., Leong, K.C. & Yang, C. Investigations of thermal conductivity and viscosity of nanofluids. *Int. J. Therm. Sci.* 47, 560-568 (2008).

245. Duangthongsuk, W. & Wongwises, S. Measurement of temperature-dependent thermal conductivity and viscosity of TiO2-water nanofluids. *Exp.Therm. Fluid Sci.* 33, 706-714 (2009).

246. Patel, H.E., Sundararajan, T. & Das, S.K. An experimental investigation into the thermal conductivity enhancement in oxide and metallic nanofluids. *J. Nanopart. Res.* 12, 1015-1031 (2010).

247. Corcione, M. Rayleigh-Bénard convection heat transfer in nanoparticle suspensions. *Int. J. Heat Fluid Flow* 32, 65-77 (2011).

248. Wang, X., Xu, X. & S. Choi, S.U. Thermal Conductivity of Nanoparticle - Fluid Mixture. *J. Thermophys Heat Transfer* 13, 474-480 (1999).

249. Jiang, H., Li, H., Xu, Q. & Shi, L. Effective thermal conductivity of nanofluids considering interfacial nano-shells. *Mater. Chem. Phys.* 148, 195-200 (2014).

250. Yu, W. & Choi, S.U.S. The Role of Interfacial Layers in the Enhanced Thermal Conductivity of Nanofluids: A Renovated Maxwell Model. *J. Nanopart. Res.* 5, 167-171 (2003).

251. Yu, W. & Choi, S.U.S. The role of interfacial layers in the enhanced thermal conductivity of nanofluids: A renovated Hamilton–Crosser model. *J. Nanopart. Res.* 6, 355-361 (2004).

252. Nan, C.-W., Birringer, R., Clarke, D.R. & Gleiter, H. Effective thermal conductivity of particulate composites with interfacial thermal resistance. *J. Appl. Phys.* 81, 6692-6699 (1997).

253. Jang, S.P. & Choi, S.U.S. Role of Brownian motion in the enhanced thermal conductivity of nanofluids. *Appl. Phys. Lett.* 84, 4316-4318 (2004).

254. Koo, J. & Kleinstreuer, C. A new thermal conductivity model for nanofluids. *J. Nanopart. Res.* 6, 577-588 (2004).

255. Koo, J. & Kleinstreuer, C. Impact analysis of nanoparticle motion mechanisms on the thermal conductivity of nanofluids. *Int. Commun. Heat Mass Transf.* 32, 1111-1118 (2005).

256. Özerinç, S., Kakaç, S. & Yazıcıoğlu, A.G. Enhanced thermal conductivity of nanofluids: a state-of-the-art review. *Microfluid Nanofluid* 8, 145-170 (2010).

257. Keblinski, P., Phillpot, S.R., Choi, S.U.S. & Eastman, J.A. Mechanisms of heat flow in suspensions of nano-sized particles (nanofluids). *Int. J. Heat Mass Trans.* 45, 855-863 (2002).

258. Tawfik, M.M. Experimental studies of nanofluid thermal conductivity enhancement and applications: A review. *Renew. Sustainable Energy Rev.* (2016).

259. John, P., Shima, P.D. & Baldev, R. Evidence for enhanced thermal conduction through percolating structures in nanofluids. *Nanotechnology* 19, 305706 (2008).

260. Shima, P.D., Philip, J. & Raj, B. Role of microconvection induced by Brownian motion of nanoparticles in the enhanced thermal conductivity of stable nanofluids. *Appl. Phys. Lett.* 94, 223101 (2009).

261. Gavili, A., Zabihi, F., Isfahani, T.D. & Sabbaghzadeh, J. The thermal conductivity of water base ferrofluids under magnetic field. *Exp.Therm. Fluid Sci.* 41, 94-98 (2012).

262. Philip, J., Shima, P.D. & Raj, B. Enhancement of thermal conductivity in magnetite based nanofluid due to chainlike structures. *Appl. Phys. Lett.* 91, 203108 (2007).

263. Xuan, Y., Li, Q. & Hu, W. Aggregation structure and thermal conductivity of nanofluids. *AIChE Journal* 49, 1038-1043 (2003).

264. Keblinski, P., Eastman, J.A. & Cahill, D.G. Nanofluids for thermal transport. *Mater. Today* 8, 36-44 (2005).

265. Xuan, Y. & Li, Q. Investigation on Convective Heat Transfer and Flow Features of Nanofluids. *J. Heat Transfer* 125, 151-155 (2003).

266. Vanaki, S.M., Ganesan, P. & Mohammed, H.A. Numerical study of convective heat transfer of nanofluids: A review. *Renew. Sustainable Energy Rev.* 54, 1212-1239 (2016).

267. Sohn, C.H. & Kihm, K.D. Nonhomogenous modeling of nanofluidic energy transport accounting for the thermophoretic migration of nanoparticles inside laminar pipe flows. *J. Korean Phys. Soc.* 55, 2200 (2009).

268. Bahiraei, M. & Hosseinalipour, S.M. Particle migration in nanofluids considering thermophoresis and its effect on convective heat transfer. *Thermochimica Acta* 574, 47-54 (2013).

269. Heyhat, M.M. & Kowsary, F. Effect of Particle Migration on Flow and Convective Heat Transfer of Nanofluids Flowing Through a Circular Pipe. *J. Heat Transfer* 132, 062401-062401-062409 (2010).

270. Ryzhkov, I.I. & Minakov, A.V. The effect of nanoparticle diffusion and thermophoresis on convective heat transfer of nanofluid in a circular tube. *Int. J. Heat Mass Transf.* 77, 956-969 (2014).

271. Hong, J. in Faculty of Engineering, Vol. PhD (the University of Nottingham, Nottingham; 2016).

272. Yu, W. et al. Heat transfer to a silicon carbide/water nanofluid. *Int. J. Heat Mass Transf.* 52, 3606-3612 (2009).

273. Goharkhah, M., Salarian, A., Ashjaee, M. & Shahabadi, M. Convective heat transfer characteristics of magnetite nanofluid under the influence of constant and alternating magnetic field. *Powder Technology* 274, 258-267 (2015).

274. Shahsavar, A., Saghafian, M., Salimpour, M.R. & Shafii, M.B. Experimental investigation on laminar forced convective heat transfer of ferrofluid loaded with carbon nanotubes under constant and alternating magnetic fields. *Exp. Thermal Fluid Sci.* 76, 1-11 (2016).

275. Sha, L., Ju, Y., Zhang, H. & Wang, J. Experimental investigation on the convective heat transfer of Fe3O4/water nanofluids under constant magnetic field. *Appl. Therm. Eng.* 113, 566-574 (2017).

276. Ghofrani, A., Dibaei, M.H., Hakim Sima, A. & Shafii, M.B. Experimental investigation on laminar forced convection heat transfer of ferrofluids under an alternating magnetic field. *Exp. Therm. Fluid Sci.* 49, 193-200 (2013).

277. Yarahmadi, M., Moazami Goudarzi, H. & Shafii, M.B. Experimental investigation into laminar forced convective heat transfer of ferrofluids under constant and oscillating magnetic field with different magnetic field arrangements and oscillation modes. *Exp. Therm. Fluid Sci.* 68, 601-611 (2015).

278. Ge, J. & Yin, Y. Magnetically responsive colloidal photonic crystals. *J. Mater. Chem.* 18, 5041-5045 (2008).

279. Wang, T. et al. Shape-Controlled Synthesis of Colloidal Superparticles from Nanocubes. *J. Am. Chem. Soc.* 134, 18225-18228 (2012).

280. Hayashi, K. et al. Superparamagnetic Nanoparticle Clusters for Cancer Theranostics Combining Magnetic Resonance Imaging and Hyperthermia Treatment. *Theranostics* 3, 366-376 (2013).

281. Chantrell, R.W., Walmsley, N., Gore, J. & Maylin, M. Calculations of the susceptibility of interacting superparamagnetic particles. *Physical Review B* 63, 024410 (2000).

282. Sieder, E.N. & Tate, G.E. Heat Transfer and Pressure Drop of Liquids in Tubes. *Ind. Eng. Chem.* 28, 1429-1435 (1936).

283. Moffat, R.J. Describing the uncertainties in experimental results. *Exp. Therm. Fluid Sci.* 1, 3-17 (1988).

284. Carrey, J., Mehdaoui, B. & Respaud, M. Simple models for dynamic hysteresis loop calculations of magnetic single-domain nanoparticles: Application to magnetic hyperthermia optimization. *J. Appl. Phys.* 109, 083921 (2011).

285. Ma, M. et al. Size dependence of specific power absorption of Fe3O4 particles in AC magnetic field. *J. Magn. Magn. Mater.* 268, 33-39 (2004).

286. Kita, E. et al. Ferromagnetic nanoparticles for magnetic hyperthermia and thermoablation therapy. *J. Phys. D: Appl. Phys.* 43, 474011 (2010).

287. Hergt, R., Dutz, S. & Röder, M. Effects of size distribution on hysteresis losses of magnetic nanoparticles for hyperthermia. *J. Phys.: Condens. Matter* 20, 385214 (2008).

288. Hergt, R., Dutz, S. & Zeisberger, M. Validity limits of the Néel relaxation model of magnetic nanoparticles for hyperthermia. *Nanotechnology* 21, 015706 (2010).

289. Garc et al. Influence of the cubic anisotropy constants on the hysteresis loops of single-domain particles: A Monte Carlo study. *J. Appl. Phys.* 85, 2287-2292 (1999).

290. Tan, R.P., Carrey, J. & Respaud, M. Magnetic hyperthermia properties of nanoparticles inside lysosomes using kinetic Monte Carlo simulations: Influence of key parameters and dipolar interactions, and evidence for strong spatial variation of heating power. *Phys. Rev. B* 90, 214421 (2014).

291. Ruta, S., Chantrell, R. & Hovorka, O. Unified model of hyperthermia via hysteresis heating in systems of interacting magnetic nanoparticles. *Sci. Rep.* 5, 9090 (2015).

292. Nowak, U., Chantrell, R.W. & Kennedy, E.C. Monte Carlo Simulation with Time Step Quantification in Terms of Langevin Dynamics. *Phys. Rev. Lett.* 84, 163-166 (2000).

293. Cheng, X.Z., Jalil, M.B.A., Lee, H.K. & Okabe, Y. Mapping the Monte~Carlo Scheme to Langevin Dynamics: A Fokker-Planck Approach. *Phys. Rev. Lett.* 96, 067208 (2006).

294. Melenev, P.V., Raikher, Y.L., Rusakov, V.V. & Perzynski, R. Modeling the magnetization kinetics of ferromagnetic particles by the Monte Carlo method. *Math Models Comput Simul* 4, 471-483 (2012).

295. Fry, D., Mohammad, A., Chakrabarti, A. & Sorensen, C.M. Cluster Shape Anisotropy in Irreversibly Aggregating Particulate Systems. *Langmuir* 20, 7871-7879 (2004).

296. Stoner, E.C. & Wohlfarth, E.P. A mechanism of magnetic hysteresis in heterogeneous alloys. *IEEE Trans. Magn.* 27, 3475-3518 (1991).

297. Benkoski, J.J. et al. Dipolar assembly of ferromagnetic nanoparticles into magnetically driven artificial cilia. *Soft Matter* 6, 602-609 (2010).

298. Varón, M. et al. Dipolar Driven Spontaneous Self Assembly of Superparamagnetic Co Nanoparticles into Micrometric Rice-Grain like Structures. *Langmuir* 26, 109-116 (2010).

299. Wang, T., Wang, X., LaMontagne, D., Wang, Z. & Cao, Y.C. Macroscale Lateral Alignment of Semiconductor Nanorods into Freestanding Thin Films. *Journal of the American Chemical Society* 135, 6022-6025 (2013).

300. Kobayashi, M., Seki, M., Tabata, H., Watanabe, Y. & Yamashita, I. Fabrication of Aligned Magnetic Nanoparticles Using Tobamoviruses. *Nano Letters* 10, 773-776 (2010).

301. Itoh, H. & Sugimoto, T. Systematic control of size, shape, structure, and magnetic properties of uniform magnetite and maghemite particles. *J Colloid Interface Sci* 265, 283-295 (2003).

302. Sun, J. et al. Synthesis and characterization of biocompatible Fe3O4 nanoparticles. *J Biomed Mater Res A.* 80A, 333-341 (2007).

303. De Palma, R. et al. Silane Ligand Exchange to Make Hydrophobic Superparamagnetic Nanoparticles Water-Dispersible. *Chem. Mater.* 19, 1821-1831 (2007).

304. Korolev, V.V., Ramazanova, A.G. & Blinov, A.V. Adsorption of surfactants on superfine magnetite. *Russian Chemical Bulletin* 51, 2044-2049 (2002).

305. Willis, A.L., Turro, N.J. & O'Brien, S. Spectroscopic Characterization of the Surface of Iron Oxide Nanocrystals. *Chem. Mater.* 17, 5970-5975 (2005).

306. Tao, K., Dou, H. & Sun, K. Facile Interfacial Coprecipitation To Fabricate Hydrophilic Amine-Capped Magnetite Nanoparticles. *Chem. Mater.* 18, 5273-5278 (2006).

307. Yamaura, M. et al. Preparation and characterization of (3-aminopropyl)triethoxysilane-coated magnetite nanoparticles. *J. Magn. Magn. Mater.* 279, 210-217 (2004).

308. Wang, Y., Teng, X., Wang, J.-S. & Yang, H. Solvent-Free Atom Transfer Radical Polymerization in the Synthesis of Fe2O3@Polystyrene Core−Shell Nanoparticles. *Nano Lett.* 3, 789-793 (2003).

309. Yan, F., Li, J., Zhang, J., Liu, F. & Yang, W. Preparation of Fe3O4/polystyrene composite particles from monolayer oleic acid modified Fe3O4 nanoparticles via miniemulsion polymerization. *J. Nanopart. Res.* 11, 289-296 (2009).

310. WH, A. Engine coolant testing: state of the art. (ASTM STP 705, 1980).

311. Li, K., Zhang, W., Huang, Y. & Chen, Y. Aggregation kinetics of CeO2 nanoparticles in KCl and CaCl2 solutions: measurements and modeling. *J. Nanopart. Res.* 13, 6483-6491 (2011).

312. Kirby, B.J. & Hasselbrink, E.F. Zeta potential of microfluidic substrates: 1. Theory, experimental techniques, and effects on separations. *Electrophoresis* 25, 187 (2004).

313. Saeeduddin, Khanzada, A.W.K. & Mufti, A.T. Dissociation constant studies of citric acid at different temperatures and in different organic-water solvent systems *Journal of The Chemical Society of Pakistan* 18 (1996).

314. Chiavazzo, E. & Asinari, P. Reconstruction and modeling of 3D percolation networks of carbon fillers in a polymer matrix. *International Journal of Thermal Sciences* 49, 2272-2281 (2010).

315. Buongiorno, J. et al. A benchmark study on the thermal conductivity of nanofluids. *Journal of Applied Physics* 106, 094312 (2009).

316. Wang, X.-j., Zhu, D.-s. & yang, S. Investigation of pH and SDBS on enhancement of thermal conductivity in nanofluids. *Chemical Physics Letters* 470, 107-111 (2009).

Appendix 1

Matlab programme of assemble particles into a sphere-like cluster

```
config_stab=dlmread('config_100');
config=config_stab;
[N,~]=size(config_stab);
num_cluster=2;
r_par=6;
r=randi(num_cluster,N,1);
r(:,2)=[1:1:N]';
tingxia=0;
while tingxia==0
for ll=1:num_cluster
geshu(ll,1)=length(find(r(:,1)==ll));
geshu(ll,2)=ll;
end

if length(find(geshu(:,1)<50))==0
   tingxia=1;
else
   [N_duo,duo]=max(geshu(:,1));
   [~,bugou]=min(geshu(:,1));
   duo_max=r(find(r(:,1)==geshu(duo,2)),:);
   r(duo_max(randi(N_duo,1,1),2),1)=geshu(bugou,2);
end
end
config(:,14)=r(:,1);
config_clusters=cell(num_cluster,1);

for l=1:num_cluster
   config_clusters{l,1}=config(config(:,14)==l,:);
   [N_par_cluster,~]=size(config_clusters{l,1});
   conf_par=zeros(N_par_cluster,4);
   conf_par_attempted=zeros(N_par_cluster,3);
   conf_par(1,4)=1;
   new=zeros(1,3);
   r_droplet=50;
```

```
    for j=2:N_par_cluster

        num=1;
        while num~=0
            theta=unifrnd(0,180,1,1);
            phi=unifrnd(0,360,1,1);
            jing=unifrnd(0,r_droplet-r_par,1,1);
            new(1,1)=jing*sind(theta)*cosd(phi);
            new(1,2)=jing*sind(theta)*sind(phi);
            new(1,3)=jing*cosd(theta);
            conf_par_copy=conf_par(1:j-1,:);
            vec_r=bsxfun(@minus,conf_par_copy(:,1:3),new);
            modvec_r=(diag(vec_r* vec_r')).^0.5;
            num=length(find(modvec_r(:,1)<2*r_par));

        end
        conf_par(j,1:3)=new;
        conf_par(j,4)=j;


    end
    norm_velocity_dro=0.1;
    norm_velocity_par=1;
    theta_velocity_par=unifrnd(0,180,N_par_cluster,1);
    phi_velocity_par=unifrnd(0,360,N_par_cluster,1);
    velocity_par=zeros(N_par_cluster,3);

velocity_par(:,1)=norm_velocity_par*sind(theta_velocity_par).*cosd(phi_velo
city_par);

velocity_par(:,2)=norm_velocity_par*sind(theta_velocity_par).*sind(phi_velo
city_par);
    velocity_par(:,3)=norm_velocity_par*cosd(theta_velocity_par);
    tingzhi=0;
    t=0;
    S=0;
    BB=1;
    qiudao{l,1}(1,1)=0;
    qiudao{l,1}(2,1)=0;
    qiudao{l,1}(3,1)=r_droplet;
    modvec_par_par=[];
```

```
    if N_par_cluster==1
          conf_par(1,1)=0;
          conf_par(1,2)=0;
          conf_par(1,3)=0;
          r_final_dro(l,1)=r_par;
    else
   while tingzhi==0
        tic;
         aa=1;
      for k=1:N_par_cluster-1
          for o=k+1:N_par_cluster
             vec_par_par=conf_par(o,1:3)-conf_par(k,1:3);
             modvec_par_par(aa,1)=(vec_par_par*vec_par_par')^0.5;
             modvec_par_par(aa,2)=k;
             modvec_par_par(aa,3)=o;
             aa=aa+1;
          end
      end
      xishu_a_2=diag((velocity_par(modvec_par_par(:,2),:)-
velocity_par(modvec_par_par(:,3),:))*(velocity_par(modvec_par_par(:,2),:)-
velocity_par(modvec_par_par(:,3),:))');
      xishu_b_2=diag(2*(conf_par(modvec_par_par(:,2),1:3)-
conf_par(modvec_par_par(:,3),1:3))*(velocity_par(modvec_par_par(:,2),:)-
velocity_par(modvec_par_par(:,3),:))');
      xishu_c_2=diag((conf_par(modvec_par_par(:,2),1:3)-
conf_par(modvec_par_par(:,3),1:3))*(conf_par(modvec_par_par(:,2),1:3)-
conf_par(modvec_par_par(:,3),1:3))')-4*r_par^2;
      fanggen_2=xishu_b_2.^2-4*xishu_a_2.*xishu_c_2;
      fanggen_2(abs(fanggen_2(:,1))<10^-6,:)=0;
      lable_shijie=find(fanggen_2(:,1)>=0);
      dt_chong{BB,1}=zeros(length(lable_shijie),3);
      dt_chong{BB,1}(:,1)=(-1*xishu_b_2(lable_shijie,1)-
(fanggen_2(lable_shijie,1)).^0.5)/2./xishu_a_2(lable_shijie,1);
      dt_chong{BB,1}(:,2:3)=modvec_par_par(lable_shijie,2:3);
      dt_chong{BB,1}(dt_chong{BB,1}(:,1)<0,:)=[];
      [M_chong,N_chong]=min(dt_chong{BB,1}(:,1));

      if length(M_chong)==0
          dt_chu{BB,1}=zeros(N_par_cluster,2);
          xishu_a=diag(velocity_par(:,1:3)*velocity_par(:,1:3)')-
norm_velocity_dro^2;
```

```
xishu_b=2*diag(conf_par(:,1:3)*velocity_par(:,1:3)')+2*norm_velocity_dro*(r_droplet-r_par);
        xishu_c=diag(conf_par(:,1:3)*conf_par(:,1:3)')-(r_droplet-r_par)^2;
        fanggen=xishu_b.^2-4*xishu_a.*xishu_c;
        fanggen(abs(fanggen(:,1))<10^-6,:)=0;
        dt_chu{BB,1}(:,1)=(-1*xishu_b+(fanggen).^0.5)/2./xishu_a;
        dt_chu{BB,1}(:,2)=conf_par(:,4);
        [M_chu,N_chu]=min(dt_chu{BB,1}(:,1));
        t=t+M_chu;
        S=S+sum(M_chu*(diag(velocity_par*velocity_par')).^0.5);
        conf_par(:,1:3)=bsxfun(@plus,conf_par(:,1:3),M_chu*velocity_par);
unit_faxian=conf_par(dt_chu{BB,1}(N_chu,2),1:3)/(conf_par(dt_chu{BB,1}(N_chu,2),1:3)*conf_par(dt_chu{BB,1}(N_chu,2),1:3)')^0.5;

        if velocity_par(dt_chu{BB,1}(N_chu,2),:)*unit_faxian'>0
          velocity_par(dt_chu{BB,1}(N_chu,2),:)=-2*velocity_par(dt_chu{BB,1}(N_chu,2),:)*(unit_faxian)'*unit_faxian+velocity_par(dt_chu{BB,1}(N_chu,2),:)-norm_velocity_dro*unit_faxian;
        else
velocity_par(dt_chu{BB,1}(N_chu,2),:)=velocity_par(dt_chu{BB,1}(N_chu,2),:)-norm_velocity_dro*unit_faxian;
        end
        r_droplet=r_droplet-norm_velocity_dro*M_chu;
        else
        r_droplet_attempted=r_droplet-norm_velocity_dro*M_chong;
conf_par_attempted(:,1:3)=bsxfun(@plus,conf_par(:,1:3),M_chong*velocity_par);
dis_center_edge=(diag(conf_par_attempted*conf_par_attempted')).^0.5+r_par;
        lable_chu=find(dis_center_edge>r_droplet_attempted);

        if length(lable_chu)==0
        t=t+M_chong;
        S=S+sum(M_chong*(diag(velocity_par*velocity_par')).^0.5);
        conf_par(:,1:3)=conf_par_attempted;
        r_droplet=r_droplet_attempted;
        vector_par_chong=conf_par(dt_chong{BB,1}(N_chong,3),1:3)-conf_par(dt_chong{BB,1}(N_chong,2),1:3);

unit_par_chong=vector_par_chong/(vector_par_chong*vector_par_chong' )^0.5;
```

```
v_par2_xiangdui=velocity_par(dt_chong{BB,1}(N_chong,2),:)*(unit_par_chong)'*unit_par_chong;
        v_par2_fen=velocity_par(dt_chong{BB,1}(N_chong,2),:)-v_par2_xiangdui;

v_par3_xiangdui=velocity_par(dt_chong{BB,1}(N_chong,3),:)*(unit_par_chong)'*unit_par_chong;
        v_par3_fen=velocity_par(dt_chong{BB,1}(N_chong,3),:)-v_par3_xiangdui;

velocity_par(dt_chong{BB,1}(N_chong,2),:)=v_par2_fen+v_par3_xiangdui;

velocity_par(dt_chong{BB,1}(N_chong,3),:)=v_par3_fen+v_par2_xiangdui;
        else
        dt_chu{BB,1}=zeros(length(lable_chu),2);

xishu_a=diag(velocity_par(lable_chu,1:3)*velocity_par(lable_chu,1:3)')-norm_velocity_dro^2;

xishu_b=2*diag(conf_par(lable_chu,1:3)*velocity_par(lable_chu,1:3)')+2*norm_velocity_dro*(r_droplet-r_par);
        xishu_c=diag(conf_par(lable_chu,1:3)*conf_par(lable_chu,1:3)')-(r_droplet-r_par)^2;
        fanggen=xishu_b.^2-4*xishu_a.*xishu_c;
        fanggen(abs(fanggen(:,1))<10^-6,:)=0;
        dt_chu{BB,1}(:,1)=(-1*xishu_b+(fanggen).^0.5)/2./xishu_a;
        dt_chu{BB,1}(:,2)=conf_par(lable_chu,4);
        [M_chu,N_chu]=min(dt_chu{BB,1}(:,1));
        t=t+M_chu;
        S=S+sum(M_chu*(diag(velocity_par*velocity_par')).^0.5);
        conf_par(:,1:3)=bsxfun(@plus,conf_par(:,1:3),M_chu*velocity_par);

unit_faxian=conf_par(dt_chu{BB,1}(N_chu,2),1:3)/(conf_par(dt_chu{BB,1}(N_chu,2),1:3)*conf_par(dt_chu{BB,1}(N_chu,2),1:3)')^0.5;
        if velocity_par(dt_chu{BB,1}(N_chu,2),:)*unit_faxian'>0
          velocity_par(dt_chu{BB,1}(N_chu,2),:)=-2*velocity_par(dt_chu{BB,1}(N_chu,2),:)*(unit_faxian)'*unit_faxian+velocity_par(dt_chu{BB,1}(N_chu,2),:)-norm_velocity_dro*unit_faxian;
        else
```

```
velocity_par(dt_chu{BB,1}(N_chu,2),:)=velocity_par(dt_chu{BB,1}(N_chu,2),:)-norm_velocity_dro*unit_faxian;
            end

            r_droplet=r_droplet-norm_velocity_dro*M_chu;
            end

        end

        qiudao{l,1}(1,BB+1)=t;
        qiudao{l,1}(2,BB+1)=S;
        qiudao{l,1}(3,BB+1)=r_droplet;

        yijiedao=gradient(qiudao{l,1}(3,:));

        if abs(yijiedao(1,BB+1))<1*10^-8
            tingzhi=1;
        end
        % if r_droplet<(100*(r_par^3)/0.5)^(1/3) %!!!!!!!!!!!!!!!!!!!!!!!!!!!!!!!
%         if BB==10000
%         tingzhi=1;
%         end

        disp(BB);
        BB=BB+1;
        r_droplet
    end
    r_final_dro(l,1)=r_droplet;
    toc;
    end
    config_clusters{l,1}(:,1:3)=conf_par(:,1:3);
end

aaa=1;
for l=1:num_cluster
    config_clusters{l,1}(:,1:3)=config_clusters{l,1}(:,1:3)+(l-1)*1000;
    modvec_par_par_final=[];
    [N_par_cluster,~]=size(config_clusters{l,1});
    if N_par_cluster==1
        modvec_par_par_final(1,1)=2*r_par+1;
```

```
        modvec_par_par_final(1,2)=1;
        modvec_par_par_final(1,3)=1;

    else
    for k=1:N_par_cluster-1
            for o=k+1:N_par_cluster
                vec_par_par=config_clusters{l,1}(o,1:3)-config_clusters{l,1}(k,1:3);
                modvec_par_par_final(aa,1)=(vec_par_par*vec_par_par')^0.5;
                modvec_par_par_final(aa,2)=k;
                modvec_par_par_final(aa,3)=o;
                aa=aa+1;
            end
    end
    end
    shibai=modvec_par_par_final(find(modvec_par_par_final(:,1)<2*r_par),:)

    config_final(aaa:aaa+N_par_cluster-1,:)=config_clusters{l,1};
    aaa=aaa+N_par_cluster;
end
Aver_r_final_dro=sum(r_final_dro)/num_cluster;
dlmwrite('config_100_2clusters_new', config_final,'precision',6,'newline', 'pc');
```

Appendix 2

Matlab programme of standard MC simulation

```
clear all
config_stab=dlmread('config_sphere_100_1');
config_chu=dlmread('config_100');
config_stab(:,4:13)=config_chu(:,4:13);
[N,~]=size(config_stab);    %the num of particle
H0=200*1000;               %amplitude of AC magnetic field (A/m)
T=1*298;                   %temperature (K)
Keff=1*0.9*10^4;           %anisotropy constant(J/m3)
Ms=1*446*1000;             %saturation magnetization (A/m) 110*5.18*1000
Radius=5*10^-9;    %radius of particle (m)
V=(4/3)*pi*(Radius)^3;    %volume of particle
kB=1.38065*10^-23;        %Boltzmann constant(J/K)
miu=4*pi*10^-7;           %permeability of free space(N/A2)
a=12*10^-9;               %lattice parameter
attempt=0.5*(0.05*kB*T/(2*Keff*V))^0.5;  %attempt angle domain
Eanis_diff=0;              %the difference in anisotropy energy of system before
and after attempted
Edi_1=0;                   %the sum of dipole couplings energy related to particle r
before attempted
Edi_2=0;                   %the sum of dipole couplings energy related to particle r
after attempted
Efield_diff=0;               %the difference in magnetic field energy of system
before and after attempted
moment=zeros(N,3);        %the unit moment vector(xyz)(after being attempted
in thermal)
theta_e_1=zeros(N,1);     %the angle between Z and modulus of easy axis(after
being attempted in thermal)
phi_e_1=zeros(N,1);       %the angle between x and modulus of easy axis(after
being attempted)
theta_m_1=zeros(N,1);     %the angle between Z and modulus of moment(after
being attempted)
phi_m_1=zeros(N,1);       %the angle between x and modulus of moment(after
being attempted)
coord_af=config_stab;     %record after the treatment
                          %random pick particle
num=1:1:N;
pick=zeros(N,14);         %the matrix of randomly-picked particle
```

```
num1=zeros(1,N);
r=0;                    %random num for picking particle
r_1=0;                   %random num for probability determination
pro=0;                   %probability of acceptance of attempt
step=100;                 %step of MC
cycle_num=200;
magn=zeros(100,cycle_num);        %magnetization along the axis of field
Ht=zeros(101,1);
unitvec_H=[0,0,1];
t=3.6:3.6:360;
guanghua=zeros(100,cycle_num);
oushi_yuan_guang=zeros(100,1);
avera=zeros(100,cycle_num);
sum_t=zeros(N-1,1)+1;
vec_r=cell(N,1);
unitvec_r=cell(N,1);
mod_vec_r=cell(N,1);

for l=1:N
   coord_af_1=coord_af;                                   %the calculation of the
difference in dipole energy of system before and after attempted
  coord_af_1(l,:)=[];                                  %remove the row r

vec_r{l,1}(:,1:3)=bsxfun(@minus,coord_af_1(:,1:3),coord_af(l,1:3));           %r
to j

unitvec_r{l,1}(:,1:3)=bsxfun(@rdivide,vec_r{l,1}(:,1:3),sqrt(diag(vec_r{l,1}(:,
1:3)* vec_r{l,1}(:,1:3)')));
   mod_vec_r{l,1}(:,1)=sqrt(diag(vec_r{l,1}(:,1:3)* vec_r{l,1}(:,1:3)'));
end

for cycle=1:cycle_num
for t_num=1:100
   mod_H=H0*sind(t(1,t_num));
   H=mod_H*unitvec_H;
tic;
for Mc=1:step

for i=1:N

   r_2=randi(length(num));
```

```
    r=num(:,r_2);
    pick(i,:)=coord_af(r,:);

    distance=unifrnd(0,sin(attempt),1,1);                              %distance between
moment original and attempted
    rotation=unifrnd(0,2*pi,1,1);
    ang=abs(pi/2-pick(i,12)+atan(distance*cos(rotation)/(cos(attempt))));
    if ang<=0.5*pi

phi_m_1(i,1)=pick(i,13)+atan(distance*sin(rotation)/(sqrt((cos(attempt))^2+(di
stance*cos(rotation))^2)*cos(ang)));
    else

phi_m_1(i,1)=pick(i,13)+atan(distance*sin(rotation)/(sqrt((cos(attempt))^2+(di
stance*cos(rotation))^2)*cos(ang)))+pi;
    end

theta_m_1(i,1)=acos(sqrt((cos(attempt))^2+(distance*cos(rotation))^2)/sqrt((di
stance)^2+(cos(attempt))^2)*sin(pi/2-
pick(i,12)+atan(distance*cos(rotation)/(cos(attempt)))));
    moment(i,1)=sin(theta_m_1(i,1))*cos(phi_m_1(i,1));
    moment(i,2)=sin(theta_m_1(i,1))*sin(phi_m_1(i,1));
    moment(i,3)=cos(theta_m_1(i,1));

    Eanis_diff=-Keff*V*((coord_af(r,4:6)*moment(i,:)')^2-
(coord_af(r,4:6)*coord_af(r,7:9)')^2); %the calculation of the difference in
anisotropy energy of system before and after attempted
coord_af_1=coord_af;                                   %the calculation of the
difference in dipole energy of system before and after attempted
coord_af_1(r,:)=[];                              %remove the row r

    Edi_diff=-miu*(Ms*V)^2/(4*pi)/(10^-27)*(3*(((moment(i,:)-
coord_af(r,7:9))*unitvec_r{r,1}(:,1:3)').*diag(coord_af_1(:,7:9)*unitvec_r{r,1
}(:,1:3)')')-((moment(i,:)-
coord_af(r,7:9))*coord_af_1(:,7:9)'))./(mod_vec_r{r,1}(:,1)').^3 *sum_t;
    %!!!!!no a^3
    Efield_diff=-miu*Ms*V*H*(moment(i,:)-coord_af(r,7:9))';
    pro=exp(-(Eanis_diff+Edi_diff+Efield_diff)/(kB*T));
    %pro=exp(-(Eanis_diff+Efield_diff)/(kB*T));
    if pro>=1
        coord_af(r,7)=moment(i,1);
```

```
        coord_af(r,8)=moment(i,2);
        coord_af(r,9)=moment(i,3);
        coord_af(r,12)=theta_m_1(i,1);
        coord_af(r,13)=phi_m_1(i,1);
    else
        r_1=unifrnd(0,1,1,1);
        if r_1<=pro
        coord_af(r,7)=moment(i,1);
        coord_af(r,8)=moment(i,2);
        coord_af(r,9)=moment(i,3);
        coord_af(r,12)=theta_m_1(i,1);
        coord_af(r,13)=phi_m_1(i,1);
        end
    end

   num(:,r_2)=[];
   pro=0;
   r_1=0;
   Eanis_diff=0;
   Efield_diff=0;
end
   num=1:1:N;

end
toc;
magn(t_num,cycle)=sum(coord_af(:,7:9)*unitvec_H')/N;
end

     if cycle>2
     avera(:,cycle)=sum(magn(:,2:cycle),2)/(cycle-1);
     guanghua(:,cycle)=smooth(avera(:,cycle),5,'sgolay');
oushi_yuan_guang(cycle,1)=sqrt(sum((bsxfun(@minus,guanghua(:,cycle),aver
a(:,cycle))).^2));
     end
     disp(cycle);
end
oushi_guang_guang=zeros(100,1);
for i=3:cycle_num
dif=bsxfun(@minus,guanghua(:,i),guanghua(:,cycle_num));
oushi_guang_guang(i,:)=sqrt(sum((dif).^2));
end
```

```
for k=3.6:3.6:363.6
    mod_H=H0*sin(k/180*pi);
    Ht(round(k/3.6),1)=mod_H/(2*Keff/Ms/miu);
end
mian=zeros(cycle_num,1);
guanghua_1=guanghua;
guanghua_1(101,:)=guanghua_1(1,:);

for j=1:cycle_num
mian(j,1)=abs(trapz(Ht,guanghua_1(:,j)));
end
```

Appendix 3

Matlab programme of KMC simulation

```
clear all
config_stab=dlmread('config_after_easy_444_anneal');
N=length(config_stab);    %the num of particle
H0=200*1000;              %amplitude of AC magnetic field (A/m)
T=100;                    %temperature (K)
Ms=446*1000;              %saturation magnetization (A/m) 110*5.18*1000
Radius=5*10^-9;   %radius of particle (m)
V=(4/3)*pi*(Radius)^3;    %volume of particle
kB=1.38065*10^-23;        %Boltzmann constant(J/K)
Keff=10*9000;             %anisotropy constant(J/m3)
miu=4*pi*10^-7;           %permeability of free space(N/A2)
a=12*10^-9;               %lattice parameter
v_0=10^9;
coord_af=config_stab;     %record after the treatment
step=2000;                %step of MC
t=(360/step:360/step:360)/180*pi;
H_fre=100;
t_step=1/H_fre/step;
cycle_num=50;
magn=zeros(step,cycle_num);       %magnetization along the axis of field
Ht=zeros(step+1,1);
unitvec_H=[0,0,1];
guanghua=zeros(step,cycle_num);
oushi_yuan_guang=zeros(step,1);
avera=zeros(step,cycle_num);
vec_r=cell(N,1);
unitvec_r=cell(N,1);
mod_vec_r=cell(N,1);
H_dip=zeros(N,3);
theta_m_e=(-2:1:360)/180*pi;
sin_theta_m_e=sin(theta_m_e);
pro=zeros(N,1);
r_1=zeros(N,1);
E_total_jidazhi=zeros(1,1);
E_total_jixiaozhi=zeros(1,2);
E_total_jixiaozhi_final=zeros(N,2);
angle_jixiaozhi_final=zeros(N,2);
```

```
angle_jixiaozhi=zeros(N,2);
fangcheng=zeros(3,4);

for l=1:N
   coord_af_1=coord_af;                                    %the calculation of the
difference in dipole energy of system before and after attempted
   coord_af_1(l,:)=[];                                  %remove the row r

vec_r{l,1}(:,1:3)=bsxfun(@minus,coord_af_1(:,1:3),coord_af(l,1:3));          %r
to j

unitvec_r{l,1}(:,1:3)=bsxfun(@rdivide,vec_r{l,1}(:,1:3),sqrt(diag(vec_r{l,1}(:,
1:3)* vec_r{l,1}(:,1:3)')));
   mod_vec_r{l,1}(:,1)=sqrt(diag(vec_r{l,1}(:,1:3)* vec_r{l,1}(:,1:3)'));
end
for cycle=1:cycle_num
   tic;
for t_num=1:step
   mod_H=H0*sin(t(1,t_num));
   H=mod_H*unitvec_H;

   for r=1:N
      coord_af_1=coord_af;                                 %the calculation of the
difference in dipole energy of system before and after attempted
      coord_af_1(r,:)=[];                               %remove the row r

H_dip=sum(Ms*V/(4*pi)/(a^3)*bsxfun(@rdivide,(3*bsxfun(@times,unitvec_r
{r,1}(:,1:3),diag(coord_af_1(:,7:9)*unitvec_r{r,1}(:,1:3)'))-
coord_af_1(:,7:9)),(mod_vec_r{r,1}(:,1)).^3));

      H_total=H+H_dip;
      Mod_H_total=sqrt( H_total*H_total');
      unit_H_total=H_total/Mod_H_total;
      fangcheng(1,1:3)=cross(coord_af(r,4:6),unit_H_total); %equstion
      fangcheng(2,1:3)=coord_af(r,4:6);
      fangcheng(3,1:3)=unit_H_total;
      cos_zhi=unit_H_total*coord_af(r,4:6)';

      if cos_zhi<-1
         phi_H_e=pi;
      elseif cos_zhi>1
```

```
        phi_H_e=0;
    else
        phi_H_e=acos(cos_zhi);
    end

    E_total_volumetic=Keff*(sin_theta_m_e).^2-miu*Ms*Mod_H_total*cos(theta_m_e-phi_H_e);
    jidazhi=find(diff(sign(diff(E_total_volumetic)))==-2)+1;
    jixiaozhi=find(diff(sign(diff(E_total_volumetic)))==2)+1;
    num_jixiaozhi=length(jixiaozhi);

    if num_jixiaozhi==1
    angle_jixiaozhi_final(r,1)=theta_m_e(:,jixiaozhi);
    angle_jixiaozhi_final(r,2)=theta_m_e(:,jixiaozhi);
    fangcheng(2,4)=cos(angle_jixiaozhi_final(r,1));
    fangcheng(3,4)=cos(angle_jixiaozhi_final(r,1)-phi_H_e);
    coord_af(r,7:9)=(fangcheng(1:3,1:3)\fangcheng(:,4))';
    else

    E_total_jixiaozhi(1,:)=E_total_volumetic(:,jixiaozhi);
    angle_jixiaozhi(r,:)=theta_m_e(:,jixiaozhi);
    angle_m_e=acos(coord_af(r,7:9)*coord_af(r,4:6)');
   [~,m]=max(E_total_volumetic);
   angle_max=theta_m_e(:,m);
   zhuan_jixiaozhi=angle_jixiaozhi(r,:)+pi-angle_max; %To do this, I put minimum1, minimum 2 and the position of the magnetization in a [0 2pi] interval, with the maximum of the energy barrier at Pi. If the position of the magnetization is below (above) Pi, the magnetization falls directly into the left (right) minimum.
   zhuan_m=angle_m_e+pi-angle_max;

zhuan_jixiaozhi((zhuan_jixiaozhi(:)<0))=zhuan_jixiaozhi((zhuan_jixiaozhi(:)<0))+2*pi;
   zhuan_m((zhuan_m(:)<0))=zhuan_m((zhuan_m(:)<0))+2*pi;
   if zhuan_m<pi
     E_total_jixiaozhi_final(r,1)= E_total_jixiaozhi(1,zhuan_jixiaozhi(:)<pi);
     E_total_jixiaozhi_final(r,2)= E_total_jixiaozhi(1,zhuan_jixiaozhi(:)>pi);
     angle_jixiaozhi_final(r,1)=angle_jixiaozhi(r,zhuan_jixiaozhi(:)<pi);
     angle_jixiaozhi_final(r,2)=angle_jixiaozhi(r,zhuan_jixiaozhi(:)>pi);
   else
     E_total_jixiaozhi_final(r,1)= E_total_jixiaozhi(1,zhuan_jixiaozhi(:)>pi);
```

```
        E_total_jixiaozhi_final(r,2)= E_total_jixiaozhi(1,zhuan_jixiaozhi(:)<pi);
        angle_jixiaozhi_final(r,1)=angle_jixiaozhi(r,zhuan_jixiaozhi(:)>pi);
angle_jixiaozhi_final(r,2)=angle_jixiaozhi(r,zhuan_jixiaozhi(:)<pi);
      end

      E_total_jidazhi_raw(1,:)=E_total_volumetic(:,jidazhi);
      [~, n]=min(E_total_jidazhi_raw(1,:));
      E_total_jidazhi(:,1)=E_total_jidazhi_raw(:,n);
      v_1=v_0*exp(-1*(E_total_jidazhi(1,1)-
E_total_jixiaozhi_final(r,1))*V/kB/T);
      v_2=v_0*exp(-1*(E_total_jidazhi(1,1)-
E_total_jixiaozhi_final(r,2))*V/kB/T);
      pro(:,r)=v_1/(v_1+v_2)*(1-exp(-1*(v_1+v_2)*t_step));
      r_1(:,r)=unifrnd(0,1,1,1);%random number is generated
      if r_1(:,r)<=pro(:,r)
          fangcheng(2,4)=cos(angle_jixiaozhi_final(r,2));
          fangcheng(3,4)=cos(angle_jixiaozhi_final(r,2)-phi_H_e);
          coord_af(r,7:9)=(fangcheng(1:3,1:3)\fangcheng(:,4))';
      else
          fangcheng(2,4)=cos(angle_jixiaozhi_final(r,1));
          fangcheng(3,4)=cos(angle_jixiaozhi_final(r,1)-phi_H_e);
          coord_af(r,7:9)=(fangcheng(1:3,1:3)\fangcheng(:,4))';

      end
      end
    end
   magn(t_num,cycle)=sum(coord_af(:,7:9)*unitvec_H')/N;

end
  if cycle>2
     avera(:,cycle)=sum(magn(:,2:cycle),2)/(cycle-1);
     guanghua(:,cycle)=smooth(avera(:,cycle),10,'sgolay');

oushi_yuan_guang(cycle,1)=sqrt(sum((bsxfun(@minus,guanghua(:,cycle),aver
a(:,cycle))).^2));

end
     disp(cycle);
toc;
end
oushi_guang_guang=zeros(step,1);
```

```
for i=3:cycle_num
dif=bsxfun(@minus,guanghua(:,i),guanghua(:,cycle_num));
oushi_guang_guang(i,:)=sqrt(sum((dif).^2));
end
for k=1:step
   mod_H=H0*sin(t(1,k));
   Ht(k,1)=mod_H/(2*Keff/Ms/miu);

end
Ht(step+1,1)=Ht(1,1);
mian=zeros(cycle_num,1);
guanghua_1=guanghua;
guanghua_1(step+1,:)=guanghua_1(1,:);
for j=1:cycle_num
mian(j,1)=abs(trapz(Ht,guanghua_1(:,j)));
end
```